Dynamical properties of nano-structured catalysts for methane conversion: an in situ scattering study

Kehres, Jan

Publication date:
2011

Document Version
Publisher's PDF, also known as Version of record

Dynamical properties of nano-structured catalysts for methane conversion:
an in situ scattering study

Risø-PhD-Report

Jan Kehres
Report number: Risø-PhD-76(EN)
Publication date: April 2011

Risø DTU
National Laboratory for Sustainable Energy

Author: Jan Kehres
Title: Dynamical properties of nano-structured catalysts for methane conversion: *an in situ scattering study*
Division: Materials Research Division

This thesis is submitted partial fulfilment of the requirements for the Ph.D. degree at the Technical University of Denmark

Report number: Risø-PhD-76(EN)

Publication date:
April 2011

ISBN 978-87-550-3895-0

Abstract:

The reactivity of catalyst particles can be radically enhanced by decreasing their size down to the nanometer range. The nanostructure of a catalyst can have an enormous and positive influence on the reaction rate, for example strong *structure sensitivity* was observed for methane reforming and ammonia synthesis, and it is therefore crucial that catalysts preserve their nanostructures under operational conditions. Fundamental understanding of the relation between the catalytic activity and the morphology of the nanoparticle, their crystallinity and crystallite size, is required to improve the catalysts and assess the optimum conditions of operation. A powerful and suitable technique to resolve these relations is simultaneous small and wide angle X-ray scattering coupled with mass spectroscopy measurements, performed *in situ* at conditions comparable to large scale processes.

A new heater setup for an *in situ* cell, accommodated in a laboratory SAXS/WAXS camera, has been developed and a sample gas system has been designed and installed. A mass spectrometer has been implemented to monitor the chemical reactions during the *in situ* experiments. The heater permits experiments in a temperature range from 298 - 1073 K. The heater performance was tested and it was shown that no temperature calibration is needed.

The applicability of the new setup, to study nanostructured materials, was successfully demonstrated using anatase TiO_2 nanorods. Heating experiments on the nanorods were performed in a temperature range from 298 - 1023 K. Correlated crystallite and particle growth due to sintering were observed after the decomposition of the surfactant. Furthermore transformations from rod to spherical particle shape were observed.

In situ reduction experiments of a $Ni/MgAl_2O_4$ catalyst were performed. The Ni/NiO particles in a fresh catalyst sample showed a Ni/NiO core shell structure. The Ni lattice parameter decreased during the reduction due to the release of stress between the Ni core and the NiO shell. Ni particles sintered during heating in hydrogen after the reduction of the NiO shell. Dry reforming experiments were performed over a $Ru/MgAl_2O_4$. The catalyst showed a high sintering stability and no catalyst deactivation was observed.

The results presented in this thesis emphasize the advantage of the simultaneous SAXS/WAXS laboratory setup to study nanostructured materials and catalysts *in situ*.

Pages:187
References:142

Information Service Department
Risø National Laboratory for Sustainable Energy
Technical University of Denmark
P.O.Box 49
DK-4000 Roskilde
Denmark
Telephone +45 46774005
bibl@risoe.dtu.dk
Fax +45 46774013
www.risoe.dtu.dk

Resume:

Katalysatorpartikler kan udvise en drastisk forøget re-aktivitet på nano-skala. En katalysators nanostruktur kan have en enorm indflydelse på reaktionsraten. Struktur følsomhed blev observeret for reforming af metan og for ammoniak syntesen. Derfor er det altafgørende, at katalysatoren beholder sin nanostruktur under realistiske driftsbetingelser. En grundlæggende forståelse af sammenhængen mellem katalytisk aktivitet, nanopartiklers morfologi, krystallit størrelse og tilstand er påkrævet for at forbedre katalysatoren og for at vurdere de optimale driftsbetingelser. En passende metode til at undersøge disse sammenhænge er simultan små- og vidvinkel røntgen spredning, som udføres *in situ* under betingelse der er sammenlignelige med processorer på stor skala kombineret med masse spektroskopi.

Et nyt varmeelement og gas system til en *in situ* celle indbygget i et laboratorie SAXS/WAXS setup blev udviklet. Et masse-spektrometer blev indbygget til at overvåge de kemiske reaktioner under *in situ* eksperimenterne. Varmeelementet tillod eks-perimenter i temperaturområdet 298 - 1073 K. Varmeelementets virkning blev afprøvet og det blev påvist at ingen kalibrering af temperaturen var nødvendig.

Opvarmningsforsøg med anatase TiO_2 nanorods blev foretaget i temperaturområdet 298 - 1073 K. Korreleret krystallit og partikelvækst ved sintring blev observeret efter overfladen var dekomponeret. En transformation fra stang til kugleformede partikler blev observeret. Forsøget viste brugbarheden af opstillingen til studier af materialer med nanostruktur.

In situ reduktionsforsøg på en $Ni/MgAl_2O_4$ katalysator blev udført. Ni/NiO partiklerne fra en frisk katalysatorprøve udviste en Ni/NiO 'core shell' struktur. Ni gitterparametre formindskedes under reduktionen på grund af udløsning af spænding i mellem Ni kernen og NiO skallen. Ni partikler sintrerede under opvarmningen i en brintholdig atmosfære efter reduktionen af NiO skallen. Eksperimenter med tør reformering af metan over en $Ru/MgAl_2O_4$ katalysator. Katalysatoren udviste en høj grad af stabilitet overfor de sintrerede partikler, og der blev ikke observeret nogen de-aktivering af katalysatoren.

Resultaterne præsenteret i denne afhandling fremhæver fordelene ved den samtidige SAXS/WAXS opstilling, til at studere materialer med nanostruktur og især katalysatorer *in situ*.

Ph.D. Thesis

Dynamical properties of nano-structured catalysts for methane conversion: *an in situ scattering study*

Jan Kehres

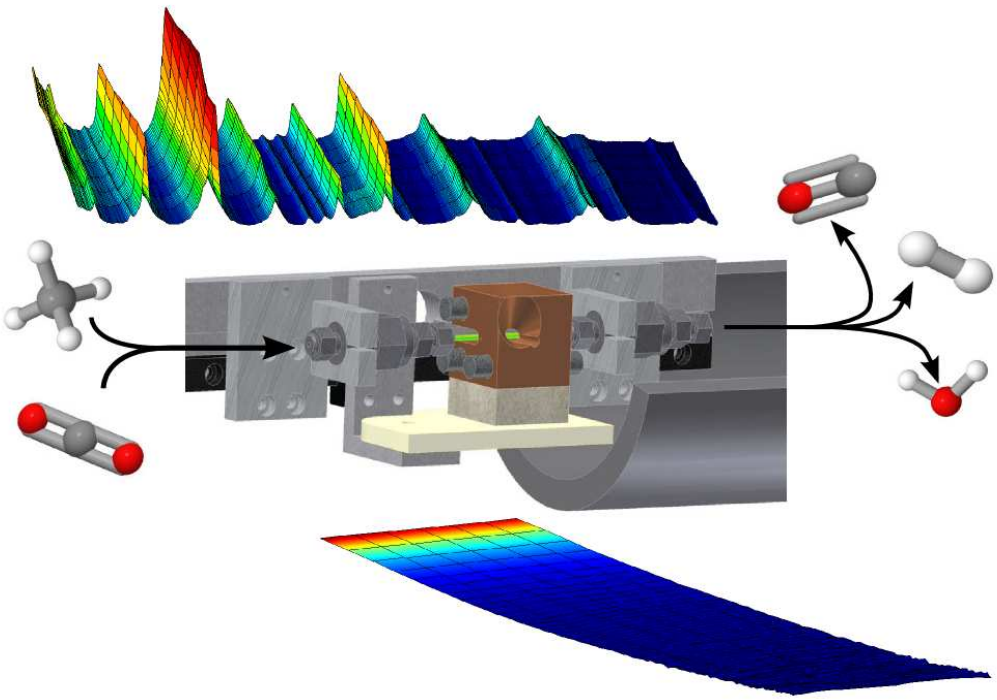

January 2011

Risø DTU
National Laboratory for Sustainable Energy

Technical University of Denmark
DTU

Preface

This thesis is submitted in candidacy for the Ph.D. degree from the Technical Universtity of Denmark (DTU). This work has been carried from September 2007 to January 2011 in the Materials Research Department of Risø DTU - National Laboratory for Sustainable Energy, in cooperation with the Center for Individual Nanoparticle Functionality (CINF), Department of Physics, DTU and Haldor Topsøe A/S. The work has been supervised by Ph.D. senior scientist Tejs Vegge and Ph.D. senior scientist Jens Wenzel Andreasen from Risø DTU, Prof. Ib Chorkendorff from CINF, DTU and Dr. Alfons Molenbroek from Haldor Tospøe A/S. The work was financial supported from the Copenhagen Graduate School for Nanoscience and Nanotechnology (C:O:N:T) and Haldor Topsøe A/S.

I would like to thank my supervisors for the numerous seminal scientific discussions and the superior guidance during this project. For excellent cooperation, fruitful discussions and support with catalyst materials I want to thank Ph.D. Jon Geest Jakobsen. Prof. Frederik Christian Krebs is thanked for his cooperation in the synthesis of titanium nanoparticles to verify the usability of the experimental setup; the results of those experiments led to an international publication. Furthermore I want to thank Ph.D. Didier Blanchard for explanatory assistance of data refinement. For improvements of the WAXS 1D transformation I would to thank Hjalte Sylvest Jacobsen. Ph.D. Haihua Lui and Ph.D. senior scientist Søren Fæster Nielsen are thanked for assistance with electron microscopy. Senior Electronics Design Engineer Henning Engelbrecht Larsen is thanked for assistance with Labview. I would like to thank Ph.D. Didier Blanchard, Steen Lysgaard, Dadi Sveinbjörnsson and Jakob Geelmuyden Howalt for proof reading of my thesis.

The present results would not have been achieved without the assistance of the technicians at Risø. In this context I would like especially to thank Steen Bang, Ove Rasmussen, Torben Kjær and Mike Wichmann. Moreover I want to thank my former and present colleges Ph.D. Qing Shi, Ph.D. Nicolai Bork and Ph.D. senior scientist Allan S. Pedersen. For financially support I would like to thank the Copenhagen Graduate School for Nanoscience and Nanotechnology (C:O:N:T) and Haldor Topsøe A/S.

Contents

List of papers

Paper I: Combined *in situ* small and wide angle X-ray scattering studies of TiO_2 nano-particle annealing to 1023 K

Paper II: Dynamical properties of a Ni/spinel methane reforming catalyst during the reduction

Paper III: Dynamical properties of a Ru/spinel catalyst during reduction and dry methane reforming

Paper IV: Hydrogen rotational and translational diffusion in calcium borohydride from quasi elastic neutron scattering and DFT

1 Introduction

1.1 Heterogeneous catalysts

Catalysts are extremely important in our modern world. Approximately 90 % of all chemical processes involve catalysts. Catalysts are indispensable for the production of bulk and fine chemicals, fuels, pharmaceuticals, food and cleaning of exhaust from automobiles and stationary sources (Dumesic *et al.* 2008, Dingerdissen *et al.* 2008). Nature also use catalysts, enzymes for example are the most specific catalysts one can think of. The term catalysis was introduced around 1835 by Berzelius and further defined by Ostwald in 1901: A catalyst is any substance that increases the rate of a chemical reaction, without being part of the product itself. Catalysts accelerate the reaction by bonding with the reactant to offer an energetically more favourable pathway, the product detaches and leaves the catalyst unaltered (Chorkendorff and Niemantsverdriet, 2003), see figure 1.

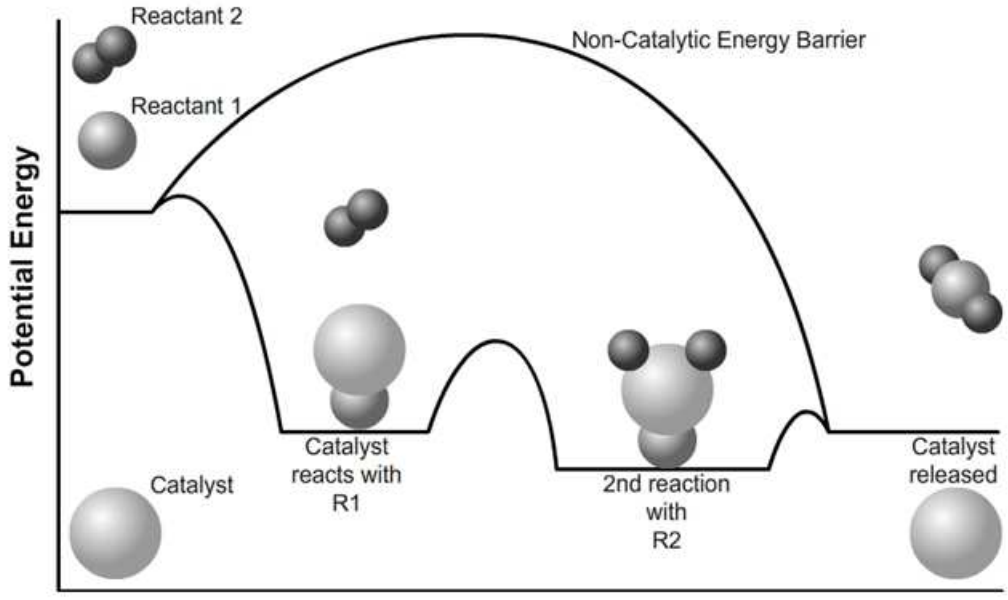

Figure 1: Energy diagram for a catalytic and non-catalytic reaction of gaseous reactants on a heterogeneous catalyst. The reaction energy barrier for the non-catalytic reaction is much higher compared to the barriers of the catalytic reaction.[from:http://www.spaceflight.esa.int/impress/text/education/Catalysis/index.html]

Catalysts, used in chemical processes, can be classified in two groups, homogeneous and heterogeneous. Homogeneous catalysts are in the same phase as the reactants, heterogeneous catalysts are solids and reactants are either gaseous or liquid. Both groups of catalysts are applied in large scale processes, though application of heterogeneous catalysts is for most large scale processes preferable since they can be easily separated from the reaction products. Oxo-synthesis of alkenes to aldehydes, catalyzed with rhodium-phoshines or cobalt carbonyls and the polymerisation of ethylene to high density polyethylene (HDPE) with aluminium alkyls (Ziegler catalyst) are important large scale processes utilizing homogeneous catalysts (Behr, 2010). Probably the most important large-scale process using a heterogeneous catalyst is the ammonia synthesis. The studies in this thesis were performed on heterogeneous catalysts.

Conventional heterogeneous catalysts consist of fine dispersed metal particles on porous support materials such as aluminium oxides, silicon oxide, zirconium oxide, magnesia aluminium, zeolites or carbon. The support itself may also be catalytically active, but its main purpose is to provide a large internal surface to allow good dispersion of the active metal and also to hinder sintering from taking place (Gallei *et al*. 2008).

1.2 Active sites and structural sensitivity

The concept of active sites in heterogeneous catalysis is attributed to the theory of the catalytic surfaces by Taylor (1928) who proposed that the number of surface sites is much larger than the number of atom sites that catalyses the reaction. The active sites are those where the catalytic reaction initiates i.e. due to adsorption or/and dissociation of a reactant molecule. Active sites are often referred to be under coordinated atoms on the catalyst particle surface such as: surface clusters, steps, step vacancies, kink edges and terrace vacancies (see figure 1). The support may also provide active sites such as oxygen vacancies, surface hydroxyl groups (Ferreira-Aparicio *et al.*, 2000) or the formation of highly active support-metal complexes ([a]Bradford and Vannice, 1999) at the interface may also occur.

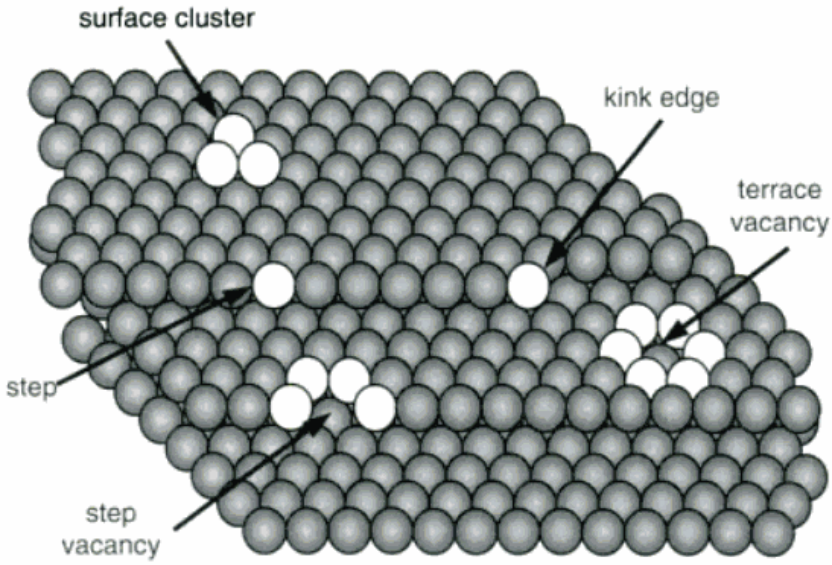

Figure 2: Schematic of irregularities of a catalyst surface [Rotenberg (2008)]

Structure sensitivity is one elemental concept in catalyst research. Reactions can be classified in *structure sensitive* or *structure insensitive* (Mark and Meier, 1996, Bond, 1991). For *structure insensitive* reactions the rates, expressed per unit metal surface area, are independent of the catalyst dispersion and correlate solely with the overall accessible surface area. The rates for *structure sensitive* reactions per unit metal surface area depend on several factors such as the metal particle dispersion, since higher dispersions result in larger numbers of under coordinated step and corner atoms, or the particle shape because a given structure might provide a larger amount of a given crystal plane or specific arranged surface atoms preferred for the catalyst turnover. Elongated Ru particles showed an increased turn over frequency for the ammonia synthesis compared to spherical ones because of large number of B_5 sites that are assumed to be the active sites for the ammonia synthesis (Karim *et al.*, 2009). *Structure sensitive* or *insensitivity* can be determined by measuring the turn over frequency of catalysts with different dispersions. If the catalytic turnover is assumed to be dependent on the arrangement of the surface atoms, the reactions rates of different planes of a single crystal can be used to assess *structure sensitivity*.

The particle size of the active metal can be crucial for the performance of a catalyst. Bulk Au is catalytically inactive, but it was reported that Au nanoparticles, finely dispersed on transition metal oxides such as α-Fe_2O_3, NiO and Co_3O_4, catalyse the CO oxidation at temperatures so low as 203 K (Haruta *et al.*, 1987, Haruta *et al.*, 1989). A strong *structure sensitivity* of Au catalysts was reported, among others, by Valden *et al.* (1998), who noted that TiO_2 supported Au clusters showed the highest turn over frequency with cluster sizes of 3.2 nm and this has been related to the unique electronic structure of these Au clusters, which exhibit a band gap in contrast to bulk gold.

1.3 In situ experiments

Heterogeneous catalyzed reaction take place at the gas/solid interface. A major topic in surface science is therefore the investigation of heterogeneous catalysts. Studies in surface science are performed in ultra high vacuum on clean single crystals or supported metal particles on single crystals to get a fundamental understanding of adsorption sites, dissociation and reaction pathways and they are therefore very valuable to develop and improve novel catalysts. However, those studies are performed under idealized conditions and the extrapolation to heterogeneous catalysts under real pressures is not always possible. Therefore it is necessary to perform *in situ* experiments under working pressures of heterogeneous catalysts in large scale processes to close this pressure gap.

In situ experiments are crucial to get fundamental understanding of the dynamics of catalyst formation and during chemical reactions and study the correlations between particle morphology, crystallinity, phase composition and activity. Furthermore, it might be possible with such experiments to identify whether a reaction is *structure sensitive* or *insensitive*. Two techniques to resolve the nanostructure of catalyst samples are electron microscopy and small angle X-ray scattering (SAXS).

Electron microscopy is a direct method to resolve the nanostructure of a catalyst. New environmental transmission electron microscopes (ETEM) permits the study of catalyst particle morphology *in situ*, i.e. at elevated temperatures and in a reactant gas flow. ETEM was utilized in various catalyst studies such as: sintering of Ni catalyst particles (Sehested 2006), carbon formation during steam reforming on Ni catalysts (Helveg *et al.*, 2004) or the evolution of the Ru particle sizes during reduction of a Ru/ZrO_2-catalyst ([b]Jacobsen *et al.*, 2010). Microdiffraction patterns of the electron beam can provide additional information about the crystalline phases. However, the structural information obtained from ETEM has, depending on the magnification, a very local character and usually projections from a few to several hundred nm^2 are observed. Furthermore the maximum applicable pressure for *in situ* experiments in an ETEM limited to a few mbar close to the sample because the microscope has to be kept in vacuum to prevent scattering of the electron beam by gases. The number of ETEM's is rather limited and the operation of such a microscope is difficult.

Another powerful method to resolve the nanostructure of the catalyst samples is SAXS, as shown for example by *ex situ* experiments to study the support material (Rasmussen, 2001) and sintering of a Ni catalyst for steam reforming (Rasmussen *et al.*, 2004) and *in situ* calcination of Pt/NaY (Brumberger *et al.*, 1996). The main advantage of this technique is that *in situ* experiments can be performed at relevant conditions for large scale processes, using a setup with a sapphire capillary permits pressures up to several

hundred bars at temperatures of a thousand Kelvin. The scattering patterns assemble the nanostructure of the volume illuminated by the incident X-ray beam that is usually in the order of 1 mm^3. A disadvantage of this technique is that the information obtained is in reciprocal space and adequate models needed for the data analysis.

Combining two different and independent techniques to probe dynamical changes of nanostructured materials, under various chemical and thermal conditions, can be advantageous since one individual method might not be sufficient to resolve the complicated relation between structure, sample composition and environment. Simultaneous data acquisition of the different techniques can be crucial if the probing conditions are not reproducible. For this thesis, simultaneous small and wide angle X-ray scattering (SAXS/WAXS) measurements were chosen to follow the dynamical changes of nanostructured catalysts during sample heating and exposure with reactant gas. SAXS is used to follow changes of the nanostructure and WAXS to track phase changes. SAXS arises from inhomogeneities of the average electron density in the material. But it does not allow to distinguish from which electron density difference the SAXS arises. A supported metal catalyst consists of at least three phases with different average electron density, the support, the metal-particles and the voids in between (pores) and this complicates the data analysis.

WAXS provides information about phase composition and crystallite sizes, but cannot provide information about amorphous materials. Combining the results of both techniques can be beneficial to resolve the nanostructure because dynamical changes in the sample morphology might be correlated with changes in the sample phase composition and crystallite size. Simultaneous SAXS/WAXS, in combination with an analytical method to probe the gas composition, in this study mass spectrometry, allow resolving correlations between crystalline structure, particle morphology and activity of the catalyst in dependence with the temperature.

Combined SAXS and WAXS experiments are often implemented at synchrotron facilities. A remarkable advantage of the setup used in this thesis is that a laboratory X-ray source is used. Indeed the number of combined SAXS/WAXS beam lines at synchrotron facilities is still rather limited (Sanker *et al.*, 2009) and their access is difficult. Our laboratory setup permits flexibility in planning and performing experiments whereas times of approximately half a year between proposal and experiment are common for synchrotron beam time. One drawback of our setup is that the resolvable time scale with a laboratory source is rather limited because of an order of magnitude lower photon flux compared to a synchrotron facility. However, the results obtained during this thesis clearly reveal that the resolvable time scale is sufficient to follow dynamical changes of heterogeneous catalysts *in situ.*

1.4 Scope of the work

Several research groups have extensively studied reforming of methane with steam and carbon dioxide. Steam reforming of hydrocarbons is a large scale process to produce synthesis gas, a mixture of CO and H_2, as feedstock for various processes such as ammonia-, methanol-, synthetic fuels- and oxo-synthesis and is commercially applied for nearly 100 years whereas reforming with carbon dioxide is still a process only performed in research laboratories. But carbon dioxide reforming is thought as an alternative to utilize the large amounts of CO_2 in natural gas. Nickel and noble metals show good catalytic activity for both processes and current large scale steam reforming plants utilize economically favoured Ni catalyst. However, Ni based catalysts exhibit a high tendency of deactivation by carbon formation (Rostrup-Nielsen and Bak Hansen, 1993). Noble metal catalysts show much lower carbon formation rates and are therefore thought as an alternative.

Relatively little is known about correlations of the particle morphology, sample phases and activity of catalysts for synthesis gas production. Simultaneous SAXS/WAXS in combination with mass spectroscopy is a powerful tool to resolve these correlations. The scope of this thesis was to gain understanding about the activation and deactivation of methane reforming catalysts and perform studies under conditions relevant for large-scale industrial processes. An existing *in situ* cell, originally designed for ASAXS experiments on a Synchroton beam line, was modified to perform simultaneous SAXS/WAXS in a laboratory pinhole camera. The goal was to redesign the heating unit of the cell to permit *in situ* experiments in the desired temperature interval from 298 - 1073 K. Furthermore a gas system was developed to apply constant flow of gases and mixtures and a mass spectrometer was implemented to monitor chemical reactions and conversion levels during the *in situ* experiments.

The heater performance was tested by measuring the specimen temperature with a thermal couple and using powder diffraction to study the thermal lattice expansion of Si, Ag powders and from the $MgAl_2O_4$ support of a catalyst sample during *in situ* experiments. The general applicability of the equipment to study nanostructured materials was tested with a model system. Titanium dioxide nanoparticles in the anatase phase, a widespread applied material for photo-catalysis, sensor-, solar- and battery-applications, were studied during annealing in a gas flow. Rod shaped particles were selected to resolve the temperature interval for the rod to sphere transformation.
Reduction and reforming on a 22 wt% $Ni/MgAl_2O_4$ and a 4 wt% $Ru/MgAl_2O_4$ were studied with simultaneous *in situ* SAXS/WAXS, the product composition was

monitored online with the mass spectrometer. Methane was used as a representative for natural gas and CO_2 reforming was performed because all reactant gas molecules are under standard temperature and pressure gaseous. The generation of a constant water steam is cumbersome and requires heat tracing of all gas lines of the *in situ* cell to prevent condensation. The usability of the experimental setup for catalytic tests was revealed by CO_2 of methane on a 4 wt% $Ru/MgAl_2O_4$ catalyst.

2 Heterogeneous transition metal catalysts for synthesis gas production by dry reforming of methane

2.1 Production of synthesis gas

Synthesis gas, a mixture of carbon monoxide and hydrogen, is an important intermediate for various large-scale processes such as production of ammonia, synthetic fuels by Fischer-Tropsch-, oxo-, methanol- and higher alcohol-synthesis. Usually synthesis gas is produced by reforming of hydrocarbons with steam. A relative inexpensive feedstock for steam and CO_2 reforming is methane because of its large concentration in natural gas and its worldwide availability (Chorkendorff and Niemantsverdriet, 2003). Steam reforming of methane

$$CH_4 + H_2O \leftrightarrow CO + 3\,H_2 \qquad \Delta H = 206\ kJ\ mol^{-1} \qquad (2\text{-}1)$$

is highly endothermic. Stoichiometric, steam reforming would yield synthesis gas with a ratio of $H_2/CO = 3$, but this is rarely observed because of the concurrent exothermic water gas shift reaction

$$CO + H_2O \leftrightarrow CO_2 + H_2 \qquad \Delta H = -41\ kJ\ mol^{-1} \qquad (2\text{-}2)$$

Reforming with carbon dioxide is thought as an alternative (Rostrup-Nielsen and Hansen, 1993).

$$CH_4 + CO_2 \leftrightarrow 2\,CO + 2\,H_2 \qquad \Delta H = 247\ kJ\ mol^{-1} \qquad (2\text{-}3)$$

Dry methane reforming yields a synthesis gas with a molar ratio of $H_2/CO = 1$, a low hydrogen to carbon monoxide ratio that are desired for feedstock of Fischer-Tropsch (Gadalla *et al.*, 1988), oxo- (Wörner *et al.*, 1998) and methanol-synthesis (Holm-Larsen, 2001). However, the molar ratio of $H_2/CO = 1$ is only observed at high temperatures because H_2, produced by dry methane reforming, reacts with CO_2 in the reverse water gas shift reaction (RWGS) to form water and carbon monoxide (Safariamin *et al.*, 2009, [b]Bradford and Vannice, 1999, Bitter *et al.*, 1997).

$$CO_2 + H_2 \leftrightarrow CO + H_2O \qquad \Delta H = 41\ kJ\ mol^{-1} \qquad (2\text{-}4)$$

Water formed by the RWGS reacts at high temperatures with methane via steam reforming to CO and H_2 and synthesis gas with a molar ratio of H_2/CO close to one will be obtained (Bitter *et al.*, 1997). Dry methane reforming is from an ecologically and economically point view also preferable since two of the most abundant greenhouse gases, methane and carbon dioxide, and also two of the cheapest carbon containing molecules that can be converted in subsequent synthesis to useful products. Dry methane reforming of biogas, which consists mainly of carbon dioxide and methane, would be a sustainable way to produce synthesis gas (Therdthianwonga *et al.*, 2008). However, biogas contains also large amounts of sulphur, mainly in form of H_2S and needs therefore a thoroughly desulphurization to avoid poisoning of the catalyst. Another attempt to produce synthesis gas sustainable is a special reactor design utilizing solar radiation as an energy source (Gokon *et al.* 2009, Wörner *et al.* 1998, Berman *et al.* 2007).

2.2 Catalysts

Transition metals such as Ni, Ru, Rh, Pd, Pt and Ir, dispersed on oxide supports like Al_2O_3, ZrO_2, MgO, $MgAl_2O_4$ and TiO_2, were reported as catalysts for dry reforming of methane ([a,b]Bradford and Vannice, 1999, [a,b]Wei and Iglesia, 2004, Rostrup-Nielsen and Bak Hansen, 1993, Rezaei *et al.*, 2006). These metals also show good catalytic activity for steam reforming of methane (Rostrup-Nielsen and Bak Hansen, 1993). The dissociation of the methane C-H bond was reported as the rate-limiting step for the different metal catalysts ([a,b]Wei and Iglesia, 2004, Mark and Meier, 1994), unaffected by the identity of co-reactants and reaction products ([b]Wei and Iglesia, 2004). Wei and Iglesia observed similar reaction rates for methane reforming with CO_2 and steam and claim that this is due to the rate limiting dissociation of the C-H bond. However, there are contradictory observations, by Rostrup-Nielsen and Bak Hansen (1993) of lower reaction rates for the dry reforming reaction than for steam reforming depending on the metal used as catalyst.

"Benchmarking" of the activity of those transition metals for dry methane reforming is controversial. Rostrup-Nielsen and Bak Hansen (1993) performed the reaction at 823 K on MgO supported catalysts and found the order to be Ru, Rh, Ni > Ir, Pt, Pd. Rezaei *et al.* (2006) reported experiments on catalysts supported on Al_2O_3 stabilized MgO (Spinel) and found the order of to be Ru, Rh > Ir > Pt > Pd, in agreement with the observations by Qin and Lapszewicz (1994) for MgO supported catalysts. These reported results emphasize that Ru and Rh are the most active metals for the dry reforming reaction although it disagrees with the reported activities by [a]Wei and Iglesia (2004) who found the order to be Pt > Ir > Rh > Ru, Ni.

Conventional steam reforming catalysts are Ni-based and this would also be economically favorable for the dry reforming reaction (Guo *et al.* 2004), but they have a main drawback in comparable high carbon formation rates (Rostrup-Nielsen and Bak Hansen, 1993, [b]Bradford and Vannice, 1999). However, the doping of Ni catalysts with small amounts of noble metals such as Ru was reported to suppress carbon formation (Jeong *et al.* 2006, Crisafulli *et al.*, 1999). Crisafulli *et al.* (1999) attributed it to the formation of a more reactive carbonaceous species on the Ru doped Ni catalyst, considering results from reduction experiments after CH_4-decomposition on Ni/SiO_2 and $Ru\text{-}Ni/SiO_2$. Noble metals have been reported to show a lower tendency for carbon formation (Rostrup-Nielsen and Bak Hansen, 1993) because of the lower equilibrium constant for carbon formation compared to Ni catalysts. Therefore, it is conceivable to substitute Ni-based reforming catalysts with catalysts based on noble metals. Ru and Rh exhibit the highest activity for the reforming reaction, however, the current price of Rh is about one order of magnitude higher because of the demand to manufacture exhaust cleaning catalysts for the automotive industry and thus Ru is the best candidate to substitute Ni.

2.3 The role of the support

Strong influences of the support on the activities of Ru catalysts for dry methane reforming were reported ([a]Bradford and Vannice, 1998, Ferreira-Aparico *et al.*, 1998, Ferreira-Aparico *et al.*, 2000), but the influence of the support in terms of activity for the dry methane reforming reaction is contradictory. [a]Bradford and Vannice (1999) reported a decrease in activity in connection with the support in the order of $Ru/TiO_2 > Ru/\gamma\text{-}Al_2O_3 >> Ru/C$ and ascribed the higher activity of TiO_2 supported Ru to the presence of a $Ru\text{-}TiO^{n+}O_x$ - sites. Ferreira-Appricio *et al.* (2000) observed higher activities of $\gamma\text{-}Al_2O_3$- compared to SiO_2 supported Ru and attributed it to a CO_2 activation by the surface OH-groups. Carrara *et al.* (2008) reported, from kinetic studies on Ru/La_2O_3, that the support plays a key role in the CO_2 activation by formation of oxycarbonate species.

However, [b]Wei and Iglesia (2004) reported from studies of Ru on ZrO_2 and $\gamma\text{-}Al_2O_3$ that the reactivity of Ru based catalysts is unaffected by the support. Dry methane-reforming studies, conducted by Mark and Meier (1996), of Rh and Ir catalysts on standard supports such as SiO_2, TiO_2, ZrO_2 and α- and $\gamma\text{-}Al_2O_3$ did also not show any effect of the support material on the activity. Even if the effect of the support material on the catalytic activity is unknown, it affects the dispersion of the metal particles ([b]Wei and Iglesia, 2004) during the catalyst preparation and stabilizes the nanoparticles during

catalyst use (Mark and Meier, 1996). A strong effect of the support material on the metal dispersion of Ni particles was reported (Guo *et al.*, 2004, Jeong *et al.*, 2006) and Ni/$MgAl_2O_4$ showed a higher dispersion of the catalyst particles than Ni/γ-Al_2O_3 and therefore higher activity and lower carbon formation rates (see section 2.5).

2.4 Structure sensitivity

The s*tructure sensitivity* of the methane reforming reaction is controversial. [a]Wei and Iglesia studied methane reforming with steam and CO_2 on Ru, Rh, Pt, Ir and Ni catalysts and observed correlation between the turn over frequency (TOF) and the metal dispersion ([a,b]Wei and Iglesia, 2004). Similar observations have been reported for steam reforming of methane by Jones *et al.* (2008) on supported Ru, Rh, Pt, Ir, Pd and Ni. Higher TOFs where ascribed to a larger number of surface atoms with low coordination like step and corner atoms (Jones *et al.*, 2008, [a,b]Wei and Iglesia, 2004). The TOF scales with (Jones *et al.*, 2008):

$$TOF = \frac{r}{A} \cong k_t + k_s g_s \frac{1}{d} + k_c g_c \frac{1}{d^2} \cong k_t + k_s g_s' D + k_c g_c' D^2 \qquad (2\text{-}5)$$

where r is the reaction rate, k the rate constant, A the surface area, g a geometrical factor, d the particle diameter, D the dispersion (D = number surface atoms / number of atoms in cluster) and the subscripts t, s and c refer to terraces, steps and corners. Equation (2-5) clearly shows that in case of *structure insensitivity*, where the rate only correlates with the overall number of surface atoms of the cluster and those surface atoms are predominantly located on the terrace sites, the dispersion will not influence the TOF. In case of *structure sensitivity*, the TOF will increase linearly with D if step sites are dominant and D^2 if corner atoms are dominant (Jones *et al.*, 2008). The observations of [a,b]Wei and Iglesia (2004) and Jones *et al.* (2008) reveal also a clear *structure sensitivity*.

Mark and Maier (1996) studied dry methane reforming over supported Rh and Ir catalysts and observed, in opposition with [a,b]Wei and Iglesia (2004) and Jones *et al.* (2008), that the TOFs were independent of the metal dispersion. They are observed reaction rates correlated only with the overall surface area of the catalyst particles and the reaction was therefore classified as *structure insensitive*. It was assumed that at the temperatures they performed their experiments, at 873 K for Rh and 973 K for Ir, surface reconstruction may cancel the effect of certain surface structures. The experiments from [a,b]Wei and Iglesia (2004) were also performed at 873 K and indicate a clear *structure sensitivity* of the methane reforming reaction.

2.5 Catalyst deactivation

Deactivation of steam and CO_2 reforming is a major problem and can occur by carbon formation (Guo *et al.* 2004, Sehested 2006), particle sintering (Sehested *et al.*, 2004 and 2006) and sulphur poisoning. Carbon formation is a fatal problem for CO_2 reforming catalysts (Guo *et al.*, 2004). Deposited carbon can block the pores, crush and block the active sites of the catalyst. Three different morphologies of carbon deposit were observed: pyrolytic carbon formed at high temperatures, encapsulating carbon covering the metal surface of the catalyst particles and carbon whiskers, marked as most destructive carbon deposit (Sehested, 2006) because they can break the catalyst pellet structure. Carbon deposit on nickel catalysts was reported to grow preferably on the Ni(211) steps in a graphene structure because the energy of carbon in graphene is lower than of any adsorbed carbon species on the step sites (Molenbroek *et al.* 2009, Sehested 2006). Graphene can either encapsulate the complete metal particle surface or be transported to the free Ni surface leading to the formation of a carbon whisker (Sehested, 2006). The rate of carbon formation was observed to depend on the Ni crystallite size, lower rates were observed with decreasing Ni crystallite size (Borowieki, 1982, Chen *et al.*, 2005).

Deactivation, by carbon formation, of Ni based reforming catalysts might be inhibited by addition of potassium, sulphur, gold (Sehested, 2006), molybdenum (Gonzáles *et al.*, 2000) or zirconium oxide (Therdthianwonga *et al.*, 2008). DFT calculations revealed that potassium, sulphur and gold locate preferably on step sites, blocking thereby the nucleation sites for carbon (Sehested, 2006). Gonzáles *et al.* (2000) reported a significant effect of Mo addition to a Ni/Al_2O_3-catalysts and concluded that this might be related to the dilution of Ni. They claimed, that this might decreases the number of assembles of at least 7 Ni atoms, that are needed to deposit carbon on the catalyst surface and decreases the Ni crystallite size below the critical diameter of 5 nm, required for carbon whisker formation. Therdthianwonga *et al.* (2008) observed lower carbon formation rates during dry methane reforming with increasing ZrO_2 addition to Ni/Al_2O_3. They believed that this is due to oxygen intermediates, formed by CO_2 dissociation on the Ni/ZrO_2 interface, reacting with deposited carbon.

Another possibility is to substitute nickel by noble metal catalysts because of their lower tendency for carbon formation (Rostrup-Nielsen, 1993) and ruthenium was considered as the best candidate and lower carbon formation rates were reported for ruthenium doped nickel catalysts (Jeong *et al.* 2006, Crisafulli *et al.*, 1999) and this was

ascribed to the formation of small bimetallic Ru-Ni clusters with predominantly Ni on the surface and a larger dispersion compared to un-doped Ni catalysts.

Sintering of dispersed metal particles leads to an irreversible deactivation of the catalyst. Particle growth of the catalyst can occur in two different mechanisms: Ostwald ripening and migration. The driving force for both processes is the minimization of the overall surface energy. Ostwald ripening is a mechanism where larger particles grow on the expense of smaller ones. Metal atoms or small clusters, formed by smaller particles, are transported along the surface or via the gas phase and accumulate on larger particles. The migration mechanism invokes movement of the entire particle over the support surface, collision of the particles leads to coalescence. Determining the initial and final particle size distribution can indicate if the particle growth occurs via Ostwald ripening or coalescence, a tail towards smaller and a steep slope towards larger particles indicates Ostwald ripening (Seheted *et al.*, 2004). Particle growth of Ni catalysts in He (Richardson and Crump 1979) and in H_2/H_2O (Sehested *et al.*, 2001) was reported to occur predominantly by migration and coalescence, because of the lower activation energy of migration compared to evaporation of atoms (Richardson and Crump, 1979). Particle migration of smaller particles is much faster than of large particles and therefore sintering of small particles is more pronounced (Richardson and Crump, 1979, Sehested *et al.*, 2001). However, the size distributions determined from ASAXS of a Ni/Al_2O_3 sintered in H_2/H_2O by Rassmussen *et al.* (2004) indicates, besides particle sintering, also a contribution from Ostwald ripening to the particle growth, at temperatures of 1073 K.

Sulphur poisoning of reforming catalysts appears due to sulphur containing compounds in the feedstock. Sulphur containing compounds are converted to H_2S under reforming conditions and sulphur strongly adsorbs on the catalyst particle surface (Sehested, 2006). Addition of molybdenum to Ni/Al_2O_3 catalysts was reported to increase the resistance of Ni against sulphur poisoning (Gonzáles *et al.*, 2000) since sulphur chemisorbs dominantly on Mo. The doping of Ru/Al_2O_3 with Ce was reported to increase the resistance against sulphur poisoning (Suzuki *et al.*, 2000). Sulphur poisoned catalysts can be reactivated by cyclic oxidation and reduction (Aguinaga and Montes, 1992). Particle sintering during the oxidation cycles, in a mixture of inert gas and oxygen, was observed to be strongly influenced by the partial pressure of oxygen as well as the oxidation time. With optimum oxygen partial pressures and oxidation times more than 80 % of the sulphur was removed and 50 % of the initial metal surface was retained.

3 Basic principles of X-ray scattering

This chapter gives a brief introduction of the basics in small and wide angle X-ray scattering, full explanations and the complete theory can be found elsewhere (i.e. Als-Nielsen and McMorrow, 2001, Glatter and Kratky, 1982, Feigin and Svergun, 1987). The incoming monochromatic X-rays are scattered by electrons of the probed material. The scattering within the herein used wavelengths λ is assumed to be elastic and consequently the magnitude of the wavevectors of the incident and scattered beam are equal, thus $\left|\vec{k}_i\right| = \left|\vec{k}_s\right| = 2\pi / \lambda$. The scattering vector is defined as $\vec{q} = \vec{k}_s - \vec{k}_i$ and it is related to the scattering angle θ by:

$$q = \left|\vec{q}\right| = \left(\frac{4\pi}{\lambda}\right)\sin\theta \tag{3-1}$$

The simplest case one can think of is scattering from a two electrons system, separated by a vector $\vec{r}$. The scattering amplitude for the two-electron system is

$$A(\vec{q}) = -r_0(1 + \exp(i\vec{q}\cdot\vec{r})) \tag{3-2}$$

with the Thomson scattering length r_0 and the phase difference of the incident and scattered X-rays is $\vec{q}\cdot\vec{r} = (\vec{k}_s - \vec{k}_i)\vec{r}$. This idea can be extended to any number of electrons, the amplitude of such a system can be written as:

$$A(\vec{q}) = -r_0 \sum_{r_j} \exp(i\vec{q}\cdot\vec{r}_j) \tag{3-3}$$

with the position $\vec{r}_j$ of the *j*'th electron.

The atomic form factor is the total scattering length of an atom and is given by the integral of its electron density:

$$f^0(\vec{q}) = \int \rho(\vec{r}) \exp(i\vec{q}\cdot\vec{r}) d\vec{r} \tag{3-4}$$

The atomic form factor is equal to the number of electrons of the atom if $\vec{q} \to 0$ and approaches zero for $\vec{q} \to \infty$ The simple description of f^0 by (3-4) is only valid for

X-ray energies that are much higher than the binding energy of the electrons in their shells. If the X-ray energies are below the binding energies, the electron response is damped by an amount of *f'*. This effect is most pronounced close to the atomic absorption edges. The response of the electron than has furthermore a phase lag that is described by the imaginary term *if''*. The terms *f'* and *f''* are the dispersion corrections and the atomic scattering length is described by:

$$f(\vec{q},E) = f^0(\vec{q}) + f'(E) + if''(E) \tag{3-5}$$

where *E* is the X-ray energy of the incident beam.

3.1 Small angle X-ray scattering

Small angle X-ray scattering (SAXS) arises from electron density inhomogeneities and allows to obtain structural information of the probed material with characteristic length scales in the order of 10 to 1000 $Å^{-1}$. Since those distances are large compared to those of electrons or even atoms in the material, it is not possible to separate their contribution to the scattering. The summation over the individual electrons is therefore replaced by the integral over the average electron density $\rho(\vec{r})$ and the amplitude is given by:

$$A(\vec{q}) = \int_V \rho(\vec{r}) \exp(-i\vec{q}\cdot r) d\vec{r} \tag{3-6}$$

corresponding to the Fourier transform of the electron density. The experimental observed scattered intensity $I(\vec{q})$ is the square of the amplitude written as:

$$I(\vec{q}) = \left|A(\vec{q})\right|^2 = \int_V \int_V \rho(\vec{r}_1)\rho(\vec{r}_2) \exp(-i\vec{q}\cdot(\vec{r}_1 - \vec{r}_2)) d\vec{r}_1 d\vec{r}_2 \tag{3-7}$$

By integration with constant $\vec{r} = (\vec{r}_1 - \vec{r}_2)$ the autocorrelation function is obtained which expresses correlations between the densities at any two points separated by a distance $\vec{r}$, averaged over the total irradiated volume *V*

$$p(\vec{r}) = \frac{1}{V}\int_V \rho(\vec{r}_0)\rho(\vec{r}_0 + \vec{r}) d\vec{r}_0 = \left\langle \rho(\vec{r}_0)\rho(\vec{r}_0 + \vec{r}) \right\rangle \tag{3-8}$$

Integration over all relative distances, including the phase factor leads to:

$$I(\vec{q}) = V\int_V p(\vec{r})\exp(-i\vec{q}\cdot\vec{r})d\vec{r} \tag{3-9}$$

Under assumption that the sample is isotropic, so that $p(r) = p(r)$ and that the sample does not show any long range-order that $p(r)_\infty = \overline{\rho}^2$, equation (3-7) can be rewritten as

$$I(q) = 4\pi V\int r^2\gamma(r)\frac{\sin qr}{qr}dr \tag{3-10}$$

where $\gamma(r)$ is the correlation functions in terms of electron density fluctuations $\eta = \rho - \overline{\rho}$ defined as

$$\gamma(r) = \langle\eta(r_0)\eta(r_0 + r)\rangle = p(r) - \overline{\rho}^2 \tag{3-11}$$

Equation (3-10) is the most general formula to describe small angle scattering from isotropic samples that do not show any long range order.

3.1.1 Particle scattering

The scattered intensity, of not interacting particles with well defined shaped particles embedded in a medium of homogeneous electron density, so that only the electron density difference $\Delta\rho$ is relevant for scattering, can be expressed analytically by using a form factor $P(q,R)$. Form factors for various shapes were reported by Pedersen (1997). During this thesis, cylindrical and spherical shaped particles were studied. The scattered intensity $I(q)$ of a homogeneous sphere with a radius R and the volume V can be calculated by :

$$I(q) = (\Delta\rho)^2V^2\left[\frac{3\sin qR - qR\cos qR}{qR^3}\right]^2 \tag{3-12}$$

and $I(q)$ of a cylinder with a radius R and a lengths L by (Pedersen, 1997):

$$I(q) = (\Delta\rho)^2 V^2 \int_0^{\pi/2} \left[\frac{2J_1(qR\sin\alpha)}{qR\sin\alpha} \frac{\sin((qL\cos\alpha)/2)}{(qL\cos\alpha)/2} \right]^2 \quad (3\text{-}13)$$

where J_1 is a Bessel function of the first order. The terms in the brackets are the $P(q,R)$ for spherical and cylindrical particles. $I(q)$ of the bodies show very characteristic profiles with fringes at higher q. Cylindrical shaped particles exhibit characteristic power law scattering with q^{-1} in between $q \sim \pi / L$ and $q \sim \pi / R$, but only if $L >> R$. $I(q)$ for monodisperse spherical and cylindrical particles are shown in figure 3.

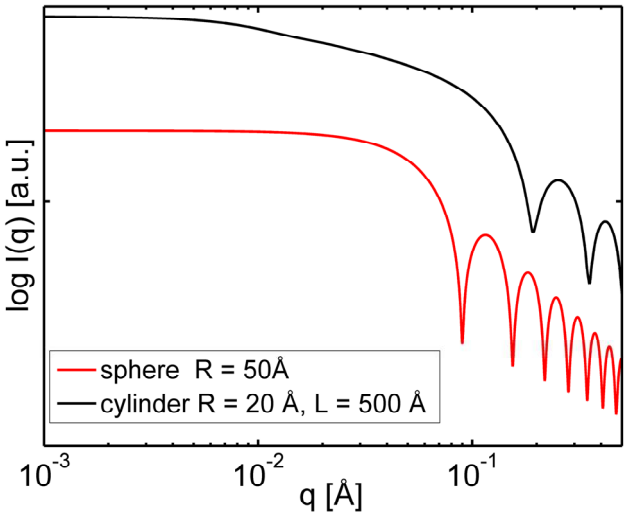

Figure 3: Calculated scattered intensity for monodisperse spherical and cylindrical particles with R_{sphere} = 50 Å, $R_{cylinder}$ = 20 Å and $L_{cylinder}$ = 500 Å.

The shape of the particles can be extracted from $I(q)$ using $P(q,R)$, but only if they are monodisperse or exhibit a very narrow size distribution. However, this is not the case for the materials studied herein and therefore the effect of polydispersity has to be taken in account by a particle size distribution $N(R)$. $I(q)$ is than written as:

$$I(q) = (\Delta\rho)^2 V^2 \int_0^{\infty} N(R) V^2(R) P(q,R) dR \quad (3\text{-}14)$$

A commonly used distribution function to describe polydisperse nanoparticle systems is the log-normal distribution

$$N(R) = \frac{1}{R\sigma\sqrt{2\pi}} \exp\left\{ -\frac{[\ln(R) - \mu]^2}{2\sigma^2} \right\} \quad (3\text{-}15)$$

where μ is the mean and σ the standard deviation. The effect of the size distribution on $I(q)$ is illustrated in figure 4. $I(q)$ was calculated assuming σ = 0.40, a realistic standard

deviation obtained from catalyst particles during this study, for the radius of the spheres and radius and lengths of the cylinders. The calculations clearly show that the characteristics of the particle shape smear out with increasing polydispersity, fringes at high q disappear for both spherical and cylindrical particles and the region of characteristic power law scattering, for cylinders at intermediate q with a slope of -1, begins to vanish. Figure 4 illustrates furthermore that the characteristic power law scattering, with q^{-1}, is only observable if $L >> R$.

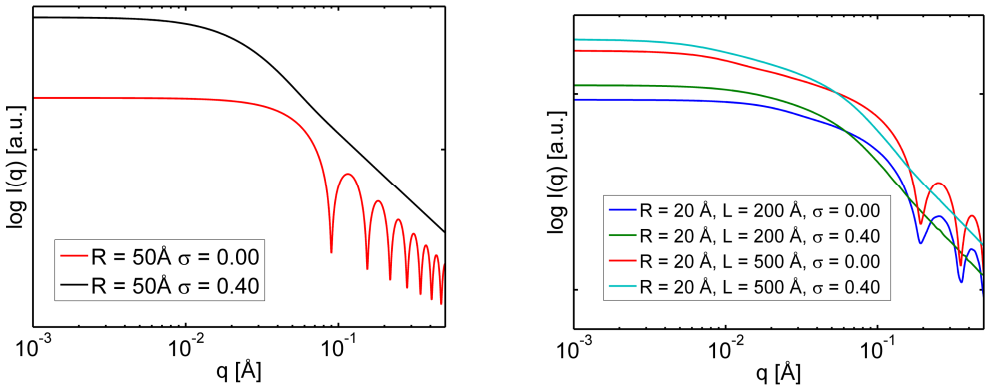

Figure 4: Calculated scattering pattern of mono and polydisperse spheres with a (mean) radius of 50 Å (left) and for mono and polydisperse cylinders with different lengths (right). The scattered intensities for polydispers particles were simulated with a lognormal size distribution.

3.1.2 Structure factor

So far $I(q)$ was described neglecting any effect of particle-particle interactions, but this is only the case for particles in very diluted systems. In dense materials, $I(q)$ might be influenced by interference due to particle interactions. The effect of the particle-particle interactions on $I(q)$ can be described by a structure factor $S(q,R)$. For monodisperse, randomly oriented and centrosymmetric particles, $I(q)$ can be described by

$$I(q) = (\Delta\rho)^2 P(q,R)^2 S(q,R) \qquad (3\text{-}16)$$

Different models for structure factors can be found in the literature (i.e. Pedersen, 1997, Kohlbrecher, 2010) and will not be discussed in detail here. For condensed matter, as studied in this thesis, the most common used structure factor is the hard sphere model. The interference due to particle interaction will influence the scattering most pronounced at lowest q. However, with increasing polydispersity the effect of the structure factor is smeared out as shown in simulations by Riello and Benedetti (1997) and observed by Ballauff (2001). Since the herein studied nanoparticles and

nano-structured catalysts showed high polydispersity the structure factor was neglected during the data analysis.

3.1.3 The Guinier approximation

At sufficient low scattering vectors, $qR < 1$, the scattered intensity $I(q)$ can be approximated by Guinier's law

$$I(q) = (\Delta\rho)^2 V^2 \exp\left(-\frac{q^2 R_{g,i}^2}{3}\right) \tag{3-17}$$

where R_g is the radius of gyration and is defined as the mean square from the center of gravity of the particle, $R_g = \sqrt{\bar{r}^2}$, in terms of electron density in analogy to the radius of gyration in classical mechanics. The radius of gyration for common shaped particles studied with small angle scattering can be found in the literature (i.e. Feigin and Svergun, 1987). During this study particles with cylindrical, hollow cylindrical and spherical shape were investigated. The corresponding R_g's in the squared form are listed in Table 1.

Shape	**Formula**
Spherical particle with radius R	$R_g^2 = \frac{5}{3}R^2$
Cylindrical particle with length L and radius R	$R_g^2 = \frac{R^2}{2} + \frac{L^2}{12}$
Hollow cylinder with length L and radii $R_1 > R_2$	$R_g^2 = \frac{R_1^2 + R_2^2}{2} + \frac{L^2}{12}$

Table 1: Radius of gyration of some simple shaped bodies studied in this thesis.

From (3-17) it is clear that a plot of ln $I(q)$ vs. q^2 of a region where Guinier's law applies should be linear. R_g^2 can be obtained from a straight line fit of the Guinier regime (see figure 5). From a fit of the Guinier regime in a q-range <0.02 Å^{-1}, a R_g of 57 Å corresponding to mean radius of 74 Å for the simulated spheres was obtained. The overestimation of the mean radius can be explained by the scaling of the Guinier regime with V^2. The obtained mean radius for polydisperse systems will consequently always represent the largest particles in the sample.

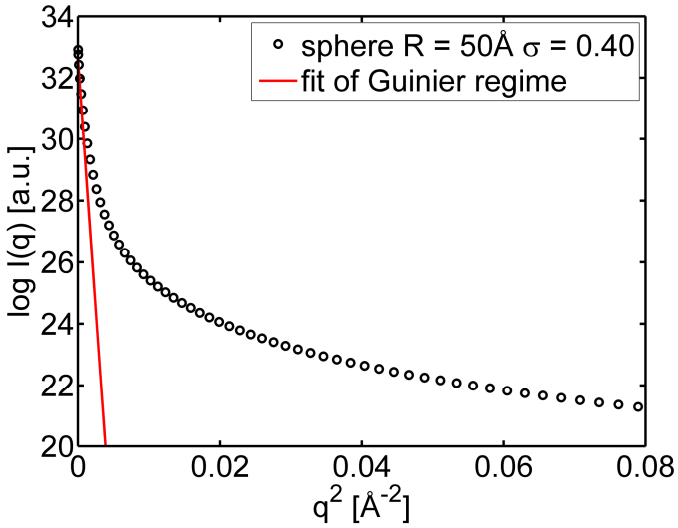

Figure 5: Guinier plot of the simulated scattered intensity for lognormal distributed spherical particles with a mean radius of 50 Å and σ=0.4. The Guinier regime was fitted with a straight line in a q-region <0.02 Å^{-1} and a R_g of 57 Å was obtained, corresponding to a radius of R = 74 Å.

3.1.4 Scattering on interfaces

At high scattering vectors, $qR >> 1$, the scattered intensity decays with power law behaviour scaling with the average surface area S of the primary particles

$$I(q) = Bq^{-P} \qquad B = 2\pi(\Delta\rho)^2 S \qquad (3\text{-}18)$$

where P is the power law coefficient. For sharp and smooth interfaces $I(q)$ decays with $P = 4$, also known as Porod's law. Deviations from Porod's law can be ascribed to surface fractals, $3 < P_i < 4$, and diffuse interfaces $P > 4$ (Schmidt 1991, Beaucage *et al.* 1994). The characteristic fringes, observed for scattering of monodisperse particles (see figure 3 and figure 4) are not described by equation (3-18). The q independent background level can be estimated from a straight line fit of a so called Porod plot ($I(q)\cdot q^4$ vs. q^4) (Glatter and Kratky, 1982). The subtracted backgrounds during this study were estimated with this method.

3.1.5 The invariant

The Porod invariant Q, a quantity independent of particle shape and size distribution, can be obtained by integration of the scattered intensity over the complete q-range for a particular structure (Glatter and Kratky, 1982, Beaucage *et al.* 2004).

$$Q = \int_0^\infty q^2 I(q) dq = 2\pi^2 N \Delta\rho^2 V \tag{3-19}$$

From the invariant the surface to volume ratio of the particles can be obtained by

$$\frac{\langle S \rangle}{\langle V \rangle} = \frac{\pi B}{Q} \tag{3-20}$$

The surface to volume ratio is independent of the particle shape and does not require measurements on an absolute scale. It can be directly compared with results obtained from nitrogen adsorption measurements (BET).

3.1.6 Unified fit function

The local scattering laws, described in equation (3-17) and (3-18), can be combined to approximate scattering curves of *n* non interrelated structural levels with the unified approach proposed by Beaucage *et al.* (1994 & 2004)

$$I(q) = \sum_{i=1}^{n} G_i \exp\left(-\frac{q^2 R_{g,i}^2}{3}\right) + B_i \left(\frac{q}{\left(\operatorname{erf}\left(qkR_{g,i}/\sqrt{6}\right)\right)^3}\right)^{-P_i} \tag{3-21}$$

where G_i and B_i are the Guinier- and Porod-prefactors and erf is an error function to "cut-off" the power law at low *q*. The unified equation can be extended to any related or unrelated level of structure. Becaucage *et al.* (2004) showed that the *B*, *G* and R_g can be related to moments of a size distribution. Under the assumption that the particles are spherical and their size is log-normal distributed, it is possible to obtain the two parameters, the median radius *m* and the standard deviation σ, to describe the distribution directly from the three fit parameters of unified approach (Beaucage *et al.* 2004) by

$$\sigma = \left\{\frac{\ln\left[B(R_g^2)^2/(1.62G)\right]}{12}\right\}^{\frac{1}{2}} \tag{3-22}$$

and

$$m = \left(\frac{5}{3} \frac{R_g^2}{\exp(14\sigma^2)} \right)^{\frac{1}{2}} \tag{3-23}$$

3.1.7 Wide angle X-ray scattering

The periodicity of the electron density is an important feature for diffraction of crystals. The scattering amplitude of a crystal $F^{crystal}(\vec{q})$ can therefore be split in two terms, the unit cell structure factor (first term 3-22) and the lattice sum (second term 3-22)

$$F^{crystal}(\vec{q}) = \sum_{r_j} F_j(\vec{q}) \exp(i\vec{q} \cdot \vec{r}_j) \sum_{R_n} \exp(i\vec{q} \cdot \vec{R}_n) \tag{3-24}$$

where $\vec{R}_n$ is the lattice vector that defines the origin of the unit cell and $\vec{r}_j$ the position of the atom in the unit cell relative to the origin. The lattice vector is given by

$$\vec{R}_n = n_1\vec{a}_1 + n_2\vec{a}_2 + n_3\vec{a}_3 \tag{3-25}$$

where $\vec{a}_1$, $\vec{a}_2$ and $\vec{a}_3$ the unit cell vectors and n_1, n_2, and n_3 are integers. The *lattice sum* can be considered as the sum of unit vectors in the complex plane and is in the order of unity except when

$$\vec{q} \cdot \vec{R}_n = 2\pi \cdot m \tag{3-26}$$

where *m* is an integer. To calculate (3-24), the reciprocal lattice is introduced, which is spanned from the reciprocal lattice basis vectors $\vec{b}_1$, $\vec{b}_2$ and $\vec{b}_3$ by:

$$\vec{b}_1 = \frac{2\pi}{v_c}\vec{a}_2 \times \vec{a}_3 \qquad \vec{b}_2 = \frac{2\pi}{v_c}\vec{a}_3 \times \vec{a}_1 \qquad \vec{b}_3 = \frac{2\pi}{v_c}\vec{a}_1 \times \vec{a}_2 \tag{3-27}$$

where $v_c = \vec{a}_1 \cdot (\vec{a}_2 \times \vec{a}_3)$ The reciprocal lattice vector is defined as

$$\vec{G} = h\vec{b}_1 + k\vec{b}_2 + l\vec{b}_3 \tag{3-28}$$

with the integers *h*, *k* and *l* and the scalar product of $\vec{G}$ and $\vec{R}$ is

$$\vec{G} \cdot \vec{R}_n = 2\pi(hn_1 + kn_2 + ln_3) = 2\pi \cdot m \tag{3-29}$$

and this shows that $F^{crystal}(\vec{q})$ is only non vanishing, if $\vec{G}$ coincides with $\vec{q}$, known as Laue condition and equivalent to Bragg's law. Scattering a from single crystal will therefore only be observed in certain directions in the reciprocal space and the scattered intensity is proportional to the squared modulus of the unit cell structure factor.

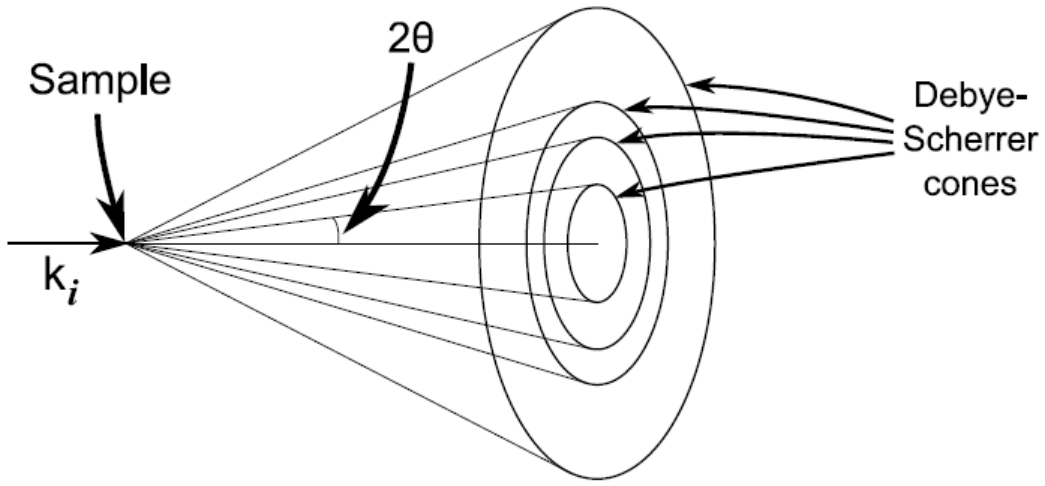

Figure 6: Debye-Scherrer cones from scattering of a powder sample

During this thesis powders were studied. Powders consisting of randomly oriented crystallites. Consequently scattering will occur in all directions of the reciprocal space and instead of diffraction spots, the so called Debye-Scherrer cones will be observed (see figure 6), each at a certain scattering angle 2θ, related to the scattering vector q by equation (3-1). The diffraction pattern is a plot of the intensity versus 2θ or q. The reflections in the pattern are labelled with the Miller indices (h,k,l), which are the numbers of the reciprocal lattice vector in (3-28). Permutations of (h,k,l) may have the same reciprocal lattice vector and thereby also the same value in 2θ or q. The multiplicity depends on the symmetry of the crystal: the multiplicity for the (100) reflection in a cubic crystal is for example 6, whereas it is 4 in a tetragonal lattice since (100) and (001) are not equivalent. The observed intensity of a reflection in the powder pattern is given by:

$$I \propto m\left|F^{unit\ cell}\right|^2 LP \tag{3-30}$$

where $F^{unit\ cell}$ is the unit cell structure factor, LP the Lorentz polarisation factor.

3.1.8 Rietveld refinement

The method was first introduced by Hugo Rietveld (1969) to refine data from neutron scattering and was later expanded for the use of X-ray data analysis. A general guideline for newcomers in the field of Rietveld refinement can be found in the literature (McCusker, 1999) and a more detailed description in Young (1993). Rietveld refinement is nowadays a common used analysis method for analyzing powder diffraction data if the structure is approximately known. The strategy of Rietveld refinement is to simulate a physical model, including structural, sample and instrumental parameters and fit it with the least square method to the experimental observed data. The advantage of this strategy is that all reflections of the contributing sample phases are taken into account, whereas the fit of multiple single peak profiles to the data might fail to resolve strong overlapping and weak reflections. In other words, Rietveld refinement minimizes the function

$$M = \sum_i w_i \left(y_i - y_{ci}\right)^2 \tag{3-31}$$

with the statistical weight w_i, the observed intensity y_i and the calculated intensity y_i at the ith step. The calculated intensity in i is obtained by summation of the intensity of the overlapping Bragg reflections and a contribution for the background y_{ib}

$$y_c = y_{ib} + \sum_p S_p \sum_{k=k_1^p}^{k_2^p} G_{ik}^p M_k L_K \left|F_{pk}\right|^2 P_k \tag{3-32}$$

with the scaling S proportional to the volume fraction of the phase p, the peak profile function G approximating both instrumental broadening and effects of the sample of the k^{th} Bragg reflection, the multiplicity of the reflection M, the Lorentz factor L, the structure factor $|F|$ and the factor P to describe preferred orientation. The background y_{ib} is often assumed by a polynomial of order 5 or higher. Most common peak profiles used for the refinement are the Voigt and pseudo Voigt function (McCusker 1999). Whereas the Voigt function is a convolution of a Gaussian and a Lorentzian the pseudo Voigt is a linear combination of both. The instrumental broadening contributes mainly to the width of the Gaussian and the strain effects to the Lorentzian. Rietveld refinement during these studies was solely performed using Voigt profile functions. The instrumental resolution function depends strongly on the width of the slits or respectively pinholes and must therefore be determined after every rearranging of the X-ray camera to determine the angular dependent *FWHM* for the Gaussian contribution of the Voigt function

$$H_K = \sqrt{U \tan^2 \theta + V \tan \theta + W} \tag{3-33}$$

and correct for it during refinement of size and strain. Refinement of the resolution should be performed with an X-ray powder standard material with a sufficient crystallite size, preferable between 1 - 5 µm (McCusker 1999). In these studies NIST Si SRM 640c was used to determine the instrumental broadening.

The quality of the refinement is normally determined by residual measures (*R*-factor). The most useful quantities are those for the profile R_p, the weighted profile R_{wp} and the goodness of the fit χ^2 (Pannetier 1993):

$$R_P = \frac{\sum_i |y_i - y_{ci}|}{\sum_i y_i} \qquad R_{wp} = \sqrt{\frac{M}{\sum_i w_i {y_i}^2}} \qquad \chi^2 = \frac{M}{(N-P)} \tag{3-34}$$

where N is the number of observations (data points) and P the least square parameters estimated. However, the quality suggested from residual measures should be treated carefully. If the sample exhibits a high background and low peak intensities good R_{wp} and χ^2 can even be obtained with a wrong structural model (McCusker *et al*. 1999). Increasing the count number also results in larger R_{wp} and χ^2 because the discrepancy between the experimental data and the model due to imperfections (features that cannot be modeled) will be increased. The same applies for an increase of the instrumental resolution, because imperfection will become more obvious due to the sharper peak (Toby 2006).

Rietveld refinement allows also quantitative phase analysis (QPA) of multiphase systems. The scaling factor S is proportional to N / V where N is the number of unit cells contributing to the scattering and V the unit cell volume. The weight fraction W of the phase p can be quantified by

$$W_P = \frac{S_P (ZMV)_P}{\sum_i (ZMV)_i} \tag{3-35}$$

with the phase index i, Z is the number of formulas per unit cell, M the molar mass of the formula and the volume of the unit cell V. QPA was performed in this thesis to follow the Ni/NiO content in a $Ni/MgAl_2O_4$ catalyst during *in situ* reduction and oxidation and to determine the rutile and anatase fractions in P-25 nano titanate powder.

4 Experimental

4.1 The combined in situ SAXS/WAXS setup

The simultaneous recorded *in situ* SAXS/WAXS data, presented in this thesis, were acquired at a recently developed laboratory setup situated in the Risø X-ray centre. A schematic of the experimental setup is shown in figure 7.

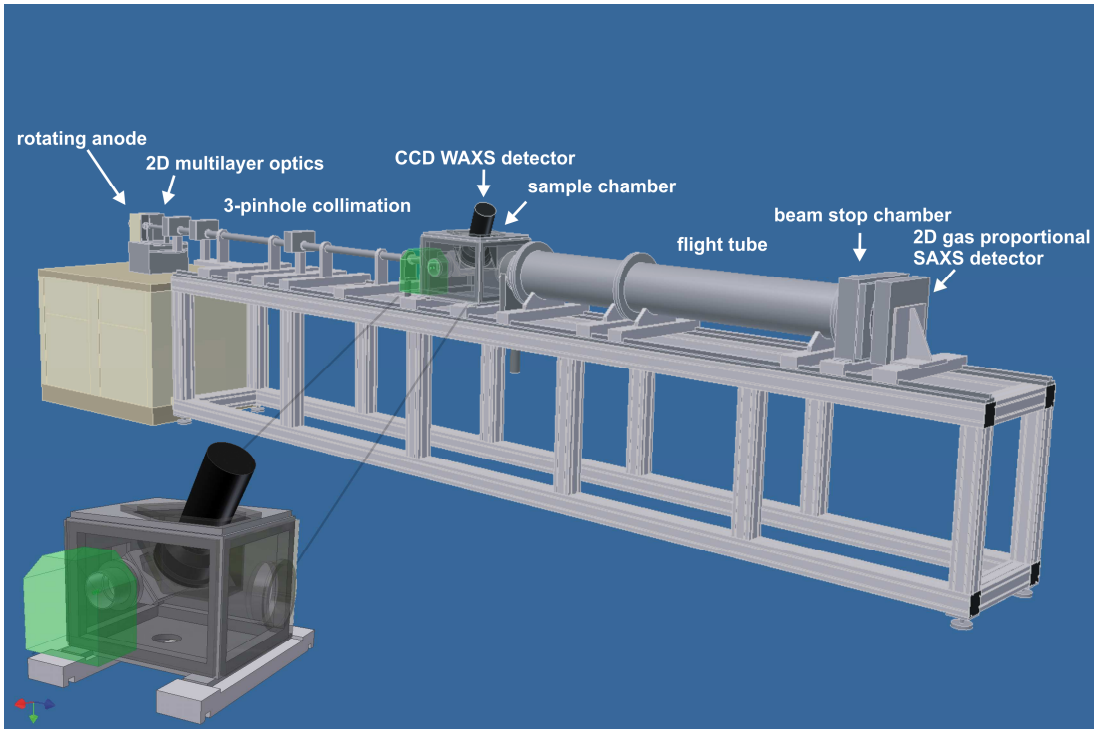

Figure 7: Schematic overview of the SAXS/WAXS in situ setup. The inset shows the sample chamber in detail, with the CCD camera in position for WAXS detection from the sample, mounted and enclosed in the inner in situ cell. The green box represents the external parts and vacuum seal of the in situ cell (Andreasen et al., 2003). The sample mount, heater and gas supply (detailed in figure 9) slides from the external part into the internal chamber, in the X-ray beam.

The X-rays are emitted by a rotating anode generator (Rigaku RU-300). The anode itself can be exchanged and that allows the use of different target materials and thereby to generate different element specific X-ray wavelengths. For the presented experimental work copper and molybdenum were used as target materials. The beam is focused and monochromatized by the 2-D multilayer optics to obtain a parallel beam

with characteristic Kα-wavelengths of the target material, in case of Cu λ = 1.5418 Å and Mo λ = 0.7107 Å. Afterwards the X-ray beam is collimated in a assembly of three pinholes whereby the first pinhole determines the beam shape and the second removes the parasitic scattering from the edges of the first pinhole. However, the parasitic scattering of the second pinhole limits the resolution of the camera. This can be overcome by inserting a third slit that does not touch the direct beam, but absorbs most of the parasitic scattering from the second pinhole (Kratky, O. 1982).

The collimated beam enters the sample chamber where the *in situ* cell is mounted and interacts with the sample. On the top plate of the sample chamber is an image intensified CCD camera (Gemstar 125, Photonic Science) mounted to detect the scattered beam in the wide angular range; the 125 mm wide screen allow to resolve a angular range in 2θ of around 13 º to 45 º, corresponding to a observable *q*-range of 2 - 6.5 $Å^{-1}$ using Mo Kα-radiation. The CCD camera is mounted 30 º off axis to the direct beam to avoid shielding of the small angle scattering. The instrumental resolution of the CCD camera was determined from powder diffraction of a silicon standard (NIST SRM 640c) and is in the order of $\Delta q/q$ = 4 – 5 $\cdot 10^{-3}$. Small angle scattering is detected by a 2 D Gabriel type gas detector (Gabriel *et al.* 1978). An assembly of flight tubes allows variations of the sample detector distance and thereby the variation of the observable *q*-range. The SAXS data in this thesis was acquired in two different geometries with a detector sample distance of 1494 mm (short geometry) and 4679 mm (long geometry) covering a *q*-range of $0.002 < q < 0.45$ $Å^{-1}$. The complete camera setup is kept in vacuum to decrease absorption and scattering by air.

4.1.1 The CCD camera position

In order to transform the WAXS data, a silicon standard (NIST SRM 640c) was measured before the experiment in the same position as the sample. From a fit of the silicon powder rings the camera position relative to the sample was determined and a matrix was generated relating each detector pixel to a certain *q*-value, a detailed description of the procedure to determine the camera position has been reported by Jacobsen (2009). Subsequently this matrix was applied for data binning of the 2D powder pattern of the samples. The fit of the powder rings from a Si standard measured in the sample position and the 1d transformation of the 2d WAXS pattern is shown in figure 8.

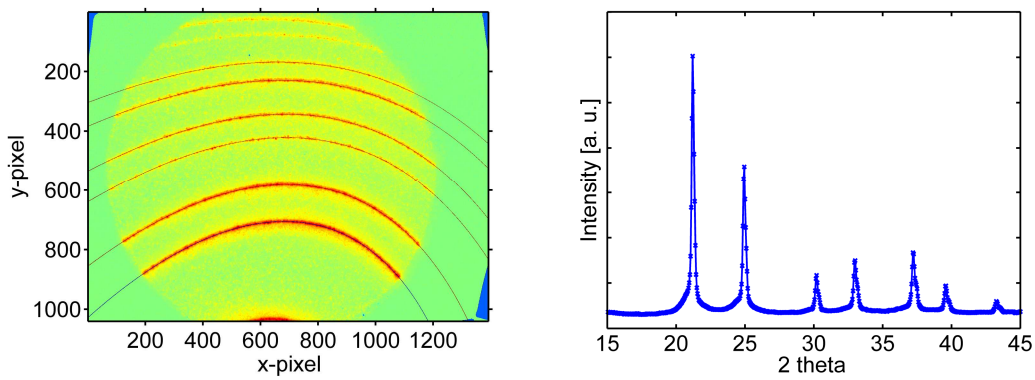

Figure 8: 2 D WAXS pattern of a silicon standard (NIST SRM 640c) measured in the standard sample position to calibrate the camera (left) and a 1D transformed pattern of this standard during sample heating to refine the specimen temperature (right).

4.1.2 The in situ cell

The green box in figure 7 represents the external parts and vacuum seals of the *in situ* cell; a detailed description was published by Andreasen *et al.* (2003). The cell was originally designed for *in situ* acquisition of SAXS data on the JUSIFA (B1) beam line at the Hamburger Synchrotronstrahlungslabor and was adapted for use with a laboratory pinhole camera with modified X-ray windows to cover also the wide-angle X-ray scattering. A detailed drawing of the heating unit is shown in figure 9. Methane reforming with carbon dioxide is a strongly endothermic process. Conversion levels, close to the thermodynamic equilibrium, are observed at temperatures above 1000 K. Therefore it is necessary to have a heater with a high power density to transfer a sufficient amount of heat to the sample and avoid temperature gradients in the catalyst bed. Conversely, as little heat as possible shall be transferred to the other parts of the *in situ* cell, especially the Kapton® windows. A new heater was developed during this study fulfilling those requirements to perform *in situ* methane reforming up to temperatures of 1073 K.

The cell consist of a quartz capillary (Markroehrchen, Hilgenberg GmbH) mounted between two Swagelok® fittings perpendicular to the direct beam. Sample heating is realized with a copper block with cut outs for the scattered beam in the small and wide angular range and equipped with three heating cartridges with an overall power of 120 W (Watlow Firerod type KMFE0035A004A). To ensure the maximum possible heat transfer to the sample, carbon black is coated on the inside of the copper block to increase the amount of emitted grey body radiation, heat emissivity coefficient ε (carbon black) = 0.96. The quartz capillary itself is a good absorber of heat radiation, ε (quartz) = 0.94. The outside of the copper block is polished,

ε (Cu, polished) = 0.03 (VDI Wärmeatlas, 1994), to decrease heat radiation to the Kapton® windows and outer parts of the *in situ* cell.

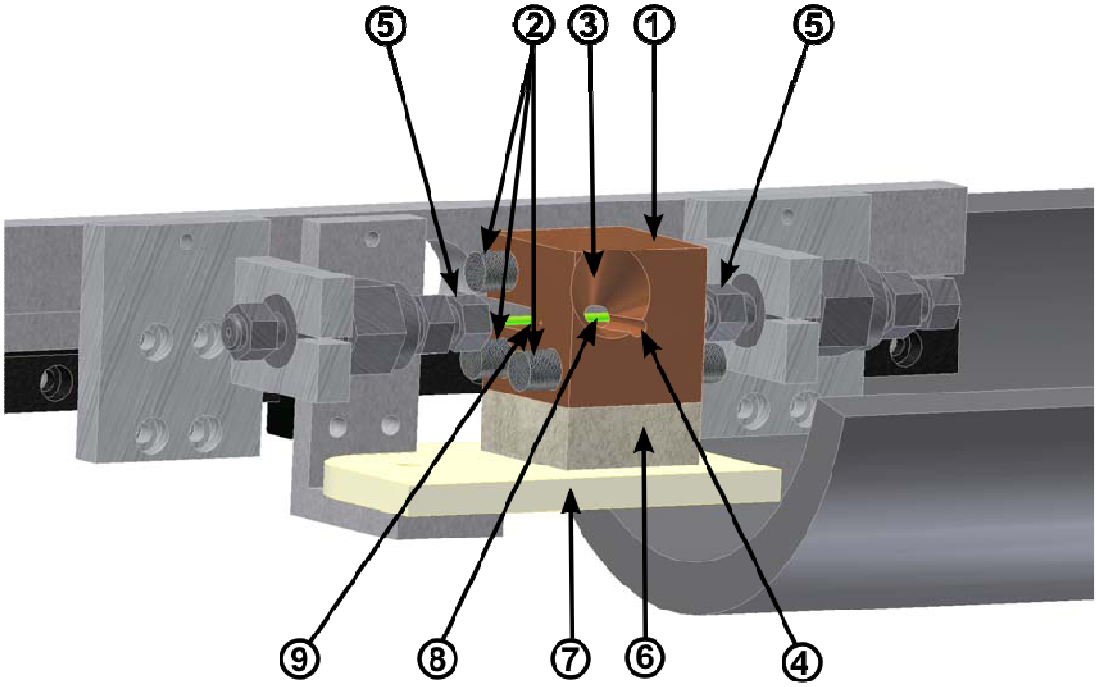

Figure 9: Schematic of the in situ cell, (1) polished copper block, (2) heating cartridges, (3) cone for WAXS, (4) hole for SAXS, (5) 1/16" Swagelok fittings, (6) porous isolating material with low thermal conductivity, (7) ceramic mounting plate, (8) quartz capillary and (9) cut out with carbon black coating.

Heat radiation to the windows is furthermore decreased by an additional installed silver heat reflector shield. The copper block is attached to a ceramic mounting plate that can be moved 90 ° anti clockwise to permit a non-restricted access to the Swagelok® fittings. Porous isolating material between the copper block and the mounting plate decreases heat loss by conduction.

The temperature is measured with a CrNi-Ni thermal couple inserted in a drill hole near the centre of the copper block. A tuned PID controller (Eurotherm 2416) with a solid state relay, operating in phase angle firing mode, ensures constant sample temperatures and overshooting during the heating of less than 2 K. Oxidation of the copper block at elevated temperatures is prevented by exclusion of oxygen. Experiments can either be performed in vacuum or in inert gas atmosphere.

4.1.3 The sample gas system

For a meaningful comparison of activities and dynamical changes of different catalysts it is indispensable to reproduce the results under comparable conditions, e.g. same temperatures and reactant gas flows. The same applies for recording of SAXS in different geometries; the overlapped SAXS is worth nothing if it was acquired at different conditions. Therefore a sample gas system, including a mass flow controller (MCF) was designed and implemented during this study. A detailed flow scheme of the gas system is shown in figure 10. The MCF, type Tylan FC-2900 M, is controlled with a LabVIEW script including conversion factors related to nitrogen, data acquisition and permits gas flows of 1 – 100 Nml/min. The design of the gas system allows to connect two different reactant gases (or gas mixtures) and one inert gas to the cell even though only one gas can be applied to the sample at any given time. An assembly of check valves avoids mixing of the sample gases, overpressure to the cell and contamination of the cell with oxygen in case of breaking of the fragile quartz capillary to avoid the rapid oxidation of the heating block at high temperatures.

An additional valve in the vent system of the *in situ* cell allows the connection of various analytical instruments to monitor the outlet gas, i.e. mass spectrometer (MS), gas chromatograph (GC), Fourier transform infra red spectrometer (FTIR) or non dispersive infrared analyzer (NDIR). For our applications a quadruple MS, type Spectramass DXM-200, with a single electron multiplier is most suitable and has been implemented during this study. Eight pre defined channels in the mass range of 1 – 300 amu can be read out and stored by an automatic routine.

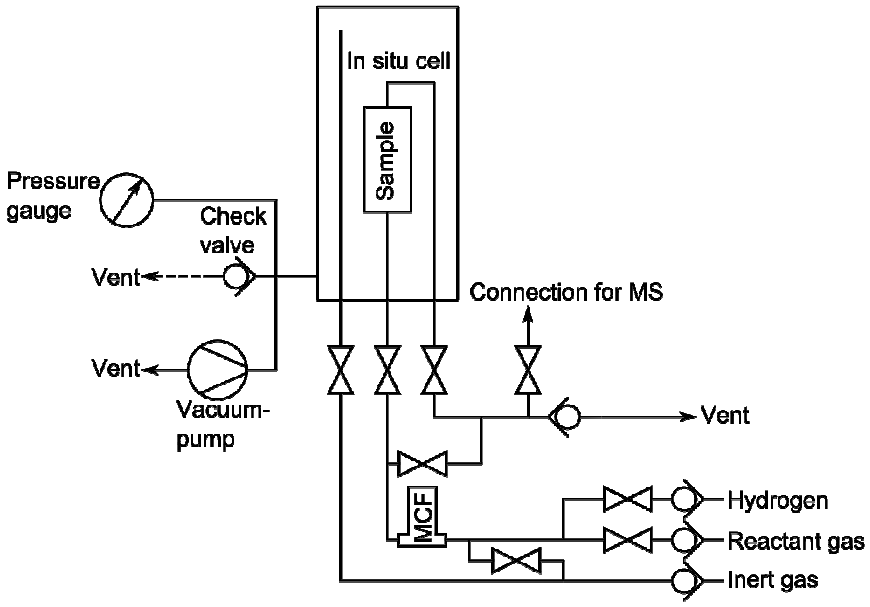

Figure 10: Flow diagram of the gas system connected with the in situ cell.

The sample gas system is connected with a permanent air monitoring system including detectors for hydrogen and carbon monoxide. In case of a leakage, the experimenter is warned optically and acoustically and a safety fail-closed valve, installed in the front of the hydrogen and reactant gas line, closes to avoid a further increase of the gas concentration.

4.2 X-ray powder diffraction

Standard powder diffraction patterns were acquired at room temperature and under atmospheric condition on a Bruker D8 in Bragg Brentano geometry using Cu Kα-radiation and an energy-dispersive solid-state detector. Typical scans were performed with a step size of 0.02 ° in 2θ in an angular range of 15 ° - 105 ° with counting times of 1 second per step.

4.3 Transmission electron microscopy

Transmission electron microscopy (TEM) and high resolution transmission electron microscopy (HRTEM) micrographs were acquired with a JEOL 3000 F microscope with acceleration voltage of 300 kV. The samples were dispersed in ethanol with a dilution of 1:1000 - 1:10000 using ultrasonic treatment. 10 µl of this dispersion were coated on a 400 mesh holey carbon grid.

4.4 Mass spectrometer

During this study a quadrupole mass spectrometer of the type Spectramass Dataquad DXM-200 was implemented to monitor chemical reactions during the *in situ* experiments. The combination of SAXS/WAXS and a mass spectrometer permits simultaneous *in situ* determinations of changes in the crystalline structure, particle morphology and reactivity of nano-scale catalysts and resolve their correlations with the sample temperature and reactant gas composition.

The DXM-200 is originally designed for residual gas analysis in high vacuum and is connected to such experiments directly with vacuum tubes with dimensions in inches. However, the pressure in the *in situ* experiments is predefined by a check valve in the vent system (see figure 10) to 1.7 bar and this is much higher than the pressure used during rest gas analysis in high vacuum. Therefore the inlet system was redesigned.

Instead of a vacuum hose, a fused silica capillary with an inner diameter of 0.1 mm was used. This type of capillary is normally applied in gas chromatography as precolumn. The capillary has two purposes, to connect the mass spectrometer with the reactor outlet and limit the overall gas flow. The performance was successfully tested with a premixed gas consisting of CH_4 and CO_2 in a molar ration 1:3.

However, reduction and dry reforming experiments over a 4 wt% $Ru/MgAl_2O_4$ catalyst revealed that the mass spectrometer, in the present configuration, was not usable for those experiments. One of the main problems was relative low efficiency of the turbo molecular pump. When pure H_2 was fed to the mass spectrometer, during the reduction of the catalyst, the pressure in the mass spectrometer increased over the maximum working pressure of the quadrupole (10^{-4} mbar) excluding a reliable performance of the mass spectrometer. An increasing pressure in the mass spectrometer leads to a mean free path length of the ions that is shorter than the distance between the filament and the detector and therefore to collision with other ions or the background gas.

The high pressure in the mass spectrometer, if hydrogen is feed instead of premixed gas, can be explained by a decrease of the compression ratio *K* that depends on the mean velocity $\bar{c}$ of the gases by:

$$K = \exp\left(\frac{v}{\bar{c} \cdot g \cdot t \cdot \sin\alpha}\right) \tag{4-1}$$

where *v* is the velocity of the turbine blade, *g* a geometric factor, *t* the distance of the turbine blades and α the angle perpendicular to the rotation axis. The mean velocity of a gas is inversely proportional to its molecular mass *M*

$$\bar{c} = \sqrt{\frac{8 \cdot R \cdot T}{\pi \cdot M}} \tag{4-2}$$

with the temperature *T* and the gas constant *R*. From (4-1) it is evident that *K* increases exponential with $\sqrt{M}$ if *v* is constant. Therefore a higher pressure will be observed in the mass spectrometer if hydrogen is ingested feed of CH_4 and CO_2. Another problem was the formation of water by the RWGS, see equation (2-4), during the dry methane reforming reaction. Several times a complete blocking of the capillary connecting the reactor outlet to the mass spectrometer by water condensation was observed.

The conversion levels, reported in this thesis, where therefore achieved with a different quadrupole mass spectrometer of the type Balzers ThermoStar GSD 300 that includes a

heat tracing of the transfer line from the reactor outlet and this avoid condensation of water and thereby a blocking of the sample transfer line. Balzers ThermoStar has furthermore, contrary to the DXM-200 residual gas analyser, an enclosed ion source. The main advantage of the enclosed ion source is that the filament are separated from the ionizing gas and evacuated separately. This allows gas analysis with higher inlet pressures and minimizes the effect of the background gas.

The ThermoStar GSD 300 was borrowed from Haldor Topsøe A/S only during the dry methane reforming study and returned afterwards. But even if the DXM-200 was not usable to follow the methane conversion during the dry reforming experiments, it might be used for other studies in the future, i.e. to determine small amounts of hydrogen or ammonia released during combined *in situ* SAXS/WAXS desorption experiments of hydrogen or ammonia storage materials.

5 Performance of the heating block

5.1 Motivation

An essential aspect during this work was to test the performance and confirm the usability of the new designed heater setup for the *in situ* SAXS/WAXS experiments on catalyst samples in the desired temperature interval from 298 - 1073 K. For the planned methane reforming experiments temperatures of more than 1000 K are indispensable, but difficult to realize because of the very limited space around the sample. The distance between the two Swagelok® fittings with a mounted capillary is only about 45 mm. The heating block is mounted very close to the Kapton® windows of the *in situ* cell housing that are separating the cell from the SAXS camera to allow fast access to the sample without ventilating the sample chamber of the camera and to protect the setup against contamination in case of a breakage of the capillary. Even though Kapton® is one of the most temperature stable polymers, the foil is glued with an epoxy resin that weakens already at temperatures of 553 K. Another difficulty is the lower surface of the heater in the region where the X-ray beam interacts with the sample and the scattering takes place. First performance tests were carried out with constant helium purge of the cell because of its preeminent heat conduction. Those tests showed very good heat transfer from the heating block to the specimen and a difference between heater and capillary of less than 2 K was observed. However, a large heat quantity was also transferred to all other parts of the cell and a weakening of the epoxy resin was observed at temperatures above 553 K.

To overcome this problem it was decided to operate the cell in vacuum. The performance test of the heater in vacuum should identify if it is possible to reach the desired temperature of 1073 K in the specimen in the region where the X-ray beam interacts with the sample. Furthermore it should be identified how the heater temperature correlates with the specimen temperature and if a temperature calibration of the setup is necessary since the knowledge of the correct specimen temperature is essential to study the thermodynamics and kinetics. In addition, a simple but accurate method to determine the temperature under the experimental conditions should be identified e.g. in a gas flow. Moreover it should be tested if there is a possibility to determine the sample temperature during *in situ* experiments directly from the sample.

The specimen temperatures were determined with three different approaches:

- Direct measurement of the specimen temperature using a thermal couple.
- From the thermal expansion of the lattice parameter of silicon and silver powder samples.
- From the lattice expansion of the magnesia spinel support from a Ni catalyst during an *in situ* reduction experiment.

5.2 Linear thermal expansion

Materials show the tendency to change their dimension with the temperature if the pressure is kept constant (Wedler G. 2004). Thermal expansion is material specific and is often described by volume expansion for gases and fluids and linear expansion for solids. Expansion along one dimension can be described by the linear thermal expansion coefficient (LTEC).

$$\alpha = \frac{1}{L}\frac{dL}{dT} \tag{5-1}$$

where l is the length and T the temperature of the specimen. The LTEC itself changes with the temperature, but can be approximated for many materials as linear in a limited temperature range ΔT to estimate the fractional length change of the specimen:

$$\frac{\Delta L}{L_0} \approx \alpha \cdot \Delta T \tag{5-2}$$

where L_0 is the length at a reference temperature T_0. If the LTEC changes significant over the temperature interval, equation (5-2) must be integrated to evaluate the fractional lengths change.

$$\frac{\Delta L}{L_0} = \int_{T_0}^{T} \alpha(T)dT \tag{5-3}$$

5.3 Experimental

5.3.1 Direct measurement with a thermal couple

A 0.7 mm quartz capillary (Markrörchen, Hilgenberg GmbH), containing a loosely packed catalyst sample to ensure a good heat transfer from the capillary thermal couple, was installed between the two Swagelok® fittings of the *in situ* cell. A 0.5 mm thermal couple, type K, was inserted through the reactor inlet gas line in the capillary to the centre position of the heating block. The *in situ* cell was evacuated to a gas pressure lower than 0.3 mbar. Different heater temperatures, in steps of 100 K, within a range of 373 to 1073 K, were applied by varying the opening angle of the solid state relay on the power supply unit. The heater and catalyst temperatures were equilibrated until the fluctuations of the heater temperature were lower than 1 K for 120 s before read out. At temperatures above 1073 K the opening angle of the solid state relay was increased gradually until the temperature in the capillary reached the desired maximum temperature of 1073 K.

5.3.2 Thermal expansion of the lattice parameter of a powder sample

The temperature inside the capillary was determined from the thermal lattice expansion of several silicon (NIST SRM 640c) samples in quartz and sapphire capillaries and from one silver powder sample in a quartz capillary. The powder samples approximately 10 mm in length, were inserted in capillaries with an inner diameter of 0.7 - 0.8 mm, embedded between two glass wool plugs and mounted gas tight between two Swagelok® fittings using graphite ferrules. The sample were purged with a continuous gas flow of 20 ml min^{-1} nitrogen (alphagaz 1, > 99.999 %) for approximately 10 min to remove trapped oxygen from the samples. Afterwards the vent valve of the *in situ* cell was closed and the samples were subjected to a pressure of around 3 bar nitrogen to ensure a good heat transfer from the capillary walls to the specimen. WAXS patterns of the Si and Ag powder samples with an exposure of 1800 s were acquired at different heater temperatures. The experimental procedure of the *in situ* reduction of a $Ni/MgAl_2O_4$ catalyst is described in detail in paper II. The temperature dependent lattice parameters of the powder samples were determined from Rietveld refinement of the 1D transformed WAXS pattern using the structural data of Si (ICDS # 67788) and Ag (ICDS # 44387). Multiphase Rietveld refinement to determine the temperature dependent lattice parameter of $MgAl_2O_4$ is described in detail in paper II. The temperature of the specimen from the thermal expansion was evaluated calculating (5-3) numerically with increments of 1 K.

5.4 Results

A plot of the heater temperature versus the sample temperature measured with a thermal couple is illustrated in figure 11.

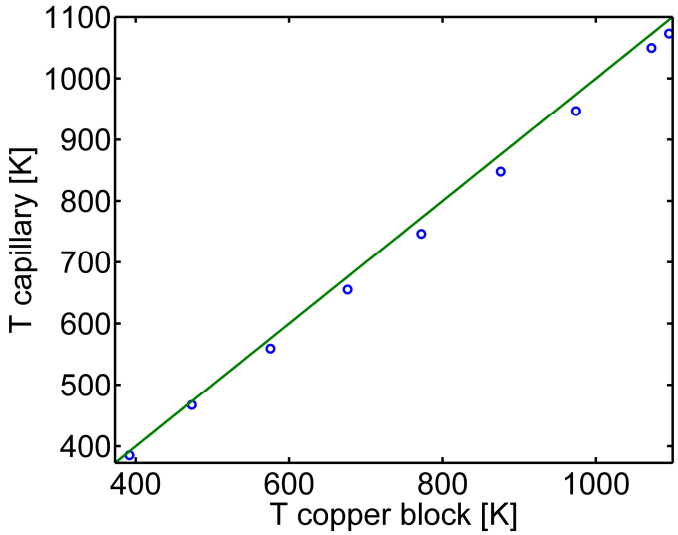

Figure 11: Temperature of the heating block versus temperature in the capillary measured with a thermal couple (o) and T vs. T plot (solid line).

The temperature, measured inside the capillary, increases linearly with the heater temperature. A temperature of 1073 K inside the capillary was obtained with a heater temperature of 1095 K. Depending on the temperature, a difference of 6 - 28 K between the heater and the capillary was observed.

Several experiments in quartz and sapphire capillaries were performed to determine the specimen temperature from thermal expansion of the Si crystal lattice from WAXS. Figure 12 shows the plots of the refined temperature inside the capillary vs. the heater temperature in a sapphire- (top) and in a quartz-capillary (bottom). Both experiments were performed under comparable conditions apart from the heating program.

The temperature inside the capillaries was determined using the thermal expansion coefficient reported by Wantanabe *et al.* (2004). Specimen temperatures, refined from the sample in the sapphire capillary, follow the temperature in the heater up to a temperature of 773 K. At higher heater temperatures variations of the refined specimen temperature up to 120 K were observed. The top of figure 12 presents the best specimen temperature refinement of all measured Si samples. An example for drastic variations of the refined temperature is shown on the bottom of figure 12. In this specific case the refined temperature exceeds the heater temperature up to 220 K. In general it was

observed that specimen temperatures, refined from the thermal expansion of Si, were either all below or all above the heater temperature.

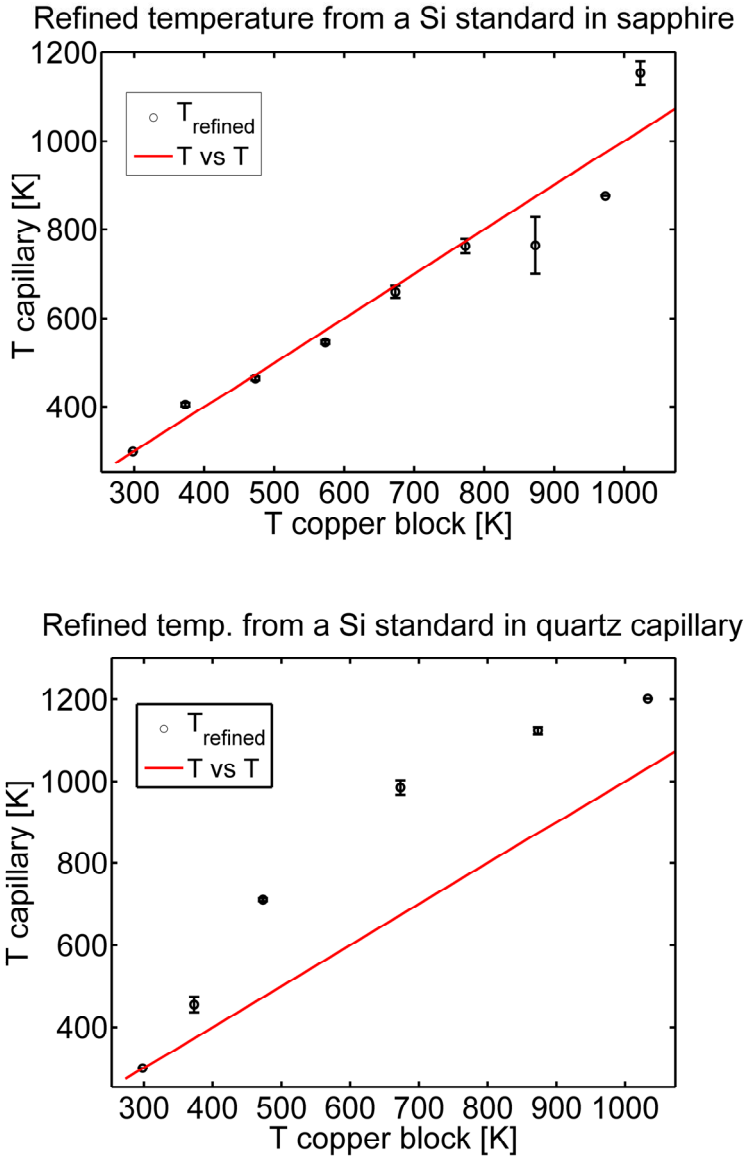

Figure 12: Determined temperature (o) inside the capillary vs. temperature of heater using a Si powder sample, sapphire- (top) and quartz-capillary (bottom).

Figure 13 shows the temperature inside the capillary, refined from an Ag powder sample, plotted versus the heater temperature.

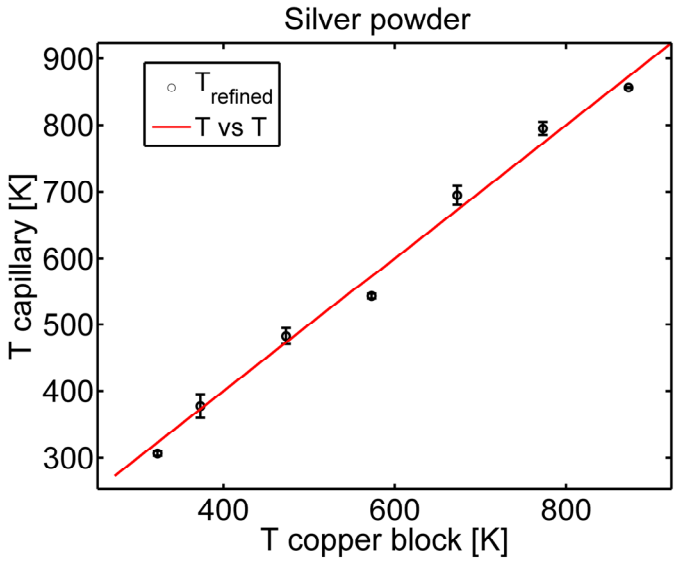

Figure 13: Temperature measured in the heating block versus the temperature in the capillary refined from the Ag lattice parameter (o) and T vs. T (solid line).

The refined temperature from the Ag powder, using the LTEC reported by Simmons and Balluffi (1960), follows the heater temperature during the complete experiment. Refined specimen temperatures are well distributed around the heater temperature, the difference between the heater and capillary was at most 30 K. The specimen temperature during an *in situ* reduction experiment of a 22 wt% Ni/$MgAl_2O_4$ catalyst, calculated from the expansion of the $MgAl_2O_4$ lattice parameter, using the LTEC for synthetic spinel by Singh *et al.* (1975) is shown in figure 14. The specimen temperature follows the heater temperature well, however, a small systematic deviation was observed.

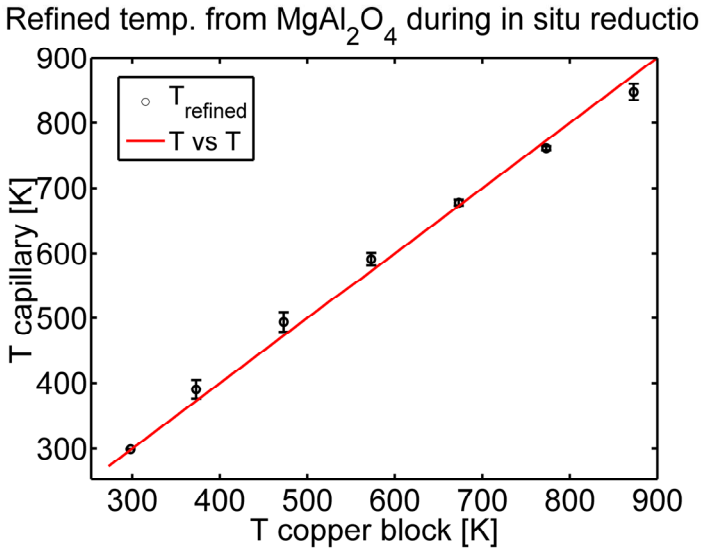

Figure 14: Temperature measured in the heating block versus the temperature in the capillary refined from the $MgAl_2O_4$ lattice parameter (o) and T vs. T (solid line) during an in situ reduction experiment of a 22 wt% Ni/$MgAl_2O_4$ catalyst.

5.5 Discussion

Determination of the specimen temperature by inserting of a thermal couple in the capillary clearly shows that the new designed heating unit is suitable to perform the catalytic experiments in a desired temperature range from 298 - 1073 K. The difference between the heater and the capillary does not exceed 5 % of the set point at any temperature and is therefore in the acceptable tolerance for such experiments and correction of the sample temperature is not necessary. However, the mounting of the thermal couple inside the quartz capillaries, with a wall thickness of just 1 µm is difficult. Since the thermal couple is inserted through the sample gas system into the capillary it is not possible to determine effects of the gas flows on the specimen temperature. The gas system is furthermore open to the atmosphere in such an experiment. Small leaks or a breaking of the capillary, due to thermal stress for example, might cause a rapid surface oxidation of the heating block at temperatures above 373 K.

Refinement of the temperature from the thermal lattice expansion of a powder sample with a known LTEC is a good alternative to the direct measurement with a thermal couple. The LTEC of silicon has been extensively studied due to the utilization in semiconductors. Therefore Si is used for testing of the reliability and temperature calibration of heating equipment for *in situ* X-ray diffraction (see e.g. Dapiaggi *et al.* 2002, Waldschlögel *et al.* 2006, Kuru *et al.* 2008). However, a variety of different LTECs can be found in the literature, Waldschlögel *et al.* (2006) refers that the reported values vary more than 20 % at 298 K. Figure 15 illustrates three different reported LTECs for Si (top) and the corresponding refined specimen temperatures (bottom) using these LTECs.

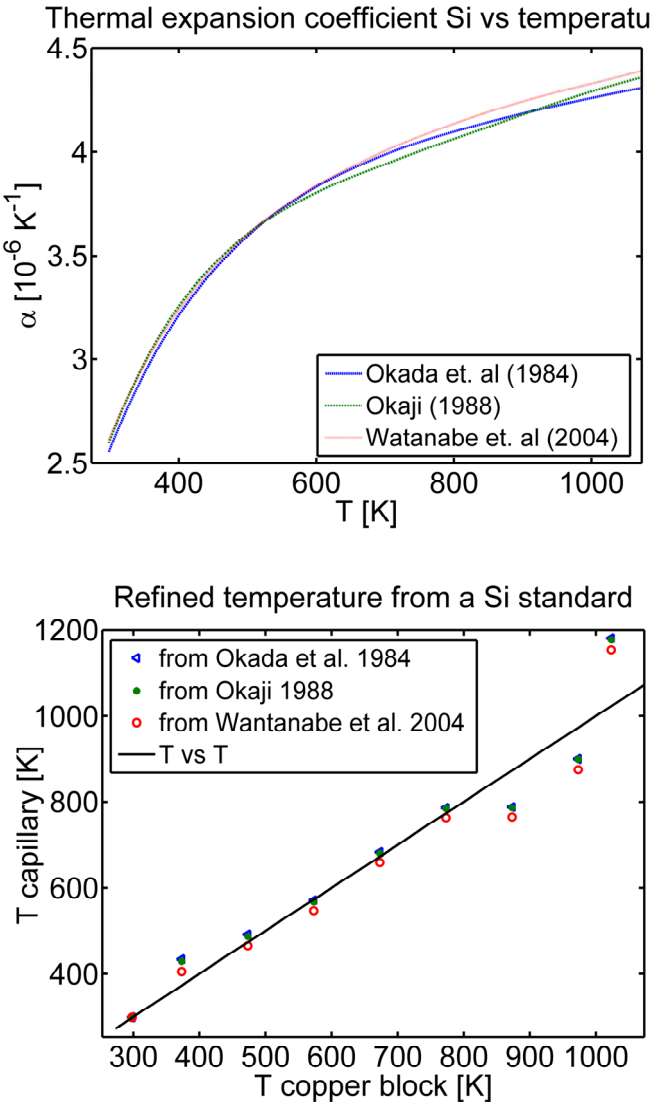

Figure 15: Reported LTECs for Si (top) and corresponding refined specimen temperature (bottom) using the reported LCTEs.

The refined specimen temperature was observed to vary up to 30 K utilizing the three different LTECs. Variations of the reported LTECs can originate from the method of their determination or different microstructures. Methods to determine the expansion of the specimen in macroscopic scale, like dilatometry, measure the length change due to lattice expansion and increase in vacancy concentration, whereas diffraction methods only determine the lattice expansion (Simmons & Balluffi, 1960). The lattice parameter of Si powder was reported to be smaller than of a Si single crystal specimen (Okada *et al.* 1984). Consequently, smaller LTECs will be measured from Si powder. The reported LTECs, used in this study to determine the specimen temperature, were measured by X-ray diffraction (Okada *et al.* 1984) and dilatometry (Okaji 1988, Wantanabe *et al.* 2004). However, even if the LTECs given by Okaji *et al.* (1984) and Wantanabe *et al.* (2004) were measured with the same technique and same kind of

specimen, the refined temperatures inside the capillary using these coefficients differ around 20 K, figure 15 (bottom).

A source of errors, that might explain the variety of too low or too large refined temperatures by using the Si powder, is the thermal expansion of the mounting and fittings of the *in situ* cell itself. Depending on the experimental conditions temperatures of more than 393 K were measured on the housing close to the X-ray windows of the cell. Temperatures close to the heater are believed to be even larger. Thermal expansion of the fittings might cause a slight bending of the capillary and thereby a shift of the relative position related to the CCD camera. Simulations showed that refinement of the specimen temperature from the fit of the Si(220) would lead to an over- or respectively underestimation by more than 2000 K if the capillary bends 1 mm away or towards the CCD. A shift of the relative sample position related to the CCD camera, due to thermal expansion of the mounting, is therefore the most probable reason for the to high refined temperatures of data shown in figure 12 (bottom) and large deviations of the refined data at temperatures above 773 K shown in figure 12 (top) and figure 15 (bottom).

During this study, it was observed that the refinement of the specimen temperature using Si was more difficult than using Ag or $MgAl_2O_4$. This might be due to the comparably small lattice expansion of Si. The reported LTECs for Si at 298 K varied between 2.551×10^{-6} and 2.612×10^{-6} K^{-1} (Wantanabe *et al.* 2004, Okaji 1988 and Okada *et al.* 1984) and this is nearly one order of magnitude lower than the reported values for Ag of 18.8×10^{-6} K^{-1} - 19.0×10^{-6} K^{-1} (Pathak and Vasavada 1970, Linde D. R. 2010, Simmons and Balluffi 1960). Reported LTECs for $MgAl_2O_4$ at 298 K vary from 4.3×10^{-6} K^{-1} - 5.9×10^{-6} K^{-1} (Fiquet *et al.* 1999, Singh *et al.* 1975) and are around twice of those for Si. However, these reported LTECs for $MgAl_2O_4$ vary around 37 % and this might be related to a difference in the sample nature. An indication for this was reported by Singh *et al.* (1975) who found a LTEC of 4.6×10^{-6} K^{-1} for natural and 5.9×10^{-6} K^{-1} for synthetic spinel at room temperature. Even though the lattice expansion of synthetic $MgAl_2O_4$ was used to determine the temperature inside the capillary during the *in situ* experiment, a systematic deviation of the refined and applied temperature was observed and might be related to a difference in the synthesis of the support material and the $MgAl_2O_4$ used by Singh *et al.* (1975). Heavily overestimated sample temperatures were obtained using the LTEC for natural spinel and the one reported by Fiquet *et al.* (1999). This emphasizes that the LTEC, to determine the sample temperature, should be chosen carefully and depending on the nature of the sample.

5.6 Conclusion

The applicability of the heater setup for experiments in a desired temperature interval from 298 - 1073 K was successfully tested. Determination of the specimen temperature inside the capillary with a thermal couple was found to be most accurate. However, inserting a thermal couple is difficult and do not allow to apply any gas flow in the current setup. The thermal expansion of the crystal lattice is a usable alternative and allows the evaluation of the specimen temperature under experimental conditions, e.g. gas flow and pressure. A reference material with a well known and sufficiently large thermal expansion coefficient has to be selected. Silver is one of those. The temperature during *in situ* experiments on magnesia spinel supported catalyst can be directly calculated from the thermal expansion of the $MgAl_2O_4$ lattice parameter with a good accuracy for the purpose of this study as shown in chapter 8.1.

6 Applicability of the setup for in situ studies of nano-structured materials

6.1 Motivation

Nanostructured TiO_2 exhibits unique electronic and photonic properties and can therefore be utilized in various applications such as materials for sensors (Benkstein *et al.*, 2006, Manera *et al.*, 2005), electrodes in dye sensitized solar cells (Jiu *et al.*, 2006), hybrid organic solar cells (Lira-Cantu *et al.*, 2007), optical spacer layers (Andersen *et al.*, 2009) and anode materials for batteries (Kim *et al.*, 2007). Furthermore, TiO_2 nanoparticles show high photocatalytic activity for various chemical reactions (Fox and Dulay, 1993), the water splitting reaction (Kahn *et al.* 2002) and for pollutant elimination (Nagaveni *et al.*, 2004, Zeng *et al.*, 2008). Nano-crystalline TiO_2 can also be used as catalyst support material, in example to support Au nanoparticles for the low temperature oxidation of CO ([a,b]Grunwaldt *et al.* 1999).

Titanium dioxide exists in three different polymorphs, thermodynamically stable rutile and metastable anatase and brookite. The anatase phase was reported to show the highest catalytic activity for most of the applications as photocatalysts (Fox and Dulay, 1993). Apart from the polymorphic modification of TiO_2, its crystallinity (Shimizu *et al.*, 2005, Akurati *et al.*, 2007) nanostructure (Nagaveni *et al.*, 2003, Liao *et al.*, 2006) are essential parameters for the photocatalytic activity. Akurati *et al.* (2007) reported a strong effect of the crystallinity of flame synthesized TiO_2 nanoparticles on the activity for photodegradation of methylene blue. It was concluded that the higher crystallinity prevents fast recombination of the electron-hole pairs generated by photo-excitation. Lioa *et al.* (2006) studied the activity with different shaped TiO_2-particles for the methyl orange decomposition. The results indicate that the reaction is *structure sensitive*. The different observed activities were attributed to different band gap energies due to the particle size and shape.

Anisotropic TiO_2 nanoparticles such as rods (Cozzoli *et al.*, 2003), ellipses or cubes (Lioa *et al.*, 2006) are often synthesized by wet chemical routes, whereby the shape is varied by the choice of the organic surfactant, the Ti-precursor and the synthesis conditions. The surface of those TiO_2 particles will therefore be covered with surfactant molecules. However, high photocatalytic activity, application as chemical sensor and electrode materials, require readily accessible surfaces and therefore removal of the surfactants. One simple approach for a complete removal is to anneal dry particles in a gas stream above the decomposition temperature of the organic surfactant. But elevated

temperatures also facilitate particle growth and the anatase-rutile phase transition, processes that are in general regarded as detrimental even though particle sintering up to a certain degree might be favored to maintain a stable and highly porous 3-dimensional network (Benkstein *et al*., 2006, Bao *et al.*, 2007, Zeng *et al*., 2008).

Because of their utilization in versatile applications, and the fact that many of those applications require readily accessible surface and a high degree of crystallinity, both being easily obtained by thermal pretreatment, we chose TiO_2 nanoparticles to test the applicability of the simultaneous *in situ* SAXS/WAXS setup to study dynamical changes of nanostructured materials. Oleic acid capped rod shaped TiO_2 nanoparticles were heated in inert gas stream to resolve the correlations of particle and crystallite growth. The experiments should furthermore resolve the temperature interval in which the rod-sphere transition takes place and indicate if the anatase-rutile phase transition takes place in the selected time and temperature-frame. The performance of the *in situ* setup was validated by measuring a standard anatase-rutile TiO_2 sample, Degussa P25, and by measuring an annealed TiO_2 sample of our preparation in a standard X-ray powder diffraction. The results of the heating experiments on the TiO_2 nanorods were published in a scientific article in the *Journal of applied crystallography* (Kehres *et al.*, 2010). This chapter is not intended to give a full presentation of the experimental results. It rather gives an overview of the most important results and those not included in the paper. The detailed explanation and discussion of the results, together with a conclusion, can be found in the attached paper 1.

6.2 Results and discussion

Figure 16 (left) shows a HRTEM micrograph of the fresh oleic acid capped antase TiO_2 nanorods, prepared by the wet chemical route described by Cozzoli *et al.* (2003). The micrograph shows a multiplicity of characteristic anatase (101) lattice fringes with a distance of 3.56 Å. Anisotropic growth of the TiO_2 nanorods seems to occur along the [001] direction. WAXS patterns, acquired at low temperatures, also reflect the anisotropic crystallite shape of the anatase nanorods. A sharper anatase (004) and a broader (200) reflection were observed, indicating as well extended crystallite domains along the [001] direction. The growth of the anatase TiO_2 nanorods in the [001] direction can be explained by a 1.4 times larger surface energy of the {001}-facets compared to the {101}-facets predicted from the Donay-Harker rules (Penn and Banfield, 1999).

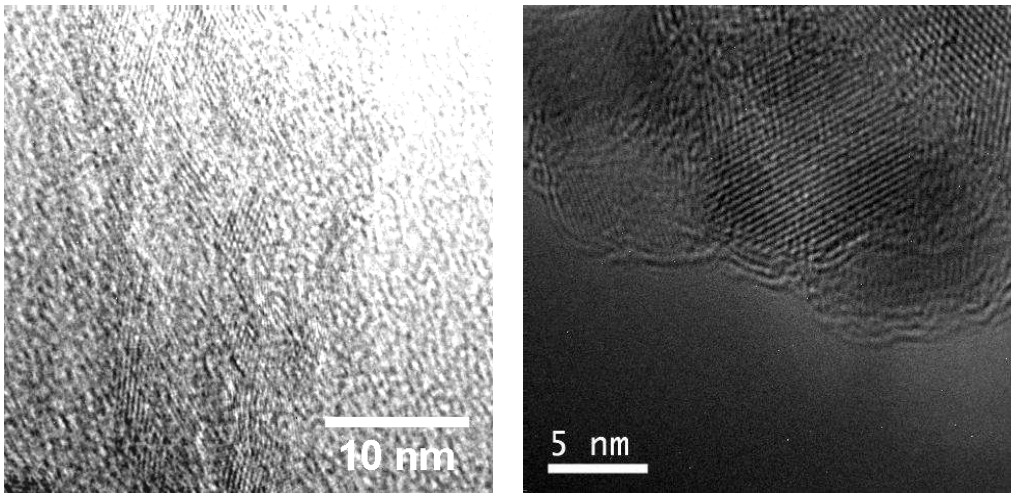

Figure 16: HRTEM of freshly prepared anatase TiO_2 nanorods (left) and after a heating experiment to 1023 K in inert atmosphere (right).

To resolve the temperature interval in which the rod to sphere transition takes place, the anatase (004) and (200) peaks were fitted with a Lorentzian profile function to obtain the corresponding full width at half maxima (FWHM) of the reflections, see figure 17 (left).

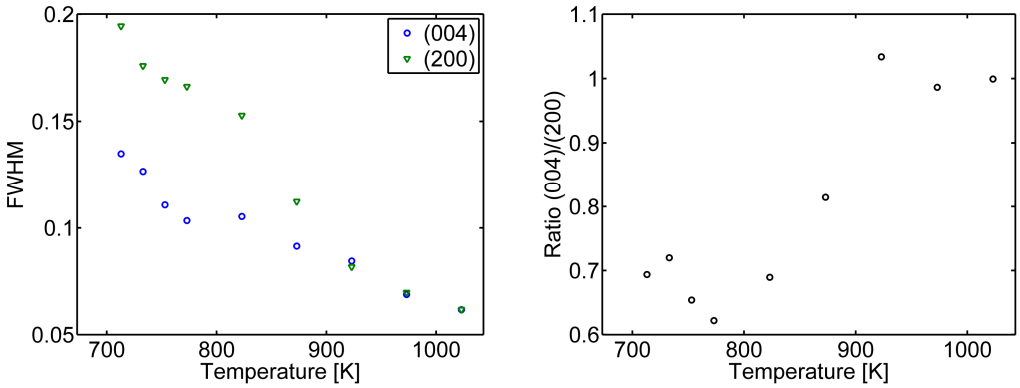

Figure 17: FWHM from fits of Lorentzian profiles on the anatase (004) and (200) peak (left) and FWHM ratio anatase (004)/(200) (right).

The FWHM of both reflections due to size broadening effects should be approximately equal in case of a spherical crystallite shape. Consequently, the rod-sphere transformation should be indicated by an increase of the FWHM ratio of the (004) / (200) reflection close to one. A plot of the ratio versus the sample temperature is shown in figure 17 (right). The FWHM ratio of both reflections seems to be unaltered at temperatures below 753 K. The slight increase of the ratio might be explained by the accuracy of the unconstraint fit of the Lorentzian profiles on the relatively broad reflections. A decrease of the FWHM ratio in the temperature interval from 753 - 773 K was observed and this might be explained by a connection of different crystallite

domains along the [001] direction. The FWHM of the anatase (200) reflection decreases in the same temperature interval and indicates sintering of the aligned TiO_2 rods. However, the results should not be over-interpreted because of the low accuracy of the unconstraint fit. A clear increase in the FWHM ratio from 0.62 to 1.03 in the temperature interval of 773 - 923 K indicates the transformation from rod to spherical crystallite shape.

SAXS patterns, acquired at all temperatures, were analyzed using the unified equation (3-21 comprising two size regimes to obtain the radii of gyration R_g corresponding to the radius of the cluster aggregates consisting of several parallel aligned nanorods, and the cylindrical cross section orthogonal to the long axis of the rods., After the occurrence of the rod-sphere transformation, the fitted R_g corresponds to the radius of a sphere. Crystallite diameters were obtained from refining the particle size broadening with Rietveld refinement, neglecting any effect of the anisotropic crystallite shape and using the Rietica software (Hunter, 1998).

The evolution of the particle diameter determined from SAXS and the crystallite size determined from WAXS is strongly correlated, see figure 18.

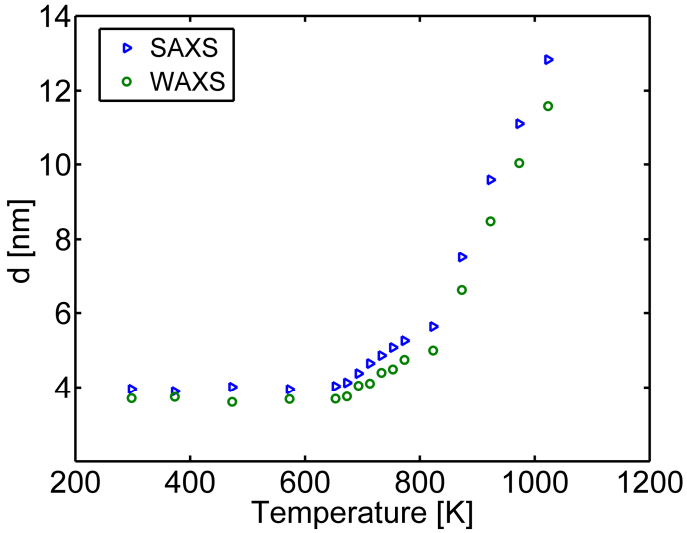

Figure 18: Particle diameter from fits of the SAXS data (o) and crystallite sizes from Rietveld refinements (<).

At temperatures below 653 K, the particle diameter and crystallite size remain constant and are consistent around 4 nm. Both the particle diameter and the crystallite size increase slowly in a temperature interval of 653 - 823 K. This correlates well with the loss of surfactants observed by thermo-gravimetric analysis (TGA) with a maximum at ~ 650 K and indicates the initiation of rod sintering, i.e. the loss of individual rod

character and the onset of spherical particle growth. The driving force for those processes is the minimisation of the overall surface energy. The difference between the particle diameter and the crystallite size increases in the same temperature interval. At temperatures above 823 K, both the particle diameter and the crystallite size increase rapidly, which is consistent with the rod-sphere transformation. At those temperatures, all surfactant molecules are decomposed, which allows good contact between the unprotected TiO_2 particles. However, the specific transition temperatures are likely to be influenced by the different heating steps used during the annealing of the sample, since the crystallite growth is a function of time and temperature (Li *et al.*, 2005). Figure 19 sketches a possible physical transformation in accordance with the experimental observations.

The small discrepancy between the particle and crystallite diameter was retained at temperatures above 823 K. High resolution transmission electron microscopy revealed that the TiO_2 particles exhibit a core/shell structure, consisting of a single crystal core and some material that appears to be separate domains in a shell of 0.5-1.4 nm thickness, see figure 16 (right). This was consistent with the slightly larger particle diameter determined from SAXS at 1023 K. But it is possible that the increased discrepancy between particle and crystallite size is also partly due to an artefact of either the crystallite or particle diameter determination, because the shape changed during the sintering.

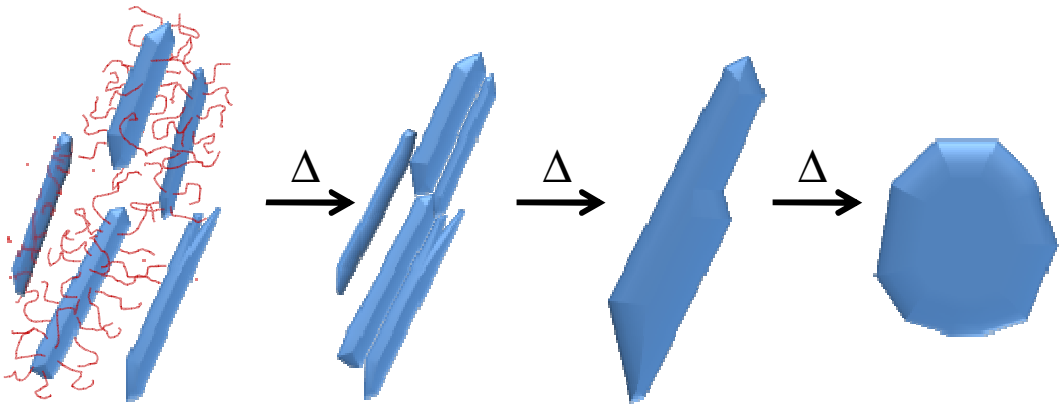

Figure 19: Sketch showing a possible sequence of physical transformations that are in accordance with the experimental observations.

Rietveld refinement of the WAXS revealed the absence of the anatase-rutile phase transition during the experiments to 1023 K. The irreversible transition is a function of time, temperature (Ikuma *et al.*, 1996) and crystallite size (Li *et al.*, 2005). Anatase exhibits a lower surface energy than rutile and this fact becomes significant because of

the large surface to volume ratios of nanoparticles (Gilbert *et al.*, 2003). Similar experiments on oleic acid capped rod shaped anatase nanoparticles by Chen *et al.* (2009) showed also no anatase-rutile transition at temperatures up to 1023 K, although a time dependent transition was reported to occur at 1123 K. However, Chen *et al.* (2009) assumed that the absence of the anatase-rutile phase transition at 1023 K and a slow transition at 1073 K were related to the small rod diameter and therefore large surface area resulting in low surface free energy. The heating experiments presented in this thesis clearly refute their assumption since the rod-sphere transformation already occurred at temperatures below 923 K.

A standard TiO_2 material, P25 from Degussa (now Evonik), a mixture of nanocrystalline anatase and rutile, which is used for a large variety of applications, including research in photocatalysis, was measured in the *in situ* setup, to validate the capability for phase distinction and refinement. Rietveld refinement of the P25 sample is shown in figure 20. The anatase/rutile fractions were determined to be 67.4 % anatase and 32.6 % rutile which is in reasonable agreement with values reported in the literature, which vary from 73 - 78.8 % anatase, 14 - 27 % rutile and 0 - 18 % amorphous TiO_2 (Jensen *et al.*, 2006, Porter *et al.*, 1999, Bakardjeva *et al.*, 2005, Ohtani *et al.*, 2010). The successful refinement confirms the capability of the instrumental setup to resolve the anatase rutile phase transition.

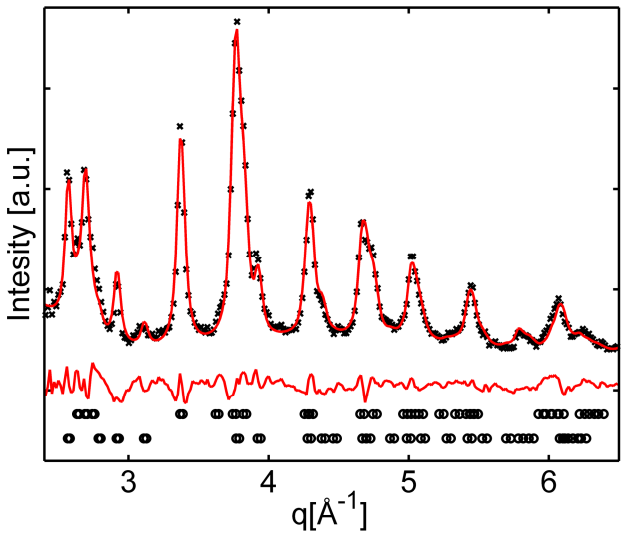

Figure 20: Rietveld refinement of P25 with theoretical peak positions (o) for anatase (top) and rutile (bottom).

6.3 Conclusion

The results of the heating experiments on the anatase TiO_2 nanorods proved the applicability of the simultaneous *in situ* SAXS/WAXS setup to study the dynamical changes of nanostructured materials. Correlated crystallite and particle growth was observed, initiated at temperatures where the oleic acid surfactant decomposes.

The morphology transition from rod to spherical particle shape occurs in a temperature interval from 723 - 923 K. The anatase-rutile phase transition was not observed at any temperature, TiO_2 remained in the anatase crystalline phase which is favoured for most applications. However, Rietveld refinement of the WAXS, acquired on a P25 sample, validates the capability of the instrumental setup to resolve this phase transition.

The experimental results emphasize the benefit of *in situ* combined SAXS/WAXS for tracking the dynamical processes during sample annealing, i.e. the application of one isolated technique would not resolve the formation of TiO_2 core/shell particles. Time and temperature resolved *in situ* combined SAXS/WAXS is essential to overcome the difficulties of exactly reproducing the experimental conditions for the different experimental techniques.

7 Dynamical properties of Ni/spinel catalyst during reduction, oxidation and dry methane reforming

After it had been successfully shown that the heating unit of the *in situ* cell permits work in the desired temperature range from 298 - 1073 K and that the instrumental setup can be used to study the dynamics of nanostructured materials *in situ*, reduction in hydrogen and dry reforming experiments on the 22 wt% $Ni/MgAl_2O_4$ were performed to follow the dynamical changes of methane reforming catalysts under conditions comparable to large scale processes. In this chapter the main results of the paper about the *in situ* reduction experiments on a model 22 %wt $Ni/MgAl_2O_4$ catalyst are presented (see paper II). A detailed description of the tested catalyst sample can be found elsewhere (Sehested *et al.*, 2001). Heating experiments of the catalyst sample in helium are described to confirm that the observed decrease of the Ni lattice parameter during heating in hydrogen is solely related to the reduction. The heating experiments in helium revealed the problem of a possible contamination with oxygen during the experiments. The unsuccessful attempts to perform *in situ* dry methane reforming on this catalyst are also described and discussed.

7.1 In situ reduction

7.1.1 Motivation

Ni based catalysts are advantageous when compared to noble metal catalysts for methane reforming with steam and carbon dioxide considering the higher costs for noble metals and their limited availability (Guo *et al.*, 2004). However their drawback is their higher carbon deposition rate compared to most of the noble metals (Rostrup-Nielsen *et al.*, 1993), this leads to a faster catalyst deactivation. The rate of carbon formation was observed to depend strongly on the Ni crystallite size, as lower rates were observed with decreasing Ni crystallite sizes (Borowieki, 1982, Chen *et al.*, 2005). This emphasizes the importance of the metal dispersion on the performance of the catalyst. Highly efficient and long time stable Ni based catalysts, for methane reforming, should exhibit a high initial metal dispersion and retain it during the reforming. The final step of the catalyst preparation is the activation by reduction in hydrogen. Furthermore it was reported that sulphur poisoned Ni catalysts can be regenerated by cyclic oxidation and reduction in hydrogen (Aguinaga and Montes,

1992). An increase of the Ni crystallite size with an increasing reduction temperature was noted (Borowiecki 1982). Whereas a mean Ni crystallite size of 6.5 nm was noted for 50 wt% Ni/MgO catalyst reduced at 773 K showed the same catalyst, reduced at 973 K, a mean Ni crystallite size of 9.7 nm.

Since the activity and resistance against carbon deposition of Ni based methane reforming catalysts are correlated to its dispersion, it is crucial to follow and understand dynamical processes during the reduction and thus improve start-up processes. This section describes the heating experiments of a prereduced and reoxidized 22 wt% $Ni/MgAl_2O_4$ catalysts, to follow the dynamical changes during the reduction in pure hydrogen and resolve the correlations between reduction of the NiO phase and particle growths.

7.1.2 Results and discussion

The low resolution of the CCD detector to acquire the WAXS in the present instrumental setup results in strong overlapping of most of the observed reflections thereby making simple data analysis impossible i.e. phase identification with the peak matching method and profile function fitting on single reflections to evaluate the size parameter using the Scherrer equation. A WAXS pattern of the fresh 22 %wt $Ni/MgAl_2O_4$ catalyst is shown in figure 21 (right) and it shows clearly that most of the interesting Ni- and NiO-reflections overlap with reflections from the support material. To overcome this problem a WAXS pattern of a fresh catalyst sample was acquired in a standard powder diffractometer and the sample phases were identified with the peak matching method as Ni (space group #225: Fm-3m), NiO (space group #225: Fm-3m), $MgAl_2O_4$ (space group #227: F d3mS) and α-Al_2O_3 (space group # 167: R-3c). With this knowledge a structural model for Rietveld refinement was created using the following cards from the inorganic crystal structure database: ICSD-52231 (Ni), ICSD-61324 (NiO), ICSD-31373 ($MgAl_2O_4$) and ICSD-92628 (α-Al_2O_3). Rietveld refinement was first performed on the higher resolution WAXS pattern acquired in the standard powder diffractometer (see figure 21 a) and applied afterwards to refine the patterns recorded with the CCD camera, taking the different instrumental resolution determined from a Si standard (NIST SRM 640 c) into account (see figure 21 b). The simulated pattern, from Rietveld refinement, and experimental observed data acquired in both experimental setups are in good agreement and the deviations between the model and experiments seem to be systematic.

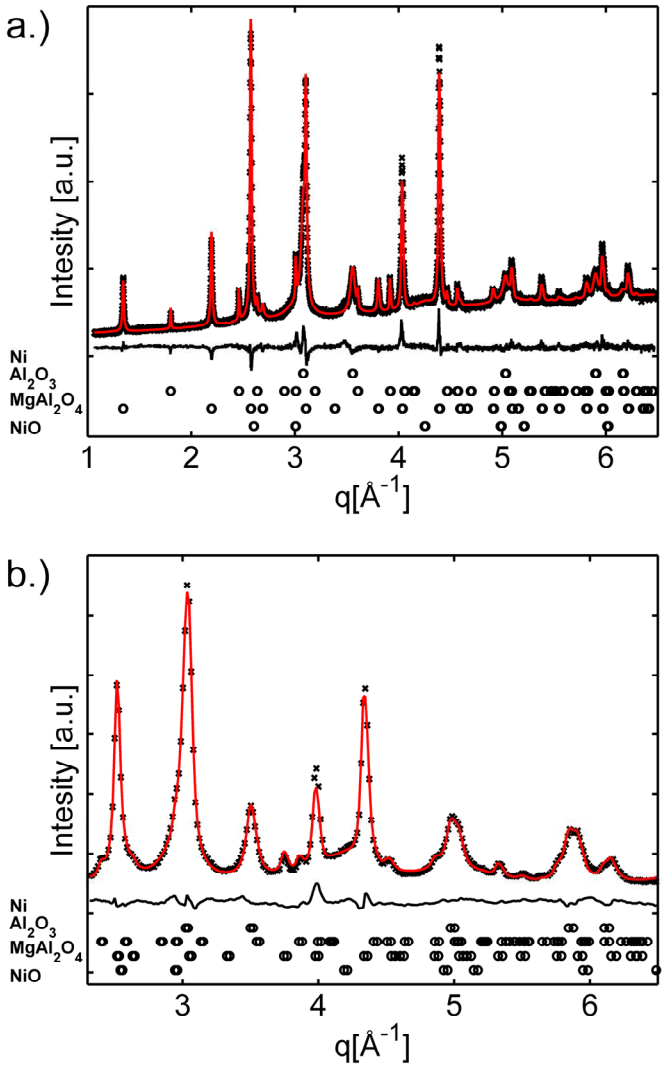

Figure 21: Rietveld refinement of a fresh Ni/$MgAl_2O_4$ catalyst sample at 298 K from data acquired with the standard powder diffractometer setup (a.) and the CCD detector (b.). Refined sample phases (o) from top to bottom, Ni, alpha-Al_2O_3, $MgAl_2O_4$ and NiO.

The Ni lattice parameter was observed to increase linearly with temperature during heating in hydrogen and that can be related to thermal expansion of the Ni crystal lattice. However, with initiation of the reduction, in a temperature interval from 413 - 453 K, a decrease of the Ni lattice parameter was noted, see figure 22.

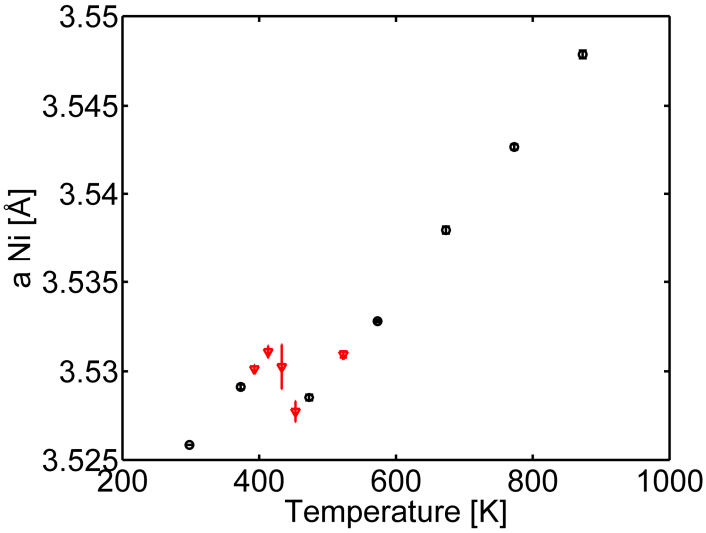

Figure 22: Evolution of the Ni lattice parameter, obtained from Rietveld refinement, during a heating experiment in steps of 100 K (o) and an additionally acquired data at intermediate temperatures (v) on another sample to resolve the decrease between 373 and 473 K.

The decrease of the Ni lattice parameter can be explained as the following: Ni particles form a passivating NiO shell of around 2 nm irrespectively of the grain size (Seto *et al.* 2005, Phung *et al.* 2003, Sakiyama *et al.* 2004). Ni and NiO crystallize both in the cubic phase and the Ni lattice parameter under standard conditions is about 19 % smaller than the one of NiO. Due to interface stress between the core and the oxidic shell (Rellinghaus *et al.* 2001) the Ni lattice parameter expands. This effect was reported to be particle size dependent, with decreasing particle sizes, increasing Ni lattice parameters were noted (Rellinghaus *et al.* 2001, Duan *et al.* 2004). The decrease of the Ni lattice parameter is therefore related to the reduction of the NiO shell, whereby stress due to the lattice mismatch disappears.

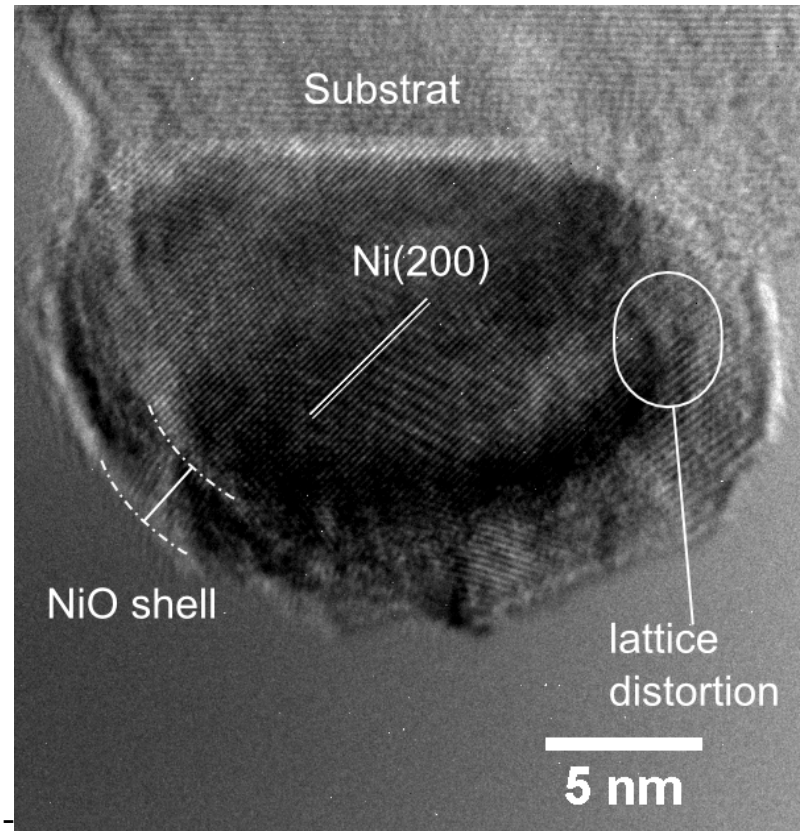

Figure 23: Ni/NiO core shell particle on $MgAl_2O_4$-support

The existence of Ni/NiO core-shell particles in the catalyst sample was also confirmed with HRTEM, see figure 23. The Ni core shows characteristic fringes for the Ni(200) crystal planes. Lattice distortions are visible close to the Ni/NiO interface indicating stress due to the lattice mismatch between Ni and NiO. The shown core in figure 23 is a single crystallite, however, some of the other particles showed grain boundaries from several Ni crystallite domains. The NiO shells were observed to be polycrystalline, domains with fringes attributed to the NiO(111) and NiO(200) planes were observed.

The evolution of the Ni/NiO particle diameter, determined from a least square fit of the unified equation (3-21) comprising four size regimes, two for the scattering from the support particles and one for the Ni/NiO particles. The SAXS pattern showed an artifact at highest q that is most probably related to a wavelength dependent sensitivity of the gas detector. This artifact was well described and fitted with an additional size regime. A least square fit of all size regimes was only performed on the first SAXS pattern (see paper 2 for a figure of the least square fit and detailed discussion of the results). During the heating in hydrogen only the fit parameters of the size regime describing small angle scattering from the Ni/NiO-particles were left free, all other size regimes were fixed since we did not expect any reaction or sintering of the support under the conditions. The evolution of the Ni/NiO particle size is shown in figure 24. The Ni/NiO

particles of the studied catalyst have a broad size distribution. Scattering of the largest Ni/NiO particles contributes to the SAXS pattern in a *q*-region where scattering of the support particles occurs. They are therefore most properly fitted with the terms of the unified equation describing scattering of the support particles. The evaluated Ni/NiO particle diameter does not represents the mean diameter of the size distribution, but can still be used to describe the dynamics of the processes, keeping in mind that it is not an absolute value.

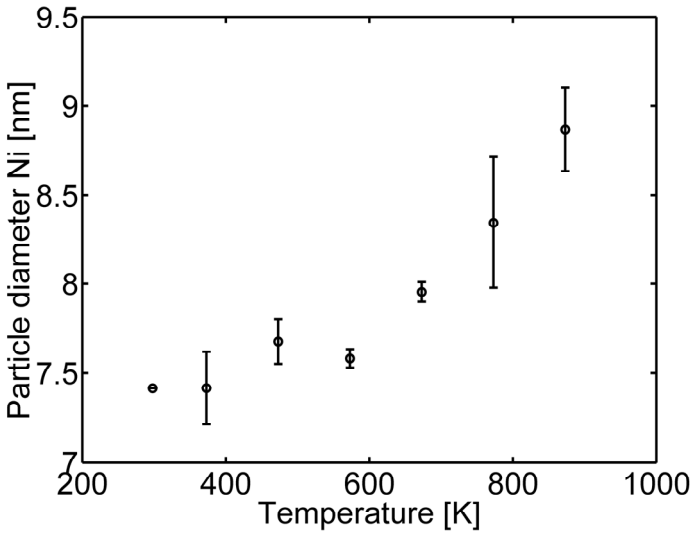

Figure 24: Evolution of the Ni particle size from SAXS during the in situ reduction. The error bars show the standard deviation of diameter. Only one SAXS pattern was acquired at 298 K. The diameter at 298 K has therefore no error bar.

Overall, the Ni particle diameter increases at temperatures above 373 K. It was reported that growth of unsupported Ni/NiO core shell particles only occurs after reduction of the protective NiO shell (Setthi and Thölén, 1994). The reduction of the NiO shell, studied herein, was observed from in a temperature interval from 413 - 453 K from WAXS. The growth of supported Ni particles occurs predominately by a migration coalescence-mechanism (Richardson and Crump ,1979, Sehested *et al.*, 2001), because the activation energy for the migration of Ni particles is smaller than for the evaporation of atoms, which would facilitate Ostwald ripening (Richardson and Crump, 1979). The mobility of the Ni particles on the support surface is a function the temperature and their size, smaller particles show a higher mobility than larger ones (Richardson and Crump, 1979), therefore the fraction of smaller particles diminish during the sintering process. The increasing rate of particle growth, at temperatures above 573 K, might reflect the temperature dependence of the particle mobility on the catalyst surface.

The Ni/NiO particle diameter increases slightly at temperatures above 373 K, however, a slight decrease of around 0.1 nm was observed in a temperature interval between

473 and 573 K. At temperatures above 573 K the Ni/NiO particle diameter increases monotonic. The slight decrease in the temperature interval between 473 K and 573 K can be related to the reduction. Ni has with 8.9 g cm^{-3} a larger mass density than NiO with 7.5 g cm^{-3}, thus the reduced Ni particles will have a smaller diameter compared to the initial Ni/NiO particles, if the number of atoms in the Ni-cluster remains constant. However, the decrease is rather small and inside the limit of accuracy of the fit, since the contributions of Ni/NiO to the SAXS are small compared to those of the support.

7.1.3 Conclusion

Simultaneous *in situ* SAXS/WAXS was applied to follow the dynamics of a 22 wt% $Ni/MgAl_2O_4$ methane reforming catalyst during the reduction in pure hydrogen. The Ni particles in a fresh catalyst sample exhibit a Ni/NiO core-shell structure[1]. The reduction of NiO, that begins in the temperature interval from 413 - 453 K, is observed by the decrease of the Ni lattice parameter. This decrease can be explained by contraction of the Ni lattice due to release of interfacial stress during the reduction of the NiO shell. Coalescence of the Ni particles was observed at higher temperatures after reduction of the protective NiO shell.

7.2 In situ heating

7.2.1 Motivation

In situ heating experiments of the supported 22 wt% $Ni/MgAl_2O_4$ were performed to confirm that the decrease of the lattice parameter at temperatures from 413 - 453 K is intrinsically related to the reduction of the NiO shell and therefore to the disappearance of interfacial stress. The heating experiments were performed in the same manner as the reduction, with a catalyst sample of approximately 5 mg, but instead of H_2 a continuous He flow of 2 mL min^{-1} was applied (Helium HG, Air Liquide, > 99.996 vol%). The experiments in He were performed using only the camera in short geometry since the photon flux in this setup is approximately two orders of magnitude higher compared to the long geometry because of the shorter collimation lengths. The short setup allows therefore better count statistics of the CCD detector and this is desirable since the experiments were only performed to resolve the evolution of the Ni lattice parameter depending on the sample temperature. An unexpected oxidation of the Ni particles was observed. Reasons for the oxidation are discussed in this section.

[1] The Ni/NiO core shell structure has its origin in the preparation of the catalyst sample. The catalyst sample was prereduced after the calcination and then passivated with a mixture of oxygen and nitrogen at moderate temperatures

7.2.2 Results

A section of the WAXS pattern obtained during the heating experiments in He acquired is shown in figure 25 (top). The WAXS clearly shows that oxidation of the Ni catalyst particles occurs at temperatures above 473 K indicated by a increasing intensity of the NiO(220) peak and respectively decreasing intensity of the Ni(200) reflection. This correlates with the changes of the SAXS at lowest resolvable *q*.

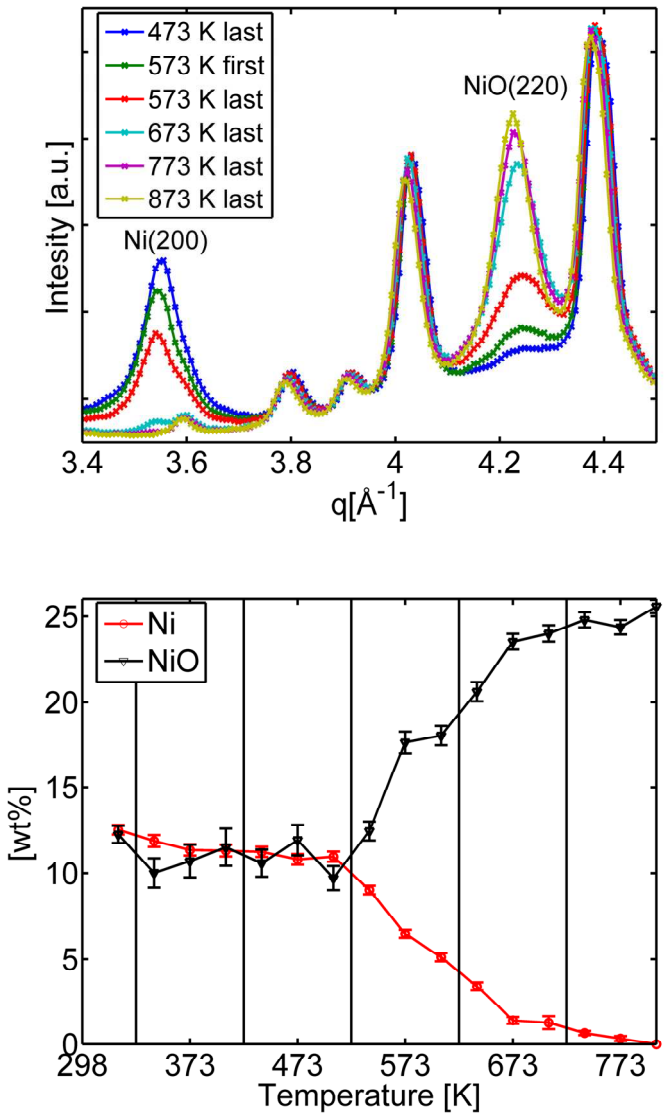

Figure 25: Section of the WAXS (top) during an in situ heating experiment in short geometry acquired using Mo Kα-radiation and phase composition of Ni/NiO from Rietveld refinement (bottom).

Rietveld refinement was performed refining the lattice parameters and crystallite sizes of Ni and NiO from the peak broadening. The phase composition (Ni/NiO) as a function of temperature and time obtained from Rietveld refinement is shown in figure 25

(bottom). At temperatures below 573 K both the Ni and NiO fractions seem to be unaltered. At higher temperatures, the oxidation is a function of time and temperature. Unfortunately, the data is not sufficient to make any predictions about the kinetics of the oxidation reaction. The Ni lattice parameters refined during the *in situ* reduction and heating in He is shown in figure 26 (top) along with the NiO crystallite size (bottom) during the oxidation.

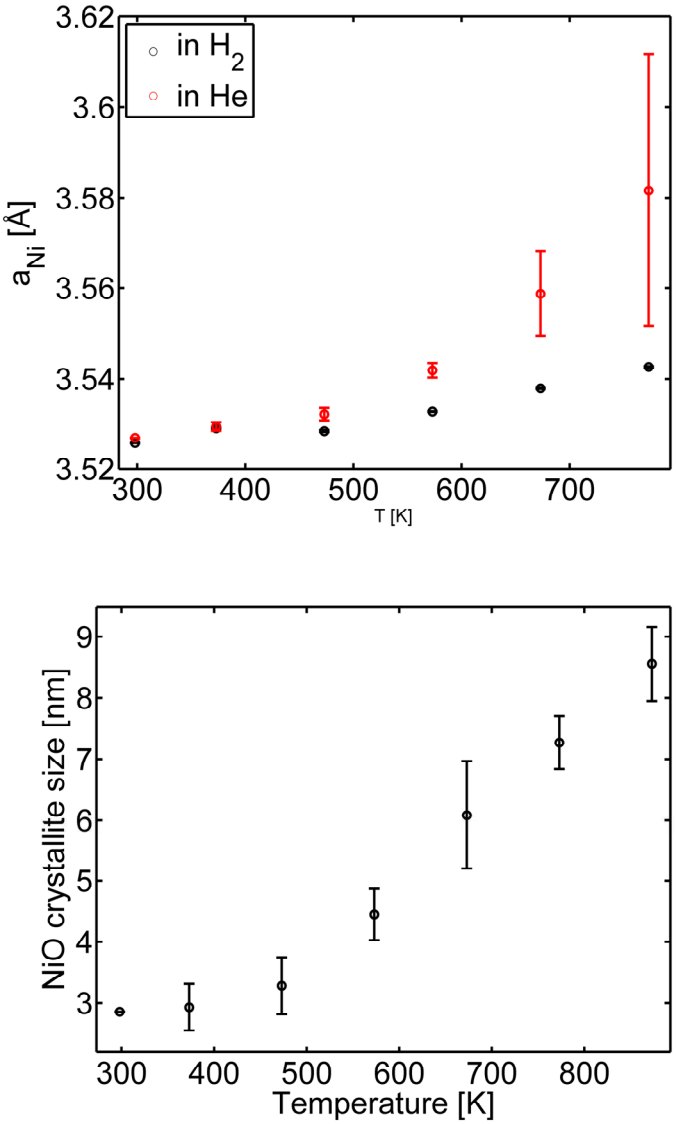

Figure 26: Ni lattice parameter during in situ reduction oxidation (top) and NiO crystallite size (bottom) from Rietveld refinement. The increase of Ni lattice parameter during the reduction is due to thermal expansion of the crystal lattice. During the oxidation it is a combination of thermal lattice expansion and size dependent lattice expansion of the Ni lattice parameter to match the NiO lattice.

During the reduction experiments the Ni lattice constantly decreases in a temperature interval from 373 - 473 K whereas it seems to increase continuously during the

oxidation. However, at temperatures where the oxidation of the Ni particles occurs, the Ni lattice parameter increases faster than expected from thermal expansion. The mean NiO crystallite size increases linearly during the oxidation at temperatures above 373 K, from 2.9 to 8.6 nm at 873 K. However, the mean Ni crystallite remains constant up to a 573 K, but at 673 K a decrease from 9 nm to around 2 nm was observed.

7.2.3 Origin of the oxygen contamination

Despite all the precautions that were taken to control the atmosphere around the sample, small amounts of O_2 were found even when the gas line was fed with He > 99.996 vol%. There are at least four possibilities that might explain the presence of O_2 and therefore the complete oxidation of the Ni catalyst.

1. The capillary became untight at high temperature, because of thermal expansion of the capillary mounting and O_2 from the sample chamber diffused into the capillary.
2. Presence of O_2 as an impurity in the used helium.
3. O_2 in the system due to insufficient purging.
4. Backwards diffusion of O_2 through the vent system into the capillary.

To 1.), the sample chamber was kept in vacuum better than 0.05 mbar to avoid oxidation of the copper block at high temperatures. A gas pressure of 1.7 bar inside the capillary is predetermined by a check valve installed in the *in situ* cell vent system. Major leaks of the capillary can easily be detected by an increase of the pressure in the sample chamber, but the cell pressure was observed to be constant during the experiments.

To 2.), the complete oxidation of the Ni particles assuming a catalyst mass of 5 mg would require 0.22 mL O_2. Assuming that the used gas fulfils the certified specification of < 5 ppm O_2 content, it would require, with the applied flow, a duration of the experiment of about 350 hours for the complete oxidation of the Ni particles. However, a complete oxidation of the Ni particles was observed in less than 13 h, that excludes the possibility that the oxidation was solely caused by impurities, assuming that the He has the certified quality.

3.) and 4.) are on the contrary possible explanations even if the sample was purged with He before the experiments. The present setup of the gas system is not connected to any vacuum pump and that precludes repeating evacuation and purging of the system with a reactant gas. The vent system does not include any washers to prevent back diffusion of

oxygen. However, the heating experiments in helium where performed at the very end of this thesis so this excluded any implementation of proposed technical solutions and repetitions of all experiments. Since the oxygen contamination might also have influenced some of my other experiments and can also represent a problem for future users of the equipment and it is necessary to mention it here.

7.2.4 Discussion

The evolution of the Ni lattice parameter, that decreases with the reduction and increase with the oxidation of the NiO shell, has been reported to be related to interfacial stress between the Ni core and the NiO shell (Rellinghaus *et al.*, 2001). An increase of the Ni lattice parameter, more than expected from thermal expansion, along with an increasing mean NiO crystallite size, indicates the growth of the NiO shell and consequently the shrinking of the Ni core. The observations clearly reveal the size dependent expansion of the Ni lattice to match the NiO lattice (Rellinghaus *et al.* 2001, Duan *et al.*, 2004). The constant mean Ni crystallite size at temperatures below 673 K, even when growths of the NiO shell were already observed, might be explained by the polydispersity of the Ni particles. The diffraction peaks, resulting from polydisperse crystallites, exhibit a sharper maximum and a longer tail compared to peaks from monodisperse crystallites (Langford & Wilson 1978). The evaluation of the size parameter from the FWHM takes only scarcely the tail resulting from the small particles into account leading in general to an overestimation of the mean crystallite size (Bergeret & Gallezot 2008). The Ni/NiO particles in the initial catalyst sample showed a very broad size distribution, particles sizes from 2.1 up 57.8 nm were measured. Since the smaller particles will most likely be oxidized faster than the larger particles, the mean crystallite size might be overestimated at temperatures below 673 K.

7.2.5 Conclusion

Oxidation experiments of the 22 wt% Ni/$MgAl_2O_4$ in helium clearly revealed that the decrease of the Ni lattice parameter during heating in hydrogen is solely related to the reduction of the NiO shell and thereby to the disappearance of interfacial stress between the Ni-core and the NiO-shell. A further increase of the Ni lattice parameter with the shrinking of the Ni core was observed, this shows the size dependent relaxation of the Ni lattice parameter to match the NiO shell. The crystallite size of the initial Ni particles and NiO, after complete oxidation of the sample where comparable, indicating no effect of crystallite growths during the oxidation.

7.3 Dry methane reforming experiments

7.3.1 Motivation

Subsequently to the reduction experiments of the 22 wt% $Ni/MgAl_2O_4$, *in situ* dry methane reforming experiments should be performed in a reactant gas mixture of 1 CH_4 : 3 CO_2[2] to follow the changes in catalyst particle morphology and crystallite structure during heating and cooling cycles at different temperatures. The product gas mixture should be monitored with an online quadrupole mass spectrometer to resolve correlations between changes in particle morphology and crystallite structure with changes of the catalytic activity. The results should then be compared with those of dry reforming experiments over Ru-based catalysts that were conducted in a later stage of this study.

7.3.2 Results

Numerous attempts to perform dry methane reforming over the reduced 22 wt% $Ni/MgAl_2O_4$ have been made, but in all experiments a breaking in the capillary was observed. At first the experiments were performed in 0.7 mm quartz capillaries with a wall thickness of 1/100 mm (Mark tubes, Hilgenberg GmbH). The breaking occurred in all cases in the first hour after switching from hydrogen to a premixed reforming gas composed of 1 CH_4 : 3 CO_2 and at temperatures between 723 - 873 K. The capillary broke in most cases directly at the beginning of the catalyst bed, however, in rare cases breaking was also observed in the middle and in the end. During experiments under same experimental conditions over pure $MgAl_2O_4$-support, 4 wt% $Ru/MgAl_2O_4$- and 8 wt% Ru/ZrO_2-catalysts the capillary was stable, it also never broke during reduction of the 22 wt% $Ni/MgAl_2O_4$ catalyst. This excludes that the breaking is due to mechanical stress caused by thermal expansion of the capillary mounting and emphasises that it is rather related to the dry reforming reaction over $Ni/MgAl_2O_4$. In a later stage, the dry methane reforming on the $Ni/MgAl_2O_4$ was performed in single crystal and highly mechanical stable sapphire capillaries, with an inner diameter of 0.8 mm and a wall thickness of 0.1 mm. But even sapphire capillaries got brittle and also broke, after longer experimental durations though.

The WAXS data of the experiments, conducted in sapphire capillaries in the short geometry, were analysed with Rietveld refinement to find out which changes in the

[2] The pre-mixed gas with an excess of CO_2 was chosen from thermodynamic considerations. Carbon deposition on the metal catalyst particles occurs by decomposition of CH_4 and CO. Hence a pre-mixed gas with a lower CH_4 concentration will also show lower carbon formation rates.

catalyst sample preceded the break in the capillary. The Ni crystallite seemed to increase during the first 1.5 h of the experiment at a temperature of 723 K from 9.1 to 13.6 nm, see figure 27 (left) and seems to remain constant afterwards. In the same timeframe, the capillary was blocked, indicated by a decreasing output signal of the mass flow controller, figure 27 (right). An increase of the scattered intensity in SAXS, in a *q*-region where scattering of the Ni particles contributes, was observed, indicating an increase in the Ni particle size. However, since experiments in sapphire capillaries were exclusively performed in the short and very short geometry, with sample detector distances of 1493 mm and 791 mm, the Guinier regime for the Ni particles was not resolved and a determination of Ni particle size from SAXS data analysis not possible.

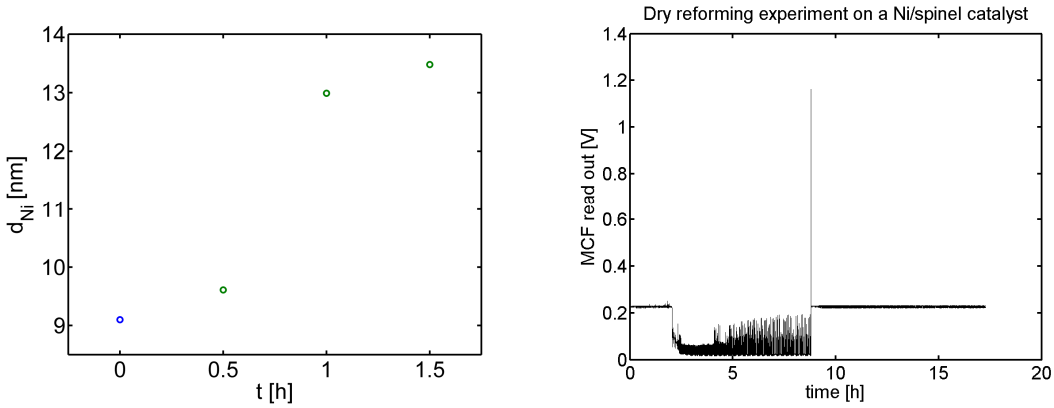

Figure 27: The Ni crystallite size increases after switching to a pre mixed gas with a ratio of 1CH_4 : 3 CO_2 at a temperature of 723 K from around 9.1 to 13.5 nm (left), the blue tick . The read out of the MFC indicates clearly a blocking after 1.5 h and this corresponds to the time interval were the sample was heated from 723 - 773 K by a decrease of the voltage (right). The breaking of the capillary occurs after 9 h, the heater was this time at 1023 K as indicated by the increase of the read out to the initial value.

The reason for the breaking of the capillaries is still unknown. Rapid carbon whisker formation leading to a breakdown of the catalyst structure, causing a blocking of the capillary and mechanical stress on the fragile quartz capillary walls by an increase of material where the whiskers are formed, was considered as one reason. However, carbon formation during the CO_2 reforming reaction is facilitated at high temperatures and pressures (Shimasi and Johnson, 2003, Wang and Xu, 2005). The breaking of the quartz capillaries was observed at low temperatures and at a pressure of only 1.7 bar. (HR)TEM of the samples after performing CO_2 reforming did not show any indication of carbon formation as well.

Another possibility was thought to be a reaction of Ni-catalyst particles under CO_2 reforming conditions with the capillary, since capillaries did not break during experiments on pure $MgAl_2O_4$ and 4 wt% $Ru/MgAl_2O_4$. Therefore several of the broken

quartz capillaries where crushed and measured in a standard powder diffractometer setup, but despite scattering from amorphous quartz and some very weak Ni peaks, most probably due to a contamination with catalyst sample, no new phase was detected.

Coalescence of the Ni particles rapidly initiates after applying a premixed dry reforming gas to the sample until the capillary is completely blocked, this indicates a high mobility of Ni under the experimental conditions. The fact that even sapphire capillaries get brittle support the indication that an intermediate Ni species forms that reacts with the walls of the capillary to form $NiAl_2O_4$. $Ni(CO)_4$ might possibly be such a species, but that is unlikely because it is formed at low temperatures and decomposes agian at temperatures below 523 K to form Ni and CO and this is 200 K below the lowest temperature used for the dry reforming experiments. The only possibility for $Ni(CO)_4$ formation are therefore large temperature gradients inside the catalyst bed. In a last attempt the Ni catalyst sample was diluted with diamond powder. Diamond is one of the best heat conductors and might therefore suppress heat gradients in the catalyst bed. However, a break in the capillary in the same temperature interval was also observed with a diamond diluted sample. Dry reforming experiments over the 22 wt% $Ni/MgAl_2O_4$ were therefore impossible.

7.3.3 Summary

In situ dry methane reforming experiments of a 22 wt% $Ni/MgAl_2O_4$ catalysts could not be performed because of the breaking and blocking of the capillaries that occurred in every attempt after switching to a pre mixed gas. Even sapphire capillaries, with high mechanical strength got brittle, indicating a reaction of the Ni catalyst with capillary walls under dry reforming conditions. The reason for the capillaries breaking is still unknown.

8 Dynamical properties of Ru/spinel catalyst during reduction and dry methane reforming

8.1 Motivation

[a]Jakobsen (2010) performed cyclic heating and cooling experiments on Ru, Rh and Ir catalysts during steam reforming of methane and observed a strong deactivation of the catalysts in a temperature interval from 823 - 923 K. At a temperature of 1023 K the catalysts were observed to reactivate again and the degree of reactivation was dependent on time. The deactivation was observed to be most pronounced during the first heating cycle and less pronounced during the second one. [a]Jakobsen (2010) also reported an influence of the methane conversion level on the deactivation/reactivation phenomena. The temperature, at which the catalyst deactivation initiates, was observed to increase with the amount of catalyst in the reactor if the experiments were conducted with similar mass flows of reactant gas. The deactivation was less noticeable with increasing amount of catalyst and more pronounced for crushed, diluted and retabletted catalyst samples. In the latter case, the more pronounced deactivation was attributed to the presence of smaller catalyst grains and therefore lower methane conversion inside the grain, since transport limitations inside the catalyst grain are reduced.

During the thesis, the planned *in situ* dry reforming experiments were dedicated to investigate if the observed deactivation and reactivation could be correlated with changes of the nanoparticle morphology, the crystallite size or the crystalline structure of the catalysts.

This chapter describes simultaneous SAXS/WAXS experiments during *in situ* reduction and dry methane reforming over a 4 wt% $Ru/MgAl_2O_4$ catalyst. Mass spectroscopy measurements were performed during those experiments to monitor the methane conversion level and possibly relate changes in the catalytic activity to changes of the catalyst nano- and crystalline structure. These dynamical changes were investigated during cyclic heating and cooling, with parameters comparable to the experiments performed by Jakobsen (2010), in a reactant gas mixture of CH_4 and CO_2 with a molar ratio of 1:3. However, the deactivation/reactivation phenomenon, described by Jakobsen (2010), was not observed.

The results of this study will be published in form of a scientific article, therefore only the main results and those not included in the article are discussed in this chapter and further information, discussions and conclusions can be found in the attached paper III.

8.2 Results and discussion

The fresh catalyst sample was investigated by HRTEM to get a good estimate of the nanoparticle morphology for the SAXS data analysis. A HRTEM micrograph of a fresh catalyst sample is shown in figure 28.

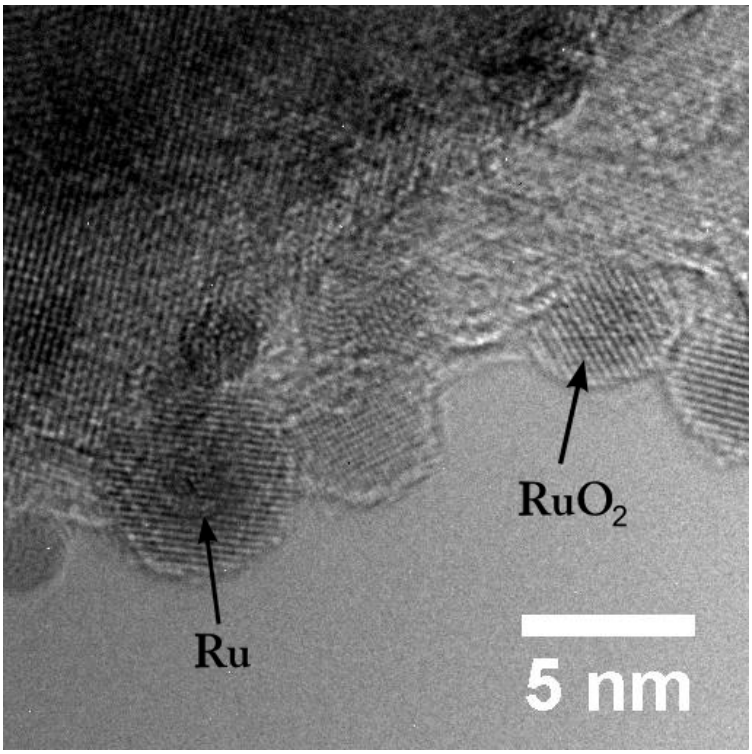

Figure 28: HRTEM image of the fresh Ru/spinel sample. The arrows show particles of pure Ru and RuO_2

In the HRTEM micrographs, atomic distances matching to Ru, RuO_2 and $MgAl_2O_4$ crystallite planes were measured. The HRTEM micrographs did not show any indication for the existence of Ru/RuO_2 core/shell-particles as reported by [b]Jakobsen *et al*. (2010) for a Ru/ZrO_2 catalyst, in fact the observations suggest more a coexistence of spherical Ru and RuO_2 particles. The differences of the Ru-particle morphology might be explained by the use of different support materials or in the mean particle diameter. [b]Jakobsen *et al.* (2010) reported that a mean Ru-particle diameter of 4.9 nm on a ZrO_2 support and herein an average of 1.8 nm from the TEM micrographs on the $MgAl_2O_4$

substrate was observed. However, we do not have any physical explanation for coexistence of the pure Ru and RuO_2 particles yet.

The Reduction of RuO_2 occurred in a temperature interval between 373 K and 393 K, indicated by a increase of the scattered intensity of the Ru-phase and correspondingly a decrease from the RuO_2-phase (see attaches paper 2) and this is comparable with the reported reduction temperature of unsupported RuO_2 (Madhavaram *et al.*, 2001 and Prudenziati *et al.*, 2003). The SAXS data were fitted with the unified equation (3-21), comprising two size regimes for the scattering from Ru/RuO_2 and $MgAl_2O_4$, the support. During the reduction a slight decrease of the mean Ru/RuO_2 particle diameter from 3.4 - 3.3 nm was observed and might be explained by the following. The fresh catalyst sample indicates a coexistence of pure Ru and RuO_2 particles. Due to the difference in mass density, RuO_2 particles will shrink during the reduction around 25 %, if the number of Ru atoms remains constant. Since the particle size from SAXS include both Ru and RuO_2, the decrease in mean particle diameter of 0.1 nm is reasonable.

Prudenziati *et al.* (2003) observed a temperature dependent induction period for the reduction of RuO_2 powders and a wide variety of reduction temperatures, depending on the substrates, ranging from 358 K - 466 K, were reported (Rezaei *et al.*, 2006, Jeong *et al.* 2006, Safariamin *et al.*, 2009 and Bossi *et al.*, 1983). This emphasizes the influence of the metal-support interactions and metal loading on the observed reduction temperatures. The heating ramp has also an extreme impact on the reduction temperatures because of the temperature dependent induction period and heating ramps of 2 - 20 K min^{-1} are commonly used for temperature programmed reduction (TPR) experiments. In this study, heating of the catalyst was performed with temperature steps instead of constant heating ramp and SAXS/WAXS data were acquired during periods of 1.5 h under isothermal conditions. Therefore it is difficult, to evaluate the observed reduction temperature with these reported for the supported Ru catalysts in the literature. For a meaningful comparison of reduction temperature with those reported in the literature one should perform experiments with comparable heating ramps. This could either be done by TPR measurements or by *in situ* powder diffraction experiments with a constant heating ramp at a synchrotron facility, as shown for the reduction of NiO by Rodriguez *et al.* (2001).

After the Ru/RuO_2 catalyst was reduced, in-situ dry reforming experiments were performed. The evolution of the particle diameter during reforming in a gas mixture composed of 1 CH_4: 3 CO_2 is shown in figure 29.

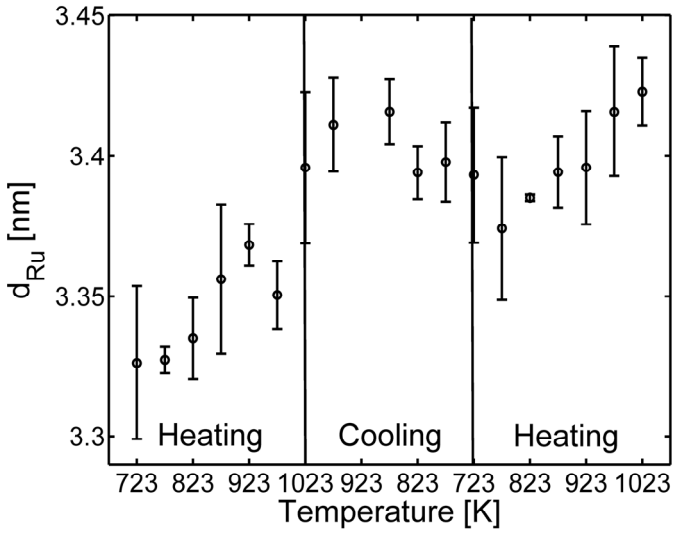

Figure 29: Evolution of the Ru particle diameter during methane reforming.

The Ru-particle diameter increased, of around 0.1 nm from 3.3 to 3.4 nm, during the first heating cycle from 723 to 1023 K, showing sintering of the particles. A slight decrease of the particle diameter was observed during the cooling back period to 723 K. The particle diameter increased again during the second heating cycle and reached a comparable value to the one observed after the first heating at 1023 K. The change of the particle diameter, during the cooling and second heating cycle, are comparable to those expected from thermal expansion of ruthenium (Shirasu *et al.*, 2002) and it can be concluded that particle sintering only occurs during the first heating cycle.

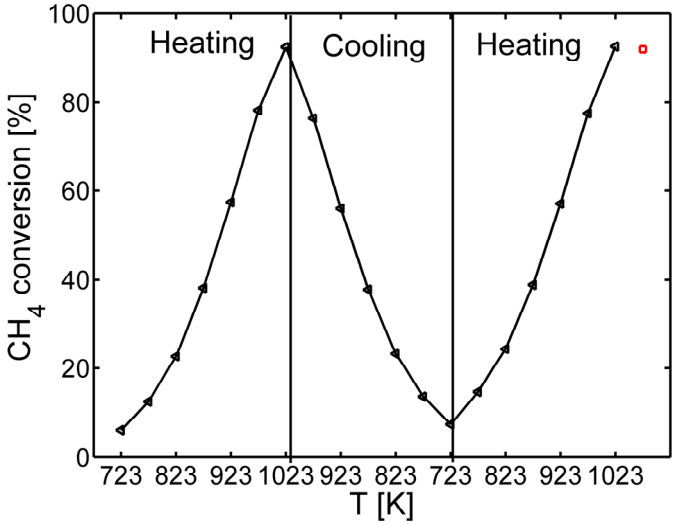

Figure 30: CH_4 conversion level determined from the $CH_3^{+\bullet}$ signal as a function of sample temperature (<) and after 20 h at 1023 K (□).

The methane conversion level increased during the first sample heating in the premixed gas stream from 6 % at 723 K to 92 % at 1023 K, see figure 30. Cooling and reheating

of the sample yielded approximately the same conversion levels. A subsequent long time experiment over the same catalyst sample, at a temperature of 1023 K, did not show any deactivation of the catalyst and the CH_4 conversion level remained constant around 92 %. The constant methane conversion level indicates no deactivation; this result is in agreement with the high sintering stability observed by SAXS. TEM micrographs of the sample after the long time dry reforming experiment did not show any carbon whisker formation and display low tendency of carbon deposition over Ru catalysts (Rostrup-Nielsen *et al.*, 1993).

Reaction rates

To compare the observed catalytic activity during the dry reforming experiments with those reported in the literature, the temperature dependent turn over frequency (TOF) was calculated. The metal dispersion D was calculated from the particle size distribution (PSD) measured from 125 Ru/RuO_2 particles of a fresh catalyst sample. Every surface atom of the Ru-clusters was assumed to be an active catalytic centre. This is not necessarily true if one takes the observation made by [a,b]Wei and Iglesia (2004) and Jones *et al.* (2008) in account, who reported *structure sensitivity* for methane reforming. D can be related to the PSD, if spherical particle shape is assumed, by

$$D = \frac{6v}{s} \cdot \frac{\sum n_i d_i^2}{\sum n_i d_i^3} \qquad (8\text{-}1)$$

where n_i is the number of particles with diameter d_i, v and s the atomic volume and surface area (Lööf *et al.*, 1993). A relative good estimation of D for Ru can be obtained, under the assumption that the particle surface exhibits preferentially facets with the lowest surface energy, in case of ruthenium the Ru(001) planes, by

$$D = \frac{\sum n_i d_i^2}{\sum n_i d_i^3} \cdot 3 \cdot c \qquad (8\text{-}2)$$

where c is the lattice parameter. A metal dispersion of $D_{Ru} = 0.44$ is obtained from equation (8-2) using the PSD from a lognormal fit of the TEM image analysis (see paper III) for Ru/RuO_2 in a fresh catalyst sample. The observed reaction rates, in the unit of g(Ru) per $mol^{-1}(CH_4)$ h^{-1}, calculated from the methane conversion level observed with the MS are listed together with the TOF for the low temperatures in Table 2.

Temperature [K]	Reaction rate [g (Ru) mol^{-1} h^{-1}] *	TOF [surf. $atom^{-1}$ s^{-1}]
723 (h1)	$1.6 \cdot 10^{-3}$	0.06
773 (h1)	$3.2 \cdot 10^{-3}$	0.13
823 (h1)	$5.9 \cdot 10^{-3}$	0.23
873 (h1)	$9.9 \cdot 10^{-3}$	0.38
923 (h1)	$1.5 \cdot 10^{-2}$	0.58
873 (c1)	$9.8 \cdot 10^{-3}$	0.38
823 (c1)	$6.1 \cdot 10^{-3}$	0.24
773 (c1)	$3.5 \cdot 10^{-3}$	0.14
723 (c1)	$1.9 \cdot 10^{-3}$	0.07
773 (h2)	$3.8 \cdot 10^{-3}$	0.15
823 (h2)	$6.3 \cdot 10^{-3}$	0.25
873 (h2)	$1.0 \cdot 10^{-2}$	0.39
923 (h2)	$1.5 \cdot 10^{-2}$	0.57

Table 2: Reaction rates of the 4 wt% Ru/$MgAl_2O_4$ catalyst, h1 - first heating, c1 - first cooling, h2 - second heating.

The TOF's only depend on the temperature and the catalyst deactivation in the temperature interval from 823 - 923 K, as reported by [a]Jacobsen (2010), was not observed. A comparison of the observed TOF's with those reported for dry methane reforming over Ru based catalysts in the literature is listed in Table 3.

Temp. [K]	$TOF_{observed}$ [s^{-1}]	$TOF_{reported}$ [s^{-1}]	Catalyst	*D*	Literature
723	0.06 - 0.07	0.2	0.64 % wt Ru/Al_2O_3	0.510	Ferreira-Aparicio (1998)
823	0.23 - 0.25	2.9	1.4 % wt Ru/MgO	-	Rostrup-Nielsen (1993)
873	0.38	2.0	0.5 % wt Ru/Al_2O_3	0.35	Mark & Maier (1996)
873	0.38	3.1	3.2% wt Ru/Al_2O_3	0.442	[b]Wei & Iglesia (2004)

Table 3: Evaluation of the experimental observed TOFs with reported ones for Ru catalysts in the literature.

The observed TOFs during this study are only in the order of 12 - 35 % of the reported ones. To ensure that the observed TOFs were not limited by the thermodynamic equilibrium, the temperature dependent equilibrium conversion, including the RWGS

was evaluated. A plot of the equilibrium conversion together with the observed conversion is shown in figure 31.

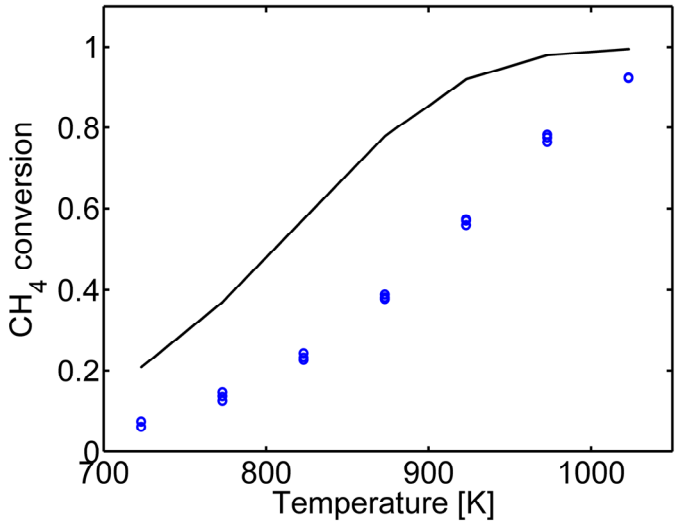

Figure 31: observed methane conversion level (o) and thermodynamic equilibrium including RWGS (-) as a function of temperature.

The observed conversion, at temperatures below 923 K, was below 50 % and therefore still far from the thermodynamic equilibrium. However, [a]Jakobsen (2010) reported an influence of the methane conversion level on the deactivation/reactivation phenomenon. The phenomenon was less pronounced with increasing methane conversion. The most probable explanation for the absence of the deactivation/reactivation phenomenon during this study is that the methane conversion levels were closer to the thermodynamic equilibrium in this study compared to those conducted by [a]Jakobsen (2010).

The low observed TOFs, compared to the literature, might be explained by the relative high methane conversion. The conversion should not exceed 10 - 20 % of the thermodynamic equilibrium to obtain representative reaction rates (Mark and Maier, 1996). During these experiments, the methane conversion level at 723 K approached already 30 % and at 873 K even 50 % of the thermodynamic equilibrium. Consequently, the observed reaction rates are most likely not representative. Another reason for the relatively low reaction rates might be due to limitations by pore diffusion. These limitations can be indicated by a decrease of the activation energy to about one half of those observed without pore diffusion (Chorkendorff and Niemantsverdriet, 2003). As a result the reaction rate was plotted in form of an Arrhenius plot to extract the activation energy, see figure 32.

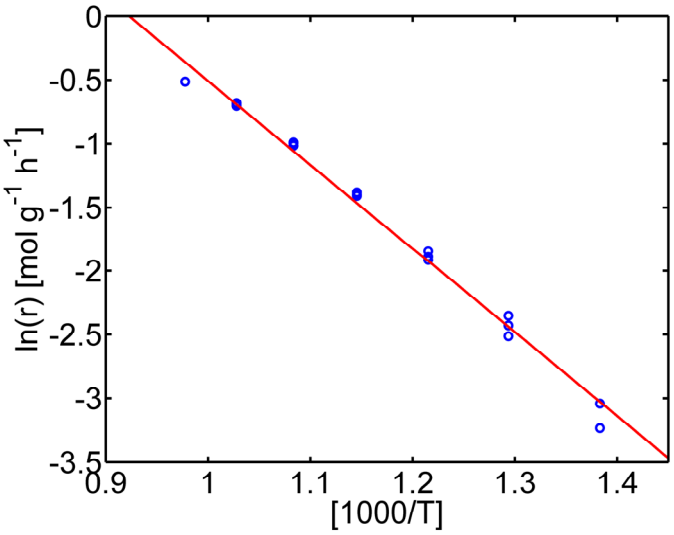

Figure 32: Arrhenius plot of the observed reaction rates from the methane conversion

The activation energy extracted from the Arrhenius plot is E_a = 54.6 kJ mol^{-1}. [b]Wei and Iglesia (2004) reported a value of E_a = 96 kJ^{-1} mol for the dry methane reforming on Ru/Al_2O_3 and Ru/ZrO_2. The observed E_a is 0.5 times the one reported by Wei and Iglesia. This might indicate that the experiments were carried out with mass transport limitations by pore diffusion. To probe if the reaction was limited by pore diffusion the Thiele modulus Φ and the effectiveness factor η were evaluated. The Thiele modulus is a dimensionless number and is proportional to the ratio of the reaction rate without the effect of pore diffusion to the diffusive mass transport inside the pore, if the concentration drops there to zero. A large Thiele modulus will be observed for high reaction rates combined with slow diffusion, indicating mass transport limitations by diffusion. Conversely, a small Thiele modulus indicates a reaction that is only little influenced by pore diffusion. The Thiele modulus can be calculated by

$$\Phi = L\sqrt{\frac{k}{D_{eff}}} \qquad (8\text{-}3)$$

where L is the characteristic size of the catalyst particles, k the rate constant and D_{eff} the effective diffusion coefficient. D_{eff} can be evaluated by

$$D_{eff} = \frac{D\varepsilon}{\tau} \qquad (8\text{-}4)$$

with D the molecular diffusion coefficient, ε the porosity and τ the tortuosity that describes the complexity of the pore system due to convolutions and branching of the pores. The effectiveness factor is the ratio of the observed reaction rate to the bulk

reaction rate, without limitations by diffusion. The effectiveness factor for a spherical catalyst particle can be calculated by

$$\eta = \frac{3}{\Phi}\left(\frac{1}{\tanh(\Phi)} - \frac{1}{\Phi}\right) \tag{8-5}$$

With typical values of ε = 0.54 and τ = 2.5, observed for similar catalysts, and L = 125 µm, defined by the maximum grain size used in the *in situ* experiments, a Thiele modulus of 0.041 and respectively a effectiveness factor close to 1 was obtained, revealing that the reaction rate, in principle, should not be limited by pore diffusion in contrast to the observed E_a, with a factor of 0.5 of the reported value, that suggest mass transport limitations. For that reason it should be tested, if mass transport phenomena did limit the intrinsic kinetic performance of the catalyst experimentally determined by varying the reactant gas flow (Mark and Meier, 1996, Chorkendorff and Niemantsverdriet, 2003) and the catalyst particle size (Chorkendorff and Niemantsverdriet, 2003).

An explanation that would describe both, the low TOFs and the activation energy, with value half of the reported one could be the adsorption of CO on the active sites. Lower activities for methane reforming catalysts, when steam was replaced by CO_2, were observed by Rostrup-Nielsen and Bak Hansen (1993). This was attributed to a higher CO concentration when CO_2 was fed instead of steam and it was assumed that CO covered the surface of the active metal. [b]Jakobsen *et al.* (2010) studied methane reforming with steam over a Ru/ZrO_2 and modelled the activity. The activity was well described with a model using methane dissociation as the rate limiting step and assuming partial coverage of the active sites by adsorbed CO both H. Jones *et al.* (2008) and [a,b]Wei and Iglesia reported methane reforming to be *structure sensitive*, the TOF being therefore predominately determined by step edge and corner atoms. An activation energy for methane dissociation, on Ru(001) single crystal surface, of 51 kJ mol^{-1} ± 6 kJ mol^{-1} was reported by Egeberg *et al.* (2002) and this is comparable to the activation energy of 54.6 kJ mol^{-1} obtained in this study. If nearly all active sites are blocked by adsorbed CO, the activation energy for the CH_4 dissociation, reported as the rate limited step for methane reforming, should be comparable for the single crystal surface and the catalyst nanoparticle. And due to the fact that the reaction is *structure sensitive*, lower TOFs will be observed if corner and step atoms are blocked. This explanation, while giving a good interpretation of our results is not supported by any experimental evidence and thus requires more experiments to support it.

Determination of the temperature inside the catalyst bed

The relative temperature increase in the catalyst bed (ΔT), during the dry reforming experiments, was determined form the thermal lattice expansion of $MgAl_2O_4$, the catalyst support. The temperature evolution was evaluated using the linear thermal expansion coefficient for synthetic spinel reported by Singh (1975). The lattice parameter, refined from the WAXS at 723 K, was used as a reference to calculate the fractional lengths change and thereby the change in temperature in the catalyst bed. A plot of the temperature increase in the heater vs. the evaluated temperature increase in the catalyst bed during a heating cycle, from 723 - 1023 K, is shown in figure 33.

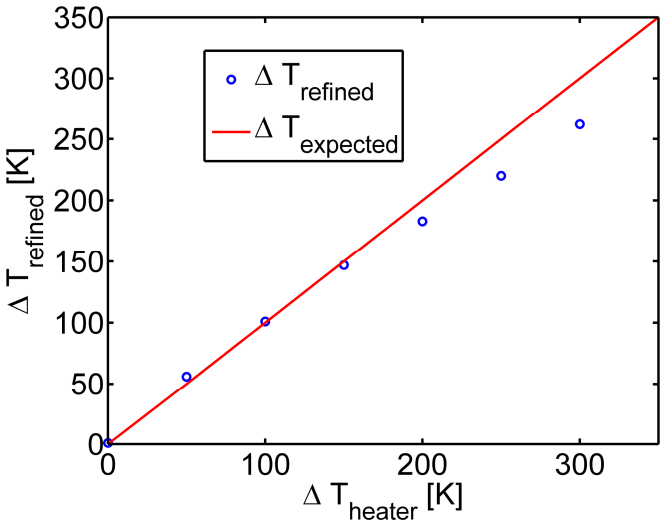

Figure 33: Temperature increase of the heater versus temperature increase inside the catalyst bed, refined from the lattice expansion of $MgAl_2O_4$.

The temperature inside the catalyst bed follows the heater temperature, though with some acceptable deviations. After the first heating step of ΔT= 50 K, the temperature inside the catalyst bed exceeds the heater temperature. A divergence of the heater temperature and the temperature inside the capillary occurs after heating of ΔT = 200 K, corresponding to heater temperatures above 873 K. These deviations might be explained by the heat consumption by the reforming reaction, but we have experimental evidences which indicate that they most probably originate from the bending of the quartz capillary, used in this experiment (see chapter 5.4 and 5.5). Overall, the temperature increases about 262 K during the heating cycle, from 723 K to 1023 K, and this is 13 % less than expected. However, in other experiments the refined temperature inside the catalyst bed was observed to exceed the temperature of the heater of around 40 K. The best agreement between the heater and capillary temperatures, in an interval between 723 and 1023 K, were obtained from experiments with sapphire capillaries, their high mechanical strength limited the bending problem. In this case, an increase of 280 K and 302 K, for a heater ΔT of 300K, were evaluated.

Nevertheless, even if a slight bending of the quartz capillaries might reduce the accuracy of the temperature refined from the fractional lengths changes of the $MgAl_2O_4$ lattice parameter, good estimations of the temperature evolutions are obtained, with sufficient accuracy to identify the influence of the reactant gas flow changes during strongly exo- or endothermic reactions.

8.3 Conclusion and outlook

Simultaneous SAXS/WAXS measurements, in combination with mass spectroscopy, were utilised to follow the dynamical changes of a 4 wt% $Ru/MgAl_2O_4$ catalyst during reduction in pure hydrogen and subsequently in-situ dry methane reforming. A marginal increase of the mean Ru particle diameter, from around 3.3 nm to 3.4 nm, was observed during the first heating cycle of the *in situ* dry reforming experiments. The Ru particle diameter remained afterwards constant revealing a high sintering stability of the catalyst. Equivalent temperature dependent methane conversion levels during heating and cooling of the sample and a consistent methane conversion level of 92 %, during the subsequent 20 hours experiment at 1023 K, displays the good performance and the absence of any deactivation that could occur because of carbon deposition for example. HRTEM of the fresh catalyst sample indicates the coexistence of pure Ru and RuO_2 nanoparticles.

The observed TOFs, for the dry reforming reaction, were in the order of 12 - 35 % of the ones reported in the literature and the obtained E_a was half of the reported one. The low TOFs and small E_a might be explained by a blocking of the active sites by adsorbed CO. But further experiments are required to prove this assumption.

The deactivation/reactivation phenomenon was not observed, most probably because the methane conversion was closer to the thermodynamic equilibrium in these experiments than in the ones from Jakobsen (2010). The results from Jakobsen showed a strong dependency of the deactivation/reactivation with the catalyst mass and grain size. Further experiments, to identify if this phenomenon is correlated with changes in the nanoparticle morphology, crystallite size or crystalline structure are required. These experiments should be performed with smaller amounts of catalyst, smaller catalyst grain sizes and higher mass flows.

Overall, the experiments revealed the applicability of the instrumental setup to test catalysts under conditions comparable to large scale processes. It permits simultaneous *in situ* determinations of changes in the crystalline structure, particle morphology and

reactivity of nano-scale catalysts and resolve their correlations with the sample temperature and reactant gas composition.

9 GISAXS of TiO_2 nanotube array micro reactor lid

9.1 Motivation

Another possibility for *in situ* catalyst testing is the use of a micro reactor etched in a Si chip. The main advantage is the very compact design that can therefore easily be accommodated in nearly every experimental SAXS, WAXS or combined SAXS/WAXS setup to study dynamics of supported metal catalysts *in situ*. Another advantage is that the etching of the Si-chip allows almost every desired reactor design. The reactor lid of such micro reactors consists of Pyrex, a borosilicate glass that is connected to the Si-wafer containing the reactor itself. Instead of loading the microreactor with the desired catalyst material to be tested, it was considered to use a reactor lid with a highly ordered TiO_2 nanotube array[3] grown on top of the lid. Such highly ordered nanotube arrays were already successfully applied in photocatalysis (Vestborg *et al.*, 2010) for degradation of pollutants (Liang and Li, 2009, In *et al.*) and synthesis of hydrocarbon fuels from CO_2 and H_2O (Varghese *et al.*, 2009) as well as for sensor and photovoltaic applications (Mor *et al.*, 2006). In this study it was considered to use the TiO_2 nanotube array as a support for Ru nanoparticles to perform *in situ* dry methane reforming. A photograph and a schematic of a microreactor is shown in figure 34.

The highly ordered TiO_2 nanotube array is synthesised by electrochemical anodization of titanium deposited on the reactor lid in a fluorine containing electrolyte (Mor *et al.*, 2006). During the synthesis, the resulting tube diameter can be controlled by the applied voltage while the length and the wall thickness are controlled by the bath temperature. Thus, the pore diameter and the surface to volume ratio can be adjusted. Furthermore, it is easier to separate the small angle scattering of the well ordered structure of the support from those of the polydisperse catalyst particles. This section describes an *ex situ* grazing incidence small angle scattering (GISAXS) and scanning electron microscopy (SEM) on a TiO_2 nanotube array. It is also explained why *in situ* experiments with the actual reactor design were not possible.

[3] The microreactors and the examined reactor lid were designed and manufactured in the group of Prof. Ib Chorkendorff, CINF, DTU.

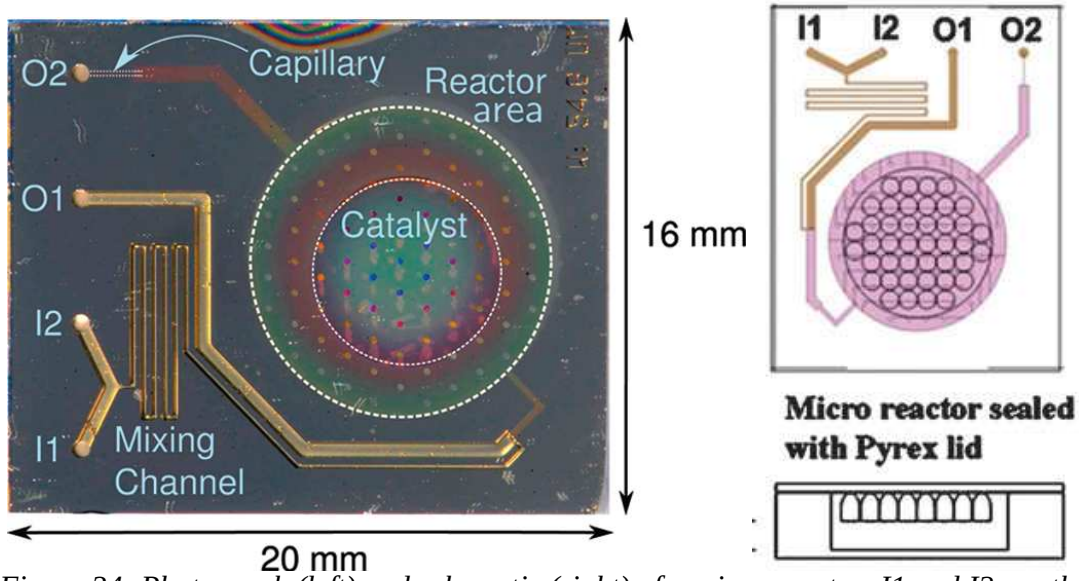

Figure 34: Photograph (left) and schematic (right) of a micro reactor. I1 and I2 are the gas inlets, O1 is the outlet over the bypass and O2 the outlet of the reactor. The transparent TiO_2 nanotube array is on the inside of the Pyrex reactor lid [photograph (left) from Vesborg et al. (2010) and schematic (right) from In et al.]

9.2 Results and discussion

Grazing incidence small angle scattering (GISAXS) was performed on the reactor lid in long geometry at an incident angle of 0.3º using Cu K-alpha radiation. The 1D projection of the scattered intensity along the surface parallel is shown in figure 35.

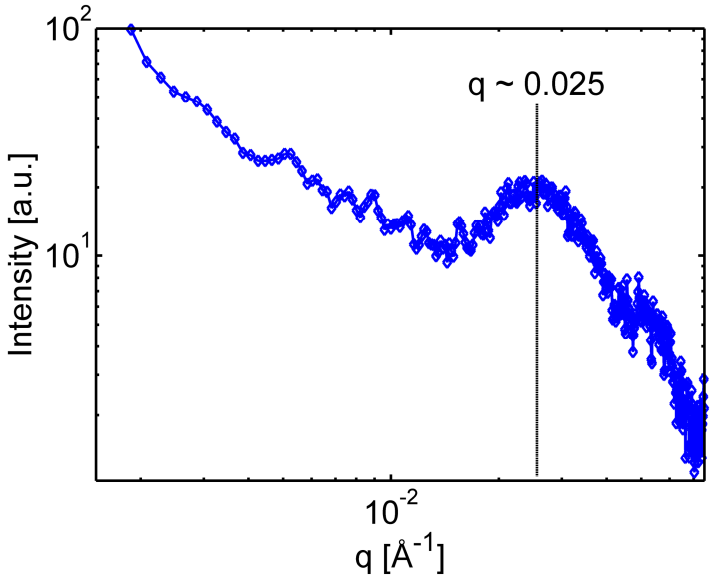

Figure 35: GISAXS from reactor lid with a TiO_2 nanotube array.

The GISAXS data at low q shows characteristic power law scattering with a slope of q^{-1} reflecting the cylindrical geometry of the nanotubes. The peak at $q \sim 0.025$ Å^{-1} indicates a structure with characteristic lengths of around 25 nm. Scanning electron microscopy (SEM) was performed on the reactor lid to get an estimate of the dimensions of the nanotubes, see figure 36 (top). The mean nanotube diameter was determined from a measurement over 120 nanotubes, the size distribution of the outer tube diameter is displayed in figure 36 (bottom). The mean nanotube diameter of 28.6 nm ± 4.6 nm determined from SEM agrees well with the measured dimension of around 25 nm determined from GISAXS.

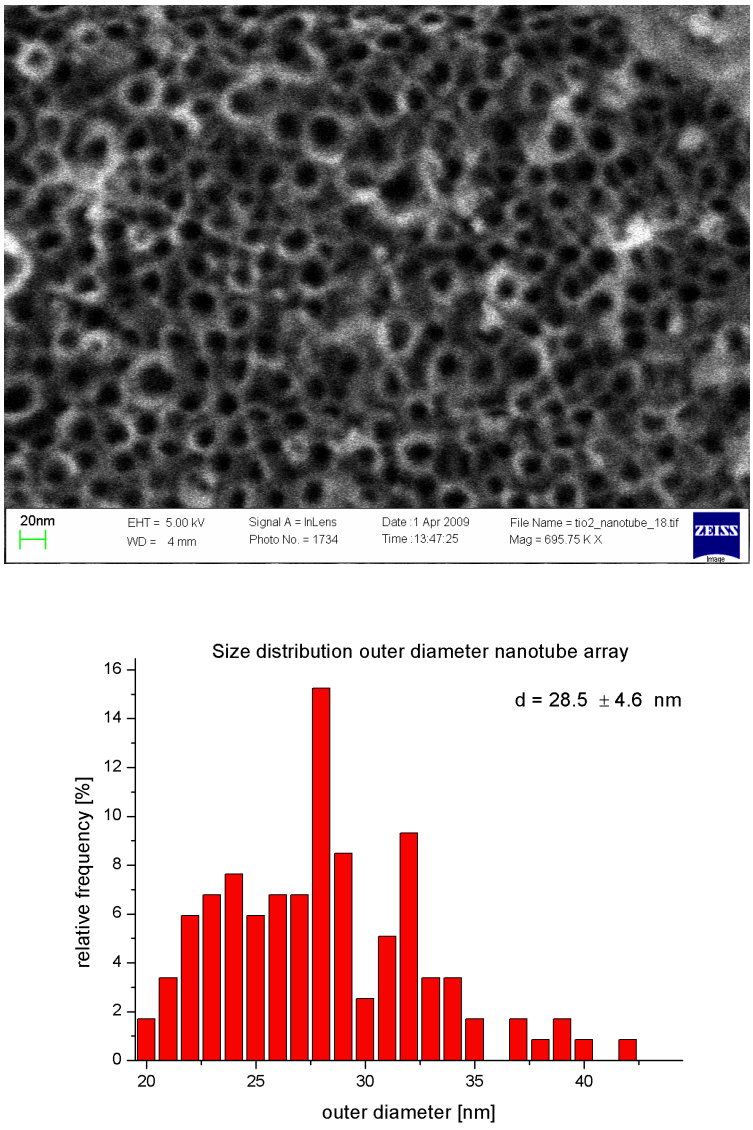

Figure 36: SEM TiO_2 nanorod array (top) distribution of the outer diameters (bottom).

The reactor was made from Pyrex, a borosilicate glass with a Na_2O content of around 4.1 wt%. Typically Pyrex is welded on the silicon wafer by anodic bonding at

temperatures from 573 - 773 K by applying a negative potential of -700 to -1000 V to the Pyrex glass, the Si wafer being grounded. Na^+-ions begin to migrate towards the cathode and leaving unsaturated O-bonds on SiO_2 from Pyrex. Unsaturated O atoms bond chemically to the Si-wafer by forming SiO bonds.

In the present design, the reactor lid has a thickness of 100 µm. This would result in X-ray path lengths through the lid of around 23 mm when the reactor is installed with an incident angle of 0.5° with respect to the direct beam. This long path length leads to nearly complete absorption of all X-ray photons. However, if one can reduce the thickness of the reactor lid to 10 µm, the transmission for Mo K-alpha radiation will be sufficient to perform experiments with incident angles of 0.5° and 1.0°. Table 4 shows the X-ray transmission through a 10 µm reactor lid for Cu and Mo K-alpha radiation and incident angle of 0.5° and 1.0°.

Incident angle (path lengths)	**Radiation**	**Transmission**
0.5° (2.3 mm)	Cu K-alpha	$0.31 \cdot 10^{-7}$
	Mo K-alpha	0.17
1.0° (1.2 mm)	Cu K-alpha	$0.17 \cdot 10^{-3}$
	Mo K-alpha	0.41

Table 4: X-ray transmission through a 10 µm reactor lid in dependency of the incident angle and wavelengths.

Unfortunately it was not possible to find any supplier for a Pyrex glass sheet below 30 µm in thickness, even not as a special request. Mica, a phyllosilicate with the chemical formula $KAl_2(AlSi_3O_{10})(OH)_2$ and a potassium content of 9.8 wt%, was thought of as an alternative since it is available with a thickness of 10 µm and potassium as an alkali ion that might migrate in the electric field and weld the sheet to the Si-wafer. However, it was not possible to connect the mica glass to the Si-wafer.

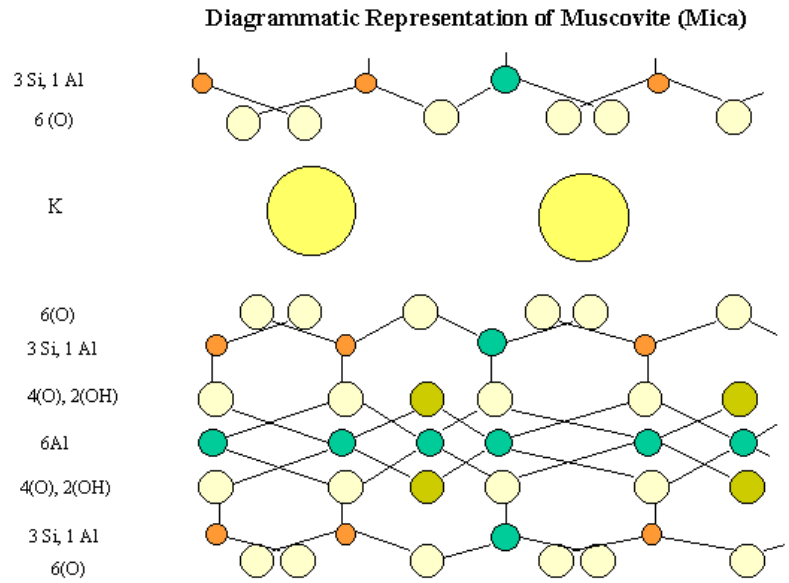

Figure 37: Structure of Mica [from Casey (2007)]

This might be explained by the different structure of mica and borosilicate glass. Mica has a well ordered structure consisting of aluminosilicate layers connected with K^+ ions (see figure 37), borosilicate glass has an amorphous structure with Na^+ ions as network modifiers between the SiO_4 tetrahedral. Na^+ migration in borosilicate is therefore possible along the three dimensions, whereas the structure of Mica only allows two-dimensional migration of K^+ between the aluminosilicate layers.

9.3 Conclusion

GISAXS was performed on a TiO_2 nanotube array used as a lid for a microreactor to perform photocatalysis. The nanotube diameter of around 25 nm evaluated from GISAXS agrees well with the one of 28.5 nm measured by SEM. However, *in situ* experiments could not be performed with the present microreactor design because of the strong X-ray absorption due to the long path lengths through a reactor lid of 100 µm. It was revealed that a reactor lid of 10 µm should have sufficient X-ray transmission to perform *in situ* GISAXS experiments. Since borosilicate glass is not available with this thickness, mica was considered as an alternative, but it was not possible to weld it with the Si-wafer.

10 Quasi elastic neutron scattering experiments on $Ca(BH_4)_2$

Another possibility to study structures and dynamics inside condensed materials and hydrogen containing materials is thermal neutron scattering, because the wavelengths of thermal neutrons is in the order of inter-atomic distances in solids and their energies close to the atomic excitations. Thermal neutron are particularly suited to study the dynamics of proton, because of its large incoherent scattering cross-section compared to that of other elements (H ~ 81 barns and versus ~ 4–5 barns). The accessible time windows are about 100 fs to 1 ns and the upper limit can be extended to several 10 nanoseconds by spin-echo techniques. Inelastic neutron scattering and quasi-elastic neutron scattering (QENS) experiments are used either to study the localized and periodic motions like vibrations or rotations or to study thermally activated single-particle motions like diffusion, all showing up in Doppler-broadened elastic lines.

During this thesis, QENS measurements were performed as a side project, to investigate the dynamics of hydrogen in $Ca(BH_4)$, the results are shown in the enclosed paper IV. These studies were performed with two different instruments: MARS, located at PSI - Switzerland and SPERES located at FRMII - Munich - Germany, the instrumental characteristics are listed in table 5. In the future, QENS experiments might also be performed to investigate dynamics in heterogeneous catalysts, to determine the diffusivity of hydrocarbons in the pores of catalysts pellets as shown by Conan Dewitt *et al.* (2005) for mesoporous silica and by Jobic *et al.* (2006) for a zeolite.

	MARS	SPHERES
Resolution – energy range	15 μeV -10 meV	0.65 μeV - 30μeV
Range of observable time scale	300 ps - 3 ps	9000 ps – 90 ps
Final wavelength	6.65 Å	6.27 Å
Incident energy	2 meV	2 meV
Detectors angles	$2\theta = 36 .. 143^{o}$	$2\theta = 9.5 .. 134^{o}$
Scattering wavenumber	$Q = 0.46 .. 1.66$ Å^{-1}	$q = 0.59 .. 1.84$ Å^{-1}

Table 5: Instrumental characteristics of MARS and SPHERES

Theory of quasi elastic neutron scattering

Neutrons are uncharged particles. Scattering of neutrons occurs, in contrast to electromagnetic radiation, in the nuclei. The charge neutrality allows deep penetration

of the neutrons in matter. Due to their spin, neutrons can be used to study magnetic materials. A Neutron can be described either as classical particles with a momentum $\vec{p} = m\vec{v}$, m being its mass and $\vec{v}$ its velocity, or according to the de Broglie relation as a plane wave, with a wave vector $\vec{k} = \vec{p}/\hbar$ and a wavelength $\lambda = 2\pi / \vec{k} = h / \vec{p}$, where h is the Planck constant. The kinetic energy of the neutron can be written as:

$$E_{kin} = \frac{1}{2} m\vec{v}^2 = \frac{\vec{p}^2}{2m} = \frac{\hbar^2 \vec{k}^2}{2m} \tag{10-1}$$

During the scattering event the neutron may exchange energy and momentum with the sample. The energy transfer is given by:

$$\Delta E = \hbar\omega = E_f - E_i = \frac{\hbar^2}{2m}\left(\vec{k}_f^{\,2} - \vec{k}_i^{\,2}\right) \tag{10-2}$$

where ω is the angular frequency, E_i and E_f are the energies of the incident and the scattered neutron and $\vec{k}_i$ and $\vec{k}_f$ the wavevector of the incident and scattered neutron, respectively. The momentum transfer is described by:

$$\Delta\vec{p} = \hbar\vec{q} = \vec{p}_f - \vec{p}_i = \hbar\vec{k}_f - \hbar\vec{k}_i \tag{10-3}$$

The scattering process is considered as elastic if the neutrons do not exchange energy with the probed matter, thus $\vec{k}_f = \vec{k}_i$ and $\Delta E = 0$ and it is inelastic if the neutrons exchange energy with the sample. The neutrons can either loose ($\hbar\omega < 0$) or gain energy ($\hbar\omega > 0$) during the inelastic scattering event. Quasi elastic neutron scattering occurs in form of a Doppler-broadening around zero energy transfer in the spectrum and has its origin in motions processes like vibration, rotational or translational diffusion. A schematic of a neutron scattering spectrum is shown in figure 38.

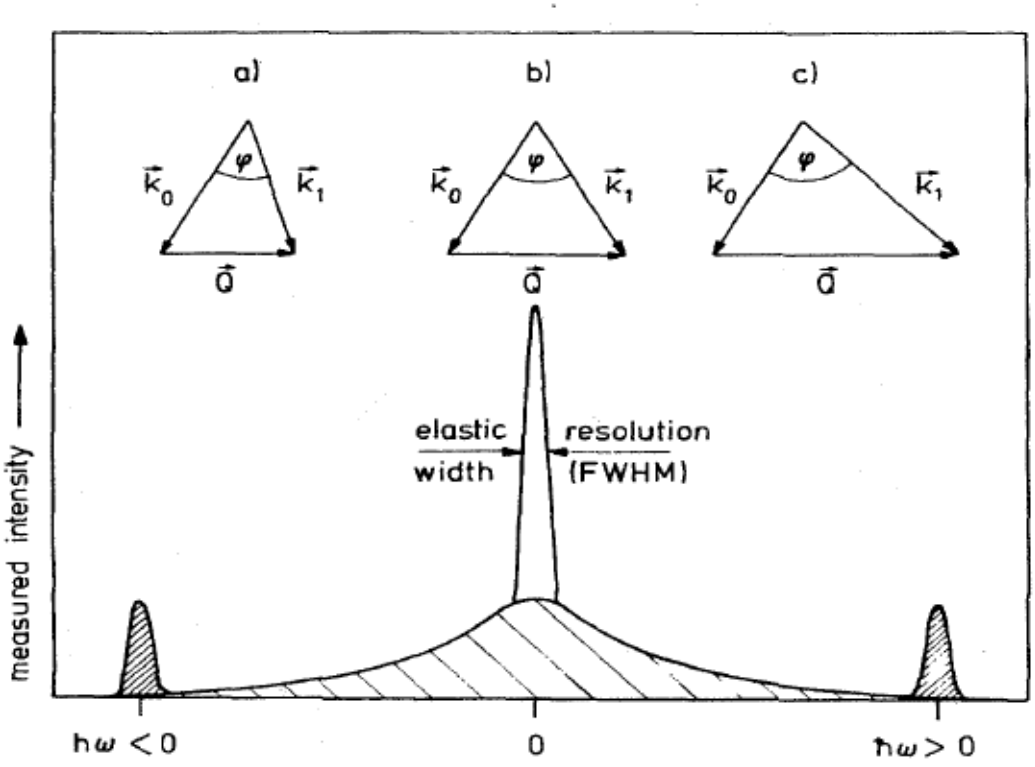

Figure 38: Schematic representation of a neutron scattering spectrum with the elastic peak and quasi elastic broadening at ħω = 0 and the inelastic peaks at ħω ≠ 0. The triangles show scattering events with neutron energy loss (a), neutron energy conservation (b) and neutron energy gain [from Jalarvo, 2005].

The measured intensity during a neutron scattering experiments is proportional to the scattering function $S(\vec{q},\omega)$, which is the sum of the coherent and incoherent contributions

$$S(\vec{q},\omega) = S_{coh}(\vec{q},\omega) + S_{inc}(\vec{q},\omega) \tag{10-4}$$

Seeing as our study focused on hydrogen dynamics, the contribution of coherent scattering will be neglected in the following. The dynamic scattering function is the space and time Fourier transform of the self-correlation function and is described by:

$$S_{inc}(\vec{q},\omega) = \frac{1}{2\pi\hbar}\int G_S(\vec{r},t)\exp(i(\vec{q}\cdot\vec{r}-\omega t))d\vec{r}dt \tag{10-5}$$

where $G_S(\vec{r},t)$ is the self correlation function which represents the probability to find the same particle at its origin at $t = 0$ and at a distance $\vec{r}$ at a time t. $S(\vec{q},\omega)_{inc}$ can also be expressed in terms of the intermediate scattering function

$$I(\vec{q},t) = \int G_S(\vec{r},t)\exp(i\vec{q}\cdot\vec{r})dr \tag{10-6}$$

which is the space Fourier transform of the self-correlation function. The experimental observed total incoherent scattering function can be described by:

$$S_{inc}^{tot}(q,\omega) = R(q,\omega) \otimes (A_0(q)\delta(\omega) + \sum_i A_i(q)L(\Gamma_i,\omega)) + B(q) \tag{10-7}$$

where $R(q,\omega)$ is the instrumental resolution function, δ the Dirac delta function describing the elastic scattering and $L(\Gamma_i,\omega)$ a Lorentzian profile function describing the quasi elastic scattering. Γ_i, the half width of the Lorentzian is related to the reciprocal of the time scale of the motion. B is the incoherent background in the quasielastic region. The term $A_0(q)$ is the elastic incoherent structure factor (EISF). The EISF can be calculated from the ratio:

$$A_0(q) = \frac{I_{el}(q)}{I_{el}(q) + I_{inel}(q)} \tag{10-8}$$

where I_{el} and I_{inel} are the integrated intensities of the elastic and inelastic signal. It determines the static properties of accessible site to the atoms, the location of these sites and the normalized probability that the atom is at these sites.

For isotropic long-range diffusion of particles, the time and spatial dependency of the self-correlation function can be expressed by Fick's second law and the intermediate scattering function becomes:

$$I(q,t) = \exp(-q^2 Dt) \tag{10-9}$$

where D is the diffusion coefficient (Zabel, 1993). The time Fourier transform of (10-9) yields the incoherent scattering function for an isotropic diffusive particle

$$S_{inc}(q,\omega) = \frac{1}{\pi}\frac{\Gamma(q)}{\Gamma(q)^2 + \omega^2} \tag{10-10}$$

which has a Lorentzian peak shape profile with $\Gamma(q) = \hbar Dq^2$ being the half width half maximum (HWHM). Equation (10-9) is not valid for long-range diffusion of atoms in crystal lattices, like diffusion of hydrogen in complex metal hydride, since the motion

of atoms can only occur in finite steps. This is taken into account by the Chudley-Elliot model (Chudley and Elliot, 1961). $\Gamma(q)$ of the Lorentzian is than defined as:

$$\Gamma(q) = \frac{\hbar}{\tau_D}\left(1 - \frac{\sin qL}{qL}\right) \tag{10-11}$$

where L is the jump length and τ_D the time the atom stays at one site before jumping to another site. A more detailed description of quasi elastic neutron scattering can be found in the literature (Bée, 1988, Zabel, 1993).

11 Conclusion and Outlook

In the present thesis a new heater setup and gas system for an *in situ* cell, accommodated in a laboratory SAXS/WAXS camera, has been developed. A mass spectrometer was implemented to monitor the chemical reactions during the *in situ* experiments. With this instrumental setup it is possible to follow simultaneous changes of crystalline structures, particle morphologies and chemical reactions of nano-scale materials and resolve their correlations with the temperature. Combined SAXS/WAXS cameras are normally used at synchrotron facilities. Therefore experiments have to be thoroughly planned, samples have to be prepared in advance and waiting times of several weeks up to month between proposals and realisation of the measurements are unfortunately common. The advantage of our combined SAXS/WAXS setup is that it is located close to our chemical laboratories thus giving an appreciable flexibility in the planning of the experiments. Even if the photon flux of our X-ray laboratory source, a rotating anode, is of some orders of magnitude lower than at synchrotron facilities, descent scattering patterns can be collected in 30 minutes. The results presented in this study show that such a resolution in time is appropriate to follow dynamical changes of condensed nano-structured materials and catalysts. Various *in situ* experiments will be performed with this instrumental setup in the near future: formation of catalysts during calcination, follow up of the dynamical changes in hydrogen and ammonia storage materials during adsorption and desorption and follow up of the dynamics of battery related materials during the charging and discharging processes.

Performance tests of the heater confirmed its usability in a temperature range from 298 - 1073 K, a useful range to study catalyst materials under conditions comparable to large scale processes in the chemical industry. It was shown that the temperature inside the capillary follows with a good accuracy the temperature set for the heater and that further calibration is therefore not necessary. Furthermore, the specimen temperature, during *in situ* experiments, can be obtained from thermal expansion of the probed material from analysis of the WAXS data.

The applicability of the setup to study nanostructured materials has been confirmed during heating experiments of anatase TiO_2 nanorods. A clear correlation between crystallite and particle growth was observed. The advantage of combining SAXS and WAXS has been clearly emphasized, since the use of one technique alone would not have resolved the existence of core shell/particles. The temperature interval for the rod to sphere transition has been resolved. The probed TiO_2 particles remained in the

metastable, but for most applications preferable, anatase phase during the heating up to 1023 K.

In situ reduction experiments, performed with 22 %wt $Ni/MgAl_2O_4$ catalysts and *in situ* reduction and dry methane reforming experiments on 4 %wt $Ru/MgAl_2O_4$ catalysts, showed that the experimental setup is also appropriate for testing nano-structured catalysts. The temperature for the initiation of the reduction of both catalysts has been resolved within a temperature interval of 20 K. Ni particles, in a fresh catalyst sample, showed a Ni/NiO core shell structure and this has been indirectly observed by a decrease of the Ni lattice parameter during the reduction. The Ni particle diameter increased after reduction of the protective NiO shell. The dry reforming experiments over the $Ru/MgAl_2O_4$ showed no deactivation, even during long time experiments of 20 h at 1023 K. Only marginal particle sintering was observed and the absence of the deactivation can be attributed to the fact the catalyst retained its nanostructure.

The broad particle size distribution of the metal nanoparticles, in particular for Ni, did not allow the estimation of an absolute particle size from SAXS. Small angle scattering of the Ni particles, strongly overlapped with scattering from the support particles. Further SAXS experiments, to determine the absolute particle sizes and distributions, should be performed. This should be done with pore masking, to suppress scattering from the support particles and observe only the scattering from the metal particles. The obtained size distribution from such an experiment should then be used as an input value to model the SAXS data obtained during the *in situ* experiments. Another possibility that one should consider is to perform *in situ* anomalous small angle scattering (ASAXS) to separate scattering from the support and from the metal particles. For such measurements, preliminary studies with our in-situ SAXS/WAXS laboratory setup should be performed to define the most interesting experimental conditions to observe dynamical changes of the catalyst material. The deactivation/reactivation phenomenon was not observed for the Ru catalyst, most likely because to high methane conversion levels during the experiments. Future experiments on the Ru catalyst should therefore be performed to identify if the deactivation/reactivation phenomenon can be correlated with changes of the nanoparticle morphology, crystallite size or crystalline structure. These experiments should be performed with smaller catalyst grain size, shorter catalyst bed length and higher mass flows of the reactant gas.

References

Aguinaga, A., Montes, M. (1992) *Appl. Catal. A* **90** 131 - 144

Akurati, K. K., Vital, A., Fortunato, G., Hany, R., Nueesch, F., Graule, T. (2007). *Solid State Sci.* **9** 247 - 257

Als-Nielsen, J., McMorrow, D (2001) *Elements of Modern X-ray Physics*, Chichester: Jon Wiley & Sons, Ltd

Andersen, P. D., Skårhøj, J. C., Andreasen, J. W., Krebs, F. C. (2009). *Optical Materials* **31**, 1007 - 1012

Andreasen, J. W., Rasmussen, O., Feidenhans'l, R., Rasmussen, F. B., Christensen, R. Molenbroek, A. M., Goerigk, G. (2003). *J. Appl. Cryst.* **36**, 812-813

Bakardjieva, S., Šubrt J., Štengl, V, Dianez, M. J., Sayagues, M. J. (2005) *Appl. Cat. B* **58** 193 - 202

Ballauff, M. (2001) *Curr. Opin. Colloid Interface Sci.* **6**, 132-139

Bao, S.-H., Bao, Q.-L., Li, C.-M., Dong, Z.-L. (2007). *Electrochem. Commun.* **9**, 1233 - 1238

Beaucage, G., Kammler, H. K., Pratsinis, S. E. (2004) *J. Appl. Chryst.* **37** 523 - 535

Beaucage, G., Schaefer, D. W. (1994) *J. Non – Cryst. Solids* **172**, 795 – 805

Bée (1988) *Quasielastic Neutron Scattering* Philadelphia: Adam Hilger

Behr, A. (2010) *Catalysis, Homogeneous, Ullmann's Encyclopedia of Industrial Chemistr, Online edition.*

Benkstein, K. D., Semancik, S. (2006). *Sensors and Actuators B* **113**, 445 – 453

Bergeret, G., Gallezot, P. (2008) *Particle Size and Dispersion Measurements - Handbook of Heterogeneous Catalysis* 738 - 765

Berman, A., Karn, R. K., Epstein, M. (2007) *Green Chem.* **9** 626 - 631

Bitter, J. H., Seshan, K. Lercher, J. A. (1997) *J. Catal.* **171** 279 - 286

Bond, G. C., (1991) *Chem. Soc. Rev.* **20** 441 - 475

Borowieki, T. (1982) *Appl. Catal.* **4** 223 - 231

Bossi, A., Cattalani, A., Gabrassi, F., Petrini, G., Zanderighi, L. (1983) *J. Therm. Anal.* **26** 81 - 86

[a]Bradford, M. C. J., Vannice, M. A. (1999) *J. Catal.* **183** 69 - 75

[b]Bradford, M. C. J., Vannice, M.A. (1999) *Catal. Rev. Sci. Eng.* **41** 1 - 42

Brummberger, H., Goodisman, J.,Ramaya, R., Ciccariello S. (1996) *J. Appl. Cryst.* **29** 526 - 530

Carrara, C. Múnera, J., Lombardo, E. A., Cornaglia, L. M. (2008) *Top. Catal.* **51** 98 - 106

Casey, K. (2007) *Mineral of the month December 2007 - Delaware Muscovite Mica*, http://www.delminsociety.net/motm/motm_dec2007.shtml

Chen, D., Christensen, K. O., Ochoa-Fernández, E., Yu, Z., Tøtdal, B., Latorre, N., Monzón, A., Holmen, A. (2005) *J. Catal.* 82 - 96

Chen, Y., Kang, K. S., Yoo, K. H., Jyoti, N., Kim, J. (2009). *J. Phys. Chem. C.* **113**, 19753 - 19755

Chorkendorff, I., Niemantsverdriet (2003) *Concepts of Modern Catalysis and Kinetics*. Weinheim: Wiley-VCH

Chudley, C. T., Elliot, R. J. (1961) *Proc. Phys. Soc.* **77** 353 - 361

Conan Dewitt, A., Herwig, K. W., Lombardo, S. J. (2005) *Adsorption* **11** 491 - 499

Cozzoli, P.D., Kornowski, A., Weller, H. (2003). *J. Am. Chem. Soc.* **125**, 14539 - 14548

Crisafulli, C., Scirè S., Maggiore, S., Minicò, S., Galvagno, S. (1999) *Catal. Lett* . **59** 21 - 26

Dapiaggi, M., Artiolo, G., Petras, L. (2002) *The Rigaku Journal* **19** 35 - 41

Dingerdissen, U., Martin, A., Herein, D. and Wernicke, H. J. (2008) *The Development of Industrial Heterogeneous Catalysis - Handbook of Heterogeneous Catalysis* 37–56.

Duan, Y., Li, J. (2004) *Mater. Chem. Phys.* 87 452 - 454

Dumesic, J. A., Huber, G. W. and Boudart, M. (2008) *Principles of Heterogeneous Catalysis - Handbook of Heterogeneous Catalysis* 1 - 15

Egeberg, R. C., Ullmann, S., Alstrup, I., Mullins, C. B., Chorkendorff, I. (2002) *Surf. Sci.***497** 183 - 193

Feigin, L. A., Svergun, D. I. (1987) *Structure Analysis by Small-Angle X-ray and Neutron Scattering*, New York: Plenum Press

Ferreira-Aparicio, P., Guerrero-Ruiz, A., Rodríguez-Ramos, I. (1998) *Appl. Catal. A* **170** 177 - 187

Ferreira-Aparicio, P., Rodríguez-Ramos, I., Anderson, J. A., Guerrero-Ruiz, A. (2000) *Appl. Catal. A* **202** 183 - 196

Fique, G., Richert, P., Montagnac, G. (1999) *Phys. Chem. Minerals* **27** 103 - 111

Fox, M. A., Dulay, M. T. (1993). *Chem. Rev.* **93** 341 - 357

Gabriel, F., Dauvergne F. & Rosenbaum, G. (1978). *Nucl. Instrum. Methods* **152** 191–194

Gadalla, A. M., Bower, B. (1988) *Chem. Eng. Sci*. **1988** 3049 - 3062

Gallei, E. F., Hesse, M. and Schwab, E. (2008) *Development of Industrial Catalysts - Handbook of Heterogeneous Catalysis* 57–66

Gilbert, B. Zhang, H., Huang, F., Finnegan, M. P., Waychunas, G. A., Banfield, J. F. (2003). *Geochem. Trans.*, **4**, 20 – 27

Glatter O., Kratky, O. (1982) *Small Angle X-ray Scattering*, New York: Academic Press

Gokon, N., Osawa, Y., Nakazawa, D., Kodama, T. (2009) *Int. J. Hydrogen Energie* **34** 1787 - 1800

González, M. G., Ponzi, E. N., Ferretti O. A., Quincoces, C. E., Marecot, P. , Barbier, J. (2000) *Adsorpt. Sci. Technol.* **18** 541 - 550

[a]Grunwaldt, J.-D., Kiener, C. Wörgerbauer, C., Baiker, A. (1999) *J. Catal.* **181** 223 - 232

[b]Grunwaldt, J.-D., Maciejewski, M., Becker, O. S, Fabrizioli, P., Baiker, A. (1999) *J. Catal* **186** 458 – 469

Guo, J., Lou, H., Zhao, H., Chai, D., Zheng, X (2004) *Appl. Catal. A* **273** 75 - 82

Harutaa, M., Kobayashi, T., Sano. H., Nobumasa, Y. (1987) *Chem. Lett.* 405 - 408

Harutaa, M., Yamadab, N., Kobayashia, T., Iijimac S. (1989) *J. Catal.* **115** 301 - 309

Helveg, S., López-Cartes, C., Sehested, J., Hansen, P. L., Clausen, B. S., Rostrup-Nielsen, J. R., Abild-Pedersen, F., Nørskov, J. K. (2004) *Nature* **427** 426 - 429

Helveg, S., Hinnemann, B., Rostrup-Nielsen, J. R., Chorkendorff, I., Sehested, J., Nørskov, J. K. (2008) *J. Catal.* **259** 147 - 160

Holm-Larsen, H. (2001) *Stud. Surf. Sci. Catal.* **136** 441 - 446

Hume-Rothary, W., Reynolds, P. (1938) *Proc. R. Soc. Lond. A.* **167** 25 - 34

Hunter B. (1998). Int. Union Cryst. Newsletter **20**, 21

Ikuma, Y, Shigemura, T., Hirose, T. (1996). *J. Am. Ceram. Soc.* **79**, 2533 – 2538

In, S.-I., Nielsen, M. G., Vesborg, P. C. K, Hou, Y., Abrams, B. L., Henriksen, T. R., Hansen, O., Chorkendorff, I. (2010) *Chem. Comm.* DOI: 10.1039/c0cc02570d (in press)

Jacobsen, H. S. (2009) *Hydrogen storage materials - investigated by in situ small and wide angle X-ray scattering,* Master thesis, Copenhagen University

[a]Jakobsen, J. G. (2010) *Noble metal catalysts for methane steam reforming,* Ph.D. thesis, DTU

[b]Jakobsen, J. G., Jørgensen, T. L., Chorkendorff, I., Sehested, J. (2010) *Appl. Catal., A* **377** 158 - 166

Jalarvo, N. (2005) *Quasi elastic neutron scattering on the dynamical properties of an aromatic hydrogen bond,* Ph.D. thesis, TU-Berlin

Jensen, H., Pedersen, J. H., Jørgensen, J. E., Pedersen, J. S., Joensen, K. D., Iversen, S. B., Søgaard, E. G. (2006) *Experimental Nanoscience* **1** 355-373

Jeong, J. H., Lee, J. W., Seo, D. J., Soe, Y., Yoon, W. L., Lee, D. K., Kim, D. H. (2006) *Appl. Catal., A* **302** 151 - 156

Jiu, J., Isoda, S., Wang, F., Adachi, M. (2006). *J. Phys. Chem. B* **110**, 2087 - 2092

Jobic, H., Laloué, N., Laroche, C., van Baten, J. M., Krishna, R. (2006) *J. Phys. Chem. B* **110** 2195 - 2201

Jones, G., Jakobsen, J. G., Shim, S. S., Kleis, J., Andersson, M. P., Rossmeisl, J., Abild-Pedersen, F., Bligaard, T., Helveg, S., Hinnemann, B., Rostrup-Nielsen, J. R., Chorkendorff, I., Sehested, J., Nørskov, J. K. (2008) *J. Catal.* **259** 147 - 160

Karim, A. M, Prasad, V., Mpourmpakis, G. Lonergan, W. W., Frenkel, A. I., Chen, J. G., Vlachos, D. G. (2009) *J. Am. Chem. Soc.* **131** 12230 - 12239

Kehres, J., Andreasen, J. W., Krebs, F. C., Molenbroek, A. M., Chorkendorff, I., Vegge, T. (2010) *J. Appl. Cryst.* **43** 1400 - 1408

Khan, S. U. M., Al-Shary, M., Ingler Jr, W. B. (2002). *Science* **297** 2243 - 2245

Kim, J., Cho, J. (2007). *J. Electrochem. Soc.* **154**, A542 – A546

Kohlbrecher, J. (2010) *SASfit: A program for fitting simple structural models to small angle scattering data,* Villigen: PSI

Kuru, Y., Wohlschlögel, M., Welzel, U., Mittemeijera, E. J. (2008) **41** 428 - 435

Langford, J. I., Wilson, A. J. C. (1978) *J. Appl. Cryst.* 11 102 - 113

Li, G., Li, L., Boerio-Goates, J., Woodfield, B. F. (2005). *J. Am. Chem. Soc.* **127,** 8659 - 8666

Liang, H.-C. Li, X.-Z. (2009) *J. Hazard. Mater.* **162** 1415 - 1422

Liao, D. L., Liao, B.Q. (2006) *J. Photochem. Photobiol. A: Chem.* **187**, 363 - 369

Linde D. R. (2010) *CRC Handbook of Chemistry and Physics - Internet Version 2011*. 12-205 - 12-206

Lira-Cantu, M., Norrman, K., Andreasen, J. W., Casan-Pastor, N., Krebs, F. C. (2007) *J. Electrochem. Soc.* **154**, B508 - B513

Lööf, P. Stenbom, B., Nordén, H., Kasemo, B. (1993) *J. Catal.* **144** 60 - 76

Madhavaram, H. Idriss, H., Wendt, S., Kim, Y. D., Knapp, M., Over, H., Aßmann, J., Löffler, E., Muhler, M. (2001) *J. Catal.* **202** 296 - 307

Manera M. G., Cozzoli, P. D., Curri, M. L, Leo, G., Rella, R., Agostiano, A. Vasanelli, F. (2005). *Synthetic Metals* **148**, 25 – 29

Mark, M. F., Maier, W. F. (1996) *J. Catal.* **164** 122 - 130

Marsh, A. L., Ribeiro, F. H. and Somorjai, G. A. (2008) *Single Crystal Surfaces - Handbook of Heterogeneous Catalysis* 1259–1276.

McCusker, L. B., von Dreele, R. B., Cox, D. E., Louër, D., Scardi, P. (1999) *J. Appl. Cryst.* **32** 36 -

Molenbroek, A. M., Helveg, S., Topsøe, H., Clausen, B. S. (2009) *Top. Catal.* **52** 1303 - 1311

Mor, G. K., Varghese, O. K., Paulose, M., Shankar, K., Grimes, C. A. (2006) *Sol. Energy Mater. Sol. Cells* **90** 2011 - 2075

Nagaveni K, Hegde M. S., Ravishanker, G. N., Subbanna, G. N., Madras, G. (2004). *Langmuir* **20**, 2900 - 2907

Ohtani, B., Prieto-Mahaney, O. O., Abe, R. (2010) *J. Photochem. Photobiol. A* doi:10.1016/j.jphotochem.2010.07.024 (in press)

Okada, Y., Tokumaru, Y. (1984) *J. Appl. Phys.* **56** 314 - 320

Okaji, M. (1988) *Int. J. Thermophys.* **9** 1101 - 1109

Pannetier, J. (1993) *Powder diffraction Techniques - Neutron and Synchroton Radiation for Condensed Matter Sudies, Theory, Instruments and Methods*. Springer-Verlag: Berlin, Heidelberg, New York

Pathak, P. D., Vasavada, N. G. (1970) *J. Phys. C.* **3** L44

Pedersen J. S. (1997) *Adv. Colloid Interface Sci.* **70** *171-210*

Penn, R. L., Banfield, J. F. (1999) *Geochim. Cosmochim. Acta* **63** 1549 - 1557

Phung, X., Groza, J., Stach, E. A., Williams, L. N., Ritchey S. B. (2003) *Mater.Sci.Eng.A* **359** 261 - 268

Porter J. F., Li, Y.-G., Chan, C. K. (1999) *J. Matter. Sci.* **34** 1523 - 1531

Prudenziati, M.,Morten, B.,Travan E. (2003) *Mater. Sci. Eng., B* **98** 167 - 176

Qin, D., Lapszewicz, J. (1994) *Catal. Today* **21** 551 - 560

Rasmussen, B. F. (2001) *Colloids Surf. A* **187-188** 327 - 335

Rasmussen, F. B., Sehested, J., Teunissen, H. T., Molenbroek, A. M., Clausen, B. S. (2004) *Appl. Catal. A* **267** 165 - 173

Rellinghaus, B., Stappert, S., Wassermann, E. F., Sauer, H., Spliethoff, B. (2001) *Eur. Phys. J. D.* **16** 249 - 252

Rezaei, M., Alavi, S. M., Sahebdelfar, S., Yan, Z.-F. (2006) *J. Nat. Gas. Chem.* **15** 327 - 334

Richardson, J. T., Crump, J. G. (1979) *J. Catal.* **57** 417 - 425

Riello, P., Benedetti, A. (1997). *J. Chem. Phys.* **106**, 8660-8663.

Rietveld, H. M. (1969) *J. Appl. Cryst.* **2** 65

Rostrup-Nielsen, J. R., Bak Hansen, J.-H. (1993) *J. Catal.* **144** 38-49

Rothenberg, G. (2008) *Catalysis: Concepts and green applications.* Weinheim: Wiley-VCH

Safariamin, M., Tidahy, L. H., Abi-Aad, E., Siffert, S., Aboukaïs, A. (2009) C. R. Chimie **12** 748 - 753

Sakiyama, K., Koga, K., Seto, T., Hirsawa, M., Orii, T. (2004) *J. Phys. Chem. B* **108** 523 - 529

Sanker, G., Bras, W. (2009) *Catal. Today* **145** 195 - 203

Schmidt, P. W. (1992) *J. Appl. Chryst*. 24, 414-435

Sehested, J. (2006) *Catal. Today* **111** 103 - 110

Sehested, J., Carlsson, A., Janssens, T. V. W., Hansen, P. L. Datye, A. K. (2001) *J. Catal.* **197** 200 - 209

Seto, T, Akinaga, H., Takano, F., Koga, K. Orii, T., Hirasawa, M. (2005) *Phys. Chem. B.***109** 13403 – 13405

Setthi, S. R., Thölén, A. R. (1994) *Nanostruc. Mater*. **4** 903 - 913

Shamasi, A., Johnson, C. D. (2003) *Catal. Today* **84** 17 - 25

Shimizu, K.-I., Murayama, H., Nagai, A., Shimada, A., Hatamachi, T. Kodama, T., Kitayama, Y. (2005). *Appl. Calal. B* **55**, 141 - 148

Shirasu, Y., Minatu, K. (2002) *J. Alloys Compd.* **335** 224-227

Simmons, R. O., Baluffi, R. W. (1960) *Phys. Rev.* **119** 600 - 605

Singh, H. P., Simmons, G. McFarlin, P. F. (1975) *Acta Cryst.* **A 31** 820

Suzuki, T., Iwanami, H., Yoshinari, T. (2000) *Int. J. Hydrogen Energy* **25** 119 - 126

Taylor, H. S. (1925) *Proc. R. Soc. Lond. A* **108**, 105-111

Therdthianwonga, S., Siangchina, c., Therdthianwongb A. (2008) *Fuel Process. Technol*. **89** 160 - 168

Toby, B. H. (2006) *Powder Diff.* **21** 67 - 70

Valden, M., Pak, S., Lai, X. Goodman, D. W. (1998) *Catal. Lett.* **56** 7- 10

Varghese, O. K., Paulose, M., LaTempa, T. J., Grimes, C. A. (2009) *Nano Lett.* **9** 731 - 737

VDI Wärmeatlas (1994), Düsseldorf : VDI-Verlag

Vesborg, P. C. K In, S.-I., Olsen, J. L., Henriksen, T. R., Abrams, B. L.,Hou, Y., Kleiman-Shwarsctein, A., Hansen, O., Chorkendorff, I. (2010) *J. Phys. Chem. C* **114** 11162 - 11168

Waldschlögel, M., Welzel, U., Maier, G., Mittemeijer, E. J. (2005) *J. Appl. Cryst.* **39** 194 - 201

Wang, Y.-H., Xu, B.-Q. (2005) *Catal. Lett.* **99** 89 - 96

Wantanabe H., Yamada, N., Okaji, M. (2004) *Int. J. Themophys.* **25** 211 - 236

Wedler, G. (2004) *Lehrbuch der physikalischen Chemie - 5th eddition*. Weinheim: Wiley-VCH

[a]Wei, J. M., Iglesia, E. (2004) *J. Catal*. **224** 370 - 383

[b]Wei, J. M., Iglesia, E. (2004) *J. Phys. Chem. B.* **108** 7253 - 7262

Wörner, A., Tamme, R. (1998) *Catal. Today* **46** 165 - 174

www.spaceflight.esa.int/impress/text/education/Catalysis/index.html

Young, R. A. (1993) *The Rietveld Method*, Oxford: Oxford University Press

Zabel (1993) *Interactions of Neutrons with Matter: Neutrons- Inelastic case, Neutron and Synchroton Radiation for Condensed Matter Sudies, Theory, Instruments and Methods*. Berlin, Heidelberg, New York: Springer-Verlag

Zeng, Y. P., Jiang D. (2008) *J. Appl. Ceram. Technol.* **5**, 505 - 512

Paper I

Journal of
Applied
Crystallography
ISSN 0021-8898

Received 4 June 2010
Accepted 16 October 2010

Combined *in situ* small- and wide-angle X-ray scattering studies of TiO_2 nanoparticle annealing to 1023 K

Jan Kehres,[a] Jens Wenzel Andreasen,[b]* Frederik Christian Krebs,[b] Alfons M. Molenbroek,[c] Ib Chorkendorff[d] and Tejs Vegge[a]

[a]Materials Research Division, Risø National Laboratory for Sustainable Energy, Technical University of Denmark, Denmark, [b]Solar Energy Programme, Risø National Laboratory for Sustainable Energy, Technical University of Denmark, Denmark, [c]Haldor Topsøe A/S, Characterization Department, Research and Development Division, Denmark, and [d]Centre for Individual Nanoparticle Functionality, Department of Physics, Technical University of Denmark, Denmark. Correspondence e-mail: jewa@risoe.dtu.dk

Combined *in situ* small- and wide-angle X-ray scattering (SAXS/WAXS) studies were performed in a recently developed laboratory setup to investigate the dynamical properties of dry oleic acid-capped titanium dioxide nanorods during annealing in an inert gas stream in a temperature interval of 298–1023 K. Aggregates formed by the titanium dioxide particles exhibit a continuous growth as a function of temperature. The particle size determined with SAXS and the crystallite size refined from WAXS show a correlated growth at temperatures above 673 K, where the decomposition of the surfactant is expected. At temperatures above 823 K, the particle and crystallite sizes increase rapidly. An increasing discrepancy between particle and crystallite size indicates growth of a shell structure on the single-crystalline core of the particles. This was confirmed by high-resolution transmission electron microscopy studies of the sample. Transmission electron microscopy shows a transformation from a rod to a spherical particle shape; the WAXS data indicate that the shape change occurs in a temperature interval of 773–923 K. The highly crystalline titanium dioxide particles remain in the metastable anatase phase during the entire annealing process. The transition to the thermodynamically stable rutile phase was not observed at any temperature, in agreement with existing experimental observations.

1. Introduction

TiO_2 nanoparticles have been extensively studied because of their unique electric, photonic and catalytic properties. TiO_2 can be utilized in various applications, such as materials for sensors (Benkstein & Semancik, 2006; Manera *et al.*, 2005), electrodes in dye-sensitized solar cells (Jiu *et al.*, 2006), hybrid organic solar cells (Lira-Cantu *et al.*, 2007), optical spacer layers (Andersen *et al.*, 2009), anode materials for batteries (Kim & Cho, 2007), photocatalysts in chemical processes (Yeung *et al.*, 2003) and pollutant elimination (Nagaveni *et al.*, 2004; Zeng & Jiang, 2008). Three different polymorphs of TiO_2 occur in nature, thermodynamically stable rutile and metastable brookite and anatase, the latter showing the highest activity for photocatalytic processes (Fox & Dulay, 1993). Besides the polymorphic modification of TiO_2, the crystallinity (Shimizu *et al.*, 2005) and the nanostructure (Nagaveni *et al.*, 2004; Liao & Liao, 2006) are essential parameters for the photocatalytic activity. The distribution of crystalline polymorphs with respect to the particle nanostructure, *e.g.* with anatase as a surface layer on a rutile core, has also been shown to have a significant impact on photocatalytic activity (Zhang *et al.*, 2008).

TiO_2 nanorods synthesized by a wet chemical route are often capped with organic surfactant molecules – in this study oleic acid – to preserve the particle shape and inhibit particle growth. However, high photocatalytic activity and applications such as chemical sensor and electrode materials require a readily accessible surface and therefore the removal of the surfactants. One simple approach for a complete removal is annealing of dry particles in a gas stream above the decomposition temperature of the organic surfactant, but elevated temperatures also facilitate particle and crystallite growth and the anatase/rutile phase transition, processes that are in general regarded as detrimental even though particle sintering up to a certain degree might be favoured to maintain a stable and highly porous three-dimensional network (Benkstein & Semancik, 2006; Bao *et al.*, 2007; Zeng & Jiang, 2008).

The design of highly efficient TiO_2 photocatalyst, sensor and electrode materials requires a deep understanding of

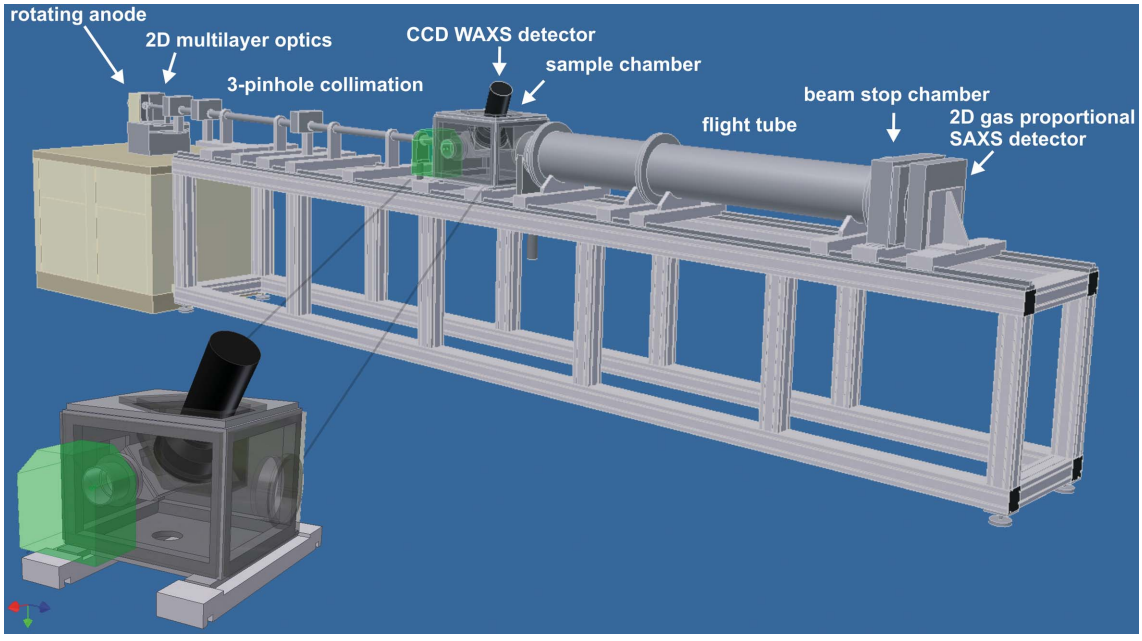

Figure 1
Schematic overview of the SAXS/WAXS *in situ* setup used in this study. The inset shows the sample chamber in detail, with the CCD camera in position for WAXS detection from the sample, mounted and enclosed in the inner *in situ* cell. The green box represents the external parts and vacuum seal of the *in situ* cell (Andreasen *et al.*, 2003). The sample mount, heater and gas supply (detailed in Fig. 2) slide from the external part into the internal chamber, in the X-ray beam.

dynamical processes like particle growth, crystallite growth and phase transitions in connection with the gas atmosphere and temperature used for surfactant decomposition. A suitable technique to follow these changes is combined *in situ* small- and wide-angle X-ray scattering (SAXS/WAXS). The presented experiments were performed on a recently developed laboratory setup for simultaneous *in situ* SAXS/WAXS using a rotating-anode X-ray source.

In this paper, we describe an experiment involving the heating of oleic acid-capped TiO_2 nanorods in inert atmosphere and resolve the correlations between particle and crystallite growth and their dependence on temperature.

2. Experiments and methods

2.1. Experimental setup

Simultaneous *in situ* SAXS/WAXS was performed in a laboratory pinhole camera setup (Fig. 1) with sample-to-SAXS-detector distances of 1494–4679 mm covering a q range of $0.008 < q < 0.45$ Å^{-1}, by using Mo $K\alpha$ radiation with $\lambda = 0.7107$ Å, monochromated and focused by two-dimensional multilayer optics. SAXS patterns were acquired with a two-dimensional 'Gabriel'-type gas detector (Gabriel & Rosenbaum, 1978) and WAXS patterns with an image-intensified Gemstar 125 CCD camera, mounted 30° off-axis to the direct beam to avoid shielding of the SAXS. The 125 mm CCD scintillator screen permits in that setup the resolution of a q range from 2 to 6.5 Å^{-1}. The instrumental resolution of the CCD camera was determined from powder diffraction of a silicon standard (NIST SRM 640c) and is of the order of $\Delta q/q = 4 \times 10^{-3}$. The performance of the *in situ* setup was validated by measuring a standard TiO_2 sample, Degussa P25, and by measuring an annealed TiO_2 sample of our preparation in a standard X-ray powder diffraction setup [see supplementary information;[1] results were consistent with literature reports (Bakardjieva *et al.*, 2005; Jensen *et al.*, 2006; Ohtani *et al.*, 2010; Porter *et al.*, 1999; Raj & Viswanathan, 2009).]

Heating experiments were performed in a specially designed *in situ* cell, which is described in detail by Andreasen *et al.* (2003). The cell was originally designed for *in situ* acquisition of SAXS data at the JUSIFA (B1) beamline of the Hamburger Synchrotonstrahlungslabor and was adapted for use with a laboratory pinhole camera with modified X-ray windows to cover also the wide-angle X-ray scattering. The *in situ* cell, *i.e.* sample mount, heater and gas assembly, is illustrated in Fig. 2. The cell consists of a quartz capillary (Markroehrchen, Hilgenberg GmbH) mounted between two Swagelok fittings perpendicular to the direct beam. Gas flows of 1–100 ml min^{-1} can be applied to the sample using the gas system equipped with a mass flow controller. Sample heating in a temperature interval from 298 to 1073 K is realized with a newly designed copper block with cut outs for the scattered beam in the wide- and small-angular ranges equipped with three heating cartridges (Watlow Firerod type KMFE0035A004A). The copper block is carbon black coated

[1] Experimental information and analysis of validation experiments on one TiO_2 sample annealed to 1023 K, measured in a standard Debye–Scherrer X-ray diffraction setup, and on the measurement of a P25 TiO_2 sample in the *in situ* setup are given as supplementary information, available from the IUCr electronic archives (Reference: AJ5162). Services for accessing this material are described at the back of the journal.

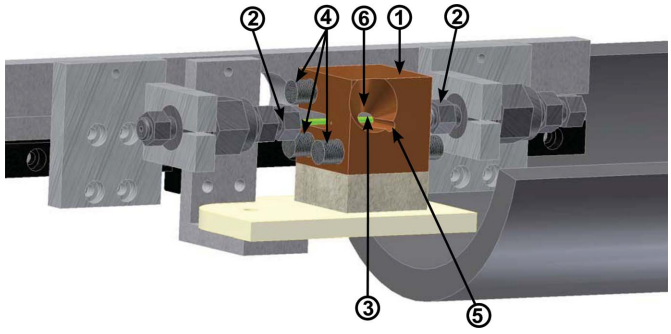

Figure 2
Schematic of the *in situ* cell: (1) copper block, (2) 1/16 inch (1.6 mm) Swagelok fittings, (3) quartz capillary, (4) heating cartridges, (5) hole for direct beam and SAXS, and (6) cut-out for WAXS.

on the inside to increase the heat transfer by emitted grey-body radiation to the sample; quartz itself is a good absorber of heat radiation.

2.2. Transmission electron microscopy

Transmission electron microscopy (TEM) and high-resolution transmission electron microscopy (HRTEM) images were acquired with a Jeol 3000 F microscope with an acceleration voltage of 300 kV, before and after annealing experiments, with TiO_2 samples redispersed in ethanol with a dilution of 1:1000 on carbon-coated copper grids.

2.3. Thermogravimetric analysis

Thermogravimetric analysis (TGA) was performed using a NETZSCH STA 449 C thermal analyser. TiO_2 nanorod powder (24.3 mg) was placed in an open aluminium oxide crucible and annealed in a constant argon stream from room temperature to 1065 K with a heating ramp of 2 K min^{-1}.

2.4. Data interpretation

The SAXS data were analysed using the unified equation (Beaucage & Schaefer, 1994) to approximate the scattering curve for n non-interrelated structural levels,

$$I(q) = \sum_{i=1}^{n} G_i \exp\left(-\frac{q^2 R_{g,i}^2}{3}\right) + B_i \left\{\frac{q}{\left[\operatorname{erf}\left(qkR_{g,i}/6^{1/2}\right)\right]^3}\right\}^{-P_i}, \quad (1)$$

where erf is an error function, $R_{g,i}$ is the radius of gyration, G_i the Guinier prefactor and B_i the prefactor specific to the power-law scattering with an exponent P_i, where $3 < P_i < 4$ for surface fractals, $P_i > 4$ for diffuse interfaces and $1 < P_i < 3$ for mass fractals. The mass fractal dimension is commonly used to describe highly polydisperse nanoparticles forming aggregates (see, for example, Hyeon-Lee *et al.*, 1998; Camenzind *et al.*, 2008), in systems where structural levels are well separated in size (Beaucage, 1996). For rod-shaped particles a decay with $P = 1$ is expected in the intermediate q range between the Guinier regime for the mean length and diameter, although this is typically only visible for $l >> r$. The empirical constant k is 1 for steep power-law decays with $P > 3$, and 1.06 for weak power-law decays (Beaucage, 1996). One may argue that it would be appropriate to include a structure-factor term to account for the packing of particles in the relatively dense material. However, the effect of a structure factor is generally not observed in the small-angle scattering cross sections of highly polydisperse materials. Riello & Benedetti (1997) demonstrated by simulation that the structure factor is increasingly smeared with increasing polydispersity. The same observation was made experimentally by Ballauff (2001).

Rietveld refinement of the WAXS data was performed by refining the lattice-parameter and particle-size broadening with the structural data for TiO_2 in the anatase (Horn & Meagher, 1972) and rutile phases (Bokhimi *et al.*, 2002) using the *Rietica* software (Hunter, 1998) and assuming the peak profiles as Voigt functions. The instrumental peak broadening was refined against data from a silicon reference (NIST SRM 640c).

2.5. Sample preparation

The oleic acid-capped TiO_2 nanorods were prepared by the method reported by Cozzoli *et al.* (2003) with some modification. Oleic acid (240 g) was heated to 393 K in a flow of argon with vigorous stirring for 1 h, after which $Ti(OiPr)_4$ (10 g) was added and the stirring was continued for 5 min while cooling to 363 K. Trimethylamine-*N*-oxide dehydrate (7.6 g) dissolved in water (34 ml) was added in one portion. A reflux condenser was added and the mixture was kept under argon and stirred at 353–373 K for 22 h. The mixture became milky and frothy after 1 h and the temperature was lowered to around 358–363 K. After 16 h, ethanol (500 ml) was added to the milky solution. The solutions were distributed in centrifuge buckets and centrifuged at 2000 r min^{-1} for 30 min. The supernatants were decanted and the solids from each flask were combined in one flask. The combined solids were washed three times by resuspension and recentrifugation in ethanol (250 ml). The solids were isolated by decantation of the final washing and drained by placing the flask bottom up for 1 h. Chlorobenzene (40 ml) was added, dissolving the solids immediately to give a clear light-yellow solution that was filtered through a microfilter with a 0.45 µm pore size. The concentration of TiO_2 nanorods was 80 mg ml^{-1}. The TiO_2 nanorods were precipitated with ethanol, dried in vacuum for 12 h at 343 K and pestled, producing a white to slightly yellow powder.

2.6. Annealing experiment

A sample bed of approximately 10 mm length, consisting of dry TiO_2 nanorods capped with oleic acid, was packed in a 0.7 mm quartz capillary, embedded between glass wool plugs and mounted gas tight between the two Swagelok fittings using graphite ferrules. The sample was kept in a constant gas flow of 1 ml N_2 min^{-1} at ambient temperature and pressure. Combined SAXS/WAXS patterns were acquired for 30 min at room temperature and in steps of 100 K in an interval from 373 to 573 K, in steps of 20 K from 653 to 773 K and in steps of 50 K from 823 to 1023 K. The experiments were performed in

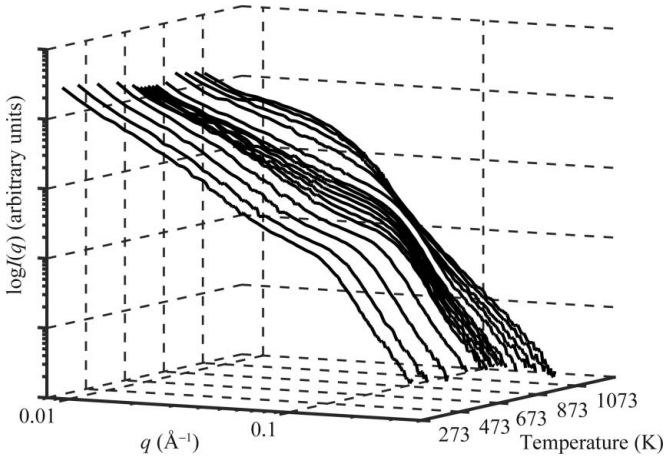

Figure 3
Thermal evolution of the SAXS pattern of TiO_2.

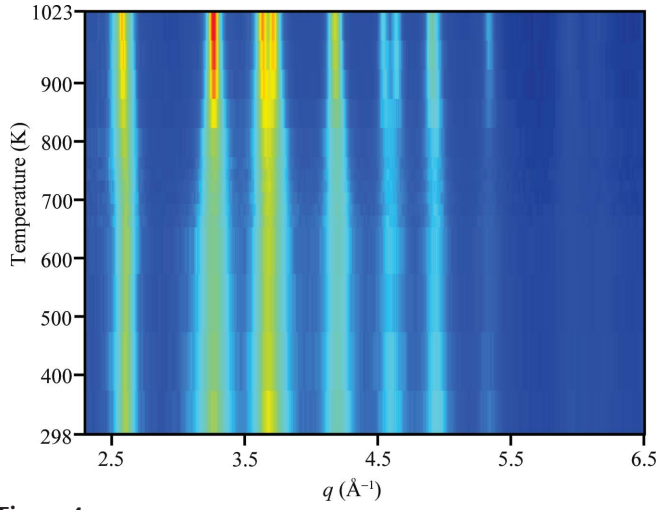

Figure 4
Thermal evolution of the WAXS pattern of TiO_2.

two different geometries with sample–detector distances of 1494 and 4679 mm and a beam radius of 0.25 mm. The chamber of the *in situ* cell was kept at a pressure level of 1.0 Pa during the experiments.

3. Data transformation and presentation

The two-dimensional SAXS data, acquired in both geometries during the heating of the TiO_2 nanorods, were azimuthally averaged using the *Fit2d* software package from the ESRF (Hammersley, 1997). After background subtraction, the data were scaled to interpolate intensities in the overlapping q region, calculating the quotient for the individual data points and using the mean to determine a scaling factor. The *in situ* SAXS data are illustrated in Fig. 3 as a $\log I(q)$ *versus* $\log q$ plot, where q is the scattering vector ($q = 4\pi \sin\theta/\lambda$, λ being the X-ray wavelength and θ half the scattering angle). The log–log plot of the data shows a distinct 'knee'-like Guinier regime (Beaucage, 1996) at high q at room temperature, corresponding to the nanorod diameter. The sample seems to be unaltered up to a sample temperature of 573 K. A shift of the Guinier regime towards lower q at temperatures between 653 and 1023 K indicates an increase in nanorod diameter with temperature.

In order to transform the WAXS data, a silicon standard (NIST SRM 640c) was measured before the experiment in the sample position. From a fit of the silicon powder rings the camera position relative to the sample was determined and a matrix was generated relating each detector pixel to a certain q value. Subsequently, this matrix was applied for data binning of the two-dimensional powder pattern of the TiO_2 nanorods. The one-dimensional transformed WAXS data at all temperatures are shown in Fig. 4. A sharpening of the peaks at temperatures between 653 and 1023 K indicates growth of the TiO_2 crystallites with temperature. No phase transitions were observed at any temperature.

4. Results and discussion

4.1. Transmission electron microscopy

TEM of a fresh TiO_2 sample, illustrated in Fig. 5 (left), shows rod-shaped particles with a diameter of around 4 nm and a length of approximately 45 nm. Aggregates consisting of several aligned rods with a mean total diameter of around 20 nm and overall lengths between 50 and 100 nm were observed. TEM images of the sample after annealing exhibit a change from rod to spherical particle shape with a mean diameter of around 15 nm (see Fig. 5 right).

4.2. Small-angle X-ray scattering

Fitting the SAXS data with a unified model comprising the Guinier radius for the rod diameter and length and two power-

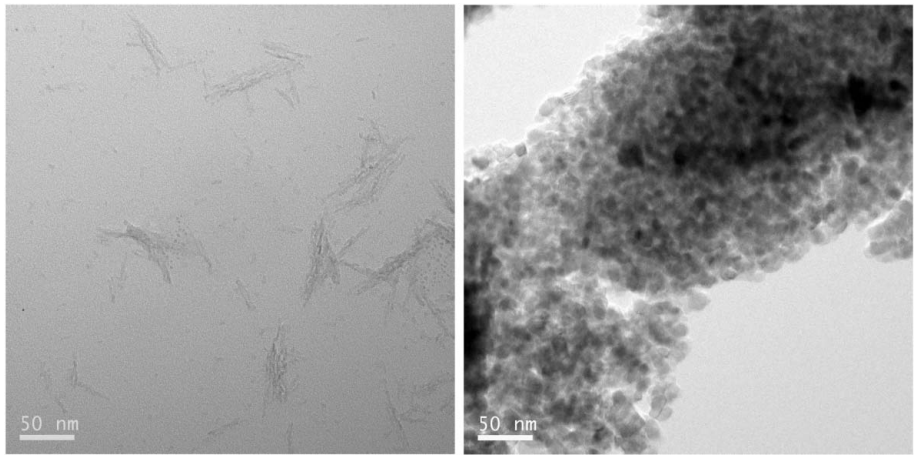

Figure 5
TEM images of TiO_2 nanorods before (left) and after heating to 1023 K (right).

law regimes was not possible because of the presence of overlapping regimes resulting from the comparable dimensions in radius and length of the rod and aggregates; hence a distinct rod-like scattering with $P = 1$ could not be resolved in the scattering patterns. An $I(q)q^2$ *versus* q plot of the scattered intensity at room temperature exhibits two pronounced peaks, with maxima at q around 0.035 and 0.13 Å^{-1}, corresponding to characteristic dimensions of about 18 and 5 nm (see Fig. 6). (π/q yields what corresponds to the Guinier radius. The reported values thus correspond to $2R$ to be consistent with values of diameters and lengths from TEM and with crystallite sizes.) A comparison with the dimensions extracted from TEM allows for the conclusion that the observed maxima can be attributed to the mean diameter of the rods and aggregates. The characteristic rod-like power-law scattering from TiO_2 monomers is superimposed by scattering from the aggregates, which precludes fitting the data with the complete unified model for cylinder-shaped particles.

The best description of the experimental data at room temperature was obtained by including the contributions specific to the aggregate [the second and third terms in equation (2)] and the rod diameter (fourth and fifth terms). The first term describes power-law scattering from large aggregates, close to the limit of resolution:

$$I(q) = B_0 q^{-4} + G_1 \exp\left(-\frac{q^2 R_{g,1}^2}{3}\right) + B_1 \left\{\frac{q}{\left[\operatorname{erf}\left(qR_{g,1}/6^{1/2}\right)\right]^3}\right\}^{-P_1} + G_2 \exp\left(-\frac{q^2 R_{g,2}^2}{3}\right) + B_2 \left\{\frac{q}{\left[\operatorname{erf}\left(qR_{g,2}/6^{1/2}\right)\right]^3}\right\}^{-P_2}. \quad (2)$$

In a temperature interval from 298 to 673 K, the complete SAXS curve is well described by equation (2) by keeping certain parameters fixed in least-squares fitting. P_1 was fixed at a value of 4 because the proximity of the size regimes related to the cluster aggregates and the rod diameter leads to a less pronounced regime of power-law scattering specific to the cluster surface and thereby to an unstable fit. An analysis based on mass fractals is therefore not possible, although this is often applied to systems with fewer, non-overlapping, structural levels, *e.g.* consisting of spherical primary particles (Hyeon-Lee *et al.*, 1998; Camenzind *et al.*, 2008). At temperatures below 573 K, P_2 was restricted to 3.9, determined from a separate power-law fit at high q of the SAXS curve at 298 K. Fits with P_2 as a free parameter were unstable because of the low intensity at high angles where the power-law scattering, specific to the rod surface, is significantly influenced by the background subtraction, such that small fluctuations in the scattered intensity can lead to over- or underestimation of the background. At temperatures above 673 K, the prefactors B_1, and above 923 K also G_1, were fixed to 0 because of the decreasing contribution of the related regimes to the entire scattering pattern. Fig. 7 illustrates the previously described least-squares fits of equation (2) at 298, 693, 973 and 1023 K.

TEM images before and after the annealing experiment revealed a particle shape change from rods to spheres during the sample annealing. The temperature range for this transition is not accessible from the SAXS data owing to the absence of characteristic power-law scattering for rod-like particles. R_g for the circular cross section orthogonal to the long axis of the rods is related to the radius R by $R_g = (1/2)^{1/2}R$ (Glatter & Kratky, 1982; Feigin & Svergun, 1987). For a sphere, the corresponding relation is $R_g = (3/5)^{1/2}R$. Since a specific transition temperature cannot be extracted, the particle and aggregate diameters at all temperatures are estimated assuming spherical shapes. This leads to an underestimation of ~9% for the diameter of rod-shaped particles at low temperatures.

The results of least-squares fitting show a continuous increase in aggregate diameter with temperature (see Fig. 8 left). This might be an indication for a temperature dependence of TiO_2 particle aggregation. A plot of the particle diameter (as obtained from the unified fit) *versus* temperature

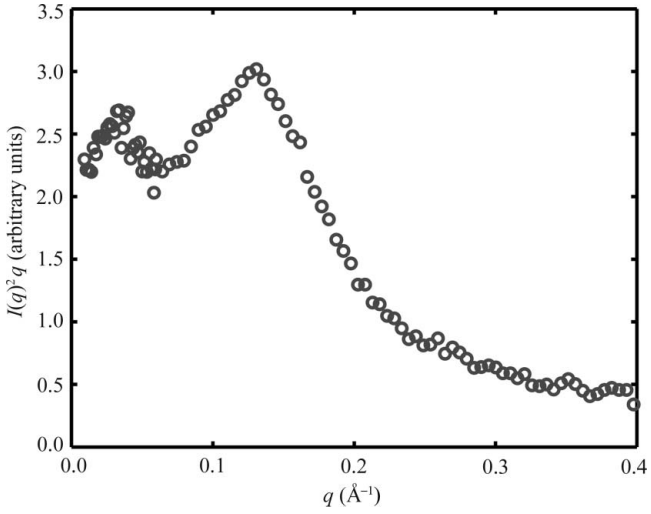

Figure 6
$I(q)q^2$ *versus* q plot of TiO_2 nanorods at room temperature.

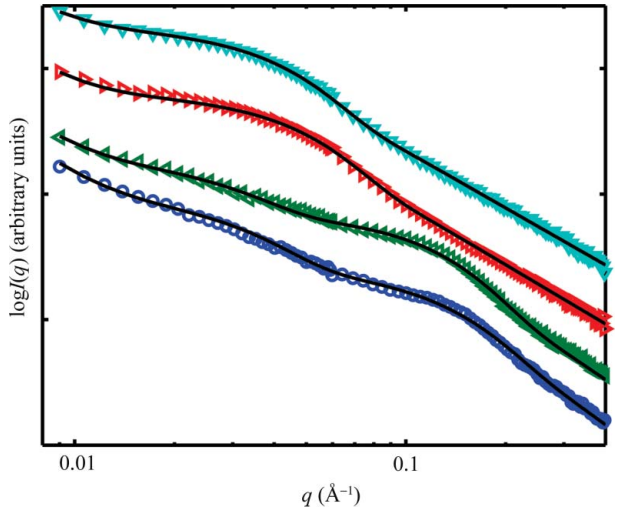

Figure 7
Fit of the SAXS data with the unified function at 298 (circles), 693 (left triangles), 973 (right triangles) and 1023 K (upturned triangles) plotted with an offset.

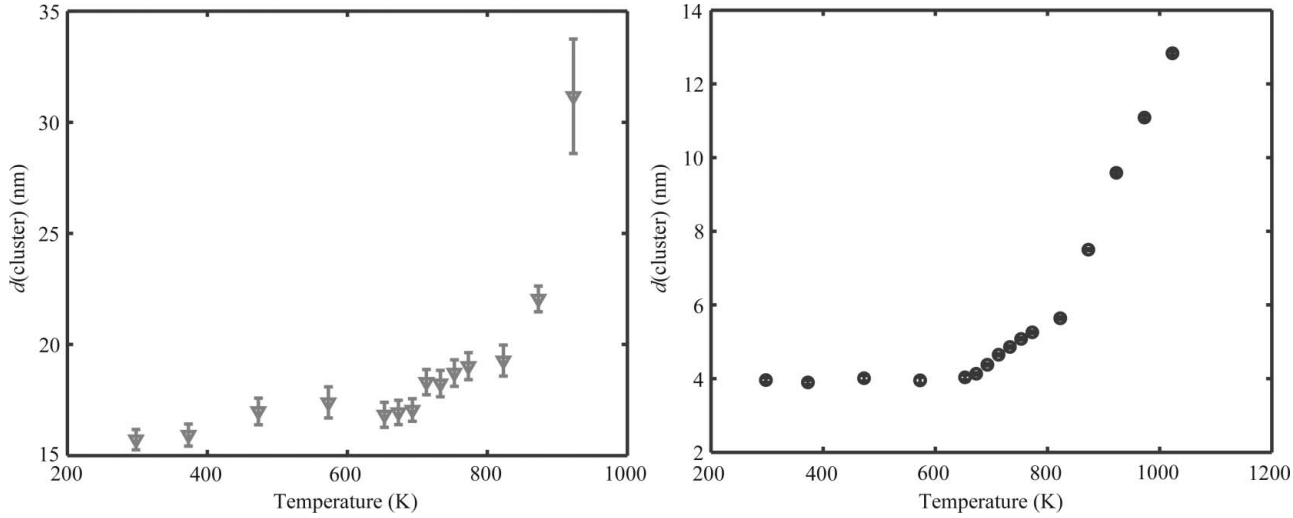

Figure 8
Aggregate diameter (left) and particle diameter (right) as a function of sample temperature from the unified fit [equation (2)].

(Fig. 8 right) shows three clear regimes (see §4.5). The particle diameter seems to be unaltered to 653 K and then increases slightly to 823 K. At temperatures above 823 K a rapid increase in the particle size was observed.

Power-law scattering at high q is ascribed to surface scattering of the aggregated subunits. In this regime the scattered intensity is estimated to decrease with $I(q) \propto q^{-(6-D)}$, where D is the fractal dimension (Bale & Schmidt, 1984); $D = 2$ indicates a smooth and $D = 3$ an exceedingly rough surface (Schaefer & Hurd, 1990). An increase in surface roughness during the sample annealing was observed (see Fig. 9). The variance of the fitted power-law coefficient at temperatures between 573 and 823 K and the outlier at 623 K might result from the appearance of surface-specific scattering from the small particle subunits close to the instrumental resolution in the experimental geometry.

Overall a growth of D from 2.1 at 573 K to 3.0 at 1023 K was noted; this indicates the transition from a nearly smooth to a virtually three-dimensional surface. However, the absolute value of the fractal dimension should be treated carefully since weaker power-law decays can also be attributed to polydisperse size distributions (Martin, 1986) and the detector gas filling (Né *et al.*, 1997).

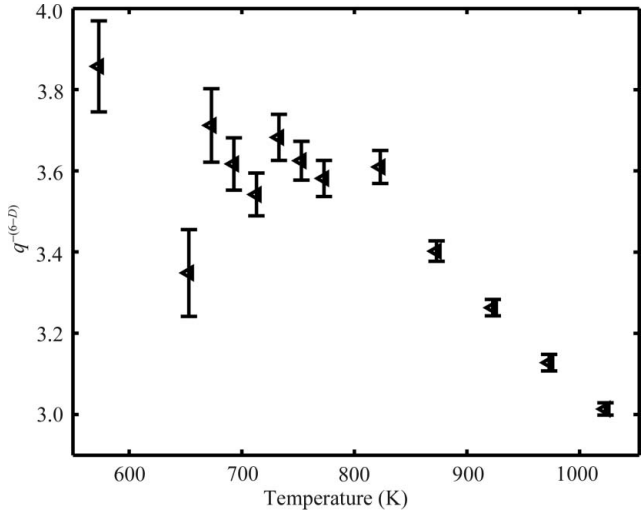

Figure 9
Power-law coefficient from the unified fit specific to the surface scattering of the aggregated TiO_2 particles.

4.3. Wide-angle X-ray scattering

Rietveld refinement of the transformed powder patterns at all temperatures was performed; the best fits of a fresh TiO_2 sample at 298 K and after the annealing to 1023 K are illustrated in Fig. 10.

All observed diffraction peaks are explained by the tetragonal anatase structure (space group No. 141, $I41/amd$). Rietveld refinement of the powder pattern acquired at 298 K and of the sample after annealing and cooling to 298 K reveals a decrease of the lattice parameter a and an increase of c and a decrease in the unit-cell volume (see Table 1). Similar observations for trends of the lattice constants and the cell volume have been reported by Swamy *et al.* (2006) and Ahmad & Bhattacharya (2009) and were ascribed to the size of the anatase nanoparticles. Lattice contraction with increasing crystallite size can be attributed to a net negative pressure induced by the repulsion of surface defect dipoles due to a distortion around the Ti surface atoms by absorbed molecules like water (Li *et al.*, 2004). The oleic acid surfactant used in this experiment might show a similar effect. If the negative pressure due to surface defect dipoles exceeds the positive pres-

Table 1
Lattice parameters refined with the Rietveld method before and after the annealing experiment compared with literature† values.

	a (Å)	c (Å)	V (Å^3)
Fresh sample	3.805	9.477	137.21
After annealing	3.786	9.514	136.37
Literature†	3.784	9.515	136.25

† Refined at 298 K by Horn & Meagher (1972).

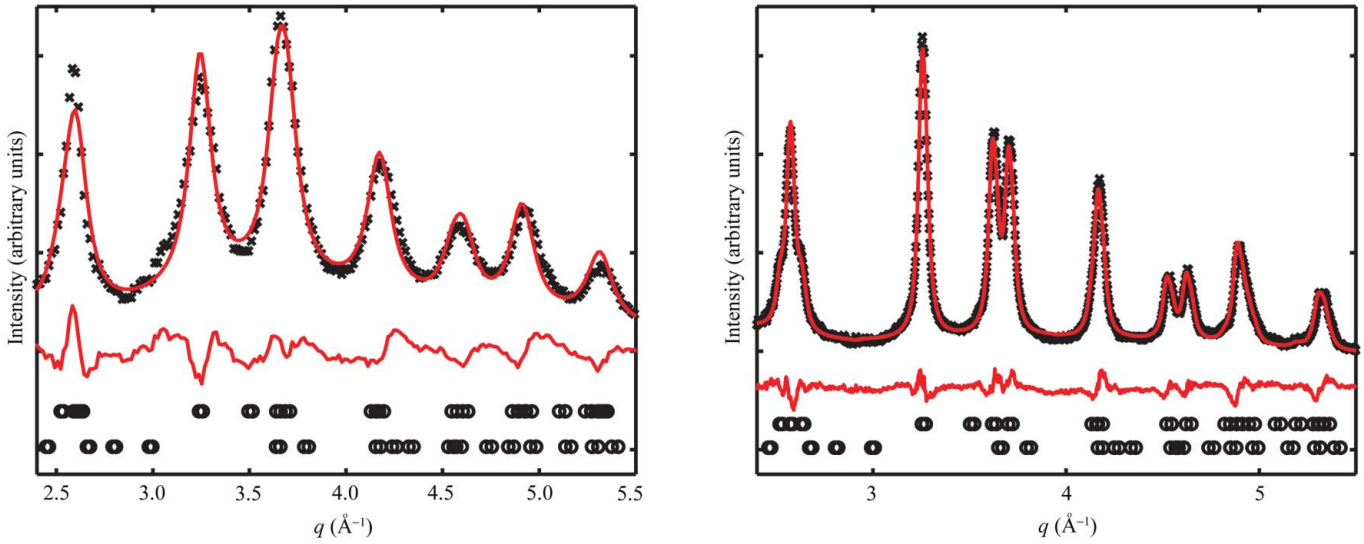

Figure 10
Rietveld refinement of TiO_2 data at 298 (left) and 1023 K (right) with theoretical peak positions (open circles) for anatase (top) and rutile (bottom).

sure related to surface stresses, an expansion of the lattice and therefore an increased unit-cell volume will be observed. The effect of negative pressure on the volume of the unit cell decreases with increasing particle size and is most pronounced at crystallite sizes below 10 nm (Swamy *et al.*, 2006). The refined lattice parameter and the cell volume of TiO_2 after the heating experiment are in good agreement with those of bulk anatase (Horn & Meagher, 1972) and do not show any effects of lattice expansion. This can be explained with the refined crystallite size of ∼12 nm at 1023 K.

No anatase-to-rutile phase transition was observed at any temperature. In bulk TiO_2, the phase transition of metastable anatase to the thermodynamically preferred rutile phase occurs at temperatures above 973 K (Grant, 1959). The irreversible transition is a function of time, temperature (Ikuma *et al.*, 1996) and particle size. Anatase exhibits a lower surface energy than rutile and this fact becomes significant because of the large surface-to-volume ratio of the nanoparticles. Anatase is the stable phase below a critical particle size of 14 nm (Gilbert *et al.*, 2003). Here, the mean crystallite size refined with the Rietveld method does not exceed 12 nm at any temperature, which explains the absence of the anatase–rutile phase transition in our experiments. Similar experiments on oleic acid-capped rod-shaped anatase nanoparticles by Chen *et al.* (2009) also revealed no anatase–rutile transition at temperatures up to 1023 K, although a time-dependent transition was reported to occur at 1123 K. Li *et al.* (2005) reported an experimentally determined critical crystallite size of 32–42 nm and a temperature of 873–973 K for the anatase–rutile phase transition.

The change from rod to spherical shape can be extracted from the ratio of the FWHM of the anatase (004) and (200) peaks: for spherical particles the ratio should be approximately 1. In a temperature interval of 773–923 K the FWHM ratio of the (004)/(200) peak changes from 0.62 to 1.03, and this indicates the occurrence of the rod-to-sphere transformation in this temperature interval.

4.4. Thermogravimetric analysis

The derivative TGA curves show two maxima for mass loss, at ∼350 and ∼650 K (Fig. 11). The first maximum can be attributed to evaporation of remaining ethanol from the sample preparation and the second maximum to the thermal decomposition of oleic acid. At temperatures above 780 K the sample mass remains constant.

4.5. Combined analyses

The evolution of particle diameter determined from SAXS and the crystallite size determined from WAXS are strongly correlated (see Fig. 12).

An increase in particle and crystallite size was observed at temperatures above 653 K. At lower temperatures, the sample seems to be unaltered and particle diameter and crystallite size are consistent. This correlates well with the TGA (see Fig. 11) results that show a major mass loss due to decom-

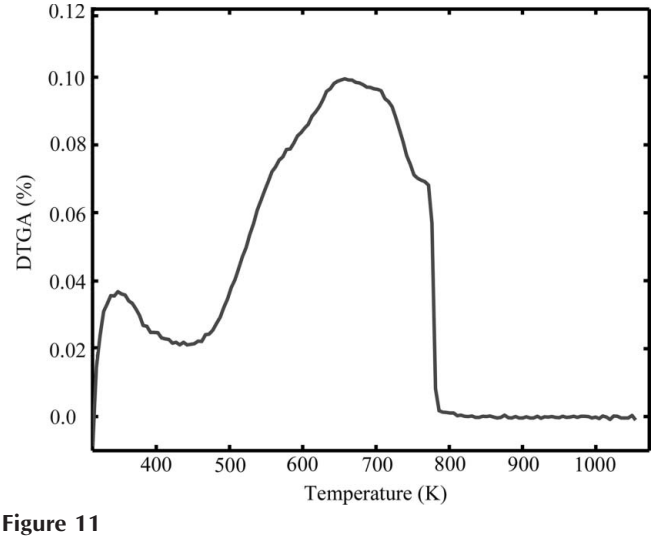

Figure 11
Derivative plot of the TGA from the TiO_2 nanoparticles.

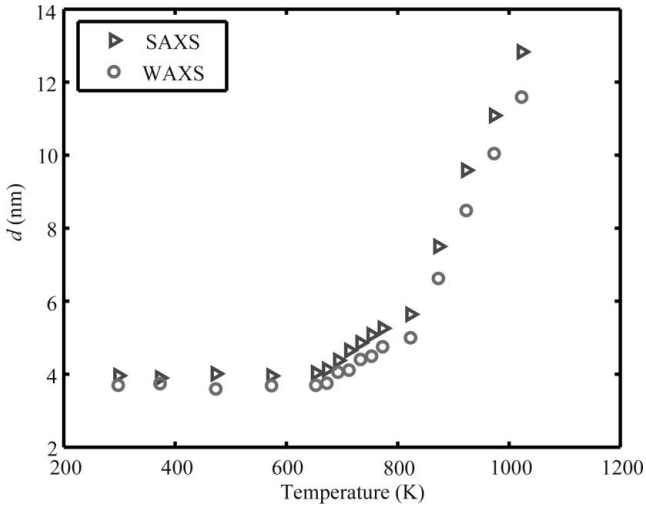

Figure 12
Particle diameter from fits of the SAXS data (circles) and crystallite sizes from Rietveld refinements (right triangles).

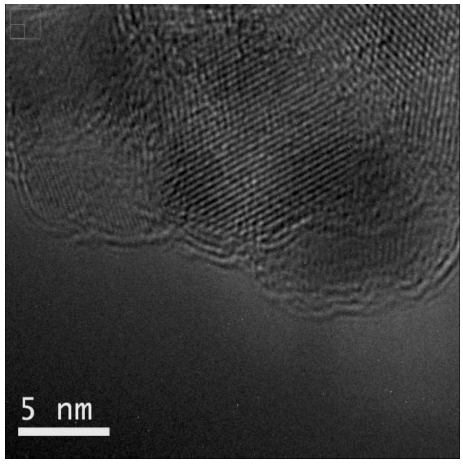

Figure 13
HRTEM of TiO_2 nanoparticles after annealing.

position of oleic acid surfactant with a maximum at ~650 K. In the temperature interval between 673 and 823 K, a slight increase in particle and crystallite size was monitored, which can be related to a decreasing coverage of the nanoparticles with surfactant molecules and particle growth to minimize the overall free surface energy.

The difference between particle and crystallite size increases with temperature in this interval. At temperatures above 823 K, both particle and crystallite sizes increase rapidly, while retaining a small discrepancy between the particle and crystallite size of around 1 nm. We have not been able to establish an unambiguous physical explanation for this discrepancy. High-resolution transmission electron microscopy reveals that the TiO_2 particles exhibit a core/shell structure consisting of a single-crystal core and what appears to be separate domains in a shell of 0.5–1.4 nm thickness (see Fig. 13). This is consistent with the slightly larger particle size in the SAXS data at 1023 K, but we have no data to indicate the composition of this shell or the reason for the apparent

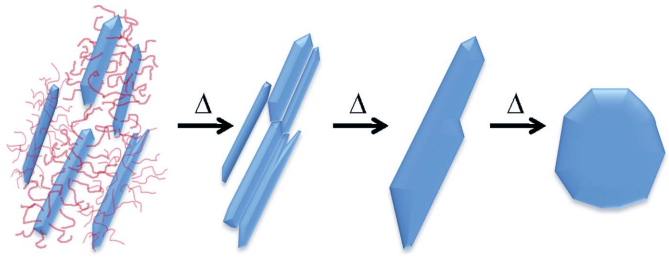

Figure 14
Sketch showing a possible sequence of physical transformations that are in accordance with the experimental observations.

growth of the shell structure with temperature. It is possible that it is partly due to an artefact of either the crystallite or the particle size determination because of the shape change during sintering.

At temperatures below 653 K, the particle and crystallite sizes remain constant at around 4 nm (Fig. 12). At temperatures between 653 and 823 K, a slow growth in the average diameter is observed. This coincides with the loss of surfactants observed in the TGA and indicates the initiation of rod sintering, *i.e.* the loss of individual rod character and the onset of spherical particle growth (Fig. 14). At temperatures above 823 K all surfactants are decomposed (see Fig. 11) and a rapid growth is observed, which is consistent with the transition from rods to spherical particles. The specific transition temperatures are likely to be influenced by the different temperature intervals used during the annealing of the sample, since the crystallite growth is a function of time and temperature (Li *et al.*, 2005).

5. Conclusion

In this study, simultaneous *in situ* SAXS/WAXS was used to investigate the dynamical changes of oleic acid-capped TiO_2 nanorods during annealing in a continuous stream of inert gas. Particle and crystallite growth was found to initiate at temperatures where the capping agent oleic acid starts to decompose in contrast to the aggregates, which exhibit a continuous growth with temperature. An increase of the fractal dimension from $D = 2.1$ to $D = 3.0$ indicates the transition from almost smooth to an exceedingly rough surface and thereby an increase in the number of potentially active Ti sites because of the corresponding increase in surface area. However, the absolute number of the fractal dimension should be treated with care.

TEM before and after the annealing experiment revealed a morphological transition from rod to spherical shape; the transition occurs in a temperature interval of 773–923 K, observed by the change of FWHM ratio between the anatase (004)/(200) peaks in WAXS. The TiO_2 particles form core/shell structures and TiO_2 remained in the metastable anatase phase even though temperatures above the bulk anatase/rutile transition were applied. This effect can be attributed to the large surface-to-volume ratio and lower surface energy of anatase nanoparticles.

The experimental results emphasize the benefit of *in situ* combined SAXS/WAXS for tracking the dynamical processes during sample annealing, *i.e.* application of one isolated technique would not resolve the formation of TiO_2 core/shell particles. Time- and temperature-resolved *in situ* combined SAXS/WAXS is essential to overcome the difficulties of exactly reproducing the experimental conditions for the different experimental techniques.

We thank Steen Bang, Ove Rasmussen, Torben Kjær and Jens Borchsenius for maintenance of the equipment and technical support during the implementation of the *in situ* laboratory setup, Hjalte Sylvest Jacobsen for improvement of the WAXS one-dimensional data transformation, Haihua Lui for assistance with TEM and HRTEM, Henning Engelbrecht for guidance regarding LabVIEW and data acquisition during the implementation of the sample gas system, and the Copenhagen Graduate School for Nanoscience and Nanotechnology and Haldor Topsøe A/S for financial support. The Centre for Individual Nanoparticle Functionality is funded by the Danish National Research Foundation.

References

Ahmad, Md. I. & Bhattacharya, S. S. (2009). *Appl. Phys. Lett.* **95**, 191906.
Andersen, P. D., Skårhøj, J. C., Andreasen, J. W. & Krebs, F. C. (2009). *Opt. Mater.* **31**, 1007–1012.
Andreasen, J. W., Rasmussen, O., Feidenhans'l, R., Berg Rasmussen, F., Christensen, R., Molenbroek, A. M. & Goerigk, G. (2003). *J. Appl. Cryst.* **36**, 812–813.
Bakardjieva, S., Šubrt, J., Štengl, V., Dianez, M. J. & Sayagues, M. J. (2005). *Appl. Catal. B*, **58**, 193–202.
Bale, H. D. & Schmidt, P. W. (1984). *Phys. Rev. Lett.* **6**, 596–599.
Ballauff, M. (2001). *Curr. Opin. Colloid Interface Sci.* **6**, 132–139.
Bao, S.-H., Bao, Q.-L., Li, C.-M. & Dong, Z.-L. (2007). *Electrochem. Commun.* **9**, 1233–1238.
Beaucage, G. (1996). *J. Appl. Cryst.* **29**, 134–146.
Beaucage, G. & Schaefer, D. W. (1994). *J. Non-Cryst. Solids*, **172**, 795–805.
Benkstein, K. D. & Semancik, S. (2006). *Sensors Actuators B*, **113**, 445–453.
Bokhimi, X., Morales, A. & Pedraza, F. (2002). *J. Solid State Chem.* **169**, 176–181.
Camenzind, A., Schulz, H., Teleki, A., Beaucage, G., Narayanan, T. & Pratsinis, S. E. (2008). *Eur. J. Inorg. Chem.* **2008**, 911–918.
Chen, Y., Kang, K. S., Yoo, K. H., Jyoti, N. & Kim, J. (2009). *J. Phys. Chem. C*, **113**, 19753–19755.
Cozzoli, P. D., Kornowski, A. & Weller, H. (2003). *J. Am. Chem. Soc.* **125**, 14539–14548.
Feigin, L. A. & Svergun, D. I. (1987). *Structure Analysis by Small-Angle X-ray and Neutron Scattering.* New York: Plenum Press.
Fox, M. A. & Dulay, M. T. (1993). *Chem. Rev.* **93**, 341–357.
Gabriel, F., Dauvergne, F. & Rosenbaum, G. (1978). *Nucl. Instrum. Methods*, **152**, 191–194.
Gilbert, B., Zhang, H., Huang, F., Finnegan, M. P., Waychunas, G. A. & Banfield, J. F. (2003). *Geochem. Trans.* **4**, 20–27.
Glatter, O. & Kratky, O. (1982). *Small Angle X-ray Scattering*. New York: Academic Press.
Grant, F. A. (1959). *Rev. Mod. Phys.* **31**, 646–674.
Hammersley, A. P. (1997). *Fit2d*. Internal Report ESRF97HA02T. ESRF, Grenoble, France.
Horn, M., Schwerdtfeger, C. F. & Meagher, E. P. (1972). *Z. Kristallogr.* **136**, 273–281.
Hunter, B. (1998). *IUCr Commision on Powder Diffraction Newsletter*, No. 20, p. 21.
Hyeon-Lee, J., Beaucage, G., Pratsinis, S. E. & Vemury, S. (1998). *Langmuir*, **14**, 5751–5756.
Ikuma, Y, Shigemura, T. & Hirose, T. (1996). *J. Am. Ceram. Soc.* **79**, 2533–2538.
Jensen, H., Pedersen, J. H., Jørgensen, J. E., Pedersen, J. S., Joensen, K. D., Iversen, S. B. & Søgaard, E. G. (2006). *Exp. Nanosci.* **1**, 355–373.
Jiu, J., Isoda, S., Wang, F. & Adachi, M. (2006). *J. Phys. Chem. B*, **110**, 2087–2092.
Kim, J. & Cho, J. (2007). *J. Electrochem. Soc.* **154**, A542–A546.
Li, G., Li, L., Boerio-Goates, J. & Woodfield, B. F. (2004). *Appl. Phys. Lett.* **85**, 2059–2061.
Li, G., Li, L., Boerio-Goates, J. & Woodfield, B. F. (2005). *J. Am. Chem. Soc.* **127**, 8659–8666.
Liao, D. L. & Liao, B. Q. (2006). *J. Photochem. Photobiol. A Chem.* **187**, 363–369.
Lira-Cantu, M., Norrman, K., Andreasen, J. W., Casan-Pastor, N. & Krebs, F. C. (2007). *J. Electrochem. Soc.* **154**, B508–B513.
Manera, M. G., Cozzoli, P. D., Curri, M. L., Leo, G., Rella, R., Agostiano, A. & Vasanelli, F. (2005). *Synth. Met.* **148**, 25–29.
Martin, J. E. (1986). *J. Appl. Cryst.* **19**, 25–27.
Nagaveni, K., Hegde, M. S., Ravishanker, G. N., Subbanna, G. N. & Madras, G. (2004). *Langmuir*, **20**, 2900–2907.
Né, F., Gabriel, A., Kocsis, M. & Zemb, Th. (1997). *J. Appl. Cryst.* **30**, 306–311.
Ohtani, B., Prieto-Mahaney, O. O. & Abe, R. (2010). *J. Photochem. Photobiol. A*, doi:10.1016/j.jphotochem.2010.07.024. In the press.
Porter, J. F., Li, Y.-G. & Chan, C. K. (1999). *J. Matter. Sci.* **34**, 1523–1531.
Raj, K. J. A. & Viswanathan, B. (2009). *Indian J. Chem.* **48**, 1378–1382.
Riello, P. & Benedetti, A. (1997). *J. Chem. Phys.* **106**, 8660–8663.
Schaefer, D. W. & Hurd, A. J. (1990). *Aerosols Sci. Technol.* **12**, 876–890.
Shimizu, K.-I., Murayama, H., Nagai, A., Shimada, A., Hatamachi, T., Kodama, T. & Kitayama, Y. (2005). *Appl. Catal. B*, **55**, 141–148.
Swamy, V., Menzies, D., Muddle, B. C., Kuznetsov, A., Dubrovinsky, L. S., Dia, Q. & Dmitriev, V. (2006). *Appl. Phys. Lett.* **88**, 243103.
Yeung, K. L., Yau, S. T., Maira, A. J., Coronado, J. M., Soria, J. & Yue, P. L. (2003). *J. Catal.* **219**, 107–116.
Zeng, Y. P. & Jiang, D. (2008). *J. Appl. Ceram. Technol.* **5**, 505–512.
Zhang, J., Xu, Q., Feng, Z., Li, M. & Li, C. (2008). *Angew. Chem. Int. Ed.* **47**, 1766–1769.

Combined *in situ* small and wide angle X-ray scattering studies of TiO_2 nano-particle annealing to 1023 K

Supplementary information

To validate the results obtained from the *in situ* set up, we acquired standard powder diffraction data in a Debye-Scherrer set up using a slit collimated beam from a RU-200 Rigaku rotating anode operated at 50 KV/200 mA, focused and monochromatized (Cu K_α) by a 1D multilayer optic (Xenocs). The detector scan was carried out with a NaI scintillation point detector (Bicron) mounted behind an evacuated flight tube with slit collimation. The sample was loaded in a 0.7 mm quartz capillary with 10µm wall thickness (Hilgenberg GmbH).

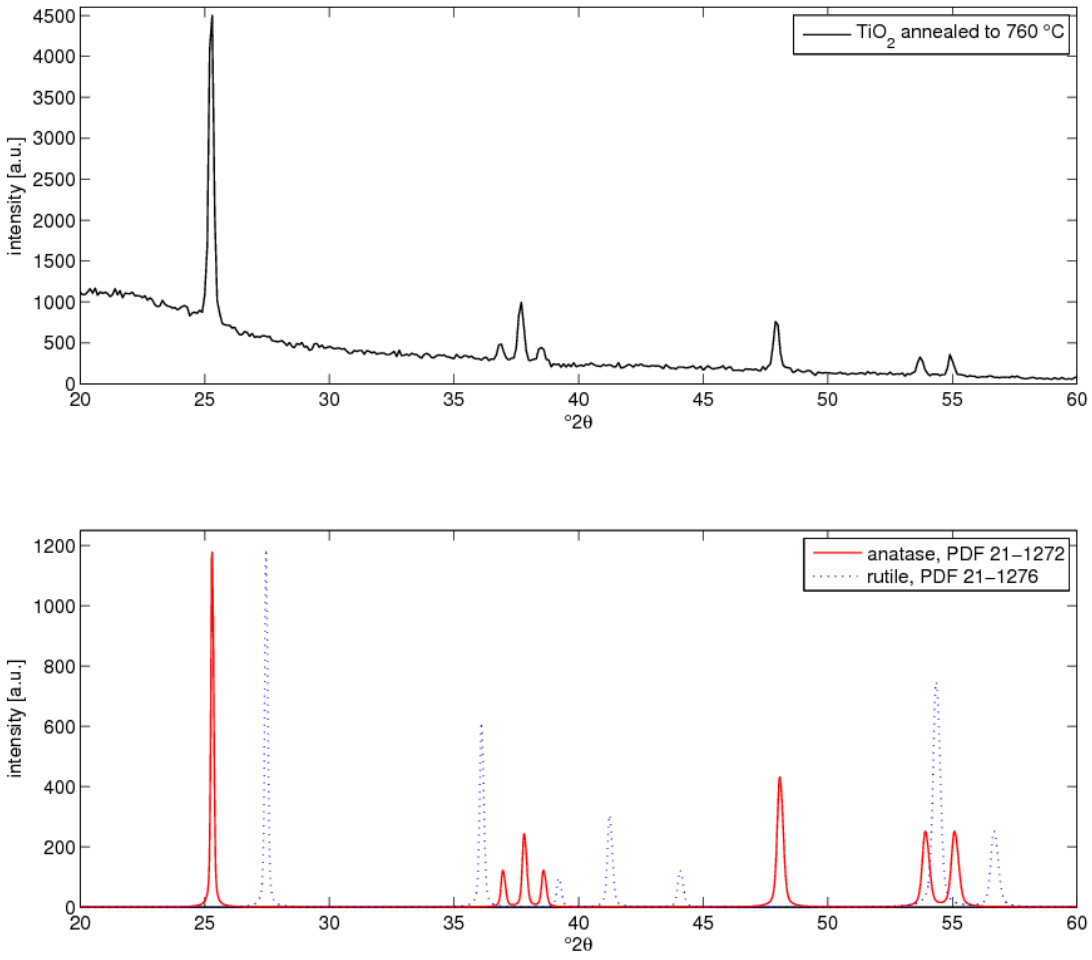

Figure 1 The top panel shows the measured XRD data of the TiO_2 powder annealed to 1023 K. The background scattering at the lowest angles is from the quartz capillary. The panel below shows the simulated patterns of Powder Diffraction File cards 21-1272 (anatase) and 21-1276 (rutile). The only crystalline phase in the powder is clearly anatase.

The standard TiO_2 material, P25 from Degussa (now Evonik), which is used for a large variety of applications, including research in photocatalysis, was measured in the *in situ* setup, loaded in the usual 0.7 mm quartz capillary, to validate the capability for phase distinction and refinement.

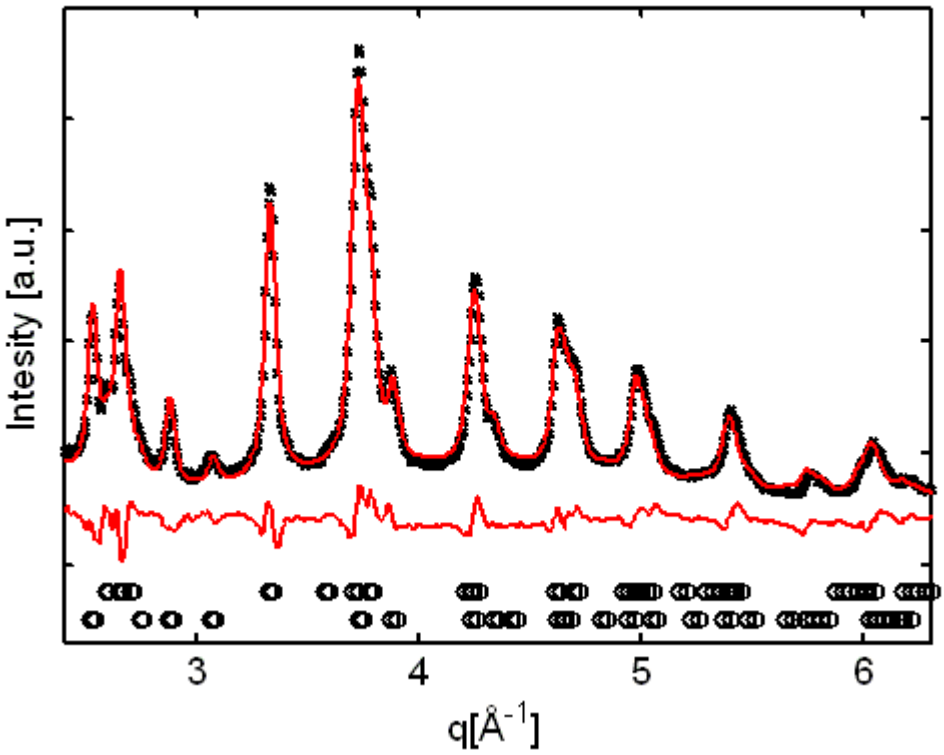

Figure 2 Rietveld refinement of P25 with theoretical peak positions (o) for anatase (top) and rutile (bottom).

The anatase/rutile fractions were determined by Rietveld refinement to 67.4 % ± 0.1 % anatase and 32.6 % ± 0.1 % rutile which is in reasonable agreement with values reported in the literature. Jensen *et al.* (2006) reported the P25 sample to consist of 71 % anatase, 27 % rutile and 2 % amorphous TiO_2 determined from data recorded on a standard powder diffractometer, Porter *et al.* reported the P25 powder consists of 78.8 % anatase[1] and 21.2 % rutile[1] and Bakardjeva *et al.* (2005) 84.7 % anatase[1] and 16.3 % rutile[1]. Ohtani *et al.* (2010) reported different compositions in the same P25 sample from 73 - 85 % anatase, 14 - 17 % rutile and 0 - 18 % amorphous TiO_2 and attributed this to variations in the production.

The crystallite sizes from the Rietveld refinement are for anatase 12.6 ± 0.1 nm and rutile 14.2 nm ± 0.6 nm. However, a wide variety of refined crystallite sizes is reported. Sigma & Aldrich reports on their website a size of ~ 21 nm (Aeroxide® P25), Bakardjeva *et al.* (2005) sizes of 20.8 nm for

[1]Calculated from reported weight fraction with ρ(anatase) = 3.7 g cm^{-3} and ρ(rutile) = 4.3 g cm^{-3}

anatase and 30.5 nm for rutile, Porter *et al.* (1999) reports 20.6 nm for anatase and 14.4 nm for rutile, *Jensen et al.* (2006) determined the crystallite size 19.4 nm and Raj *et al.* (2009) 48 nm for anatase and 51 nm for rutile.

The crystallite sizes we find are clearly in the lowest end of the range of sizes reported. But, considering the large spread in values for phase composition and crystallite sizes reported, it appears that the P25 material shows considerable inhomogeneity, both within and between production batches.

Bakardjieva, S., Šubrt J., Štengl, V, Dianez, M. J., Sayagues, M. J. (2005) *Appl. Cat. B* **58** 193 - 202

Jensen, H., Pedersen, J. H., Jørgensen, J. E., Pedersen, J. S., Joensen, K. D., Iversen, S. B., Søgaard, E. G. (2006) *Experimental Nanoscience* **1** 355-373

Ohtani, B., Prieto-Mahaney, O. O., Abe, R. (2010) *J. Photochem. Photobiol. A* doi:10.1016/j.jphotochem.2010.07.024 (in press)

Porter J. F., Li, Y.-G., Chan, C. K. (1999) *J. Matter. Sci.* **34** 1523 - 1531

Raj, K. J. A., Viswanathan, B. (2009), *Ind. J. Chem.* **48** 1378 - 1382

Paper II

will be submitted to:

Applied Catalysis A

Dynamical properties of a Ni/spinel methane reforming catalyst during the reduction

Jan Kehres,[a] Jens Wenzel Andreasen,[b*] , Jostein Bø Fløystad[c] , Alfons Molenbroek[d], Jon Geest Jakobsen[d], Liu Haihua[a], Ib Chorkendorff[e] andTejs Vegge[a]

[a]Materials Research Division, Risø National Laboratory for Sustainable Energy, Technical University of Denmark, Denmark, [b]Solar Energy Programme, Risø National Laboratory for Sustainable Energy, Technical University of Denmark, Denmark,[c]Department of Physics, Norwegian University of Science and Technology, Trondheim, Norway, [d]Haldor Topsøe A/S, Research and Development Division, Denmark an [d]Center for Individual Nanoparticle Functionality, Department of Physics, Technical University of Denmark, Denmark.

E-mail: jewa@risoe.dtu.dk

Keywords: Ni/spinel, reduction, methane reforming, in situ, combined SAXS/WAXS

Abstract

Simultaneous *in situ* small and wide angle scattering X-ray scattering (SAXS/WAXS) studies were performed in a laboratory setup to investigate the dynamical properties of a nickel/spinel ($Ni/MgAl_2O_4$) catalyst, *w*(Ni) = 22 wt%, during the reduction. The fresh catalyst sample was characterized by SAXS/WAXS and high resolution transmission electron microscopy (HRTEM). Simultaneous SAXS/WAXS was acquired during the reduction in a temperature interval from 298 - 873 K. Ni particles in the initial catalyst sample were observed to be partial oxidized. A decrease of the Ni lattice parameter during the reduction, in a temperature interval from 413 - 453 K, indicates that the Ni particles in the initial sample exhibit a Ni/NiO core shell structure. The decrease of the Ni lattice parameter can be related to the reduction of NiO shell whereby stress due to the lattice mismatch of Ni and NiO disappears. A monotonic increase of the Ni particle size due to sintering was observed after reduction of the NiO shell.

1. Introduction

Synthesis gas, a mixture of carbon monoxide and hydrogen, is an important intermediate for various large scale processes. Methane is conventional converted in synthesis gas by the steam-reforming process, but reforming with carbon dioxide is thought as an alternative (Rostrup-Nielsen and Bak Hansen 1993). Reforming with carbon dioxide yields lower H_2/CO ratios compared to reforming with steam and that is desirable for the synthesis of synthetic fuel by Fischer-Tropsch, methanol and oxo alcohols (Gadalla *et al.* 1988, Holm-Larsen 2001, Noweck and Grafahrend 2006). Many transition metals such as Ni, Ru, Pd, Ir and Pt (Rostrup-Nielsen *et al.* 1993, Wei and Iglesia 2004) have been found to show good catalytic activity for the dry methane reforming reaction. Catalysts based on Ni are commercially favorable for this process considering the high cost and limited availability of the noble metals (Guo *et al.* 2004), but they have a main draw back in higher carbon deposition rates compared to most of the noble metals (Rostrup-Nielsen *et al.* 1993). Therefore it is economically advantageous to modify Ni-based catalysts to improve their resistance against carbon formation. The rate of carbon formation was observed to depend on the Ni crystallite size, lower rates were observed with decreasing Ni crystallite size (Borowieki 1982, Chen *et al.* 2005). Crisafulli *et al.* (1999) reported a lower deactivation rate of bimetallic Ni-Ru catalysts compared to pure Ni during dry reforming experiments and ascribes this to a higher dispersion of Ni deposited on Ru nanoparticles. Lower carbon formation rates during steam-reforming of methane with Ru doped Ni catalyst were also reported by Jeong *et al.* (2006). The type of support material shows an effect on the Ni dispersion and therefore on the activity (Jeong *et al.* 2006) and carbon formation rates (Guo *et al.* 2004). Higher carbon formation rates and lower activity were reported for Ni/γ-Al_2O_3 compared to Ni/$MgAl_2O_4$. This emphasizes the importance of the metal dispersion on the performance of the catalyst, highly efficient and long time stable Ni-based catalysts for methane reforming should exhibit a high initial metal dispersion and retain it during the reforming process.

Reforming catalysts are usually prepared by incipient wetness impregnation of the support materials with an aqueous solution of a Ni salts and subsequent drying and calcination at high temperatures. The final step of the catalyst preparation is the activation by reduction of NiO with hydrogen. Cyclic oxidation and reduction can also be utilized to regenerate sulphur poisoned Ni-catalysts (Aguinaga and Montes 1992). Various studies of the reduction of unsupported and supported NiO can be found in the literature (Richardson and Twigg 1998, Parravano 1957, Richardson *et al.* 2003,

Rodriguez *et al.* 2002, Zieliński1982, Jeong *et al.* 2006, Guo *et al.* 2004). The reduction temperature of unsupported NiO-nanoparticles was reported to be independent of the particle size (Richardson and Twigg 1998). The reduction of NiO initiates after a temperature dependent induction period (Parravano 1957, Richardson *et al.* 2003, Rodriguez *et al.* 2002). Rodriguez *et al.* 2002 studied the reduction of NiO with X-ray absorption fine structure, time resolved synchroton X-ray diffraction, photo emission and first principle density functional slab calculations and concluded that during the induction oxygen vacancies are created and those vacancies lower the energy barrier for the hydrogen bond cleavage. An increase of the Ni crystallite size of an order of magnitude during the reduction compared to the initial NiO crystallite size of unsupported NiO was observed (Richardson *et al.* 2003). Cyclic reduction and oxidation studies of a 2 wt% Ni/Al_2O_3 catalyst did not show any loss in surface area and it was concluded that due to the large interparticle distance (Zieliński1982). However, an influence of the reduction temperature on the crystallite size was noted (Borowiecki 1982).

Since the activity and resistance against carbon deposition of Ni-based methane reforming catalysts is correlated with the Ni metal dispersion it is crucial to follow and understand dynamical processes during the reduction and reforming reaction to improve start-up processes and for the assortment of the optimum operating conditions. A suitable technique to resolve these dynamics is combined *in situ* small and wide angle X-ray scattering, small angle X-ray scattering (SAXS) to follow the particle growth and wide angle X-ray scattering (WAXS) to detect phase transitions and crystallite growth. In this paper we describe reduction experiments of a prereduced and reoxidized 22 wt% $Ni/MgAl_2O_4$ in pure hydrogen to follow the dynamical changes during the reduction of NiO.

2. Experiments and methods

2.1 Experimental setup

Simultaneous *in situ* SAXS/WAXS was performed in a laboratory pinhole camera setup with sample to SAXS-detector distances of 1494 (short geometry) and 4679 mm (long geometry) covering a *q*-range of $0.002 < q < 0.45$ Å^{-1} by using Mo K-alpha $\lambda = 0.7107$ Å in the short and Cu K-alpha radiation $\lambda = 1.5418$ Å in the long setup. X-rays were produced with a Rigaku RU300 rotating anode generator operating in fine focus mode at 40 kV and 60 mA. SAXS patterns were

acquired with a 2D "Gabriel" type gas detector (Gabriel *et al.*, 1978) and WAXS patterns with an image intensified Gemstar 125 CCD camera mounted 30° off-axis to the direct beam to avoid shielding of the SAXS. The 125 mm CCD scintillator screen permits a *q*-range from 2 – 6.5 $Å^{-1}$ by using Mo K-alpha radiation. The instrumental resolution of the CCD camera was determined from powder diffraction of a silicon standard (NIST SRM 640c) and is in the order of $\Delta q / q = 4 \times 10^{-3}\ Å^{-1}$.

Reduction experiments were performed in a special designed *in situ* cell, which is described in detail by Andreasen *et al.* (2003). The cell was adapted to the laboratory pinhole camera with modified X-ray windows to cover the wide angle scattering and a newly designed heater, permitting sample temperatures in an interval of 298 - 1073 K (Kehres *et al.* 2010). Constant gas flows were applied to the sample using a gas control system including a mass flow controller. The flow scheme the *in situ* is illustrated in figure 1.

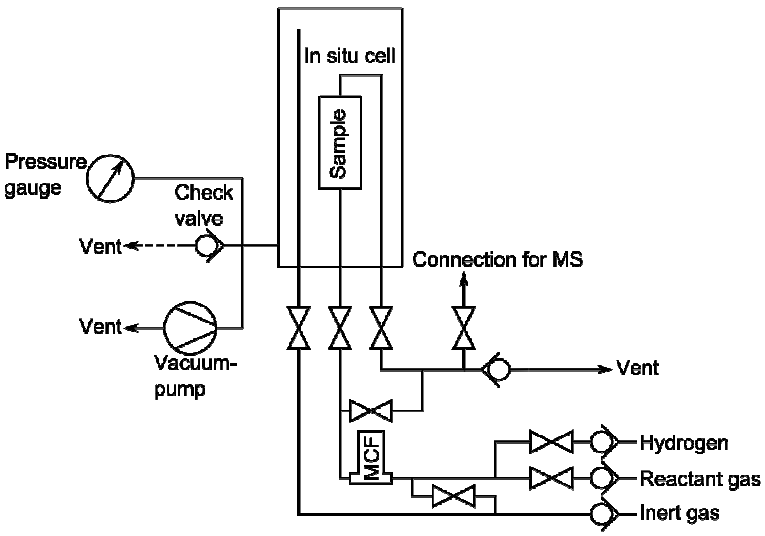

Figure 1: Flow scheme of the *in situ* cell.

The newly designed gas system permits to apply gas flows of 1 - 100 Nml min^{-1} to the sample. An online mass spectrometer is connected to the vent system of the cell to monitor chemical reactions *in situ*. Overall the instrumental setup allows simultaneous *in situ* determinations of changes in the crystalline structure, particle morphology and reactivity of nano-scale catalysts to resolve their correlations with the sample temperature and reactant gas composition.

2.2 *Ex situ* wide angle X-ray scattering

X-ray powder diffraction pattern of a fresh catalyst sample were acquired on a Brucker D8 Bragg-Brentano diffractometer using Cu K-alpha radiation with λ = 1.5418 Å at 40 kV and 40 mA. The diffraction patterns were recorded in a *q*-range from 1.1 - 6.5 $Å^{-1}$ with step sizes of $\Delta q = 1.4 \cdot 10^{-3}$ $Å^{-1}$.

2.3 Transmission electron microscopy

Transmission electron microscopy (TEM) and high-resolution electron microscopy (HRTEM) images were acquired with a JEOL 3000 F microscope with acceleration voltage of 300 kV. The $Ni/MgAl_2O_4$ catalyst was dispersed in ethanol with a dilution of 1:1500 using ultrasonic treatment. 10 µl of this dispersion were coated on a 400 mesh holey carbon grid.

2.4 Reduction experiment

A 22 wt% $Ni/MgAl_2O_4$ catalyst sample was crushed and sieved. Samples with a particle between 65 - 125 µm were inserted in 0.7 mm quartz capillaries (Mark tube from Hilgenberg GmbH) with a catalyst bed lengths of approximately 10 mm, embedded in between two bunches of glass wool and were mounted gas tight between two Swagelok® fittings using graphite ferrules. The *in situ* reduction experiments were performed in a constant gas flow of 2 ml/min hydrogen (alphagaz, Air Liquide, > 99.999 %) at standard temperature and pressure (STP). Three combined SAXS/WAXS patterns were acquired at 298 K and in an interval from 373 - 873 K in steps of 100 K. The catalyst preparation of the 22 wt% $MgAl_2O_4$ was reported in detail by Sehested *et al.* (2001).

3. Data transformation

The 2D SAXS data, acquired in both geometries during the *in situ* reduction and dry reforming experiments, were azimuthally averaged using the Fit2d software package from ESRF (Hammersley, 1997). After background subtraction, the data were scaled to interpolate intensities in

the overlapping angular region, calculating the quotient for the individual data points and using the mean to determine a scaling factor.

In order to transform the WAXS data, a silicon standard (NIST SRM 640c) was measured in the sample position before the experiments. From a fit of the silicon powder rings the camera position relative to the sample was determined and a matrix was generated relating each detector pixel to a certain angle. Subsequently, this matrix was applied for data binning of the 2D powder pattern of the Ni/$MgAl_2O_4$ catalyst.

For clarity, the scattered intensity I is plotted in all figures as a function of the scattering vector q, which is related to the scattering angle θ and X-ray wavelength, λ by $q = 4\pi \sin\theta / \lambda$ in units of $Å^{-1}$.

4. Data analysis

4.1 WAXS data analysis

Rietveld refinement of the WAXS was performed refining the lattice parameter and particle size broadening with the structural data for Ni (Owen *et al.* 1936), NiO (Schmahl *et al.* 1968), $MgAl_2O_4$ (Levi *et al.* 2003) and α-Al_2O_3 (Pillet *et al.* 2001) using the Rietica software (Hunter, 1998) and assuming the peak profiles as Voigt functions. The instrumental peak broadening was refined against data from a silicon reference (NIST SRM 640c).

4.2 SAXS data analysis

At sufficient low scattering vectors, $qR << 1$, the scattered intensity $I(q)$ can be approximated by Guinier's law

$$I(q) = G \exp\left(-\frac{q^2 R_{g,i}^2}{3}\right) \qquad G = N r_e^2 \Delta\rho_e^2 V^2 \qquad (2)$$

where R_g is the radius of gyration in terms of electron density of the particle in analogy to the radius of inertia in classical mechanics, N the number density of primary particles, r_e the classical electron

radius, $\Delta\rho_e$ the average electron density difference between particles and matrix and *V* the average particle volume. In case of spherical particle symmetry the radius of gyration is related to the radius by $R_g = \sqrt{5/3}R$ (Glatter & Kratky, 1982, Feigin & Svergun, 1987). At high scattering vectors, $qR >> 1$, the scattered intensity decays with power-law behaviour scaling with the average surface area *S* of the primary particles

$$I(q) = Bq^{-P} \qquad B = 2\pi N \Delta\rho_e^2 S \tag{3}$$

where *P* is the power law coefficient. For sharp and smooth interfaces $I(q)$ decays with $P = 4$, also known as Porod's law. Deviations from Porod's law can be ascribed to surface fractals, $3 < P_i < 4$, and diffuse interfaces $P > 4$ (Schmidt 1991, Beaucage *et al.* 1994).

The local scattering laws, described in equation (2) and (3), can be combined to approximate scattering curves of *n* non interrelated structural levels with the unified approach proposed by Beaucage *et al.* (1994 & 2004)

$$I(q) = \sum_{i=1}^{n} G_i \exp\left(-\frac{q^2 R_{g,i}^2}{3}\right) + B_i \left(\frac{q}{\left(\mathrm{erf}\left(qkR_{g,i}/\sqrt{6}\right)\right)^3}\right)^{-P_i} \tag{4}$$

where erf is an error function.

5 Results and discussion

5.1 Characterisation of the fresh catalyst sample

WAXS

Sample phases of the fresh catalyst were determined from an *ex situ* powder diffraction pattern acquired at room temperature in the standard X-ray powder diffractometer, see figure 2. The catalyst support was identified to consist of $MgAl_2O_4$ (space group #227: F d3mS) and α-Al_2O_3 (space group # 167: R-3c) and the catalyst particles as Ni (space group #225: Fm-3m) whereby Ni was observed to be partially oxidized to NiO (space group #225: Fm-3m).

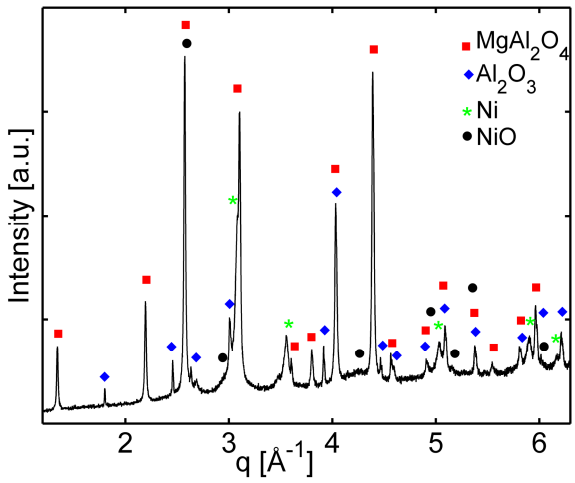

Figure 2: High resolute WAXS pattern of a fresh catalyst at room temperature

The phase content of elemental Ni in the fresh catalyst sample was identified by the appearance of the Ni (200)-, (220)-, (311)-, and (222)-peaks and by a shoulder for the (111)-reflex on the low *q*-side of the $MgAl_2O_4$ (400)-peak. The NiO content in the catalyst sample was clearly indicated by the well separated and broad NiO(220) reflex at $q = 4.16$ Å^{-1}, see figure 2.

The analysis of the *in situ* WAXS data, acquired with the CCD detector, was more complex than the analysis of pattern recorded with the standard X-ray powder diffractometer. The lower resolution of the CCD compared to the standard X-ray powder diffractometer in the present setup results in an overlapping of most of the interesting Ni- and NiO-reflections with reflections from the catalyst support and this complicated the analyses of the diffraction pattern. To overcome this problem we performed Rietveld refinement on a pattern recorded with a standard powder diffractometer setup and applied it to refine the patterns acquired with the CCD camera taking the different instrumental resolution refined with a Si standard in account. An example of Rietveld refinement from a WAXS acquired with the CCD camera of the fresh catalyst sample at 298 K is illustrated in figure 3.

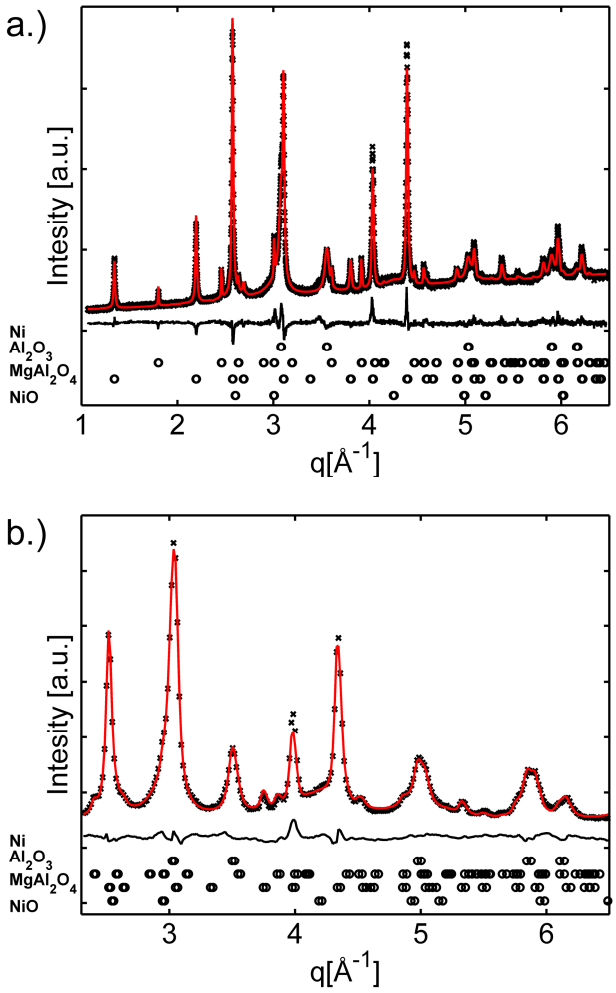

Figure 3: Rietveld refinement of a fresh Ni/spinel catalyst sample at 298 K from data acquired with the standard powder diffractometer setup (a) and the CCD detector (b). Refined sample phases (o) from top to bottom, Ni, alpha-Al_2O_3, $MgAl_2O_4$ and NiO

The experimentally observed and the simulated intensities show good agreement for both patterns recorded in a standard X-ray powder diffractometer and the with the CCD camera, the results refined from WAXS recorded at 298 K are shown in table 1.

	Phase	Std. Powd. Diff.	CCD
Crystallite size	$MgAl_2O_4$	41.4 nm	-*
	α-Al_2O_3	93.8 nm	-*
	Ni	13.1 nm	9.1 nm
	NiO	2.9 nm	2.1 nm
Weight fraction	$MgAl_2O_4$	67.2 %wt	66.5 % wt
	α-Al_2O_3	7.3 %wt	6.8 % wt
	Ni	13.9 %wt	11.3 %wt
	NiO	11.6 %wt	15.4 %wt

Table 1: Crystallite sizes from line broadening and weight fraction of a fresh catalyst sample at 298 K determined with Rietveld refinement of patterns recorded with the CCD camera and a standard powder diffractometer.
*) above resolution in this geometry

Crystallite sizes determined from Rietveld refinement of Ni and NiO from data acquired with both setups agree well, although the crystallite sizes refined from the patterns recorded with the CCD camera are about 30 % smaller compared to those observed with the standard X-ray powder diffractometer and this might be explained by differences in the instrumental resolution determined for both setups from a standard reference material. The phase quantities refined from patterns in both setup show also good agreement. Meaningful crystallite sizes for of $MgAl_2O_4$ and α-Al_2O_3 could only be refined from the WAXS acquired in the standard powder diffractometer setup since the maximum resolvable size with the CCD camera in the current setup is around 18 nm. Our primary interest in this study devotes to resolve the dynamical processes of the Ni- and NiO-particles *in situ* during sample annealing in a hydrogen atmosphere and alterations of the support particles in the measured time frame and temperature interval are not expected and therefore it is dispensable to determine the real crystallite sizes of $MgAl_2O_4$ and α-Al_2O_3.

TEM

TEM micrographs of the fresh catalyst sample were acquired to get an estimate of the particle shapes and diameters, see figure 4. Both Ni/NiO-catalyst- and $MgAl_2O_4$/α-Al_2O_3-support-particles show irregular shapes. Since catalyst- and support particle shapes were random and did not exhibit strong anisotropy we concluded that they can be well described with spherical symmetry for the SAXS data analysis.

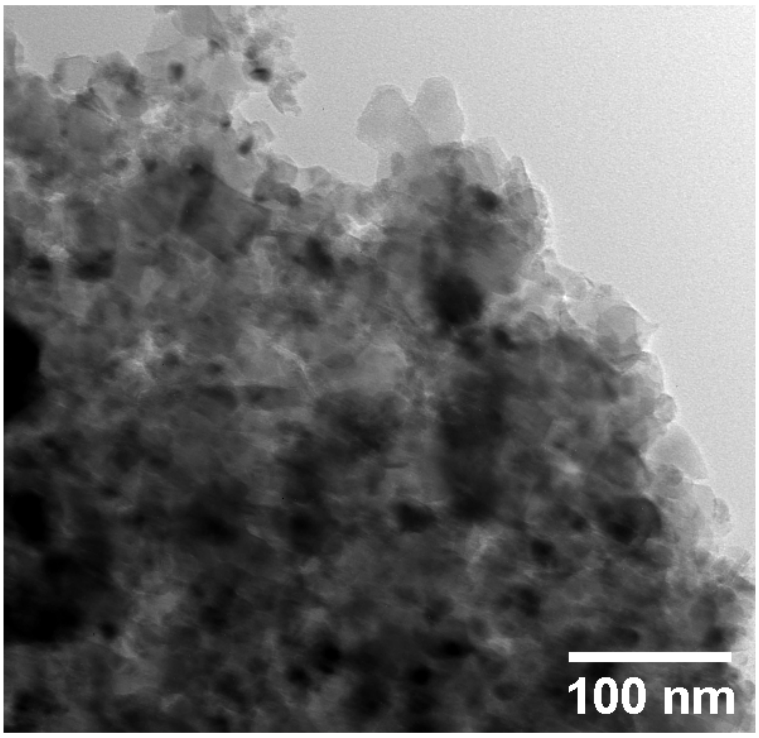

Figure 4: TEM of a fresh catalyst sample.

The (HR)TEM micrographs were utilized to achieve an estimate about the Ni/NiO particle size distribution (PSD). Both SAXS and WAXS provide information about the particle size in terms of a volume average. Therefore it is beneficial to evaluate the volume averaged diameter d_V from analysis of the TEM micrographs for comparison with results obtained with both scattering techniques. The volume averaged diameter can be evaluated with the following equation (Sehested *et al.* 2001, Borchert *et al.* 2005):

$$d_V = \frac{\sum n_i d_i^4}{\sum n_i d_i^3} \tag{5}$$

where n_i is the number of particles with the diameter d_i. The PSD of the Ni/NiO particles was evaluated from measuring 125 individual Ni/NiO particles in the TEM micrographs and can be described by a lognormal distribution

$$f(D) = \frac{1}{D\sigma\sqrt{2\pi}} \exp\left\{-\frac{[\ln(D) - \mu]^2}{2\sigma^2}\right\} \tag{6}$$

where D is the particle diameter, μ the mean and σ the standard deviation, expect for a few larger particles. From least square fitting using equation 5 we obtained μ = 1.67 and σ = 0.58 and respectively a mean diameter 6.3 ± 3.7 nm, see figure 5. The volume averaged diameter of the Ni/NiO particles, evaluated from the lognormal size distribution, is d_V = 17.6 nm.

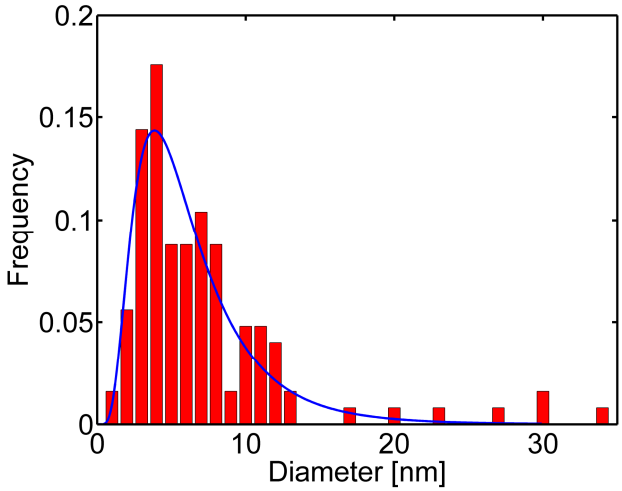

Figure 5: Particle size distribution of the Ni/NiO of a fresh 22 wt% Ni/$MgAl_2O_4$ catalyst sample determined from (HR)TEM (red bars) and fit with a lognormal probability density function (blue line).

SAXS

The transformed and overlapped SAXS data, acquired at 298 K, was well described by a unified function (equation 4) comprising four size regimes. The least square fit with contributions of the four different size regimes is illustrated in figure 6.

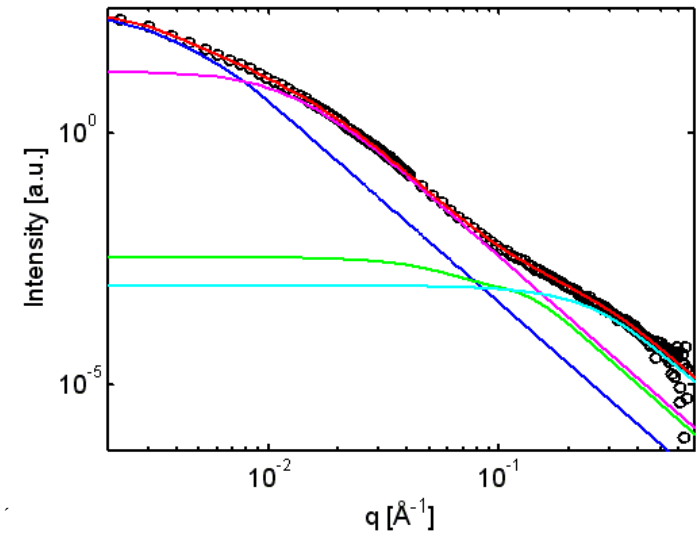

Figure 6: SAXS pattern of a fresh Ni/$MgAl_2O_4$ sample at 298 K and least square fit of equation 4 comprising (red) comprising 4 size regimes for the support- (blue and magenta) and Ni/NiO-catalyst particles (green) and the artefact (cyan).

The corresponding diameters d_{SAXS} for the four size regimes (symbolized by the blue, magenta, green and cyan curve) were determined from the fitted radius of gyration assuming spherical particle symmetry by $d = 2\,R = 2\sqrt{5/3}\,R_g$, the fitted R_g's and corresponding d_{SAXS} are compared with the crystallite diameters from WAXS d_{WAXS} in table 2. The very low contribution of the Ni/NiO- compared the $MgAl_2O_4$- and α-Al2O3-support-particles to the SAXS pattern can be explained by the V^2 dependence of the scattered intensity (see equation 2).

Regime	R_g [nm]	d_{SAXS} [nm]	d_{WAXS} [nm]	Compound
1	55.6	143.6	94	α-Al_2O_3
2	15.7	40.5	41	$MgAl_2O_4$
3	2.6	6.7	13 / 9[a]	Ni/NiO
4	0.7	1.8	-	-

Table 2: Fitted R_g from SAXS of a fresh Ni/$MgAl_2O_4$ catalyst at 298 using equation 4 and corresponding diameter compared with the particle diameter measured from TEM and the mean crystallite size obtained from WAXS.

[a] Acquired with the CCD camera

Comparing the mean particle diameter obtained from SAXS and TEM with the mean crystallite diameters refined from WAXS indicates that the first 3 size regimes might be attributed to scattering from α-Al_2O_3-, $MgAl_2O_4$- and Ni/NiO-particles. A mean crystallite diameter of 94 nm for

the α-Al_2O_3 was refined from WAXS and that matches with a diameter of 144 nm from SAXS for the first size regime assuming that the particles are not single crystalline. But the refined size for the first regime should be treated carefully since it is only described by a few data points. The particle size of 40.5 nm matches as well the crystallite size of 41 nm for the $MgAl_2O_4$ particles. It can be concluded that the first two size regimes are attributed to scattering from support particles.

The mean particle diameter d_{SAXS} = 6.7 nm for the third size regime is closest to the expected volume averaged diameter is d_V = 17.6 nm of the Ni/NiO particles. It was noted that d_{SAXS} of the Ni/NiO-particles was about 60 % smaller than d_V and that might be explained by their broad PSD. Scattering of the larger Ni particles contributes to the SAXS in the *q*-region where scattering of the support particles occurs and is therefore most probably fitted with the terms of the unified approach describing the scattering from the support.

The mean particle diameter of the Ni/NiO particles, directly measured from the TEM micrographs of 6.3 nm, matches well with the mean particle size of the third size regime. However, since SAXS provides information about the particle size in terms of a volume average d_{SAXS} and d_V should be compared. It was noted that d_{SAXS} of the Ni/NiO-particles was about 60 % smaller than d_V and that might be explained by their broad PSD, see figure 5. Scattering of the larger Ni particles contributes to the SAXS pattern in a *q*-region where scattering of the support particles is observed and is therefore most probably fitted with the terms of the unified approach describing the scattering from the support. Small variations of d_{SAXS} might also be explained by a different atomic form factor of Ni using Cu K-alpha (long geometry) and Mo K-alpha radiation (short geometry). This will introduce an error by overlapping the data acquired both geometries and consequently also influence the fitted parameter for the Ni/NiO size regime.

The diamtere of the Ni crystallites from Rietveld refinement of data acquired in the standard powder diffractometer setup of 13 nm and 9.1 nm with the CCD agrees well with d_V = 17.6 nm from TEM considering that the Ni particles are partially oxidized and not necessarily single crystalline. The refined crystallite diameters are close to the reported value of 12.0 nm determined from size broadening of the Ni(200) reflection using the Scherrer equation by Sehested *et al.* (2001) from a similar catalyst. However, even if we cannot resolve the absolute particle diameters of Ni/NiO from the SAXS, our main interest here is to follow the dynamical changes of the catalyst

operating under pressure and temperature conditions that are comparable to large scale processes in the chemical industry, and to follow those dynamics *in situ*. The mean Ni/NiO-particle diameter, obtained from SAXS, is therefore more an arbitrary parameter to describe those dynamics, than an absolute number.

The fourth size regime at highest *q* seems to be an artefact and is most probably related to an X-ray wavelengths dependent response of the 2D SAXS gas detector since it was only present during experiments using Mo K-alpha radiation in short geometry.

5.2 *In situ* reduction

The initiation of the reduction could be visually observed in the WAXS pattern, a decrease in relative intensity of the NiO (220) reflection and an increase of the intensity of the Ni peaks was noted in a temperature interval between 373 and 473 K. The first WAXS pattern at 473 K and the fresh catalyst sample at 298 K, combined with the simulated contributions of the Ni- and NiO-phase using the parameters determined from Rietveld refinement, are illustrated in figure 7. Kinetic studies of pure NiO revealed that the reduction occurs at temperatures as low as 428 K (Parravano 1957) and this agrees with the temperature interval where the reduction initiates in our experiments.

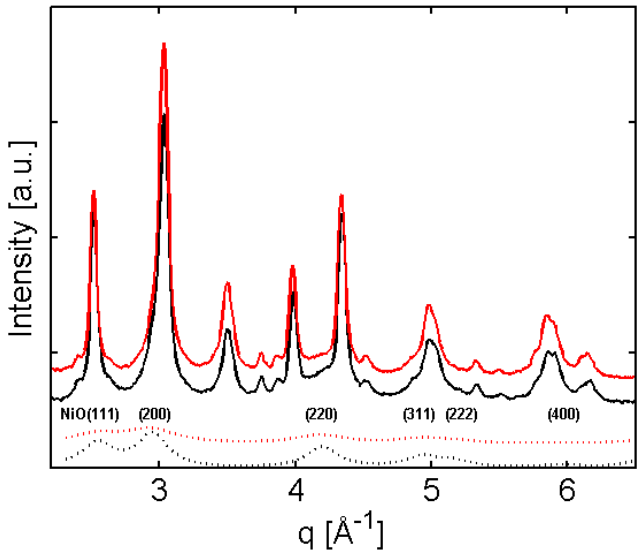

Figure 7: WAXS pattern of a fresh catalyst at 298 K (— black) and after initiation of the reduction at 473 K (— red) and the simulated contributions of the NiO phase at 298 K (···· black) and 473 K (···· red)

In the same temperature interval we observed first alterations of the SAXS in a *q*-range where the Ni/NiO-particles contribute to the pattern (see figure 8). Continuous changes in the SAXS were observed up to highest sample temperatures of 873 K.

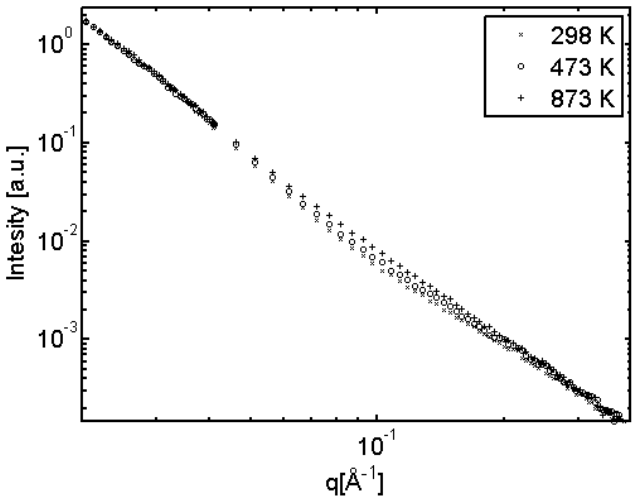

Figure 8: SAXS data at intermediate *q* at 298 K (x), first pattern at 473 K (o) and last pattern at 873 K (+)

Rietveld refinement was performed on all acquired WAXS patterns during the *in situ* reduction, the relevant sample parameters were refined at 298 K. At higher temperatures only the phase scales of all compounds, background, lattice parameter of $MgAl_2O_4$ and Ni and the size broadening of Ni and NiO were refined. Lattice parameter of α-Al_2O_3 and NiO were fixed during the refinement to obtain a stable fit. Refinement of the lattice parameters of α-Al_2O_3 or NiO was observed to be unstable due to the minor phase contribution of α-Al_2O_3 and the small crystallite size of NiO resulting yielding very broad peaks. The influence of the sample temperature on the lattice parameter was corrected by taking the linear thermal expansion for α-Al_2O_3 (6.5×10^{-6} K^{-1}) and NiO (14.1×10^{-6} K^{-1}) in account. The sample phases were quantified from Rietveld refinement. Figure 9 illustrates the molar Ni- and NiO-content as a function of time and sample temperature.

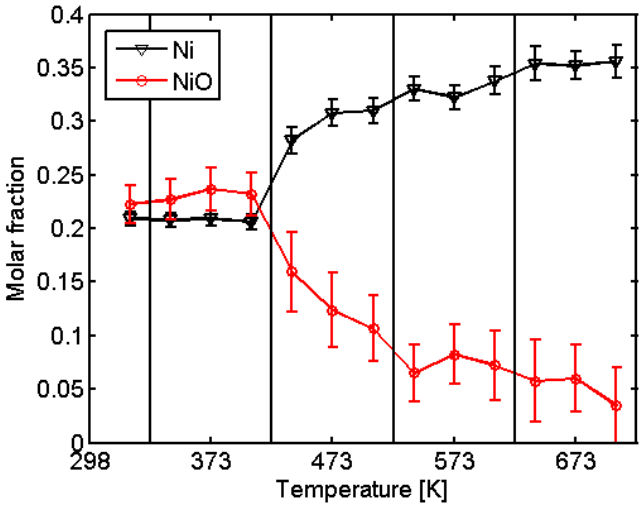

Figure 9: Molar fraction of Ni (o) and NiO(v) vs. sample temperature determined from Rietveld Refinement, the three data points at each temperature above 298 K represent the results of the three acquired WAXS pattern acquired with a frame of 1800 s in chronological order.

Quantitative phase analysis suggests that the reduction of NiO is a function of both sample temperatures and time and this is consistent with observations reported in the literature (Parravano 1957, Richardson *et al.* 2003, Rodriguez *et al.* 2002). Below sample temperatures 473 K the Ni and NiO fraction seems to be unaltered, small fluctuations of the Ni and NiO fraction can be explained by uncertainties of the Rietveld refinement. An increase of the molar Ni fraction and respectively a decrease of the molar NiO fraction were noted at temperatures above 473 K indicating the onset of the reduction. To verify the significance of the refined phase quantification we summated the molar fractions of Ni and NiO from each refined pattern because the sum of both fractions should remain constant. Overall a decrease of the summed molar fractions from 0.43 at 298 K to 0.39 at 873K was noted. This would correspond to a concentration of w(Ni) = 23.7 % ± 1.3 % at the start and w(Ni) = 21.2 ± 0.5 % at the end of the experiment, if all NiO is assumed to be Ni. The results of the quantification from Rietveld refinement are in good agreement with the actual concentration of the catalyst of w(Ni) = 22 %. Deviations of the determined molar fractions during the reduction can be most properly be related to too small refined NiO crystallite sizes. Anyway, the quality of the refinement of the NiO crystallite sizes was limited due to strong overlapping of the broad NiO reflections with those of other sample phases and their low intensity (see figure 7).

Figure 10 illustrates the refined Ni lattice parameter as a function of the sample temperature during sample heating in hydrogen.

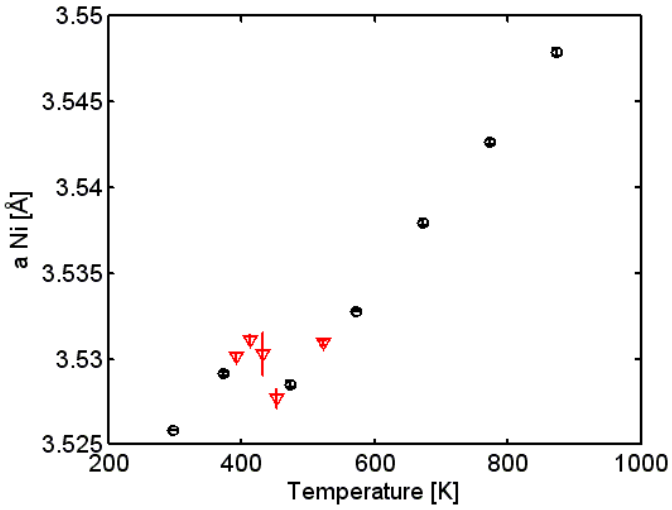

Figure 10: Ni lattice parameter obtained from Rietveld refinement during a heating experiment in steps of 100 K (o) and an additionally acquired data at intermediate temperatures (v) on another sample to resolve the decrease between 373 and 473 K.

During heating experiments in hydrogen a linear increase of the Ni lattice parameter was observed at temperatures below 373 K and above 473 K. This can be related to thermal expansion of the Ni crystal lattice. However, with initiation of the reduction, in a temperature interval of 373 - 473 K, a decrease of the Ni lattice parameter was noted. An additional experiment with the same catalyst sample was performed at temperatures of 393 K, 413 K 433 K 453 K and 533 K to resolve the interval where the lattice parameter changes and it was localized at temperatures between 413 and 453 K. Heating experiments performed in Helium did not show a decrease of the Ni lattice parameter at any temperature and we conclude that it is purely related to the initiation of the reduction.

The decrease of the lattice parameter with initiation of the reduction can be explained by the following. Ni nanoparticles are observed to form a passivating NiO surface layer of around 2 nm, irrespectively of their grain size (Seto *et al.* 2005, Phung *et al.* 2003, Sakiyama *et al.* 2004). Phase identification (see figure 2) of a fresh catalyst sample and the good agreement of the simulated and experimental data during the Rietveld refinement (see figure 3) revealing that Ni and NiO are both in the cubic phase (space group #225: Fm-3m). The lattice parameter of Ni is with 3.5243 Å (Owen *et al.* 1936) only 19 % smaller than the lattice parameter of NiO with 4.1771 Å (Schmahl *et al.* 1968). On account of this the lattice parameter of the Ni core relaxes due to interface stress between metallic core and the oxidic shell (Rellinghaus *et al.* 2001); this effect was reported to be particle size dependent, with decreasing particle sizes increasing Ni lattice parameters were noted

(Rellinghaus *et al.* 2001, Duan *et al.* 2004). The decrease of the lattice parameter during the *in situ* reduction of experiments was observed in a temperature interval where the reduction initiates, indicated by a decreasing intensity of the NiO(220)-reflex in the WAXS pattern. Therefore we conclude that the decrease of the Ni lattice parameter can be directly related to the reduction of the NiO shell, whereby stress due to the lattice mismatch disappears.

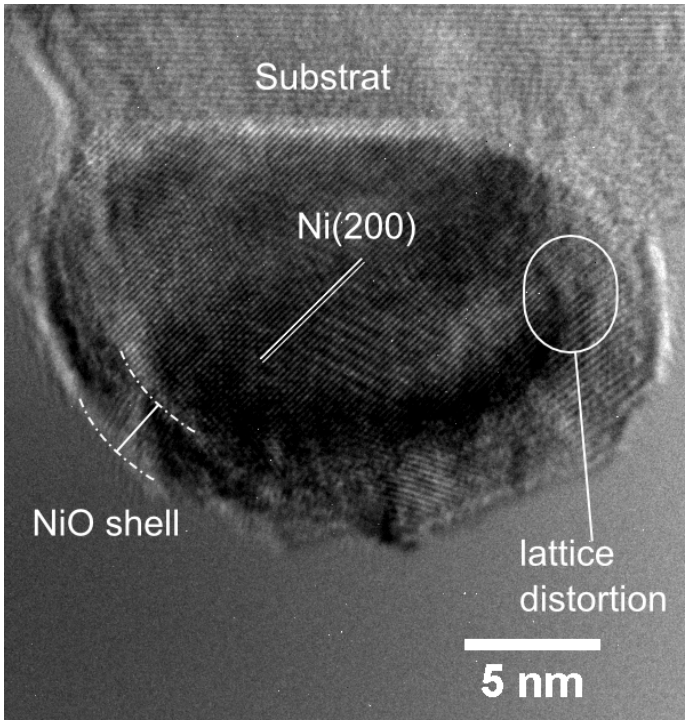

Figure 11: Ni/NiO core shell particle on $MgAl_2O_4$-support

Ni/NiO core-shell particles were also observed in HRTEM micrographs, a Ni/NiO core-shell particle on $MgAl_2O_4$ substrate shown in figure 11. The Ni core shows characteristic distances of the lattice fringes for Ni(200) planes. No evidence of grain boundaries from crystallite domains were noted indicating that this observed core consists of single crystalline Ni. However, other Ni particles have been observed to be polycrystalline and this is consistent with observations of Sehested *et al.* (2001). Lattice distortions of the Ni lattice were noted close to the Ni/NiO interface indicating stress due to the lattice mismatch of Ni and NiO. In contrast to the observed core, the shell seems to be polycrystalline, several domains with fringes comparable to the NiO(111) and NiO(200) plane were observed.

The transformed SAXS patterns, acquired during the reduction, were analysed by least square fitting of equation 4. Only the fit parameters of the size regime describing small angle scattering from the Ni/NiO-particles were left free, all other size regimes were fixed since we did not expect any reaction or sintering of the support under the conditions. The refined Ni-particle diameter at all temperatures is shown in figure 12.

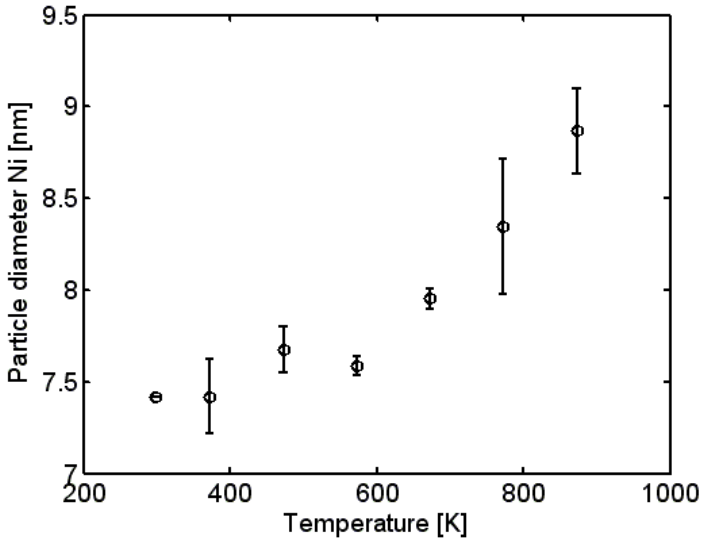

Figure 12: Evolution of the Ni particle size from SAXS during the *in situ* reduction, the error bars show the standard deviation of diameter. Only one SAXS pattern was acquired at 298 K and therefore the diameter has no errorbar.

Overall, the Ni particle diameter increases at temperatures above 373 K. It was reported that growth of unsupported Ni/NiO core shell particles only occurs after reduction of the protective NiO shell (Setthi and Thölén, 1994). The reduction of the NiO shell, studied herein, was observed from in a temperature interval from 413 - 453 K from WAXS. The growth of supported Ni particles occurs predominately by a migration coalescence-mechanism (Richardson and Crump ,1979, Sehested *et al.*, 2001), because the activation energy for the migration of Ni particles is smaller than for the evaporation of atoms, which would facilitate Ostwald ripening (Richardson and Crump, 1979). The mobility of the Ni particles on the support surface is a function the temperature and their size, smaller particles show a higher mobility than larger ones (Richardson and Crump, 1979), therefore the fraction of smaller particles diminish during the sintering process. The increasing rate of particle growth, at temperatures above 573 K, might reflect the temperature dependence of the particle mobility on the catalyst surface.

The Ni/NiO particle diameter increases slightly at temperatures above 373 K, however, a slight decrease of around 0.1 nm was observed in a temperature interval between 473 and 573 K. At temperatures above 573 K the Ni/NiO particle diameter increases monotonic. The slight decrease in the temperature interval between 473 K and 573 K can be related to the reduction. Ni has with 8.9 g cm^{-3} a larger mass density than NiO with 7.5 g cm^{-3}, thus the reduced Ni particles will have a smaller diameter compared to the initial Ni/NiO particles, if the number of atoms in the Ni-cluster remains constant. However, the decrease is rather small and inside the limit of accuracy of the fit, since the contributions of Ni/NiO to the SAXS are small compared to those of the support.

The mean crystallite diameter determined from Rietveld refinement of the WAXS data was observed to be unaltered during the complete experiment. The reason for this might be explained in the following: the crystallite sizes obtained by Rietveld refinement are determined by application of the Scherrer equation. Particle sizes of the sample phases are calculated from the full width half maxima (FWHM's) of the fitted peak profile functions taking the instrumental broadening in account. Evaluations of the size parameter from the FWHM neglect any effect of particle size distribution. However, the crystallites of heterogeneous catalysts are normally polydisperse and the peak profile of a reflection for such a distribution would have a sharper maximum and a longer tail compared to the profile of monodisperse crystallites (Langford & Wilson 1978). Evaluation of the size parameter from the FWHM takes the tail resulting from the small particles scarcely in account (Bergeret & Gallezot 2008) and display therefore consequently the mean size of the larger crystallites. Ni crystallite growth will mainly occur by coalescence of the small Ni particles, because of their high mobility compared to the larger ones. The increase of the Ni crystallite size, by sintering of smaller particles with larger ones, if sintering is assumed to result single crystalline particles, is small because their comparable small volume. Therefore seemed the crystallite size of Ni during the reduction experiments most probably unaltered.

6. Conclusion

In this study, combined SAXS/WAXS was utilised to follow the dynamical changes of a 22 wt% Ni/$MgAl_2O_4$ catalyst during reduction in pure hydrogen. Quantification of the Ni and NiO phases reveal that the reduction initiates in a temperature interval from 373 - 473 K and completes at temperatures above 673 K. A decrease of Ni lattice parameter in a temperature range from 413 -

453 K was observed and indicates that the reduction of the NiO shell. The decrease of the Ni lattice parameter can be explained by contraction of the Ni lattice due to release of interfacial stress during the reduction of the NiO shell. HRTEM confirmed the presence of Ni/NiO core shell particles in the initial catalyst sample. Ni-particle growths was observed after reduction of the NiO shell.

Acknowledgements

We thank Steen Bang, Ove Rasmussen, Torben Kjær and Jens Borchsenius for maintenance of the equipment and technical support during the implementation of the *in situ* laboratory setup, Hjalte Sylvest Jacobsen for improvement of the WAXS 1D data transformation, Henning Engelbrecht for guidance regarding LabVIEW® and data acquisition during the implementation of the sample gas system and the Copenhagen Graduate School for Nanoscience and Nanotechnology (C:O:N:T) and Haldor Topsøe A/S for financial support.
CINF is funded by the Danish National Research Foundation.

References

Aguinaga, A., Montes, M. (1992) *Appl. Catal. A* **90** 131 - 144

Andreasen, J. W., Rasmussen, O., Feidenhans'l, R., Rasmussen, F. B., Christensen, R. Molenbroek, A. M., Goerigk, G. (2003). *J. Appl. Chryst.* **36**, 812-813

Bergeret, G., Gallezot, P. (2008) *Particle Size and Dispersion Measurements - Handbook of Heterogeneous Catalysis* 738 - 765

Borowieki, T. (1982) *Appl. Catal.* **4** 223 - 231

Chen, D., Christensen, K. O., Ochoa-Fernández, E., Yu, Z., Tøtdal, B., Latorre, N., Monzón, A., Holmen, A. (2005) *J. Catal.* 82 - 96

Duan, Y., Li, J. (2004) *Mater. Chem. Phys.* **87** 452 - 454

Gabriel, F., Dauvergne F., Rosenbaum, G. (1978) *Nuclear Instruments and Methods* **152**, 191 - 194

Gadalla, A. M., Bower, B. (1988) *Chem. Eng. Sci.* **1988** 3049 - 3062

Guo, J., Lou, H., Zhao, H., Chai, D., Zheng, X (2004) *Appl. Catal. A* **273** 75 - 82

Hammersley, A. P. (1997). Internal Report ESRF97HA02T. ESRF, Grenoble, France.

Hunter B. (1998). *Int. Union Cryst. Newsletter* **20**, 21

Kehres, J., Andreasen, J. W., Krebs, F. C., Molenbroek, A. M., Chorkendorff, I., Vegge, T. *J. Appl. Cryst.* **43** 1400 - 1408

Langford, J. I., Wilson, A. J. C. (1978) *J. Appl. Cryst.* **11** 102 - 113

Levy, D., Pavese, A., Hanfland, M. (2003) *Am. Miner.* **88**, 93 - 98

Noweck, K. and Grafahrend, W (2006) *Fatty Alcohols* Ullmann's Encyclopedia of Industrial Chemistry - online edition

Owen, E. A., Yates, E. L. (1936) *Philos. Mag.* **21**, 809 - 819

Parravano, G. (1952) *J. Am. Chem. Soc.* **74** 1094 - 1198

Phung, X., Groza, J., Stach, E. A., Williams, L. N., Ritchey S. B. (2003) *Mater.Sci.Eng.A* **359** 261 - 268

Pillet, S. Souhassou, M., Lecmonte, C., Schwarz, K., Blaha, K., Rerat, M., Lichanot, A., Roversi, P. (2001) *Acta Cryst. A* **57**, 290 - 303

Rellinghaus, B., Stappert, S., Wassermann, E. F., Sauer, H., Spliethoff, B. (2001) *Eur. Phys. J. D.* **16** 249 - 252

Richardson, J. T., Crump, J. G. (1979) *J. Catal.* **57** 417 - 425

Richardson, J. T., Scates, R., Twigg, M. V. (2003) *Appl. Catal. A* **246** 137 - 150

Richardson, J. T., Twigg, M. V. (1998) *Appl. Catal. A* **167** 57 - 64

Rodriguez, J. A., Hanson, J. C., Frenkel, I., Kim, J. Y., Pérez, M. (2001) *J. Am. Chem. Soc.* **124** 346 - 354

Rostrup-Nielsen, J. R., Bak Hansen, J.-H. (1993) *J. Catal.* **144** 38-49

Sakiyama, K., Koga, K., Seto, T., Hirsawa, M., Orii, T. (2004) *J. Phys. Chem. B* **108** 523 - 529

Schmal N. G., Eikerling, G. F. (1968) *Z. phys. Chem.* **62**, 268 - 279

Sehested, J., Carlsson, A., Janssens, T. V. W., Hansen, P. L. Datye, A. K. (2001) *J. Catal.* **197** 200 - 209

Setthi, S. R., Thölén, A. R. (1994) *Nanostruc. Mater.* **4** 903 - 913

Seto, T, Akinaga, H., Takano, F., Koga, K. Orii, T., Hirasawa, M. (2005) *Phys. Chem. B.* **109** 13403 - 13405

Wei, J. M., Iglesia, E. (2004) *J. Catal.* **224** 370 - 383

Zieliński, J. (1982) *J. Catal.* 157 - 163

Paper III

will be submitted to:

Journal of Physical Chemistry C

Dynamical properties of a Ru/spinel catalyst during reduction and dry methane reforming

Jan Kehres [a], Jon Geest Jakobsen [b], Jens Wenzel Andreasen [c], Haihua Liu [a] , Alfons Molenbroek [d],Ib Chorkendorff [e], Tejs Vegge[a]*

[a] Materials Research Division, Risø National Laboratory for Sustainable Energy, Technical University of Denmark, Building 228, P.O. Box 49, DK-4000 Roskilde, Denmark, [b] Syngas Engineering R&D, Nymøllevej 55, DK-2800 Lyngby, Denmark, [c] Solar Energy Programme, Risø National Laboratory for Sustainable Energy, Technical University of Denmark, Building 111, P.O. Box 49, DK-4000 Roskilde, [d] Haldor Topsøe A/S, Physical Analytical Department, Nymøllevej 55, DK-2800 Lyngby, Denmark, [e] Center for Individual Nanoparticle Functionality, Department of Physics, Technical University of Denmark, Building 312, , Fysikvej, DK-2800 Lyngby, Denmark

E-mail: jewa@risoe.dtu.dk

Keywords: Ru/spinel, reduction, methane reforming, in situ, combined SAXS/WAXS

Abstract

Combined *in situ* small and wide angle X-ray scattering (SAXS/WAXS) studies were performed in a recently developed laboratory setup to investigate the dynamical properties of a ruthenium/spinel ($Ru/MgAl_2O_4$) catalyst, w(Ru) = 4 wt%, during the reduction and subsequent dry methane reforming. The fresh catalyst sample was characterized with simultaneous SAXS/WAXS and transmission electron microscopy. The Ru particles in the fresh catalyst sample were found to be partially oxidized with high resolution transmission electron microscopy (HRTEM), indicating a coexistence of pure Ru and RuO_2 nanoparticles. Reduction in hydrogen occurred at a temperature below 393 K as indicated by an increase in scattered intensity at q-values, where the Ru-phase contributes to the WAXS- and in a q-region where Ru/RuO_2-particles contribute to the SAXS-pattern. The mean particle diameter refined from SAXS of the size regime attributed to scattering from Ru/RuO_2-particles decreases slightly from 3.4 to 3.3 nm during the reduction. Dry methane

reforming experiments were performed in a temperature interval from 723 - 1023 K by and applying a gas mixture of carbon dioxide and methane in molar ratio of 3:1. An increase of the mean Ru-particle diameter of around 0.1 nm and a decrease of the surface to volume ratio of about 4 % was observed, revealing the high sintering stability of the $Ru/MgAl_2O_4$ catalyst. The catalyst performance was monitored with a quadrupole mass spectrometer (QMS) and stable methane conversion levels were observed during the *in situ* dry methane reforming and the catalyst did not show any significant deactivation during a subsequent 20 h experiment at 1023 K. The hydrogen / carbon monoxide ratio was noted to increase from 0.38 to 0.69 during the sample heating from 723 to 1023 K.

1. Introduction

Methane reforming with carbon dioxide yields synthesis gas with a molar ratio of $H_2/CO = 1$ and is an ideal feedstock for various large scale processes such as Fischer Tropsch, hydroformylation and synthesis of methanol (Gadalla and Bower 1988, Wörner *et al.* 1998, Holm-Larsen 2001).

$$CH_4 + CO_2 \leftrightarrow 2\ CO + 2\ H_2 \qquad \Delta H = 247\ kJ\ mol^{-1} \qquad (1)$$

However, the obtained H_2/CO ratio in practice is less than one because H_2, produced by dry methane reforming, reacts with CO_2 in the reverse water gas shift reaction (RWGS) to form water and carbon monoxide (Safariamin *et al.* 2009, [b]Bradford *et al.* 1999, Bitter *et al.* 1997).

$$CO_2 + H_2 \leftrightarrow CO + H_2O \qquad \Delta H = 41\ kJ\ mol^{-1} \qquad (2)$$

H_2/CO ratios close to one are only obtained at high temperatures where water produced by the RWGS reacts in the steam reforming reaction to yield CO and H_2 (Bitter *et al.* 1997).

$$CO + H_2O \leftrightarrow CO_2 + H_2 \qquad \Delta H = 207\ kJ\ mol^{-1} \qquad (3)$$

Many transition metals such as Ni, Ru, Pd, Ir and Pt ([a]Bradford *et al.* 1999, Rostrup-Nielsen *et al.* 1993, Rezaei *et al.* 2006, Mark and Maier, 1996) have been found to show good catalytic activity for the methane reforming reaction. Even though Ni based catalysts are commercially more

interesting (Guo *et al.* 2004), they have a main drawback in high carbon formation compared to most of the active noble metals (Rostrup-Nielsen *et al.* 1993). The doping of Ni catalysts with small amounts of Ru was reported to suppress carbon formation (Jeong *et al.* 2006, Crisafulli *et al.* 1999).

Ru and Rh were reported to be the most active catalysts for the dry reforming reaction (Rostrup-Nielsen *et al.* 1993, Rezaei *et al.* 2006, Qin *et al.* 1994) and this was confirmed first principle calculations (Jones *et al.* 2008). Besides the choice of the metal, strong influence of the support on the activities were reported ([b]Bradford and Vannice, 1998, Ferreira-Aparico *et al.* 1998, Ferreira-Aparico *et al.* 2000), but the influence of the support in terms of activity for the dry methane reforming reaction is unclear. Bradford and Vannice reported a decrease in activity in connection with the support in the order of $Ru/TiO_2 > \gamma\text{-}Al_2O_3 >> C$ and ascribed the higher activity of TiO_2 supported Ru to the presence of a $Ru\text{-}TiO^{n+}O_x$ - sites. Ferreira-Appricio *et al.* (2000) observed higher activities of $\gamma\text{-}Al_2O_3$- compared to SiO_2 supported Ru and attributed it to a CO_2 activation by the surface OH-groups. However, Wei and Iglesia (2004) reported from studies of Ru on ZrO_2 and $\gamma\text{-}Al_2O_3$ that the reactivity of Ru based catalysts is unaffected by the support and solely correlated with the dispersion of the metal particles and related higher activities to a larger number of surface atoms with low coordination. A nearly linear correlation of the metal dispersion with the activity was also reported for steam reforming of methane by Jones *et al.* (2008). Dry methane reforming studies, conducted by Mark and Meier (1996), of Rh and Ir catalysts on standard supports such as SiO_2, TiO_2, ZrO_2 and α- and $\gamma\text{-}Al_2O_3$ did not show any effect of the support material on the activity as well, but in contrast to observations by Wei and Iglesia the activity was reported to be independent of the nanoparticle dispersion and exclusively related to the accessible metal surface area. Howsoever, the support material affects the dispersion (Wei and Iglesia 2004) during the catalyst preparation and stabilizes the nanoparticles during catalyst use (Mark and Meier, 1996).

Irrespective of the assumption whether solely the dispersion or the accessible metal surface area affects the activity and which influence the support might have on the reaction pathway, it is essential that highly active and long term stable dry methane reforming catalysts exhibits, besides a low affinity for carbon formation, only a marginal tendency of particle growths to retain the nanostructure.

This paper is focused on the dynamical changes of a 4 wt% $Ru/MgAl_2O_4$ catalyst during reduction and subsequent dry methane reforming to understand changes such as phase transitions and particle growth due to sintering in connection with the gas atmosphere and sample temperature. A suitable technique to resolve these changes is combined *in situ* small and wide angle X-ray scattering , small angle X-ray scattering (SAXS) to follow the particle growth and wide angle X-ray scattering (WAXS) to detect phase transitions and crystalline growth. Additional, online mass spectroscopy of the product gas enables relating these changes to variations in the methane conversion level.

2. Experiments and methods

2.1 Experimental setup

Simultaneous *in situ* SAXS/WAXS was performed using a laboratory pinhole camera setup with sample to SAXS-detector distances of 1494 (short geometry) and 4679 (long geometry) mm covering a *q*-range of $0.002 < q < 0.45$ Å^{-1} by using Mo K-alpha $\lambda = 0.7107$ Å in the short and Cu K-alpha radiation $\lambda = 1.5418$ Å in the long geometry. SAXS patterns were acquired with a 2D "Gabriel" type gas detector (Gabriel *et al.*, 1978) and WAXS patterns with an image intensified Gemsatar 125 CCD camera mounted 30° off-axis to the direct beam to avoid shadowing the SAXS. The 125 mm CCD scintillator screen permits in that setup the resolution of a *q*-range from 2 – 6.5 Å^{-1} by using Mo K-alpha radiation. The instrumental resolution of the CCD camera was determined from powder diffraction of a silicon standard (NIST SRM 640c) and is on the order of $\Delta q / q = 4 \cdot 10^{-3}$.

Heating experiments were performed in a special designed *in situ* cell, which is described in detail by Andreasen *et al.* (2003). The cell was adapted to the laboratory pinhole camera with modified X-ray windows to cover the wide angle scattering and a newly designed heater permitting sample temperatures in an interval of 298 - 1073 K (Kehres *et al.*2010). Constant gas flows were applied to the sample using a gas system including a mass flow controller. The product gas was monitored by an online quadrupole mass spectrometer (Balzers ThermoStar GSD 300) on the outlet of the *in situ* cell.

2.2 Transmission electron microscopy

High resolution transmission electron microscopy (HRTEM) micrographs were acquired with a JEOL 3000 F microscope with acceleration voltage of 300 kV, before and after the experiment. The 4 wt% $Ru/MgAl_2O_4$ catalyst was dispersed in ethanol with a dilution of 1:1500 using ultrasonic treatment. 10 µl of this dispersion was coated on a 400 mesh holey carbon grid.

2.3 Catalyst preparation

A 4 wt% $Ru/MgAl_2O_4$ catalyst was prepared by incipient wetness impregnation of $MgAl_2O_4$ (45 m^2 g^{-1}) support with a 8.1 wt% $Ru(NO)(NO_3)$ aqueous solution. The sample was dried in air at 353 K for 4 h. Subsequently, the catalyst was reduced in pure hydrogen at 873 K at a gas pressure of 1 bar for 4 h and afterwards aged for 225 h at 1103 K in a H_2O / H_2 (1:1) at 31 bar to achieve a stable catalyst (Jakobsen *et al.* 2010).

2.4 Reduction and dry methane reforming experiments

The 4 wt% $Ru/MgAl_2O_4$ catalyst sample of approximately 10 mm length, was inserted in a 0.7 mm quartz capillary, embedded between two glass wool plugs and mounted gas tight between two Swagelok® fittings using graphite ferrules. The *in situ* reduction experiments were performed in a constant gas flow of 2 ml min^{-1} hydrogen (alphagaz 1, Air Liquide, >99.999 vol%) at standard temperature and pressure (STP). Three combined SAXS/WAXS patterns were acquired at 298 K, 393 K and in an interval from 473 - 873 K in steps of 100 K. Subsequently, the reduced samples were cooled in hydrogen to 723 K and a constant flow of 6 ml min^{-1} pre mixed gas composed of 25 vol% CH_4, 74 vol% CO_2 and 1 %vol Ar was applied to perform the dry methane reforming experiments; Ar was used as an internal standard to trace fluctuations of the sensitivity changes from the quadrupole mass analyzer due to variations of the pressure. The sample was heated in an interval from 723 to 1023 K, afterwards cooled down to 723 K and heated again to 1023 K. The temperature was increased and decreased gradually in steps of 50 K during these experiments. At

each temperature three combined SAXS/WAXS patterns were acquired to follow the dynamical properties of the catalyst at different conversion levels.

3. Data transformation

The 2D SAXS data, acquired in both geometries during the *in situ* reduction and dry reforming experiments, were azimuthally averaged using the Fit2d software package from ESRF (Hammersley, 1997). After background subtraction, the data was scaled to interpolate intensities in the overlapping angular region, calculating the quotient for the individual data points and using the mean to determine a scaling factor.

In order to transform the WAXS data, a silicon standard (NIST SRM 640c) was measured before the experiment in the sample position. From a fit of the silicon powder rings, the camera position relative to the sample was determined and a matrix was generated relating each detector pixel to a certain scattering angle. Subsequently, this matrix was applied for data binning of the 2D powder pattern of the $Ru/MgAl_2O_4$ catalyst.

For clarity, the scattered intensity I is plotted in all figures as a function of the scattering vector q, which is related to the scattering angle θ and X-ray wavelength, λ by $q = 4\pi \sin\theta / \lambda$ in units of $Å^{-1}$.

4. SAXS data analysis

At sufficient low scattering vectors, $qR << 1$, the scattered intensity $I(q)$ can be approximated by Guinier's law (Glatter & Kratky, 1982)

$$I(q) = G \exp\left(-\frac{q^2 R_{g,i}^2}{3} \right) \qquad G = N r_e^2 \Delta\rho_e^2 V^2 \qquad (4)$$

where R_g is the radius of gyration in terms of electron density of the particle in analogy to the radius of inertia in classical mechanics, N the number density of primary particles, r_e the classical electron radius, $\Delta\rho_e$ the average electron density difference between particles and matrix, and V the average particle volume. In case of spherically symmetric particles, the radius of gyration is related to the

radius by $R_g = \sqrt{5/3}R$ (Glatter & Kratky, 1982, Feigin & Svergun, 1987). At high scattering vectors, $qR >> 1$, the scattered intensity decays with power law behaviour scaling with the average surface area S of the primary particles

$$I(q) = Bq^{-P} \qquad B = 2\pi N \Delta\rho_e^2 S \tag{5}$$

where P is the power law coefficient. For sharp and smooth interfaces $I(q)$ decays with $P = 4$, also known as Porod's law (Glatter & Kratky, 1982). Deviations from Porod's law can be ascribed to surface fractals, $3 < P_i < 4$, diffuse interfaces, $P > 4$, and mass fractals, $1 < P < 3$ (Schmidt 1992, Beaucage *et al.* 1994).

The local scattering laws, described in equation (4) and (5), can be combined to approximate scattering curves of n non interrelated structural levels with the unified approach proposed by Beaucage *et al.* (1994 & 2004)

$$I(q) = \sum_{i=1}^{n} G_i \exp\left(-\frac{q^2 R_{g,i}^2}{3}\right) + B_i \left(\frac{q}{\left(\mathrm{erf}\left(qkR_{g,i}/\sqrt{6}\right)\right)^3}\right)^{-P_i} \tag{6}$$

where erf is an error function. Under the assumption that the particles are spherical and their size is log-normal distributed, it is possible to obtain the two parameters, the median radius m and the standard deviation σ, to describe the distribution directly from the three fit parameters of unified approach (Beaucage *et al.* 2004) by

$$\sigma = \sqrt{\left\{\frac{\ln\left[B(R_g^2)^2/(1.62G)\right]}{12}\right\}} \tag{7}$$

and

$$m = \sqrt{\frac{5}{3}\frac{R_g^2}{\exp(14\sigma^2)}} \tag{8}$$

The invariant *Q*, a quantity independent of particle shape and size distribution, can be obtained by integration of the scattered intensity over the complete *q*-range for a particular structure (Glatter & Kratky, 1982, Beaucage *et al.* 2004).

$$Q = \int_0^\infty q^2 I(q) dq = 2\pi^2 N \Delta\rho^2 V \tag{9}$$

The particle shape independent average surface to volume ratio can be estimated from the ratio of the Porod prefactor *B* and the invariant (Beaucage *et al.* 2004).

$$\frac{\pi B}{Q} = \frac{\langle S \rangle}{\langle V \rangle} \tag{10}$$

5. Results and Discussion

5.1 Characterization of a fresh catalyst sample

Fresh catalyst samples were characterized before the *in situ* reduction and dry reforming experiments. WAXS was used to identify the sample phases, (HR)TEM to get an estimate of particle shapes and sizes for the posterior data analysis and SAXS to determine the initial particle sizes and surface to volume ratio.

WAXS

The phases of a fresh catalyst sample were identified as hexagonal Ru (space group #194: $P6_3/mmc$), tetragonal RuO_2 (space group #136: $P4_2/mnm$) and cubic $MgAl_2O_4$ (space group #227: Fd3m S). Figure 1 illustrates the WAXS pattern of a fresh catalyst with the simulated contributions of Ru- (blue), RuO_2- (green), assuming crystallite sizes of 2 nm and the $MgAl_2O_4$-phase (red). The

simulations were performed taking the instrumental resolution of the CCD detector refined from a Si standard (NIST SRM 640c) in account, the peak profiles were simulated using Voigt functions.

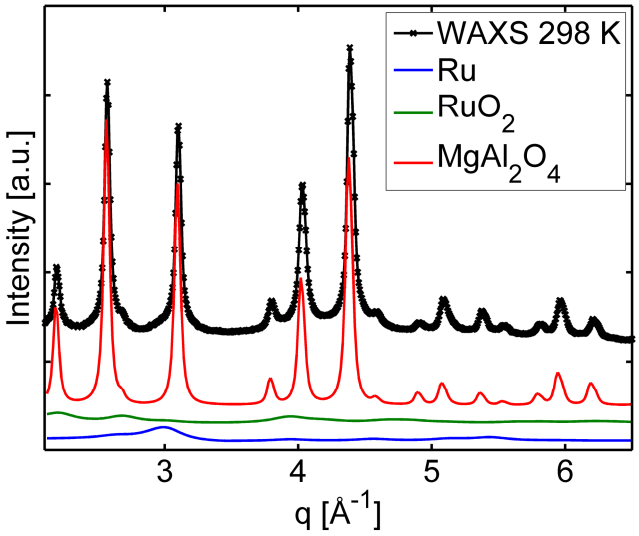

Figure 1: WAXS pattern of a fresh Ru/$MgAl_2O_4$ catalyst at 298 K (-x-) and simulated contributions for the $MgAl_2O_4$-support (—), RuO_2 (—) and Ru (—). The contributions for the RuO_2 and Ru are simulated assuming a crystallite size of 2 nm.

The WAXS pattern does not show any distinct peaks for Ru and RuO_2, in fact very broad reflections due to size effects were observed that are superimposed by peaks of the $MgAl_2O_4$ support. Simulations of theoretical scattering patterns with different Ru-crystallite sizes and a metal loading similar to the studied catalyst and taking the instrumental resolution into account, reveal that the crystallite size has to be above 6 nm to resolve a distinct peak from the strongest Ru-reflection. The presence of RuO_2 in the fresh catalyst can be explained by the exposure to air between the sample preparation and the experiments.

TEM

TEM and HRTEM of a fresh catalyst sample are illustrated in figure 2. Spherical symmetry was observed for Ru catalyst particles, the $MgAl_2O_4$ support particles showed a more irregular shape. For the SAXS data analysis we assumed a spherical particle shape and although irregular shaped particles were noted in case of $MgAl_2O_4$, the assumption of spherical particle symmetries is expected to hold.

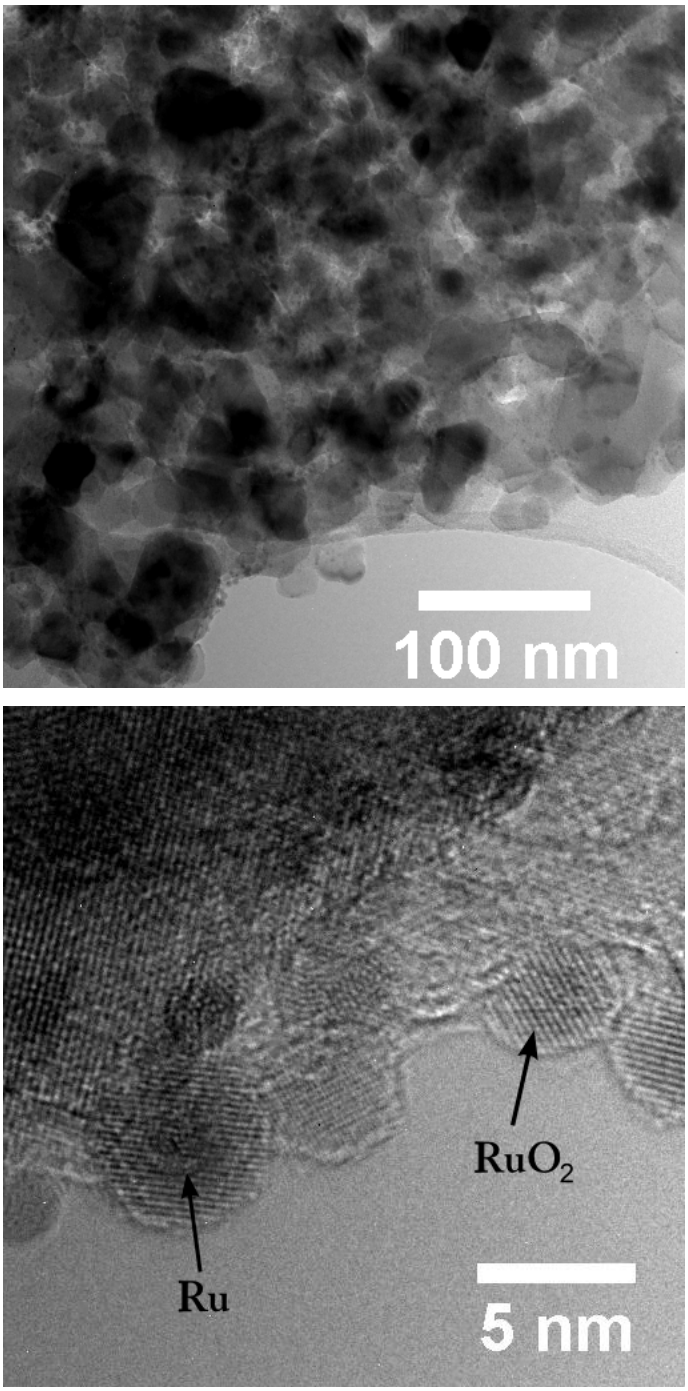

Figure 2: TEM (top) and HRTEM (bottom) images of the fresh Ru/spinel sample

The TEM images were utilized to achieve an estimate of the Ru- and $MgAl_2O_4$ particle size distribution (PSD). Since SAXS data provides information about the particle sizes in terms of a volume average it can be beneficial to evaluate the volume averaged diameter d_V from TEM micrographs to compare the results obtained with both techniques (Borchert *et al.* 2005). The

volume averaged diameter can be evaluated by the following equation (Sehested *et al.* 2001, Borchert *et al.* 2005):

$$d_V = \frac{\sum n_i d_i^4}{\sum n_i d_i^3} \tag{11}$$

where n_i is the number of particles with the diameter d_i. The PSD's were obtained by measuring 121 individual spherical Ru or RuO_2 and 115 random distances over $MgAl_2O_4$ particles. Only HRTEM allows the discrimination between Ru and RuO_2 particles. Since both TEM and HRTEM images were used to determine the PSD it reflects the distribution of Ru and RuO_2 particle diameters in the fresh catalyst sample. The PSD of the Ru-particles is well described by a lognormal distribution

$$f(D) = \frac{1}{D\sigma\sqrt{2\pi}} \exp\left\{ -\frac{[\ln(D) - \mu]^2}{2\sigma^2} \right\} \tag{12}$$

where D is the particle diameter, μ the mean and σ the standard deviation, see figure 3. From least square fitting using equation 11 we obtained μ = 0.54 ± 0.03 and σ = 0.40 ± 0.02 and respectively a mean diameter 1.84 nm. The volume averaged diameter of the Ru/RuO_2 particles, evaluated from the lognormal distribution, is $d_V(Ru/RuO_2)$ = 2.9 nm and for the support d_V ($MgAl_2O_4$) = 55.8 nm.

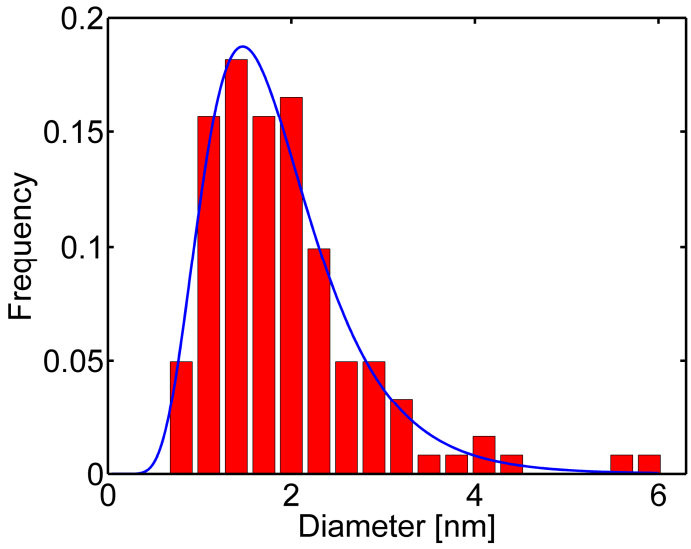

Figure 3: Particle size distribution (PSD) derived from TEM image analyses of a fresh $Ru/MgAl_2O_4$ catalyst.

From the HRTEM images, atomic distances matching to Ru, RuO_2 and $MgAl_2O_4$ crystallite planes were refined, see table 1, confirming the phase composition observed from WAXS. The HRTEM micrographs did not show any indication for the existence of Ru/RuO_2 core/shell-particles as reported by Jakobsen *et al*. (2010) for a Ru/ZrO_2 catalyst, in fact our observations suggest more a coexistence of spherical Ru and RuO_2 particles. However, differences of the Ru-particle morphology might be explained by utilization of different support materials or differences in the mean particle diameter. Jakobsen *et al.* (2010) reported a mean Ru-particle diameter of 4.9 nm on a ZrO_2 support and we observed an average of 1.8 nm from the TEM micrographs on the $MgAl_2O_4$ substrate.

Index	Lattice spacing	Measured
Ru (101)	2.08 Å	2.08 Å
Ru (100)	2.42 Å	2.38 Å
RuO_2 (200)	2.25 Å	2.28 Å
RuO_2 (101)	2.54 Å	2.56 Å
$MgAl_2O_4$ (311)	2.44 Å	2.45 Å
$MgAl_2O_4$ (220)	2.86 Å	2.88 Å
$MgAl_2O_4$ (111)	4.67 Å	4.78 Å

Table 1: Atomic distances extracted from HRTEM images of a fresh $Ru/MgAl_2O_4$ catalyst.

SAXS

The best description of the experimental data was obtained with a unified equation (comprising two structural levels for scattering from the $MgAl_2O_4$ support (second and third term equation 13) and the Ru catalyst particles (fourth and fifth term). The first term describes power law scattering from large aggregates, close to the limit of resolution.

$$I(q) = B_0 q^{-4} + G_1 \exp\left(-\frac{q^2 R_{g,1}^2}{3}\right) + B_1 \left(\frac{q}{\left(\operatorname{erf}\left(qR_{g,1}/\sqrt{6}\right)\right)^3}\right)^{-P_1} + G_2 \exp\left(-\frac{q^2 R_{g,2}^2}{3}\right) + B_2 \left(\frac{q}{\left(\operatorname{erf}\left(qR_{g,2}/\sqrt{6}\right)\right)^3}\right)^{-P_2} \quad (13)$$

During the fits, the power law coefficients P_1 and P_2 were restricted to 4 corresponding to smooth particle interfaces. Least square fitting leaving P_1 free led only to a slight deviation from the value of 4, indicating a marginal interface roughness of the $MgAl_2O_4$-support particles. Fits with P_2 as a free parameter were observed to be unstable because of the low intensity at high angles, where the power law scattering specific to the Ru particle surface is strongly influenced by the background subtraction. Small fluctuations of the scattered intensity can lead to over- or underestimation of the background and thereby to an under- or overestimation of the surface to volume ratio.

Figure 4 illustrates the previously described least square fit of equation 11 on data acquired at 298 K.

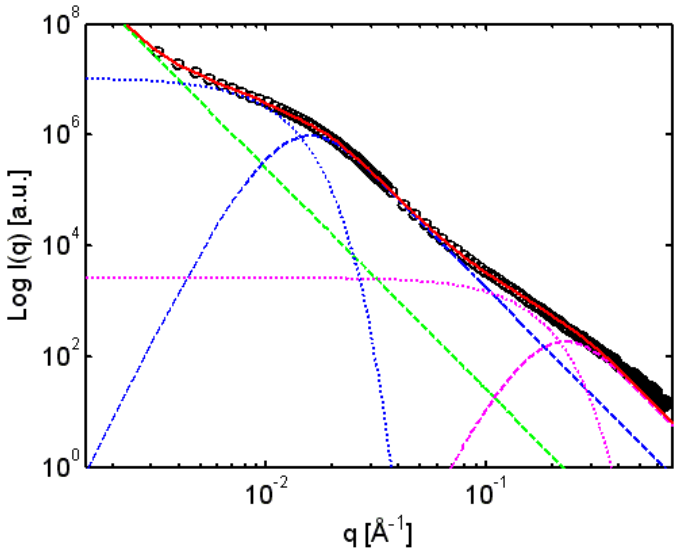

Figure 4: SAXS data fitting with unified function. The green line describes power law scattering from large aggregates, the blue dotted line the Guinier- and the dashed line the Porod term for a size regime related to the support particles and the magenta lines respectively for the Ru particles.

From the least square fit of equation 13, assuming spherical particle shapes, we determined the mean particle diameter of the two size regimes (symbolized by blue and magenta lines in figure 3). For clarity all refined sizes from SAXS below are given in diameter, $d_{SAXS} = 2\ R = 2\sqrt{5/3}\,R_g$. Particle diameters for both size regimes and the volume averaged particle diameters are compared in table 2. The standard deviation of $\sigma = 0.43$ for the Ru/RuO_2 was obtained using equation 7.

	d_{SAXS}	$d_{V,TEM}$
low q regime	49.7 nm ± 3.0 nm	55.8 nm
high q regime	3.4 nm ± 0.04 nm	2.9 nm

Table 2: Particle diameters determined from SAXS and volume averaged diameters calculated from the PSD of a catalyst sample at 298 K.

The mean particle diameters determined from SAXS and the volume averaged diameter from TEM show good agreement and we conclude that the size regime at low q is attributed to scattering from the $MgAl_2O_4$ support- and the regime at high q to scattering from Ru catalyst- particles. The same applies for the standard deviation of the Ru/RuO_2 particles obtained with both methods of $\sigma = 0.43$ from SAXS and $\sigma = 0.40$ from TEM. However, determining the geometric mean Ru/RuO_2 particle diameter from the number distribution obtained from SAXS, using equation 8, leads to an underestimation of the diameter by a factor of around 2 compared to TEM. Even though the standard deviation of the Ru/RuO_2 from SAXS and TEM shows almost congruence, an accurate determination of the geometric mean diameter from TEM requires the exact form of the size distribution and therefore measurement of approximately one order of magnitude more particles. Analysis of the TEM micrographs leading most presumable to an overestimation of the mean particle diameter since it is difficult to resolve the smallest particles.

Here, the main focus is to follow the dynamical changes of the catalyst operating under pressure and temperature conditions that are comparable to large scale processes in the chemical industry, and to follow those dynamics *in situ*, rather than resolve absolute particle diameters. We decided therefore to use the mean particle diameters obtained directly from the fitted R_g as an arbitrary parameter to describe those dynamics and neglect any effect of the particle size distributions.

5.2 *In situ* reduction

As the catalyst samples were exposed to air between preparation and dry reforming experiments, Ru was partially oxidized as observed by WAXS and HRTEM and required a pretreatment with hydrogen to reduce the RuO_2 phase. The reduction was carried out *in situ* to follow the dynamical changes of the catalyst during the treatment in hydrogen. The reduction occurs at a temperature below 393 K indicated by an increase of the scattered intensity from the Ru- and correspondingly a decrease from the RuO_2-phase in WAXS (see figure 5 a) and this correlates with changes observed

in the SAXS pattern at high *q*, in the size regime that is related to scattering of the Ru/RuO_2-particles (see figure 5 b). WAXS data acquired at 373 K during a second reduction experiment (see inlay figure 5 a blue line), exhibits a lower scattered intensity of the Ru-phase than WAXS recorded at 393 K during this experiment. We conclude therefore that the reduction emerges in a temperature interval between 373 - 393 K.

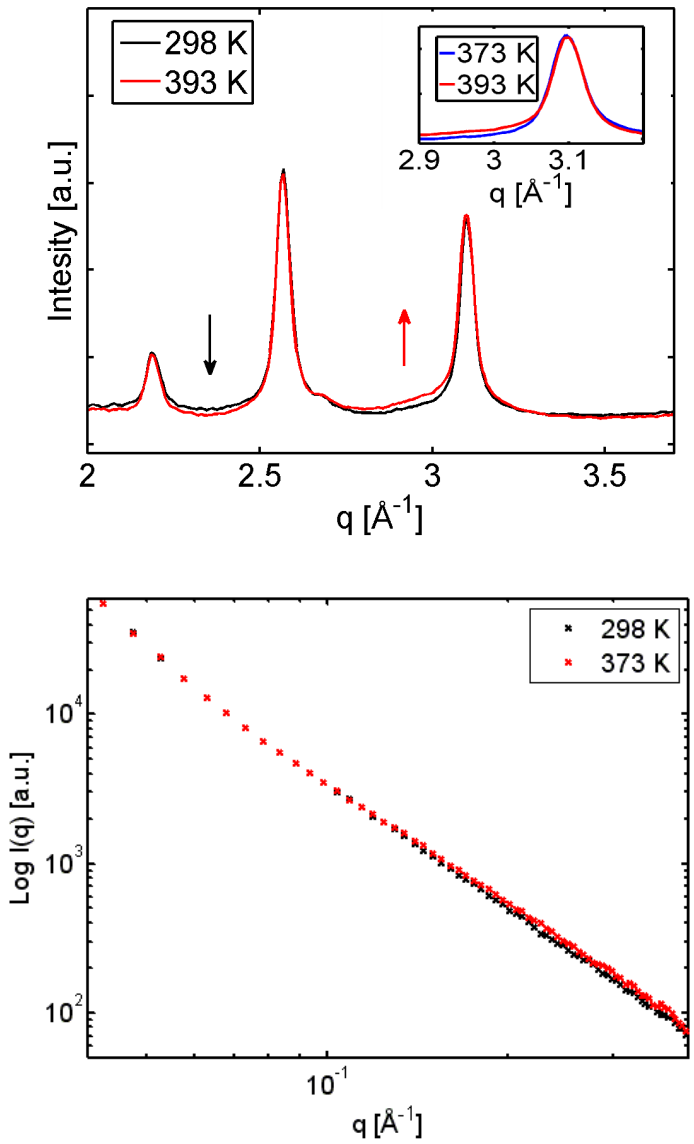

Figure 5: WAXS- (top) and SAXS-pattern (bottom) acquired at 298 K (black) and 393 K (red). The red arrow indicating the increase of scattered intensity from the Ru- and the black arrow the decrease in intensity from the RuO_2 phase in WAXS. The inlay in (a) shows WAXS data of the catalyst at 373 K (blue) and at 393 K.

Multiple peak fitting of all acquired WAXS patterns in a *q*-range from 2.1 to 3.4 $Å^{-1}$ were performed to follow the progress of the reduction and subsequently the dry reforming reaction using

the program Fityk (Wojdyr, 2010). The patterns could be well described with 6 Lorentzian shaped peaks for the $MgAl_2O_4$ <220>, <311>, <222>, <400> and the contributions of RuO_2 and Ru. The fitted Ru-peak mainly reflects the contributions of the Ru <101> reflection to the WAXS pattern, but simulations of the theoretical scattering patterns with particle sizes as determined by TEM and SAXS show an overlap with the much weaker Ru <100> and <002> peaks. However, unconstraint peak fitting of the Ru <100> and <002> was not possible due to their relative low intensity and broad peak shape. Contributions of the background over the limited *q*-range were assumed to be approximately constant and were therefore fitted with a straight line.

The center of the Ru <101> peak was fixed during the peak fitting and calculated from the ruthenium lattice parameters (a = 2.7053 Å, c = 4.2820 Å, Schröder *et al.* 1972). Shifts of the Ru <101> peak position due to sample annealing were taken into account by correcting the lattice parameters for linear thermal expansion using the polynomial reported by Shirasu *et al.* (2002), the best fit of patterns before and after reduction are illustrated in figure 6.

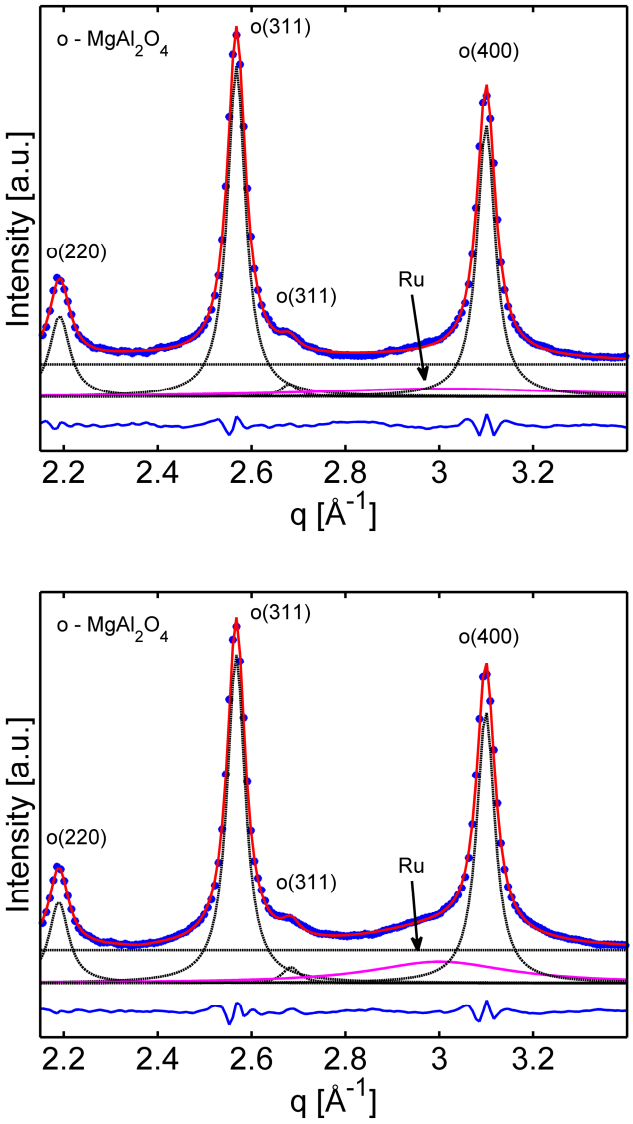

Figure 6: WAXS data fitting with Lorentzian peak profiles before reduction (top) and after reduction at 373 K (bottom) with the fitted profiles of the $MgAl_2O_4$ support and Ru.

An increase of the I_{Ru} <101> / $I_{Support}$ <400> was noted at temperatures between 298 and 393 K and remained constant at higher sample temperatures depart from small fluctuations that can be attributed to uncertainties of the fit; ratios of the integrated intensities with all other fitted $MgAl_2O_4$ peaks showed a similar trend and this reveals that the reduction initiates and completes at temperatures below 393 K.

SAXS data from the *in situ* reduction and subsequent dry reforming experiments was analysed by least square fitting of equation (13). To evaluate the surface to volume ratios with equation (10), the

invariant, using equation (9), of the Ru-particles was calculated by trapezoidal integration of the second size regime from equation (13). Figure 7 illustrates the Ru-particle diameter (a) and the surface to volume ratio (b) as a plot versus the sample temperature.

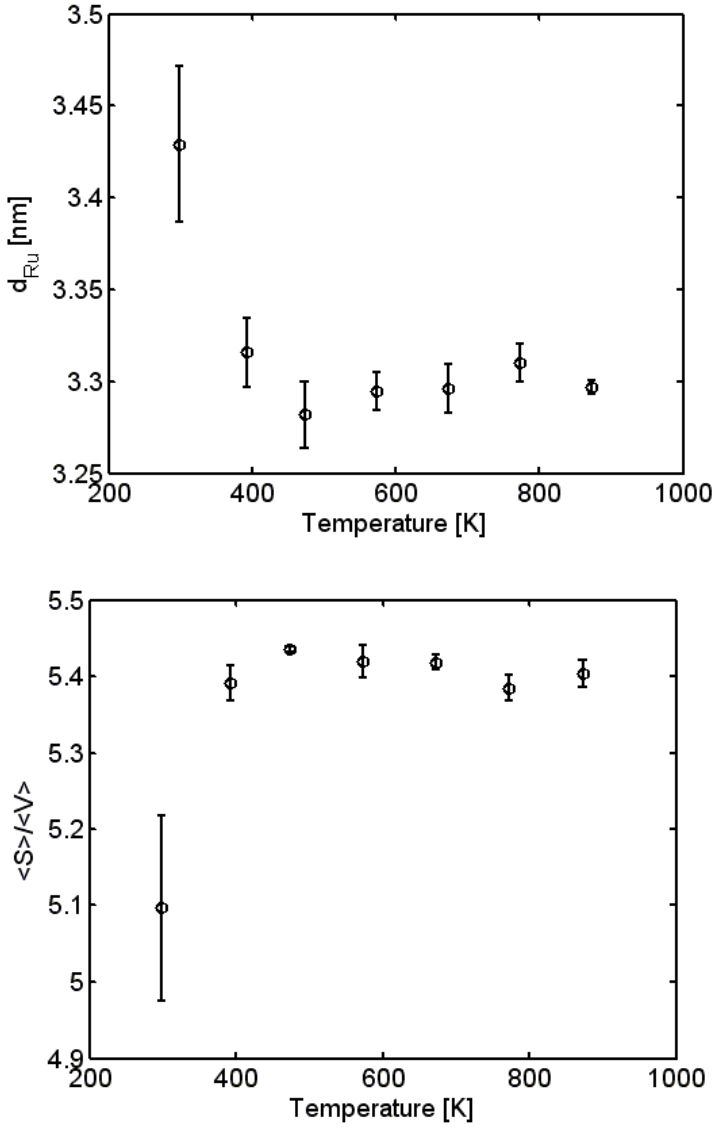

Figure 7: Mean particle diameter (top) and surface/volume ratio (bottom) for Ru from the unified fit during the *in situ* reduction.

The particle mean Ru/RuO_2 particle diameter was observed to be accompanied by a decrease in the mean Ru/RuO_2-particle diameter of about 0.1 nm, from 3.4 to 3.3 nm, and respectively the contrary trend of the surface to volume ratio of about 0.3, from 5.0 to 5.4. The Ru-particles did not show any sintering during heating in pure hydrogen at temperatures above the reduction temperature, indicated by constant particle diameters and surface to volume ratios.

The trend of the ratios of I_{Ru} <101> / $I_{Support}$ <400> let us conclude that the complete reduction of RuO_2 occurs at temperatures below 393 K. Experiments with the same catalyst, but a different heating program, did not show any evidence of the reduction at temperatures up to 373 K and we conclude that the reduction of the RuO_2 phase occurs in a temperature interval between 373 and 393 K. The reduction rate of unsupported RuO_2 is reported to be independent of the initial grain size and temperature and can emerge at temperatures as low as 373 K after an induction period (Prudenziati *et al*,. 2003); temperature programmed reduction (TPR) experiments of polycrystalline RuO_2 with a heating ramp of 2 K min^{-1} reported by Madhavaram *et al.* (2001) showed that the reduction occurs promptly at a temperature of 391 K. A variety of reduction temperatures for supported RuO_2 particles can be found in the literature (Rezaei *et al.*, 2006, Jeong *et al.* 2006, Safariamin *et al.* 2009, Bossi *et al.* 1983). The reported reduction temperatures observed from TPR measurements ranging from 358 K - 466 K, depending on metal-support interactions, catalyst loading and heating ramp.

The temperature interval where we observed the reduction of the RuO_2-phase agrees well with the temperatures reported for unsupported RuO_2. However, the variety of reported reduction temperatures suggests that the reducibility is influenced by interactions of the RuO_2 particles with the support. For a more accurate determination of the reduction temperature, powder diffraction experiments with a constant heating ramp on a synchroton facility could be performed, as shown for the reduction of NiO by Rodriguez *et al.* (2001).

The increase in SAXS intensity in a *q*-range where the Ru-particles contribute to the pattern might be explained by two different approaches, an increase in the average electron density difference $\Delta\rho^2$ since the electron density of RuO_2 is only around one half of Ru. The slight decrease in the Ru-particle diameter might be explained by the following. Coexisting spherical Ru and RuO_2 particles, observed by HRTEM, exhibited approximately similar diameters. Due to the difference in mass density the RuO_2 particles will shrink around 25 % during the reduction. Since the mean particle size from SAXS include both Ru and RuO_2, a decrease in the mean particle diameter of only 0.1 nm is conceivable.

5.3 Dry reforming experiments

After the *in situ* reduction experiments, the catalyst sample was cooled in a continuous flow of hydrogen from 873 K to 723 K. The *in situ* dry methane reforming experiments were performed in a pre mixed gas containing CO_2/CH_4 in a ratio of 3:1. The pre mixed gas, with an excess of CO_2, was chosen from thermodynamic considerations. Carbon deposition on the metal catalyst particles occurs by decomposition of CH_4 and CO. Hence a pre-mixed gas with a lower CH_4 concentration will also show lower carbon formation rates. The Ru-particle diameter and the surface to volume ratios refined from SAXS at all sample temperatures are illustrated in figure 7.

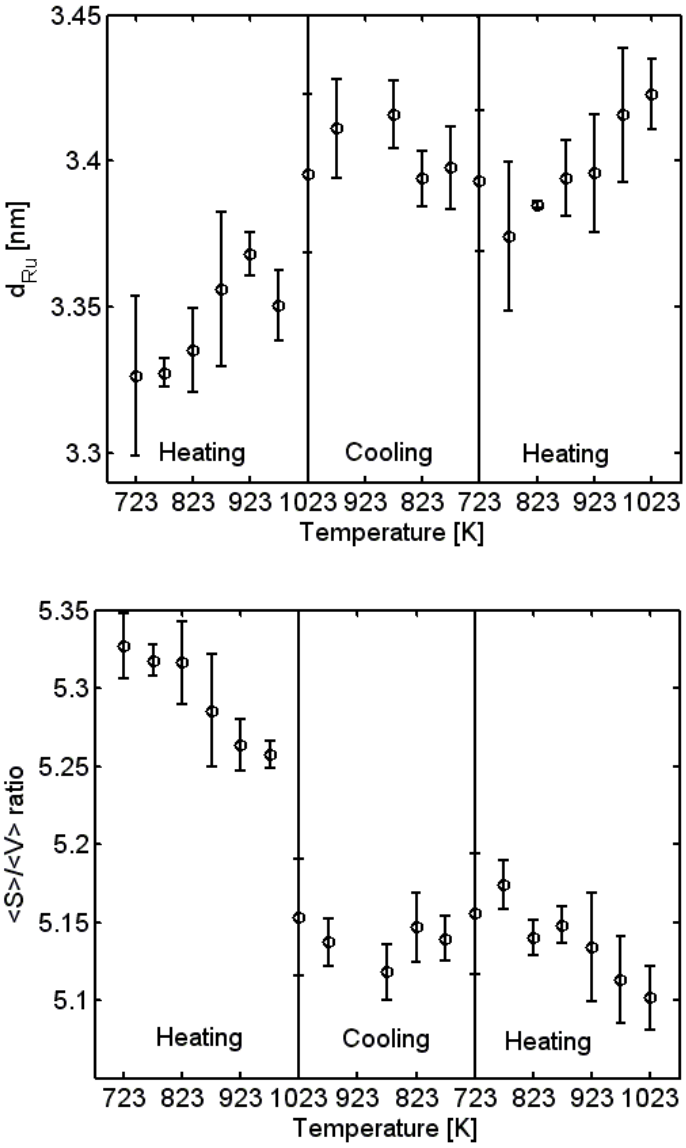

Figure 7: Mean particle radius (top) and surface/volume ratio (bottom) for Ru from the unified fit during the *in situ* dry methane reforming.

The Ru-particle diameter increased about 0.1 nm from 3.3 to 3.4 nm during the first heating cycle, from 723 to 1023 K. A similar trend for the decrease of the surface to volume ratio about 0.2 from 5.3 to 5.1 was observed. During the first cooling cycle a slight decrease and during the second heating cycle a slight increase of the particle diameter was observed. The particle diameters, determined after cooling and reheating of the sample are comparable. Changes of the particle diameter, during the cooling and second heating cycle, are comparable to those expected from thermal expansion of ruthenium (Shirasu *et al.*, 2002). The increase in diameter during the first heating cylce shows the effect of particle sintering whereby the average surface area shrinks; overall a decrease of only 4 % was noted, revealing the high sintering stability of the investigated $Ru/MgAl_2O_4$ catalyst under dry methane reforming conditions.

5.4 Methane conversion

Mass spectroscopy was performed during the dry reforming and a subsequent long time experiment for 20 h at 1023 K to resolve the effect of temperature and particle sintering on the catalytic performance. All signals detected in the mass spectra, were normalized by the argon molecule peak to correct for pressure and time dependent fluctuation of the sensitivity from the quadrupole mass spectrometer. The methane conversion was determined by the $CH_3^{+\bullet}$ fragment peak (m/z = 15), its signal can solely be related to the methane and shows no cross correlations with other fragments from the product gas, the relative methane conversion level during the reforming experiment is illustrated in figure 8.

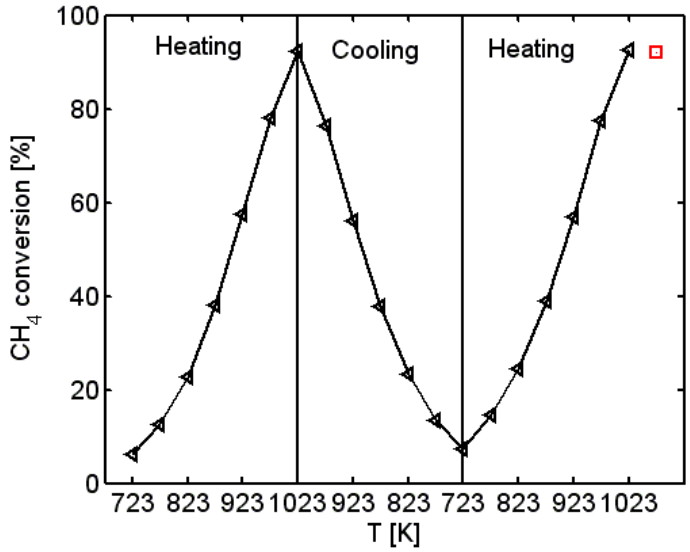

Figure 8: CH_4 conversion level determined from the $CH_3^{+\bullet}$ signal as a function of sample temperature (<) and after 20 h at 1023 K (□)

The H_2/CO ratio was determined from the molecule peaks of hydrogen ($H_2^{+\bullet}$, m/z = 2) and the carbon monoxide ($CO^{+\bullet}$, m/z = 28). The carbon monoxide molecule peak is cross correlated with the $CO^{+\bullet}$ fragment peak from excess CO_2 in the product gas. Therefore the ratio of the carbon dioxide molecule ($CO_2^{+\bullet}$, m/z = 44) and fragment peak ($CO^{+\bullet}$, m/z = 28) was determined post acquisition and the data was corrected accordingly. The H_2/CO ratio refined from the dry methane reforming experiments is plotted in figure 9.

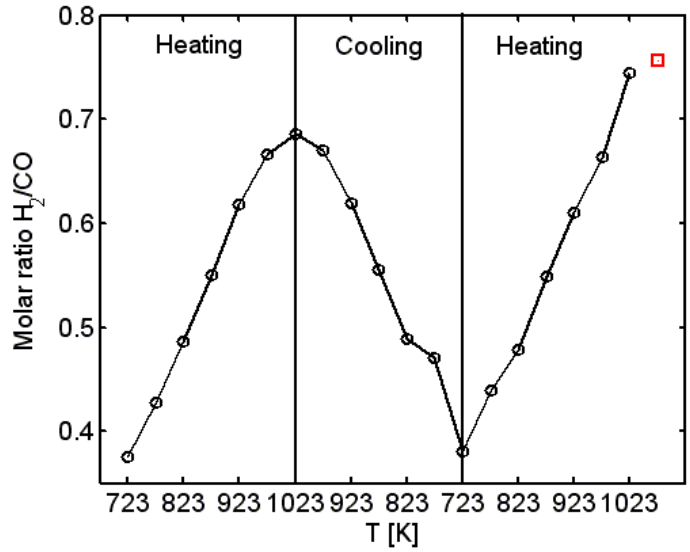

Figure 9: Evolution of the H_2/CO ratio during the dry reforming experiments

The methane conversion level increased during the first sample heating in the premixed gas stream from 6 % at 723 K to 92 % at 1023 K. Cooling and reheating of the sample yielded approximately the same conversion levels. A possible deactivation of the catalyst during long time experiment for 20 h was not observed and the CH_4 conversion level remained constant around 92 %. The constant methane conversion levels indicates no effect of deactivation and is in good agreement with the high sintering stability observed by SAXS and the low tendency of carbon deposition on Ru (Rostrup-Nielsen *et al.*, 1993). TEM micrographs of the sample after the experiment confirm the absence of carbon whisker formation.

Rezaei *et al.* (2006) reported a full methane conversion with a similar gas mixture on a 1%wt Ru catalyst on aluminum stabilized MgO already at 973 K. Here, we did not observe full methane conversion at any measured sample temperature. The conversion level at 973 K was around 77 % and this might be explained by a different space velocity or an influence of the support material, or a combination of the two. Whereas Rezaei *et al.* performed the experiments with a 1 % Ru loading on a Al_2O_3 stabilized MgO and a space velocity of 15 000 ml g^{-1} h^{-1}, were our experiments carried out with a 4 % Ru loading on $MgAl_2O_4$ with a space velocity of 57 000 ml g^{-1} h^{-1}.

At a sample temperature of 723 K, a H_2/CO ratio of 0.38 was observed, the ratio increased during the sample heating to 0.69 in the first cycle and dropped back down to a value of 0.38 during the cooling to 723 K. After the second sample heating an increase of the H_2/CO ratio to 0.74 was noted. However, the absolute value of H_2/CO ratio should be treated carefully due to fluctuations of the intensity of the cross correlated carbon dioxide fragment peak at m/z = 28. Rezaei *et al.* (2006) reported for a 1% Ru catalyst on Al2O3 stabilized MgO the H_2/CO ratio at 973 K to be 0.64 and this is in good agreement with the ratio determined in our experiments of 0.66 at similar sample temperature.

From the stoichiometry of the reaction one could expect a H_2/CO level close to one. Deviation from this ratio can be explained by the RWGS (Safariamin *et al.*, 2009, [b]Bradford *et al.*, 1998, Bitter *et al*, 1997). The H_2/CO ratio increase with the temperature, water produced by the RWGS is consumed via steam reforming (3) to yield hydrogen and carbon monoxide (Bitter *et al.*, 1997). An indication for the RWGS in our experiments was observed by a water molecule peak in the mass spectrum ($H_2O^{+\bullet}$, m/z = 18). However, the quantification of the water concentration in the product

gas stream was not possible since water condensates in the cold metal tubing connecting the mass spectrometer with the vent of the *in situ* cell.

6. Conclusion and outlook

In this study, combined SAXS/WAXS was utilised to follow the dynamical changes of a 4 %wt $Ru/MgAl_2O_4$ catalyst during reduction in pure hydrogen and subsequent dry methane reforming. A marginal increase of the mean particle diameter from around 3.3 nm to 3.4 nm and accordingly a small decrease of the surface to volume ratio from 5.3 - 5.1 during the dry methane reforming were observed by SAXS revealing a high sintering stability of the catalyst. Equivalent temperature dependent methane conversion levels during heating and cooling of the sample and a consistent methane conversion level of 92 %, during the subsequent 20 hour experiment at 1023 K, displays the good performance and the absence of any deactivation due to carbon formation of the probed $Ru/MgAl_2O_4$ catalyst under the experimental conditions. HRTEM, performed on a catalyst sample after the experiment, did not show any indication for carbon formation.

The onset of the reduction of the RuO_2-phase during the *in situ* experiments in pure hydrogen was observed at a sample temperature below or equal to 393 K by increasing intensity of the Ru peaks. At the same temperature, an increase of the scattered intensity in the SAXS pattern was observed in a q-range related to scattering of the Ru-particles and the mean particle size refined from SAXS was noted to decrease by around 0.1 nm.

Characterisation of the fresh catalyst sample was performed with combined SAXS/WAXS and (HR)TEM. Phase identification by WAXS revealed that the Ru-particles in fresh catalyst were partially oxidised to RuO_2 due to exposure to air between sample preparation and *in situ* experiments and this was confirmed by HRTEM. A coexistence of pure Ru- and RuO_2 particles in a fresh catalyst was indicated by HRTEM. A mean Ru/RuO_2 particle diameter of 3.4 nm was obtained from SAXS data analysis and is in good agreement with volume averaged diameter from TEM. The standard deviation σ to describe the Ru-particles in a fresh catalyst sample as lognormal distributed from SAXS and TEM is in good agreement.

The experiments revealed the applicability of the instrumental setup to test catalysts under conditions comparable to large scale processes. It permits simultaneous *in situ* determinations of changes in the crystalline structure, particle morphology and reactivity of nano-scale catalysts to resolve their correlations with the sample temperature and reactant gas composition. The results, shown in this paper, were obtained with relative small flow rates. Conversions levels close to the thermodynamic equilibrium were observed which excludes any predication of the kinetics and their correlations with the crystalline phase and the nanostructure of the catalyst. In a next step the experiments will be repeated under relevant conditions for kinetic testing.

Acknowledgements

We thank Steen Bang, Ove Rasmussen, Torben Kjær and Jens Borchsenius for maintenance of the equipment and technical support during the implementation of the *in situ* laboratory setup, Hjalte Sylvest Jacobsen for improvement of the WAXS 1D data transformation, Henning Engelbrecht for guidance regarding LabVIEW® and data acquisition during the implementation of the sample gas system and the Copenhagen Graduate School for Nanoscience and Nanotechnology (C:O:N:T) and Haldor Topsøe A/S for financial support.

References

Andreasen, J. W.: Rasmussen, O.: Feidenhans'l, R.: Rasmussen, F. B.: Christensen, R. Molenbroek, A. M., Goerigk, G. (2003). *J. Appl. Cryst.* 36, 812-813

Beaucage, G., Schaefer, D. W. (1994) *J. Non – Cryst. Solids* **172**, 795 – 805

Beaucage, G., Kammler, H. K., Pratsinis, S. E. (2004) *J. Appl. Chryst.* **37** 523 - 535

Bitter, J. H., Seshan, K. Lercher, J. A. (1997) *J. Catal.* **171** 279 - 286

Borchert, H., Shevchenko, E. V., Robert, A., Mekis, I., Kornowski, A., Grübel, G., Weller, H. (2005) *Langmuir* **21** 1931 - 1936

Bossi, A., Cattalani, A., Gabrassi, F., Petrini, G., Zanderighi, L. (1983) *J. Therm. Anal.* **26** 81 - 86

[a]Bradford, M. C. J., Vannice, M.A. (1999) *Catal. Rev. Sci. Eng.* **41** 1 - 42

[b]Bradford, M. C. J., Vannice, M. A. (1999) *J. Catal.* **183** 69 - 75

Crisafulli, C., Scirè S., Maggiore, S., Minicò, S., Galvagno, S. (1999) *Catal. Lett* . **59** 21 - 26

Feigin, L. A., Svergun, D. I. (1987). *Structure Analysis by Small-Angle X-ray and Neutron Scattering.* New York: Plenum Press

Ferreira-Aparicio, P., Guerrero-Ruiz, A., Rodríguez-Ramos, I. (1998) *Appl. Catal. A* **170** 177 - 187

Ferreira-Aparicio, P., Rodríguez-Ramos, I., Anderson, J. A., Guerrero-Ruiz, A. (2000) *Appl. Catal. A* **202** 183 - 196

Gabriel, F., Dauvergne F., Rosenbaum, G. (1978) *Nuclear Instruments and Methods* **152**, 191 - 194

Gadalla, A. M., Bower, B. (1988) *Chem. Eng. Sci.* **1988** 3049 - 3062

Glatter O., Kratky, O. (1982) *Small Angle X-ray Scattering*, New York: Academic Press

Guo, J., Lou, H., Zhao, H., Chai, D., Zheng, X (2004) *Appl. Catal. A* **273** 75 - 82

Hammersley, A. P. (1997). Internal Report ESRF97HA02T. ESRF, Grenoble, France.

Holm-Larsen, H. (2001) *Stud. Surf. Sci. Catal.* **136** 441 - 446

Jakobsen, J. G., Jørgensen, T. L., Chorkendorff, I., Sehested, J. (2010) *Appl. Catal., A* **377** 158 - 166

Jeong, J. H., Lee, J. W., Seo, D. J., Soe, Y., Yoon, W. L., Lee, D. K., Kim, D. H. (2006) *Appl. Catal., A* **302** 151 - 156

Jones, G., Jakobsen, J. G., Shim, S. S., Kleis, J., Andersson, M. P., Rossmeisl, J., Abild-Pedersen, F., Bligaard, T., Helveg, S., Hinnemann, B., Rostrup-Nielsen, J. R., Chorkendorff, I., Sehested, J., Nørskov, J. K. (2008) *J. Catal.* **259** 147 - 160

Kehres, J., Andreasen, J. W., Krebs, F. C., Molenbroek, A. M., Chorkendorff, I., Vegge, T. *J. Appl. Cryst.* **43** 1400 - 1408

Madhavaram, H. Idriss, H., Wendt, S., Kim, Y. D., Knapp, M., Over, H., Aßmann, J., Löffler, E., Muhler, M. (2001) *J. Catal.* **202** 296 - 307

Mark, M. F., Maier, W. F. (1996) *J. Catal.* **164** 122 - 130

Prudenziati, M.,Morten, B.,Travan E. (2003) *Mater. Sci. Eng., B* **98** 167 - 176

Qin, D., Lapszewicz, J. (1994) *Catal. Today* **21** 551 - 560

Rezaei, M., Alavi, S. M., Sahebdelfar, S., Yan, Z.-F. (2006) *J. Nat. Gas. Chem.* **15** 327 - 334

Rodriguez, J. A., Hanson, J. C., Frenkel, I., Kim, J. Y., Pérez, M. (2001) *J. Am. Chem. Soc.* **124** 346 - 354

Rostrup-Nielsen, J. R., Bak Hansen, J.-H. (1993) *J. Catal.* **144** 38-49

Safariamin, M., Tidahy, L. H., Abi-Aad, E., Siffert, S., Aboukaïs, A. (2009) C. R. Chimie **12** 748 - 753

Schmidt, P. W. (1992) *J. Appl. Chryst.* 24, 414-435

Schröder, R..H., Schmitz-Pranghe, N., Kohlhaas, R. (1972) Z. Metallkd. **63** 12-16

Sehested, J., Carlsson, A., Janssens, T. V. W., Hansen, P. L. Datye, A. K. (2001) *J. Catal.* **197** 200 - 209

Shirasu, Y., Minatu, K. (2002) *J. Alloys Compd.* **335** 224-227

Wei, J. M., Iglesia, E. (2004) *J. Phys. Chem. B.* **108** 7253 - 7262

Wojdyr, M. (2010) *J. Appl. Cryst.* **43** 1126 - 1128

Wörner, A., Tamme, R. (1998) *Catal. Today* **46** 165 - 174

Paper IV

Hydrogen Rotational and Translational Diffusion in Calcium Borohydride from Quasielastic Neutron Scattering and DFT Calculations

D. Blanchard,*,† M. D. Riktor,‡ J. B. Maronsson,†,§ H. S. Jacobsen,† J. Kehres,† D. Sveinbjörnsson,† E. Gil Bardají,|| A. Léon,|| F. Juranyi,⊥ J. Wuttke,# B. C. Hauback,‡ M. Fichtner,|| and T. Vegge†

Materials Research Division, Risø National Laboratory for Sustainable Energy, Technical University of Denmark, Building 228, P.O. Box 49, DK-4000 Roskilde, Denmark, Physics Department, Institute for Energy Technology, P.O. Box 40, NO-2027 Kjeller, Norway, Center for Atomic Scale Materials Design, Technical University of Denmark, DK-2800 Lyngby, Denmark, Institute of Nanotechnology, Karlsruhe Institute of Technology (KIT), P.O. Box 3640, D-76021 Karlsruhe, Germany, Laboratory for Neutron Scattering ETH Zurich and Paul Scherrer Institut, CH- 5232 Villigen PSI, Switzerland, Forschungszentrum Jülich, JCNS at FRM II, Lichtenbergstrasse 1, 85747 Garching, Germany

Received: July 9, 2010; Revised Manuscript Received: October 8, 2010

Hydrogen dynamics in crystalline calcium borohydride can be initiated by long-range diffusion or localized motion such as rotations, librations, and vibrations. Herein, the rotational and translational diffusion were studied by quasielastic neutron scattering (QENS) by using two instruments with different time scales in combination with density functional theory (DFT) calculations. Two thermally activated reorientational motions were observed, around the 2-fold (C_2) and 3-fold (C_3) axes of the BH_4^- units, at temperature from 95 to 280K. The experimental energy barriers ($Ea_{C2} = 0.14$ eV and $Ea_{C3} = 0.10$ eV) and mean residence times are comparable with those obtained from DFT calculations. Long-range diffusion events, with an energy barrier of $E_{aD} = 0.12$ eV and an effective jump length of ~2.5 Å were observed at 224 and 260 K. Three vacancy-mediated diffusion events, H jumps between two neighboring BH_4^-, and diffusion of BH_4^- and BH_3 groups were calculated and finally discarded because of their very high formation energies and diffusion barriers. Three interstitial diffusion processes (H, H_2, and H_2O) were also calculated. The H interstitial was found to be highly unstable, whereas the H_2 interstitial has a low energy of formation (0.40 eV) and diffusion barrier (0.09 eV) with a jump length (2.1 Å) that corresponds well with the experimental values. H_2O interstitial has an energy of formation of −0.05 eV, and two different diffusion pathways were found. The first gives a H jump distance of 2.45 Å with a diffusion barrier of 0.68 eV, the second one, more favorable, exhibits a H jump distance of 1.08 Å with a barrier of 0.40 eV. The correlation between the QENS and DFT calculations indicates that, most probably, it is the diffusion of interstitial H_2 that was observed. The origin of the interstitial H_2 might come from the synthesis of the compound or a side reaction with trapped synthesis residue leading to the partial oxidation of the compound and hydrogen release.

Introduction

Metal borohydrides are of interest as hydrogen storage materials because of their high volumetric and gravimetric capacity. However, like many of the complex hydrides, they are generally thermodynamically too stable and have slow absorption and desorption kinetics and poor reversibility.[1,2]

Among the borohydrides, $Mg(BH_4)_2$ and $Ca(BH_4)_2$ have more favorable thermodynamics than for example $LiBH_4$ while maintaining attractive hydrogen capacities (14.9 and 11.5 mass%, respectively).[2,3] Furthermore, they have both been shown to be partially reversible by utilizing high pressure,[4,5] and $Ca(BH_4)_2$ by utilizing additives[6] or destabilized routes.[7]

Noting the lack of knowledge about their structural transition and decomposition mechanisms, we have investigated the hydrogen dynamics in calcium borohydride by using quasielastic neutron scattering (QENS). This method is optimal to study hydrogen dynamics because of the large incoherent scattering cross section of hydrogen compared to all other scattering signals.[8] Although the dynamics in interstitial metal hydrides have been widely studied with neutron scattering,[9−12] only few published results on complex hydrides exist. As examples, the hydrogen dynamics in $NaAlH_4$ and Na_3AlH_6 were studied. It showed only limited hydrogen vacancy diffusion, not changed by the use of Ti additive.[13] In other work,[14,15] hydrogen rotational diffusion in $NaBH_4$ was observed, but no long-range diffusion was observed.

In $Ca(BH_4)_2$, hydrogen is covalently bound to boron, forming tetrahedral BH_4^- complexes. The possible hydrogen dynamics are long-range translational diffusion and localized motions such as rotations of the BH_4^- complexes along specific axes, librations of the complexes, and vibrations within the complexes. Rotational dynamics are often coupled to order−disorder phase

* Corresponding author. E-mail: dibl@risoe.dtu.dk.
† Risø National Laboratory for Sustainable Energy, Technical University of Denmark.
‡ Institute for Energy Technology.
§ Center for Atomic Scale Materials Design, Technical University of Denmark.
|| Karlsruhe Institute of Technology.
⊥ Laboratory for Neutron Scattering ETH Zurich and Paul Scherrer Institut.
Forschungszentrum Jülich.

10.1021/jp107281v
Published on Web 11/09/2010

TABLE 1: β-Ca(BH$_4$)$_2$ Structural Parameters Obtained from Rietveld Refinement of PXD Pattern and DFT Calculations[a]

space group $P4_2/m$ (no. 84); $Z = 2$			
DFT	$a = 6.849$ Å	$c = 4.367$ Å	
PXD	7.021(6)	4.417(6)	
ref 16	(6.946(8))[b]	(4.366(1))	
site	*x/a*	*y/b*	*z/c*
Ca/2c	0.5 (0.5)	0 (0)	0.5 (0.5)
B/4j	0.316 (0.302)	0.209 (0.200)	0 (0)
H1/4j	0.313 (0.295)	0.387 (0.347)	0 (0)
H2/4j	0.490 (0.468)	0.170 (0.185)	0 (0)
H3/8k	0.234 (0.226)	0.142 (0.161)	0.772 (0.800)

[a] In both cases, the starting values were taken from ref 16. During Rietveld refinements, the atomic positions were not refined. [b] Numbers in brackets: parameters from ref 16.

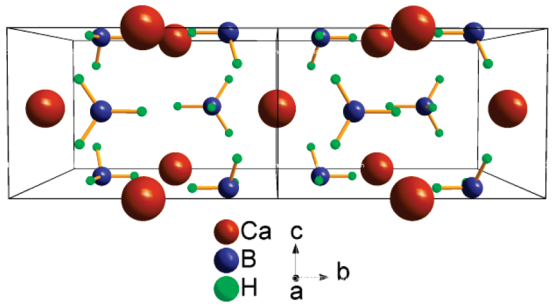

Figure 1. Structure of β-Ca(BH$_4$)$_2$. Space group $P4_2/m$. Large, medium, and small spheres: Ca, B, and H atoms, respectively.

transition in coordination compounds, and the borohydrides decomposition could possibly involve long-range diffusion of H and/or of the whole BH_4^- complexes.

At least, two different tetragonal space groups have been proposed to describe the β-Ca(BH$_4$)$_2$: Butcher et al.[16] chose the $P4_2/m$ space group, whereas Filinchuk et al.[17] proposed P-4. The differences in the proposed structures reflect the degree of order of the BH_4^- units. The possibility to refine the β-structure in different tetragonal space groups with different BH_4^- orientations suggests that the polymorph is stabilized by static or dynamic disorder of the borohydride units like for the high-temperature polymorphic transformation of LiBH$_4$.[18−20] For the Rietveld refinement as well as for the DFT calculations, the $P4_2/m$ space group and the crystallographic data from ref 16 were used (Table 1). Ca(BH$_4$)$_2$ forms ionic crystals consisting of Ca^{2+} and BH_4^- ions. The Ca^{2+} ions are coordinated by six BH_4^- tetrahedra in a bidendate configuration. The B−H interatomic distances are in the range of 1.1 Å, and the Ca−Ca distances are about 4.35 Å (Figure 1). There are two formula units per unit cell. The Ca atoms occupy the (2c) Wyckoff positions, the B atoms occupy the (4j) positions, and the H atoms are distributed over the (4j) and (8k) sites. The BH_4^- tetrahedra possess three 2-fold rotational symmetries (C_2) and four 3-fold rotational symmetries (C_3) leading to three 180° and four 120° rotations (Figure 2).

Herein, the aim was to investigate the rotational and long-range translational diffusion of H-rich species in β-Ca(BH$_4$)$_2$. Therefore, QENS combined with density functional theory (DFT) calculations have been applied.

Material and Experimental Methods

Natural B contains 20% of ^{10}B which has a high absorption cross section of 3837 barns. Therefore, to reduce neutron absorption, Ca(BH$_4$)$_2$ was synthesized via the metathesis reaction of eq 1 by using a ^{11}B-enriched precursor (5.5×10^{-3} barns).

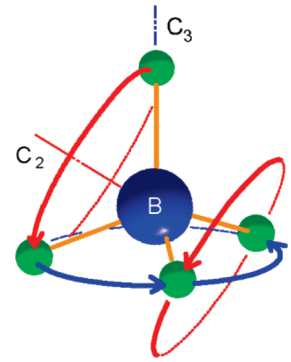

Figure 2. 2-fold C_2-axis and 3-fold C_3-axis of the BH_4^- units. Large and small spheres: B and H atoms, respectively.

$$2Na^{11}BH_4 + CaCl_2 \rightarrow Ca(^{11}BH_4)_2 + 2NaCl \qquad (1)$$

A total of 2.40 g (0.063 mol) of Na^{11}BH$_4$ (purchased from Katchem Ltd., purity 99.8%) was first ball-milled for 4 h in a Fritsch P6 planetary mill at 600 rpm, with a ball-to-powder ratio of 25:1, and then added to 3.52 g (0.032 mol) of $CaCl_2$ (purchased from Alfa Aesar, purity 96%) in 100 mL of THF. The mixture was heated under reflux at 80 °C for 24 h. After cooling to room temperature, the suspension was filtered off, and the filtrate was evaporated under vacuum to remove the solvent. The resulting Ca(^{11}BH$_4$)$_2$·n THF adduct was then dried at elevated temperature under vacuum (at 80 °C for 2 h, at 100 °C for 2 h, at 130 °C for 1 h, at 160 °C for 1 h, and at 200 °C for 16 h). The isolated yield (with respect to $CaCl_2$) was 2.0 g (90%).

Calcium borohydride crystallizes in different structure modifications depending on the synthesis conditions, and a mixture of the three structures, α-Ca(BH$_4$)$_2$, β-Ca(BH$_4$)$_2$,[16,21] and γ-Ca(BH$_4$)$_2$ may be formed. The drying procedure used during the synthesis aimed to obtain β-Ca(BH$_4$)$_2$ as a single phase.

A powder X-ray diffraction (PXD) was recorded with a BRUKER D8 diffractometer (40 kV, 40 mA, Cu radiation K_α =1.542 Å, Figure 3). Quantitative phase analysis based on Rietveld refinements performed by using Rietica software[22] gave a molar composition of 85% β-Ca(BH$_4$)$_2$, 6% α-Ca(BH$_4$)$_2$, 4% CaH_2, and 5% NaCl, and thus, ∼93% of the hydrogen in the sample belongs to β-Ca(BH$_4$)$_2$. Only the cell parameters were refined. For $CaBH_4$ (see Table 1), they are slightly larger than those in ref 16, probably because of the quality of the diffraction pattern; but they are still in reasonable agreement.

Mass spectrometry measurements (MS), obtained by using an OmniStar (GSD 320) mass spectrometer, were performed on the gas released by the sample when heated under dynamical vacuum from room temperature up to 723 K (heating ramp of 1K min^{-1}, Figure 4). The analysis of the measurement shows that H_2 accounts for ∼98.7% of the released gas, and THF accounts for ∼1.2%; the amount of H_2O, B_2H_6, and other gases such as O_2 are negligible (≪1%). Thus, the amount of THF left in the sample after its synthesis is very low, and the sample appears to be water free.

QENS experiments were performed with two complementary instruments, SPHERES and MARS, in order to cover a wide energy range with two different energy resolutions. SPHERES[23] is a high-resolution neutron backscattering spectrometer located

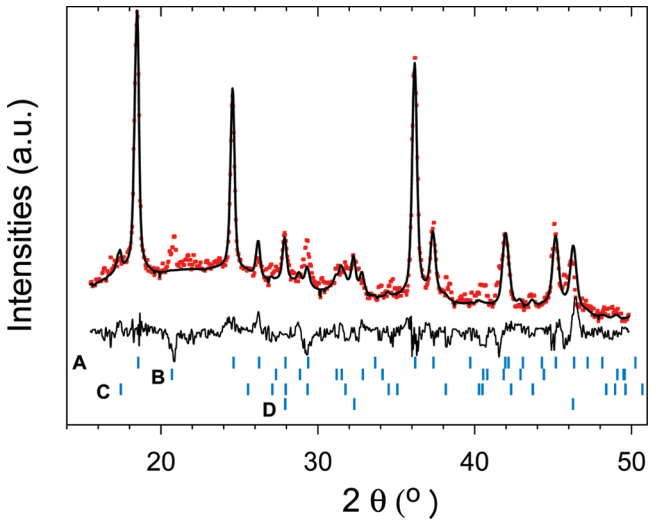

Figure 3. PXD pattern of the as-prepared β-$Ca(BH_4)_2$. The dots are the experimental points, the line is the refined pattern based on the Rietveld method, and the bottom line is the difference between the experimental and the refined pattern. The ticks are the position of the Bragg peaks for A: β-$Ca(BH_4)_2$, B: CaH_2, C: α-$Ca(BH_4)_2$, and D: NaCl.

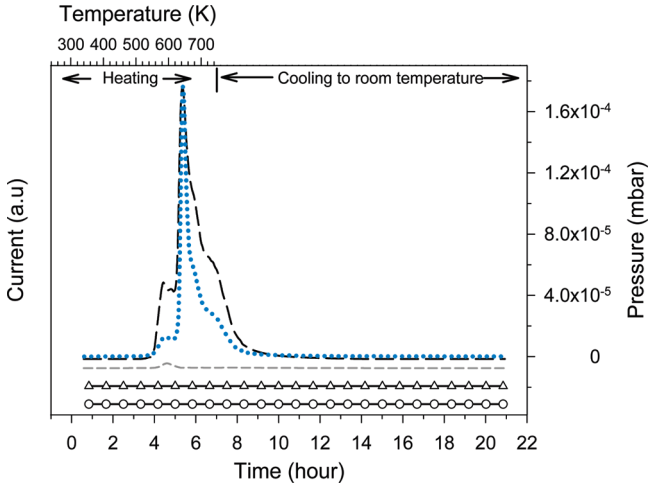

Figure 4. Mass spectrometry measurements. The sample was heated under dynamical vacuum from room temperature up to 723 K at a heating ramp of 1K.min^{-1}. Dotted line, pressure evolution; long dashed line, H_2 signal; short dashed line, THF signal; circles, B_2H_6 signal; triangles, H_2O signal.

at FRM II (Forschungs-Neutronenquelle Heinz Maier-Leibnitz), Garching, Germany. MARS[24] is an inverted geometry time-of-flight spectrometer located at the Swiss Spallation Neutron Source (SINQ), Paul Scherrer Institute, Villigen, Switzerland.

The experiments at SPHERES were performed with ~0.1 g of $Ca(BH_4)_2$, which was loaded in an Al wire sealed flat 30 × 40 × 0.5 mm^3 Al container oriented at 135° with respect to the direct beam. Si(111) monochromator and analyzer crystals were used in a backscattering geometry, giving a final neutron wavelength of 6.271 Å and an energy resolution of 0.65 μeV with an energy-transfer range selected within ±15.8 μeV. The spectra were recorded by nine detectors corresponding to a scattering vector ranging from 0.59 to 1.66 Å^{-1}. The data reduction was carried out with SLAW, a neutron histogram to scattering law converter.[25]

The experiments at MARS were performed with ~0.4 g of $Ca(BH_4)_2$, from the same batch, which was loaded in a double-wall Al container with a height of 60 mm and diameters of 9 mm and 10 mm. The spectra were recorded by five detectors on both side of the instrument corresponding to a scattering vector ranging from 0.49 to 1.86 Å^{-1}. Mica(006) analyzers were used in a near-backscattering geometry, giving a final neutron wavelength of 6.65 Å and an energy resolution of 13 μeV. The energy-transfer window was chosen differently depending on the width of the quasielastic signal, the largest being from −0.04 to 0.43 meV. The data reduction was carried out with the data analysis and visualization environment DAVE.[25]

DFT Calculations

Theoretical calculations were used to identify the possible dynamic events by calculating their energy barriers and prefactors. The calculations were performed by using the atomic simulation environment (ASE) package,[27] and the DACAPO plane-wave basis-set implementation[28] was used to solve the electronic structure problem within the DFT formalism.[29] The ion cores were described by ultrasoft pseudopotentials,[30] and the exchange and correlation effects were described by the PW91 functional.[31] The Kohn−Sham wave functions were expanded in a plane-wave basis set with a cutoff energy of 350 and 600 eV for the density grid cutoff. The wave functions were sampled on a (2 × 2 × 2) k-point mesh. The unit cell containing 2 $Ca(BH_4)_2$ units was the β-phase structure.[16] To eliminate any spurious periodic interactions, the calculations were carried out on a 176 atoms supercell, which consisted of the unit cell repeated once in each spatial direction. Iterative relaxation using the limited memory Broyden−Fletcher−Goldfarb−Shanno algorithm[32] was employed to obtain the zero-temperature structure and unit-cell parameters. A force convergence criterion of 0.001 eV/Å was used for the structure minimization.

The nudged elastic band (NEB) method,[33] along with the FIRE minimization algorithm,[34] was used to locate first-order saddle-point configurations, connecting two local minima, that could be used within harmonic transition state theory (hTST)[35] to determine the thermally activated reaction rates ($r(T)$) by using the barrier height (Ea) and the vibrational frequencies at the initial state (ν^{IS}) and saddle point (ν^{TS}).

$$r(T) = \frac{\prod_{i=1}^{3N} \nu_i^{IS}}{\prod_{i=1}^{3N-1} \nu_i^{TS}} e^{-\frac{Ea}{k_B T}} \qquad (2)$$

The vibrational frequencies were acquired by using a finite difference approximation of the Hessian matrix (back and forward displacements of 0.01 Å). The term outside the exponential in eq 2, often referred to as the prefactor, compares the vibrational frequencies at the initial state and saddle point. The characteristic times are the reciprocal values of these prefactors.

A force convergence criterion of 0.01 eV/Å was used for the NEB calculations that lead to vibrational frequencies calculations and 0.05 eV/Å for the NEB calculations that only considered the barriers.

The initial paths used when locating the rotational pathways were simple rigid rotations of all the hydrogen atoms in a single BH_4^- unit.

To calculate diffusion, vacancies were created by removing the atom(s) in question and rerelaxing the atomic coordinates. Similarly, interstitials were created by inserting the atom(s) in question and rerelaxing the atomic coordinates. Neighboring, relaxed, defect structures were then used as end points in linearly interpolated NEB calculations.

TABLE 2: Summary of the Experimental (QENS, Rotational and Translational Diffusion) and Computational (DFT, Rotational Diffusion) Results for β-$Ca(BH_4)_2$

τ_0[a] (ps)		E_a[a] (eV)	
MARS and SPHERES			
C_3	C_2	C_3	C_2
5.0×10^{-2}	5.6×10^{-2}	0.10	0.14
long-range diffusion			
4		0.12	
DFT			
C_3	C_2	C_3	C_2
1.87×10^{-2}	3.97×10^{-2}	0.11	0.15

[a] τ_0 and E_a experimental values obtained from the Arrhenius fits ($\tau = \tau_0 \exp(E_a/(k_bT))$) of the experimental mean resident times.

TABLE 3: Summary of the Computational (DFT, Translational Diffusion) Results for β-$Ca(BH_4)_2$

defect type	formation energy (eV)[a]	τ_0 (ps)	E_{aD} (eV)	diffusion length (Å)
H vacancy	2.09	8.0×10^{-1}	0.46	2.1
BH_3 vacancy	1.56	6.1×10^{-2}	1.92	3.3
BH_4 vacancy	2.83	N/A[b]	0.63	3.8
H interstitial	2.34[c]	N/A	N/A	N/A
H_2 interstitial	0.40	5.68×10^{-2}	0.09	2.1
H_2O inter. flip	−0.05	N/A	0.40	1.08
H_2O interstitial	−0.05	N/A	0.68	2.45

[a] The formation energies were calculated for neutral species. [b] N/A: not calculated. [c] The H interstitial is not stable and relaxes to a H_2 interstitial coupled to a H vacancy.

Results

QENS Spectra. Inelastic temperature scans were performed on both instruments. For each temperature, the spectra collected on each detector were summed to get one spectra. The elastic intensities were obtained by adding up the counts with an energy transfer of $|\delta E| \leq 8$ μeV and $|\delta E| \leq 0.32$ μeV for MARS and SPHERES, respectively. The inelastic intensities were deduced by summing up the counts out of the elastic regions. Figure 5 displays the evolution with temperature of the normalized elastic ($I_{N\text{-el}}$) and inelastic ($I_{N\text{-inel}}$) scattering measured at MARS and SPHERES. The sample was heated from 70 to 565 K at MARS. At 70 K, no inelastic broadening was detected because the hydrogen is frozen-in on the time scale accessible with the instrument. On heating between 70 and 120 K, $I_{N\text{-el}}$ ($|\delta E| \leq 8$ μeV) slowly decreased, whereas $I_{N\text{-inel}}$ ($|\delta E| > 8$ μeV) slowly increased; then, the same evolution is continued only faster. The maximum $I_{N\text{-inel}}$ is at 200 K followed by a decrease and then no more changes. At this temperature and above, the hydrogen motion is too fast, and the large inelastic broadening gives a flat background. When cooling from 565 to 200 K, $I_{N\text{-el}}$ is identical to that observed during heating, whereas $I_{N\text{-inel}}$ is found to be lower. At $T < 200$ K, $I_{N\text{-el}}$ is also found to be lower than on heating, indicating a loss of ~18% (weakly) bound hydrogen, that has been desorbed during heating. The MS measurement revealed a slight release of hydrogen between 520 and 565 K, corresponding to ~4% of the total hydrogen released during the measurement up to 723 K (see Figure 4). Similar observations have been made in several other published studies.[36−38] In ref 38, the sample, heated up to 603 K, was quenched and examined with high-resolution synchrotron radiation powder diffraction. Along with β-$Ca(BH_4)_2$, Bragg peaks from an unknown phase were observed, which have recently been identified and structurally resolved as an oxide of the borohydride.[39] PXD measurements made on the sample used for the temperature scans with MARS (not shown herein) also revealed the presence of this oxide phase. Thus, the hydrogen release observed during the MS measurement and temperature scan might come from a reaction of the hydride with oxygen or water. The oxygen level remains in the background level during the MS; therefore, one can exclude the existence of a leak in the experimental setup, and the only source of oxygen or water comes from the sample itself, without excluding a possible reaction with residual THF.

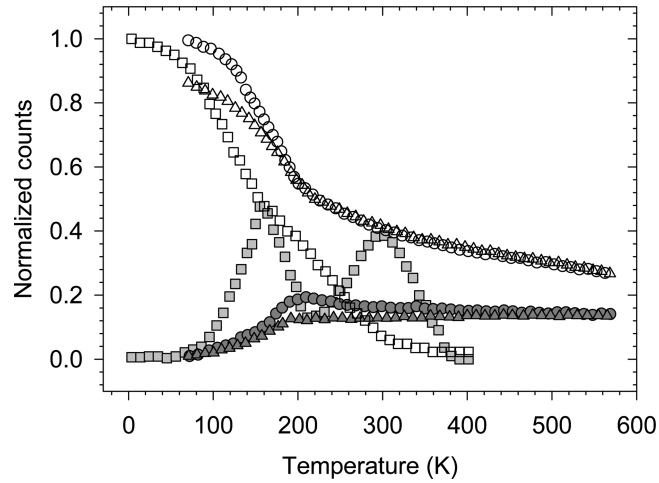

Figure 5. Normalized elastic and inelastic intensities ($I_{N\text{-el}}$ and $I_{N\text{-inel}}$) during temperature scans. Open and filled ○: $I_{N\text{-el}}$ and $I_{N\text{-inel}}$, respectively, with MARS on heating from 70 to 570 K. Open and filled △: $I_{N\text{-el}}$ and $I_{N\text{-inel}}$, respectively, with MARS on cooling from 570 to 70 K. Open and filled □: $I_{N\text{-el}}$ and $I_{N\text{-inel}}$, respectively, with SPHERES on heating from 3 to 400 K.

At SPHERES, the temperature scan (Figure 5) was performed only during heating. It showed almost the same features as those for the MARS measurements, but changes occurred at lower temperatures. The inelastic intensity ($|\delta E| \leq 0.32$ μeV) starts to increase at around 80 K, with the maximum at 160 K, and decreases significantly afterward. However, at 220 K, $I_{N\text{-inel}}$ ($|\delta E| > 0.32$ μeV) increases again with a maximum at 320 K followed by a decrease and then flatten out at 390 K. At this temperature, the hydrogen motion gives rise to a broadening too large for the instrument energy window. The two bumps in the inelastic signal were attributed to two different types of hydrogen dynamics, as it will be discussed below.

The temperatures to perform the measurements were selected from these scans (see Table 4). The QENS spectra were analyzed by using the curve fitting utility (PAN) included in the DAVE package. They consist of one elastic and some inelastic components. The elastic component comes from the scattering process with no change in the neutron energy, whereas the inelastic component reflects the energy transfer, gain, and loss, due to the hydrogen motions. The measured total incoherent scattering function, $S^{tot}_{inc}(Q\omega)$, is given by (see ref 8 for more details):

$$S^{tot}_{inc}(Q\omega) = R(Q\omega) \otimes (A_0(Q)\delta(\omega) + \sum_i A_i(Q)L(\Gamma_i, \omega)) + B(Q) \quad (3)$$

where $R(Q,\omega)$ is the instrumental resolution, $\delta(\omega)$ is the Dirac delta function describing the elastic scattering. $L(\Gamma_i,\omega)$ are Lorentzian functions which model the inelastic signal with Γ_i = half width at half maximum (HWHM). The B term represents

TABLE 4: Summary of the Experimental (QENS) Results for β-$Ca(BH_4)_2$

	τ (ps)	
temp. (K)	C_3	C_2
	MARS	
100	204	-
130	145	-
160	40	-
190	17	245
220	8	82
280	3	32
	SPHERES	
95	6582	-
116	429	-
143	141	7520
163	58	1755
204	-	131
	long-range diffusion	
224	2302	
260	977	

the inelastic background in the quasielastic region. It can originate from processes that are much faster than those observable within the time scale of the instruments used. The term $A_0(Q)$ is the elastic incoherent structure factor (EISF).[8] Its dependence on Q, the wave vector transfer, is important. It basically determines the static properties of the number of sites accessible to the hydrogen atoms, the locations of these sites, and the normalized probability to be at a given sites. It is a measurable quantity, evaluated from the ratio:

$$A_0(Q) = \frac{I_{el}(Q)}{I_{el}(Q) + I_{inel}(Q)} \quad (4)$$

where $I_{el}(Q)$ and $I_{inel}(Q)$ are the integrated intensities of the elastic and inelastic signal, respectively.

Herein and following eq 3, the QENS spectra were analyzed with the resolution-limited elastic peak, the delta function folded with the instrumental resolutions, and one or two Lorentzian, depending on the temperature. The instrumental resolutions were obtained from measurements at 3 K (SPHERES) and 70 K (MARS). At these temperatures, no dynamical motions were observed on the time scale of the two instruments. The centers of the delta function and of the Lorentzian were constrained to be the same. For the measurements performed at MARS, because the energy window of the resolution function was smaller than those used for the measurements at higher temperatures, a flat fixed background was used. For the measurements performed at SPHERES, a flat background was used to model the too broad Lorentzian at high temperatures. Figures 6 and 7 present typical examples of the spectra together with their fits with one or two Lorentzian. For the whole temperature range measured at MARS, and at least up to 220 K at SPHERES, the widths of the Lorentzian functions were found to be Q-independent over the measured Q range. This indicates that the observed inelastic broadenings originate from localized hydrogen motion.[8] Figure 8 displays the values of the average HWHMs, over all the detectors, versus temperature. At SPHERES, for two temperatures above 220 K (224 and 260 K), the HWHMs were found to be Q-dependent (Figure 11), a signature for nonlocalized motion and possibly long-range diffusion. Unfortunately, at higher temperature, the fits of the QENS spectra are no longer reliable because of the low signal

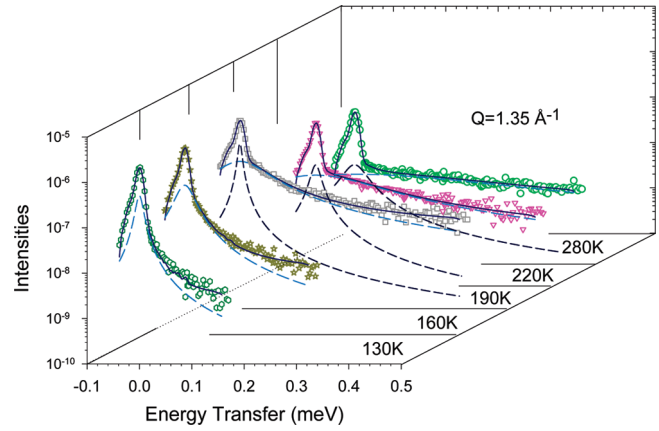

Figure 6. QENS of β-$Ca(BH_4)_2$ measured with MARS at different temperatures for $Q = 1.35$ Å^{-1}. The dots are the experimental data. The solid lines display the fits of the data, each consisting of a resolution-broadened delta function, a flat background, and one or two Lorentzian (dashed line).

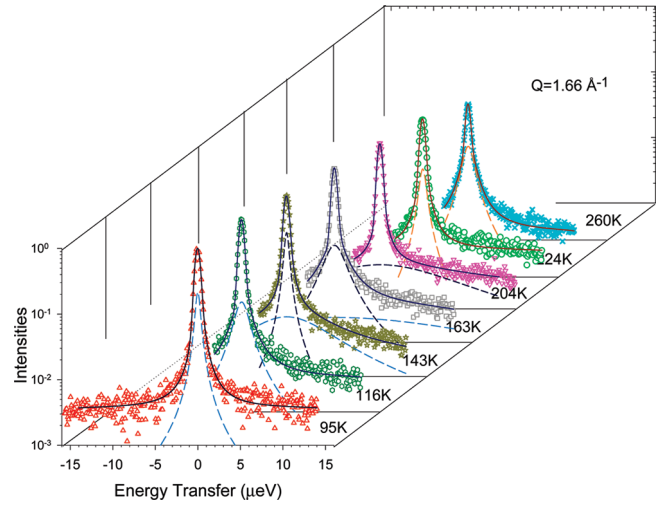

Figure 7. QENS of β-$Ca(BH_4)_2$ measured with SPHERES at different temperatures for $Q = 1.66$ Å^{-1}. The dots are the experimental data. The solid lines display the fits of the data, each consisting of a resolution-broadened delta function, one or two Lorentzian (dashed line), and a flat background for the three last temperatures (not shown on the plots).

intensity combined with the too broad inelastic component at high Q values.

The first obvious localized motions are the rotations around the 2-fold and 3-fold axis (Figure 2). For BH_4^- rotations around the C_2-axis, the tetrahedral ions have two equal equilibrium orientations, and the EISF is:[8]

$$A_0(Q) = \frac{1}{2}\left(1 + j_0\left(2\frac{\sqrt{2}}{\sqrt{3}}Qd\right)\right) \quad (5)$$

where $j_0(x) = \sin(x)/x$ is the zeroth order Bessel function and d is the bond length between B and H. This rotation gives rise to one Lorentzian with a Q-independent HWHM of

$$\Gamma_{C2} = 2\hbar\tau_2^{-1} \quad (6)$$

τ_2 represents the average time that a hydrogen atom stays at a site before jumping to a new site because of reorientation around the 2-fold axis.

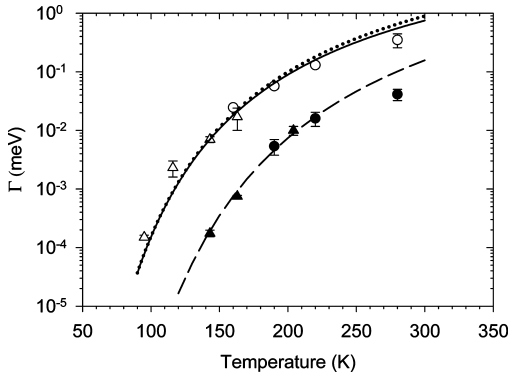

Figure 8. Experimental and theoretical HWHMs. The dots are the averaged, over all the detectors, experimental values. Triangles, SPHERES data; circles, MARS data. The theoretical values are calculated from eqs 9−11, with values of the characteristic times, energy barriers, and prefactors obtained from DFT. Dotted line, HWHMs calculated from eq 9; solid line, HWHMs calculated from eq 10; dashed line, HWHMs calculated from eq 11.

For BH_4^- rotations around the C_3-axis, the tetrahedral ions have three equal equilibrium orientations, and one hydrogen atom remains immobile. The expression for the EISF is identical to the rotation around the C_2-axis (eq 5).[8] It gives rise to one Lorentzian with a Q-independent HWHM of

$$\Gamma_{C3} = \frac{3}{2}\hbar\tau_3^{-1} \tag{7}$$

τ_3 represents the average time that a hydrogen atom stays at a site before jumping to a new site because of reorientation around the 3-fold axis.

In the case of combination of rotations around several C_2 and C_3-axis, with two different jump rates, the EISF is given by:[15]

$$A_0(Q) = \frac{1}{4}\left(1 + j_0\left(Q\frac{2\sqrt{2}}{\sqrt{3}}d\right)\right)\left(1 + j_0\left(Q\frac{2\sqrt{2}}{\sqrt{3}}d\right)\right) \tag{8}$$

The combination of these two rotations gives rise to three Lorentzian with the following Q-independent HWHMs:

$$\Gamma_1 = \hbar(2\tau_2^{-1} + \frac{3}{2}\tau_3^{-1}) \tag{9}$$

$$\Gamma_2 = \frac{3}{2}\hbar\tau_3^{-1} \tag{10}$$

$$\Gamma_3 = 2\hbar\tau_2^{-1} \tag{11}$$

with τ_2 and τ_3 defined above.

The experimental EISFs, extracted from the fitted QENS spectra (eq 4), and those calculated with the models described above (eqs 5 and 8) provide strong evidence about the nature of the localized motions. Figure 9 displays the EISFs. The model for one rotation (eq 5) follows the experimental data when one inelastic component was detected in the QENS spectra (95 and 204 K with SPHERES, 130 and 160 K with MARS). The model combining the two rotations (C_2−C_3, eq 8) reproduces the experimental EISFs when two Lorentzian were needed to fit the QENS spectra (116−163 K with SPHERES, 190 K and above with MARS). For both equations, the best fit was obtained for d = 1.11 Å, a value in agreement with the B−H distance obtained from neutron-diffraction data.[15] The characteristic times of the localized hydrogen motion, now attributed to reorientational rotations, were calculated from the average HWHMs at a given temperature. Equations 9−11 were used. In the case of the low-temperature spectra, fitted with one Lorentzian, τ_2 was considered as infinite. The results are presented in Table 4. The observed inelastic broadening follows an Arrhenius behavior, and the corresponding characteristic times can be expressed as

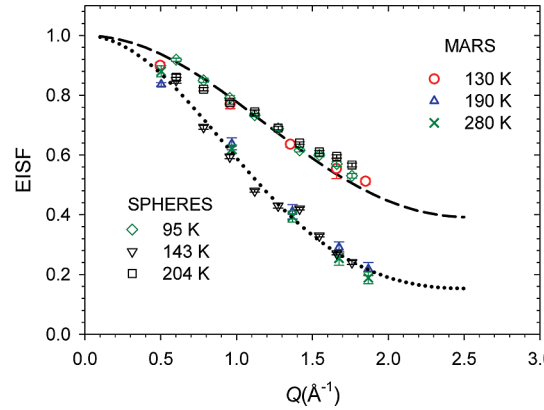

Figure 9. Measured and modeled EISFs. Dashed line, C_3 rotational diffusion model according to eq 5; dotted line, combination of C_2−C_3 rotational diffusion model according to eq 8. Not all the temperatures have been plotted in order to keep the figure clear.

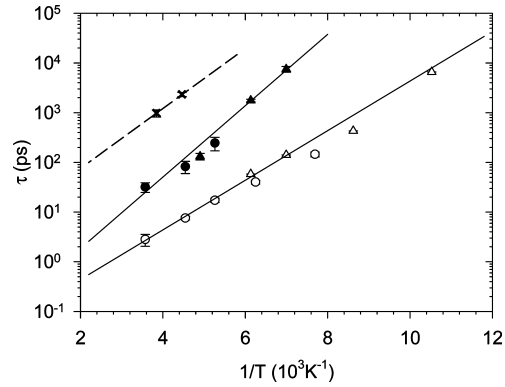

Figure 10. Thermally activated Arrhenius behavior of the rotational and translational diffusion of H in β-$Ca(BH_4)_2$. The triangles are the SPHERES experimental mean residence time (τ) and the circles the MARS experimental values. Filled symbols: rotation around the C_2 axis, open symbols rotation around the C_3 axis. The cross symbols are the mean resident time between two diffusional jumps (data from SPHERES). τ, inversely proportional to the inelastic broadening, is fitted as $\tau_0 \exp((E_a)/(k_BT))$ with $\tau_{0C2} = 5.6 \times 10^{-2}$ ps, $E_{aC2} = 0.14$ eV and $\tau_{0C3} = 5.0 \times 10^{-2}$ ps, $E_{aC3} = 0.10$ eV. The broken line is the fit for the diffusional jumps ($E_{aD} = 0.12$ eV, prefactor $\tau_{0D} = 4.7$ ps).

$$\tau = \tau_0 \exp\left(\frac{E_a}{k_B T}\right) \tag{12}$$

where the prefactor τ_0 is a constant, E_a is the energy barrier for the motion, k_B is the Boltzmann constant, and T is the temperature. Figure 10 displays the experimental characteristic times of the two thermally activated rotations together with the Arrhenius fits. The following values are obtained for the energy barriers: 0.14 and 0.10 eV for the C_2 and the C_3 rotations, respectively (see Table 4).

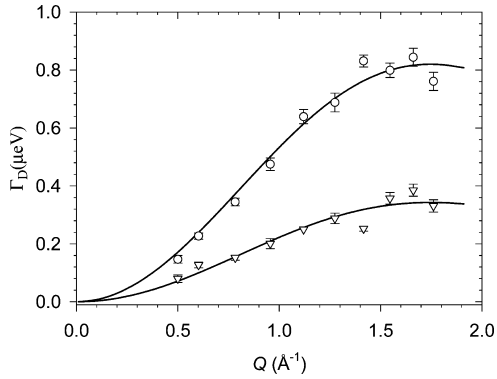

Figure 11. HWHM of the Lorentzian QENS component for β-$Ca(BH_4)_2$, as a function of Q measured with SPHERES, at 224 K (▽) and 260 K (o). The full curves show the fits of the Chudley−Elliot model (eq 13) to the data.

For a nonlocalized motion, for example, long-range translational diffusion, the inelastic line broadening is Q-dependent.[8] Because hydrogen diffusion in complex hydrides can be vacancy-mediated, it must be taken into account that only the motion of the vacancy can be considered as random walk, whereas the involved atomic motions are correlated. Thus, the so-called encounter model should be used to describe the correlated jumps.[40] Nevertheless, in a zero-order approximation, that is, one atomic jump per stochastic vacancy diffusion step, the Chudley−Elliott model[41] can be used. The only effect is a rescaling of τ_D, the mean time between two jumps.[40,42,43] In the Chudley−Elliot model, the Q-dependence of the HWHM (Γ_D) is given by[8]

$$\Gamma_D(Q) = \frac{\hbar}{\tau_D}\left(1 - \frac{\sin(QL)}{QL}\right) \qquad (13)$$

where L is the effective jump length. τ_D and L were extracted from the fits of the Chudley−Elliott model to the data obtained with SPHERES at 224 and 260 K (see Figure 11 and Table 4). The effective jump length was found to be about 2.5 Å (it corresponds to the shortest H−H distance between two neighboring BH_4^- groups). An Arrhenius fit to the QENS data for the two available temperatures yields an energy barrier of E_{aD} = 0.12 eV and a prefactor of τ_{0D} = 4.7 ps (see Figure 10 and Table 2).

DFT Calculations. The calculated structural parameters for the relaxed β-$Ca(BH_4)_2$ are displayed in Table 1. The Wyckoff positions and cell parameters are in good agreement with those from ref 16.

The results from the QENS experiments indicated localized dynamic events such as rotations of borohydride units as well as possible high-temperature diffusion. When using the Schönflies notation,[44] there are four different types of permutations possible for a single tetrahedral borohydride group. S4 axes and mirror planes can be quickly discarded because they are not rotations but rearrangements of hydrogen atoms which are much higher in energy because of the required formation of a planar BH_4 configuration during the rearrangement. Then, only various C_2 and C_3 axes remain. Figure 12 presents a 2D rigid rotation potential energy surface (PES) calculated by using a C_2-axis and a C_3-axis of a single BH_4^- as the degrees of freedom. The starting point for the calculation is the relaxed structure, and thus, the origin of the axis represents an energy minimum. As expected from their symmetry, energy minima for the rotations around the C2-axis occur at π and around the C_3-axis at $(2\pi)/3$ and $(4\pi)/3$. It shows that a slightly distorted C_3 rotation yields the lowest barrier and that a wobbly C_2-like rotation has a somewhat higher barrier (a difference of approximately 80%). The barrier heights calculated from the rigid rotation being higher than the barriers suggested by the experiments, NEB calculations were carried out with all the atoms in the supercell free to move. These calculations yielded barriers and characteristic times in good quantitative agreement with those of the experiments (see Table 2 and Figure 13). The calculated characteristic time for C_2 is about twice that of C_3. Looking at Figure 12, it can be seen that the environment of the saddle points for each rotation are quite different, and the vibrational calculations also revealed modes that involve motion of the cations, different by roughly a factor of 2. These finding are in reasonable agreement with experiments, where the prefactor for C_2 is found to be 10% larger than the one for C_3.

The theoretically expected temperature dependences of the HWHMs of the QENS spectra are plotted in Figure 8 together with the experimental values. The calculated lines were obtained

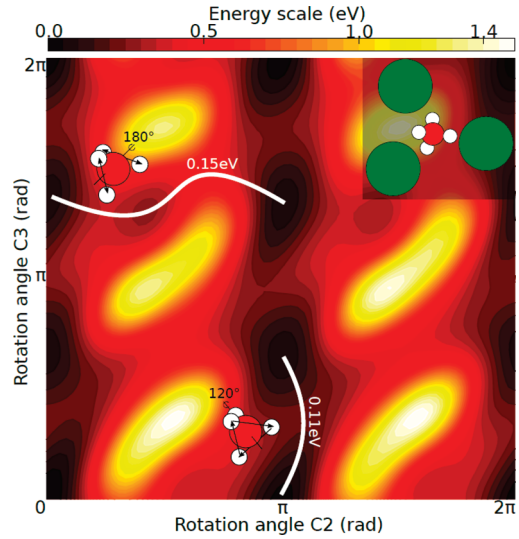

Figure 12. PES for BH_4^- rigid rotations along the C_2-axis and C_3-axis. The marked paths represent those chosen to do the NEB calculations. Their respective NEB barrier heights are written next to each one. The inset shows the immediate environment of a BH_4^- unit. Large, medium, and small spheres: Ca, B, and H atoms, respectively.

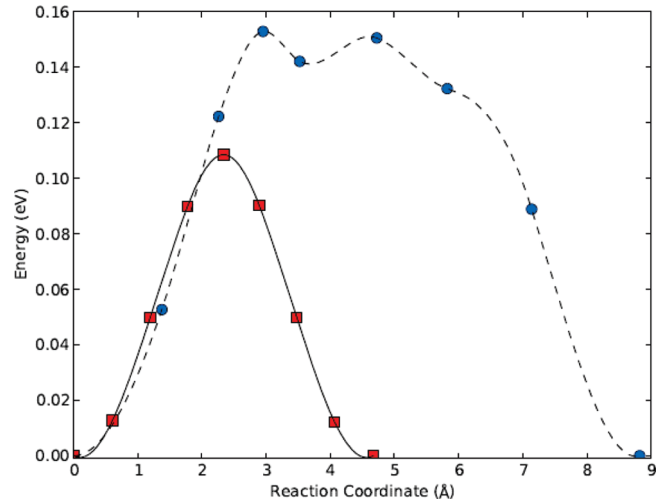

Figure 13. Calculated minimum energy path for the C_2 (blue circles) and C_3 (red squares) rotations. Each point is an NEB image; the lines are interpolations between them obtained by using also the forces. The reaction coordinate is the additive motion of atoms in the supercell.

by using eqs 9−11, with the characteristic times obtained by using the Arrhenius law (eq 12) and the energy barriers and prefactors from the DFT calculations. According to the experimental results, it should be noted that, although the combination of the two rotations (C_2-C_3) should give three Lorentzian, two have comparable HWHMs ($\Gamma_1 \approx \Gamma_2$) and can hardly be separated experimentally.

With two rotations unambiguously identified, only one dynamic event involving nonlocalized motion remained unexplained. Because further rotation could be ruled out, the diffusion process should be analyzed. Three vacancy-mediated diffusion events, H jumps between two neighboring BH_4^-, and diffusion of BH_4^- and BH_3 groups, were calculated. All were found to have high formation energies of the corresponding neutral vacancies and high diffusion energy barriers (see Table 3). Subsequently, interstitial-mediated diffusion of H, H_2, and H_2O were considered. The H interstitial is found to be unstable and formed a H_2 interstitial coupled to a H vacancy on a BH_4^-, with a very high formation energy (see Table 3). H_2O and H_2 interstitials were found to have low formation energies, that is, −0.05 and 0.4 eV, respectively. Two pathways were identified for H_2O diffusion, one involving a flip of the molecule and one giving a longer jump distance with a higher energy barrier; nevertheless, both pathways exhibit values slightly different from the experimental ones. Only interstitial H_2 diffusion gave a barrier and jump length which corresponds well to the experimentally observed value (Tables 2 and 3). The agreement between the calculated characteristic time for H_2 diffusion and the one obtained experimentally is not absolute; however it should be noted that the later was extracted from an Arrhenius fit with only two points. It is subject to caution and yields an uncharacteristically high prefactor.

All the information about the initial and final coordinates of the species to diffuse (interstitial H_2 and H_2O) are available in the Supporting Information.

Discussion

The analysis of the QENS data obtained for β-$Ca(BH_4)_2$ has shown that, within the time scale accessible by the two instruments used, two types of thermally activated hydrogen dynamics were observable in the temperature range from 90 to 320 K. The first type is described by localized H motion, that is, reorientations of the BH_4^- unit around the C_2-axis and C_3-axis. The experimental and DFT calculated energy barriers are in excellent agreement, giving $E_{aC2} = 0.14$ (0.15) eV and $E_{aC3} = 0.10$ (0.11) eV, experimental (calculated) values. The rotation about the C_3-axis is found to be energetically more favorable than the one around the C_2-axis.

The second type of hydrogen dynamics could not be described by rotational diffusion. With a Chudley−Elliot type Q-dependent broadening (nonlocalized event) giving a characteristic jump length of ∼2.5 Å, in agreement with the shortest H−H distance between two BH_4^- groups, a likely event would thus be a hydrogen-vacancy jump between neighboring groups. Nevertheless, the DFT results for this process indicated a slightly shorter jump length 2.1 Å, with the BH_3 complex becoming planar, a higher energy barrier 0.46 eV, versus ∼0.12 eV experimentally, and a high energy for the formation of the vacancy (2.09 eV). All other vacancy-mediated diffusion mechanisms were also discarded because of their high energies of formation, thus interstitial H, H_2, and H_2O diffusions were studied. H_2 interstitial diffusion gave results (0.09 eV, 2.1 Å) with the best agreement to the experimental one (∼0.12 eV, ∼2.5 Å). Nevertheless, this latter result was obtained from only two experimental points, and the H_2O interstitial diffusion cannot be strictly discarded. A possible explanation of the origin of H_2 and/or H_2O interstitials is that they are formed during the synthesis of the compound. The MS measurement did not show any trace of water nor of oxygen, and the small release of hydrogen below 565 K correlates with the formation of an oxide phase. Given the oxygen free environment, the oxide possibly results from a reaction of the hydride with trapped interstitial water, or even THF, forming interstitial hydrogen that subsequently desorbs.

In $LiBH_4$, motion of entire BH_4^- units has been identified as the main mass transport mechanism above the melting temperature,[45,46] whereas at low temperatures, a net transport of atomic hydrogen, probed by hydrogen/deuterium exchange, was also observed, although at a very low rate.[47,48] From the results presented in this study, no such hydrogen dynamics have been detected, and it will be too speculative to conclude here that the observed translational diffusion of hydrogen is part of the mechanism for the bulk decomposition of $Ca(BH_4)_2$. The correlation between the QENS and DFT calculations indicates that, most probably, it is the diffusion of interstitial H_2 that was observed; but it is probably due to a side reaction with trapped synthesis residue, leading to the partial oxidation of the compound and hydrogen release.

The combined DFT−QENS approach has been shown to be very useful both in the interpretation of the data and to determine crucial quantities useful to develop new experiments including the characteristic times and the energies barriers.

Acknowledgment. This work is based on experiments performed at the Swiss spallation neutron source SINQ, Paul Scherrer Institute, Villigen, Switzerland and at FRMII, JCNS Garching, Germany. The authors would like to acknowledge the European Graduate School for Sustainable Energy Technology and the Nordic Center for Excellence on Hydrogen Storage Materials. The Danish Center for Scientific Computing is acknowledged for super-computer access. The Center for Atomic Materials Design (CAMD) is supported by the Lundbeck Fondation. Financial support by EU-IP NESSHY (Contract #518271) and the ERA-NET project Hy-CO is also gratefully acknowledged.

Supporting Information Available: Initial and final coordinates of the species (interstitials H_2 and H_2O) to diffuse together with plots of the surrounding atoms. This material is available free of charge via the Internet at http://pubs.acs.org.

References and Notes

(1) Züttel, A.; Rentsch, S.; Fischer, P.; Wenger, P.; Sudan, P.; Mauron, P.; Emmenegger, C. *J. Alloy. Compd.* **2003**, *356−357*, 515.
(2) Nakamori, Y.; Miwa, K.; Ninomiya, A.; Li, H.; Ohba, N.; Towata, S.-I.; Züttel, A.; Orimo, S.-I. *Phys. Rev. B* **2006**, *74*, 045126−1.
(3) Miwa, K.; Aoki, M.; Noritake, T.; Ohba, N.; Nakamori, Y.; Towata, S.-I.; Züttel, A.; Orimo, S.-I. *Phys. Rev. B* **2006**, *74*, 155122–1.
(4) Severa, G.; Rönnebro, E.; Jensen, C. M. *Chem. Commun.* **2010**, *46*, 421.
(5) Rönnebro, E.; Majzoub, E. H. *J. Phys. Chem. B.* **2007**, *111*, 12045.
(6) Kim, J.-H.; Shim, J.-H.; Cho, Y. W. *J. Power Sources* **2008**, *181*, 140.
(7) Barkhordarian, G.; Jensen, T. R.; Doppiu, S.; Rösenberg, U.; Borgschulte, A.; Gremaud, R.; Cerenius, Y.; Dornheim, M.; Klassen, T.; Bormann, R. *J. Phys. Chem. C* **2008**, *112*, 2743.
(8) Bée, M. *Quasielastic Neutron Scattering*; Adam Hilger: Philadelphia, PA, 1988.
(9) Richter, D.; Hempelmann, R.; Vinhas, L. A. *J. Less Common Met.* **1982**, *88* (2), 353.
(10) Campbell, S. I.; Kemali, M.; Ross, D. K.; Bull, D. J.; Fernandez, J. F.; Johnson, M. R. *J. Alloys Compd.* **1999**, *293−295*, 351.
(11) Skripov, A. V.; Udovic, T. J.; Rush, J. J. *Phys Rev. B* **2007**, *76*, 104305–1.

(12) Skripov, A. V.; Udovic, T. J.; Cook, J. C.; Hempelmann, R.; Rempel, A. A.; Gusev, A. I. *J. Phys.: Condens. Matter* **2009**, *21*, 175410–5.

(13) Voss, J.; Shi, Q.; Jacobsen, H. S.; Lefmann, K.; Zamponi, M.; Vegge, T. *J. Phys. Chem. B.* **2007**, *111*, 3886.

(14) Remhof, A.; Łodziana, Z.; Butcher, F.; Martelli, P.; Pendollino, F.; Friedrichs, O.; Züttel, A.; Embs, J. P. *J. Phys. Chem.* **2009**, *113*, 16834.

(15) Verdal, N.; Hartman, M. R.; Jenkins, T.; DeVries, D. J.; Rush, J. J.; Udovic, T. J. *J. Phys. Chem. C* **2010**, *114*, 10027.

(16) Butcher, F.; Łodziana, Z.; Remhof, A.; Friederichs, O.; Borgschulte, A.; Mauron, P.; Züttel, A.; Sheptyakov, D.; Barkhordarian, G.; Bormann, R.; Chlopek, K.; Fichtner, M.; Sørby, M.; Riktor, M.; Hauback, B.; Orimo, S. *J. phys. Chem. B* **2008**, *112*, 8042.

(17) Filinchuk, Y.; Rönnebro, E.; Chandra, D. *Acta Mater.* **2009**, *57*, 732.

(18) Łodziana, Z.; Vegge, T. *Phys. Rev. Let.* **2004**, *93* (14), 145501.

(19) Łodziana, Z.; Vegge, T. *Phys. Rev. Let.* **2006**, *97* (11), 119602.

(20) Filinchuk, Y.; Chernyshov, D.; Cerný, R. *J. Phys. Chem. C* **2008**, *112*, 10579.

(21) Riktor, M. D.; Sørby, M. H.; Chlopek, K.; Fichtner, M.; Buchter, F.; Züttel, A.; C., H. B. *J. Mater. Chem.* **2007**, *17*, 4939.

(22) Hunter, B. *IUCR Powder Diffraction Newsletter,* **1998**, 20.

(23) Wuttke, J. To be published; http://www.jcns.info/jcns_spheres.

(24) http://sinq.web.psi.ch/sinq/instr/mars.html.

(25) Wuttke, J. http://www.messen-und-deuten.de/slaw.

(26) Azuah, R. T.; Kneller, L. R.; Qiu, Y.; Tregenna-Piggott, P. L. W.; Brown, C. M.; Copley, J. R. D.; Dimeo, R. M. *J. Res. Natl. Inst. Stan. Technol.* **2009**, *114*, 341.

(27) Bahn, S. R.; Jacobsen, K. W. *Comput. Sci. Eng.* **2002**, *4*, 56.

(28) Hammer, B.; Hansen, L. B.; Nørskov, J. K. *Phys. Rev. B* **1999**, *59*, 7413.

(29) Kohn, W.; Sham, L. J. *Phys. Rev.* **1965**, *140*, 1133.

(30) Vanderbilt, D. *Phys. Rev. B* **1990**, *41*, 7892.

(31) Perdew, J. P.; Chevary, J. A.; Vosko, S. H.; Jackson, K. A.; Pederson, M. R.; Singh, D. J.; Fiolhais, C. *Phys. Rev. B* **1992**, *46*, 6671.

(32) Liu, D. C.; Nocedal, J. *Math. Program.* **1989**, *45*, 503.

(33) Henkelman, G.; Uberuaga, B. P.; Jonsson, H. *J. Chem. Phys.* **2000**, *113*, 9901.

(34) Bitzek, E.; Koskinen, P.; Gähler, F.; Moseler, M.; Gumbsch, P. *Phys. Rev. Lett.* **2006**, *97*, 170201.

(35) Vineyard, G. H. *J. Phys. Chem. Solids* **1957**, *3*, 121.

(36) Maoa, J.; Guoa, Z.; Poha, C. K.; Ranjbara, A.; Guoc, Z.; Yuc, X.; Liua, H. *J. All. Compd.* **2010**, *500*, 200.

(37) Kim, Y.; Reed, D.; Lee, Y.-S.; Lee, J. Y.; Shim, J.-H.; Book, D.; Cho, Y. W. *J. Phys. Chem. C* **2009**, *113*, 5865.

(38) Riktor, M. D.; Sørby, M. H.; Chlopek, K.; Fichtner, M.; B.C., H. *J. Mater. Chem.* **2009**, *19*, 2754–2759.

(39) RiktorM, M. D. To be published.

(40) Levingston, R. C.; Rowe, J. M.; Rush, J. J. *J. Chem. Phys.* **1974**, *60*, 4541.

(41) Wolf, D. *Solid State Commun.* **1977**, *23*, 853.

(42) Didisheim, J. J.; Yvon, K.; Shaltiel, D.; Fischer, P. *Solid State Commun.* **1979**, *31*, 47.

(43) Dickens, M. H.; Hayes, W.; Schnabel, P.; T., Hutchings M.; Lechner, R. E.; Renker, B. *J. Phys. C: Solid State Phys.* **1983**, *16*, L1.

(44) Bender, O.; Schroeder, K. *Phys. Rev. B* **1979**, *19*, 3399.

(45) Schoenflies, A. *Math. Ann.* **1889**, *34*, 172.

(46) Shane, D. T.; Bowman, R. C.; Conradi, M. S. *J. Phys. Chem. C* **2009**, *113*, 5039.

(47) Corey, R. L.; Shane, D. T.; Bowman, R. C.; Conradi, M. S. *J. Phys. Chem. C.* **2008**, *112*, 18706.

(48) Borgschulte, A.; Züttel, A.; Hug, P.; Racu, A. M.; Schoenes, J. *J. Phys. Chem. A* **2008**, *112*, 4749.

(49) Gremaud, R.; Łodziana, Z.; Hug, P.; Willenberg, B.; Racu, A.-M.; Schoenes, J.; Ramirez-Cuesta, A. J.; Clark, S. J.; Refson, K.; Züttel, A.; Borgschulte, A. *Phys. Rev. B* **2009**, *80*, 100301–1.

JP107281V

Risø DTU is the National Laboratory for Sustainable Energy. Our research focuses on development of energy technologies and systems with minimal effect on climate, and contributes to innovation, education and policy. Risø has large experimental facilities and interdisciplinary research environments, and includes the national centre for nuclear technologies.

Risø DTU
National Laboratory for Sustainable Energy
Technical University of Denmark

Frederiksborgvej 399
PO Box 49
DK-4000 Roskilde
Denmark
Phone +45 4677 4677
Fax +45 4677 5688

www.risoe.dtu.dk